UNIVERSITY OF THE
WITWATERSRAND,
JOHANNESBURG

Miniaturised Charpy Impact Toughness Testing for the Characterisation of Laser Powder Bed Fusion - Built and Laser Shock Peened Ti-6Al-4V

MSc Dissertation

Abhay Nookant Netrapal Chundunsing

Student Number: 2634879
Supervisors: Prof. C. Polese and Mr T. Strydom

A dissertation submitted to the Faculty of Engineering and the Built Environment, University of the Witwatersrand, Johannesburg, in fulfilment of the requirements for the degree of Master of Science in Mechanical Engineering.

Johannesburg, 22 September 2025

Declaration

I declare that this dissertation is my own, unaided work, except where otherwise acknowledged. It is being submitted for the Master of Science in Mechanical Engineering degree at the University of the Witwatersrand, Johannesburg. It has not been submitted before for any other degree or examination at any other university.

Signed this on the 22 September 2025

A. N. N. Chundunsing

Abstract

Laser Powder Bed Fusion (L-PBF) Additive Manufacturing (AM) might produce inconsistent results that require testing and documentation for qualification and, eventually, certification for aerospace applications. Literature has shown that the inconsistent results in part mechanical performance could be attributed to part features such as porosity and imperfections, residual stresses, microstructure, surface integrity, and microhardness. These inconsistencies can compromise the reliability, safety, and performance of aerospace components, necessitating rigorous testing and documentation to ensure compliance with stringent industry standards. Therefore, a preliminary testing method called the Miniaturised Charpy V-Notch (MCVN) impact testing is used to qualitatively assess the integrity of the parts produced. It also assesses the variations in the identified features that result from the manufacturing technique. Ti-6Al-4V test samples were manufactured with the intentional variation of the hatch spacing distance, stress-relieved, and prepared according to specification. Laser Shock Peening (LSP) post-processing was also selectively performed on some samples. MCVN tests, which were performed on the modified and recalibrated equipment, revealed that increasing hatch spacing of ideal settings by around 80% resulted in a significant and discernible impact toughness difference. The corresponding peened samples, tested under the same conditions, indicated a slight improvement in the recorded absorbed energy values. While the microstructural structure remained the same for both sample sets, the % porosity, the surface average, and the microhardness showed some changes. Another significant contributing factor was also the induction of compressive residual stresses recorded post-LSP, which was beneficial in countering crack propagation. This work provides significant information on the subject matter that can help as a stepping stone to achieve a standard procedure in the preliminary qualification of parts at minimal costs.

Acknowledgements

I want to take this opportunity to express my sincere gratitude to those who have contributed to my MSc journey:

- To my family, especially my parents and sister, for their unwavering support.
- To my supervisors, Prof. Claudia Polese, for granting me the opportunity to pursue this master's program, and Mr Tristan Strydom, for his willingness to engage in discussions and offer valuable insights.
- To the Collaborative Programme in Additive Manufacturing of the Department of Science, Technology and Innovation (Memorandum of Agreement CSIR-NLC-CPAM-21-MOA-WITS-01) and the laser Rental Pool Programme of the Council for Scientific and Industrial Research (Agreement number CSIR-NLC-LRETA21-CON-001) for the funding provided to realise this work.
- To the African Laser Centre for encouraging students to showcase their research through their annual workshop, and for fully funding the trip to make this opportunity possible.
- To Mrs Marina Labuschagne, of the DST-NRF Centre of Excellence in Strong Materials, for her administrative assistance throughout this work.
- To the teaching, technical, and administrative staff at the School of MIA Engineering, Wits, for their dedicated support.
- To Mr Marius Vermeulen and his team at Aditiv Solutions for their valuable time, guidance, and input into this work.
- To Mr Nicholas Stiekema, for his assistance and expertise in executing Laser Shock Peening at the CSIR.
- To Mr Jacques Gerber of the MMU, for his help in using the electron microscope.
- To Prof. Michael Bodunrin from the School of CHMT Engineering at Wits, for his insightful contributions and advice.
- To Mr Zamokuhle Luthuli from Efficiency Projects for his significant time and efforts in acquiring accurate micro-CT readings at NMISA.

- To Dr Dreyer Bernard and the staff at NMU for their diligent efforts in achieving optimal residual stress measurements.
- Lastly, I want to thank my friends Marc, Takunda, Aliah, Natsai, and my postgraduate colleagues at the School of MIA Engineering for their collaboration and support throughout this journey.

Thank you all for your invaluable contributions.

Contents

List of Figures

List of Tables

List of Equations

Symbols and Nomenclature

AM	Additive Manufacturing
ANOVA	Analysis of Variance
ASM	American Society for Metals
ASTM	American Society for Testing and Materials
BCC	Body-Centred Cubic
BCT	Body-Centred Tetragonal
BSE	Backscattered Electrons
CCT	Continuous Cooling Transformation
CHMT	Chemical and Metallurgical
CM	Certification Memorandum
CPAM	Collaborative Programme in Additive Manufacturing
CSIR	Council of Scientific and Industrial Research
Cv	Coverage
DMLS	Direct Metal Laser Sintering
DSTI	Department of Science, Technology and Innovation
EASA	European Union Aviation Safety Agency
EDM	Electrical Discharge Machining
EDS	Explanatory Data Analysis
EDS	Energy-Dispersive X-Ray Spectroscopy
EU	European Union
FAA	Federal Aviation Administration
FGM	Functionally Graded Material
HAZ	Heat-Affected Zone
HCP	Hexagonal Close-Packed
HIP	Hot Isostatic Pressing
ISO	International Organisation for Standardisation
LoF	Lack of Fusion
L-PBF	Laser Powder Bed Fusion
LSP	Laser Shock Peening
MCVN	Miniaturised Charpy V-Notch
MIA	Mechanical, Industrial and Aeronautical
NASA	National Aeronautics and Space Administration
NIST	National Institute of Standards and Technology
NLC	National Laser Centre
Np	Pulse Density
OFAT	One Factor at a Time
PI	Power Intensity

RoI	Region of Interest
RPP	Rental Pool Programme
RS	Residual Stresses
SE	Secondary Electrons
SLM	Selective Laser Melting
SS	Spot Size
UCR	Unstable Crack Region
UTS	Ultimate Tensile Strength
XRD	X-Ray Diffraction
YS	Yield Strength

Chapter 1. Introduction

Laser Powder Bed Fusion (L-PBF), also known as Selective Laser Melting (SLM) or Direct Metal Laser Sintering (DMLS), is a relatively new additive manufacturing (AM) technique that has garnered significant attention across various industries in recent decades. The process is notable for its versatility and rapid adaptability to a wide array of materials and applications. However, despite the interest surrounding L-PBF, there is often a general hesitance in certain industries, such as aerospace and medical, regarding its use for medium to large-scale production. While it excels at quickly producing geometrically complex components, manufacturers often express reservations about its suitability for mechanically critical parts. This caution is frequently linked to the process's inherent complexity and the insufficient documentation available to evaluate the integrity of the produced components, which can lead to inconsistencies and unpredictable performance.

Many professionals in the aerospace field confidently assert that the L-PBF fabrication technique is the future of manufacturing. This technology has a high buy-to-fly ratio, which allows for using significantly less material and resources compared to conventional manufacturing methods. Furthermore, it enables the creation of intricate parts with fewer manufacturing constraints and opens the door to producing functionally graded materials (FGMs). While the technology has evolved rapidly, researchers and engineers are actively working to catch up by generating substantial documented evidence and deepening their understanding of the technique. This knowledge gap is not limited to aerospace, as it affects other industries. The medical and automotive sectors are also eager to commercialise this innovative manufacturing technique, although progress can sometimes be impeded. However, its potential remains clear, and the future trajectory appears highly promising.

As a South African research group specialising in L-PBF for aeronautical applications at the University of the Witwatersrand in Johannesburg, we initiated a comprehensive study on the characteristics of the manufacturing process and an evaluation methodology for the produced parts. Our focus was on the fabrication of the titanium alloy Ti-6Al-4V. This work was

supported by funding from the Collaborative Programme in Additive Manufacturing (CPAM) of the Department of Science, Technology and Innovation (DSTI) (Memorandum of Agreement CSIR-NLC-CPAM-21-MOA-WITS-01) and the laser Rental Pool Programme (RPP) of the Council of Scientific and Industrial Research (CSIR) for the LSP technology development (Agreement number CSIR-NLC-LRETA21-CON-001). One of the key objectives is to tackle the hurdles the technology faces in gaining market access.

Recent developments regarding these challenges have been articulated in a certification memorandum (CM) issued by the European Union Aviation Safety Agency (EASA), which is responsible for ensuring civil aviation safety in the European Union (EU). It carries out certification of aircraft, components, and related equipment. The agency has classified the L-PBF manufacturing process as 'highly dependent on material properties, process variables, and configuration,' emphasising that a thorough understanding of the process is essential for the certification of parts [1]. It is imperative to recognise the sensitivity of components in relation to their engineering properties to ensure the safety of the final products. The aerospace sector requires thorough testing and detailed documentation for part accreditation. Therefore, effective laboratory experimentation is essential for researchers and manufacturers to optimise part capabilities.

This study examines an uncommon, yet innovative and cost-effective method known as the Miniaturised Charpy V-Notch (MCVN) Impact Test, which could serve as a preliminary testing strategy for accreditation. It also examines the characteristic features of parts produced by the L-PBF manufacturing process and provides insightful explanations for the MCVN test results. The research evaluates the effectiveness of Laser Shock Peening (LSP), a mechanical post-manufacturing treatment that utilises a high-energy pulsed laser to generate shock waves through confined surface ablation. By characterising the L-PBF process and its outcomes, this work aims to provide critical insights and a robust early-stage testing methodology for part qualification, facilitating market acceptance and certification of L-PBF components, particularly in the aerospace industry.

1.1 Format of this Dissertation

Below is a detailed chapter-wise work plan that seamlessly integrates each aspect of the research.

Literature Review: This section provides an overview of the status of L-PBF AM for aerospace applications, highlighting discrepancies and their implications. It also summarises the relevant historical findings for context.

Aim and Objectives: The project's goals are outlined, and a comprehensive list of requirements has been developed to evaluate all essential components of the work.

Methods and Techniques: To meet the project requirements, a detailed experimental and investigative approach was developed. Additionally, a well-defined strategy outlining the practical steps to be taken was formulated, setting a clear path forward.

Testing and Evaluation: The experimental process was thoroughly documented, with each phase elaborated. This included detailed descriptions of the methodologies employed and encompassed a comprehensive account of the results that emerged.

Analysis and Discussions: The information gathered from a series of test results was analysed in detail and systematically compiled to identify any underlying relationships that could provide insight into the results. The understanding was aligned with the literature, so that any observation made was documented with appropriate reasoning.

Conclusions: A summary of all significant aspects of the work, as well as key findings and insights, are elaborated.

Further works: The shortcomings of the current work were pointed out as potential avenues for exploration in the future.

Chapter 2. Literature Review

This chapter examines the fundamental aspects of this research, with a particular emphasis on synthesising the extensive body of existing knowledge and analysing findings from previously published studies. It systematically identifies their limitations and potential areas for further advancement. The chapter is structured to facilitate the progressive integration of key concepts, fostering a coherent and analytically rigorous discussion. The principal objective is to define the scope of this study by undertaking a comprehensive exploration of the subject matter, thereby enabling a nuanced understanding of its intricacies and complexities.

2.1 Laser Powder Bed Fusion (L-PBF)

Additive Manufacturing (AM) is a transformative process that involves the strategic and incremental addition of material to construct a precise 3D object. The techniques for joining layers and bonding atoms are largely determined by the specific system, the materials employed, and the material delivery method. The standard ISO/ASTM 52900 categorises these methods and techniques into subgroups. One such subgroup is Powder Bed Fusion, which uses a heat source to selectively fuse layers of powdered material. In the case of Laser Powder Bed Fusion (L-PBF), a laser beam acts as the heat source [2], [3].

The L-PBF AM technique allows intricate shape designs to be produced efficiently without traditional methods [4]. The advancements in manufacturing techniques, particularly in cost efficiency, design customisation, and innovative material performance, present significant incentives for developing this technology. Over the past several decades, the number of 3D printing facilities across the globe has experienced substantial growth. Prominent companies such as EOS GmbH, 3D Systems, SLM Solutions, Renishaw plc, VELO3D, and Aditiv Solutions in South Africa, among others, have developed equipment utilising diverse systems to enhance the manufacturing method. However, despite all the progress made, improvement was mainly towards the technology, with limited emphasis on the potential diversity of product outputs that could result from these improvements.

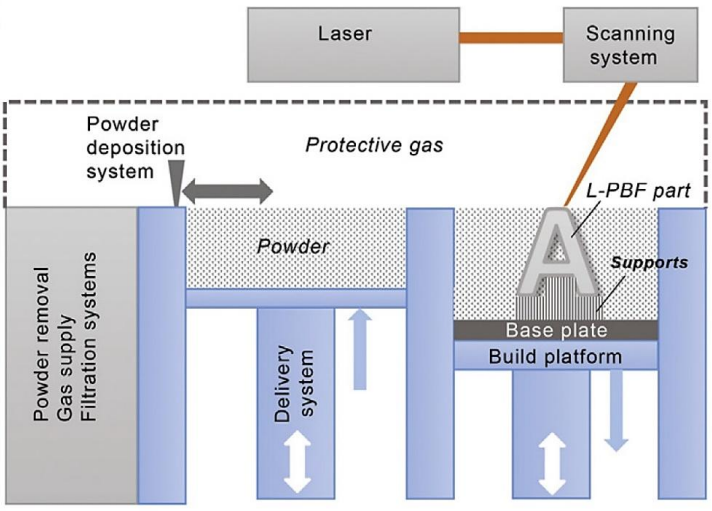

Figure 2-1 - The main components of the L-PBF manufacturing process [2].

The main components of the manufacturing technique are clearly labelled and outlined in Figure 2-1. This process produces parts on a build platform within a controlled environment. A high-energy laser beam selectively melts a thin layer of powdered material, effectively fusing the powder particles and the underlying layer or base plate. Given the numerous factors and possible manufacturing parameter combinations, the process can exhibit considerable variability, reflecting a complex interplay across multiple scientific disciplines. The key parameters can be categorised into four broad groups: "Machine-based," "Material-based," "Process-based," and "Post-treatment." These may also be further divided into predefined and variable parameters for more detailed analysis. Figure 2-2 and Table 2-1 below provide an understanding of the parameters, their classification, and how their possible combinations affect the melt pool characteristics that define L-PBF manufacturing. Although significant research has been conducted in this area, many instances still lack clear definitions and a thorough understanding of how these parameters interact [2].

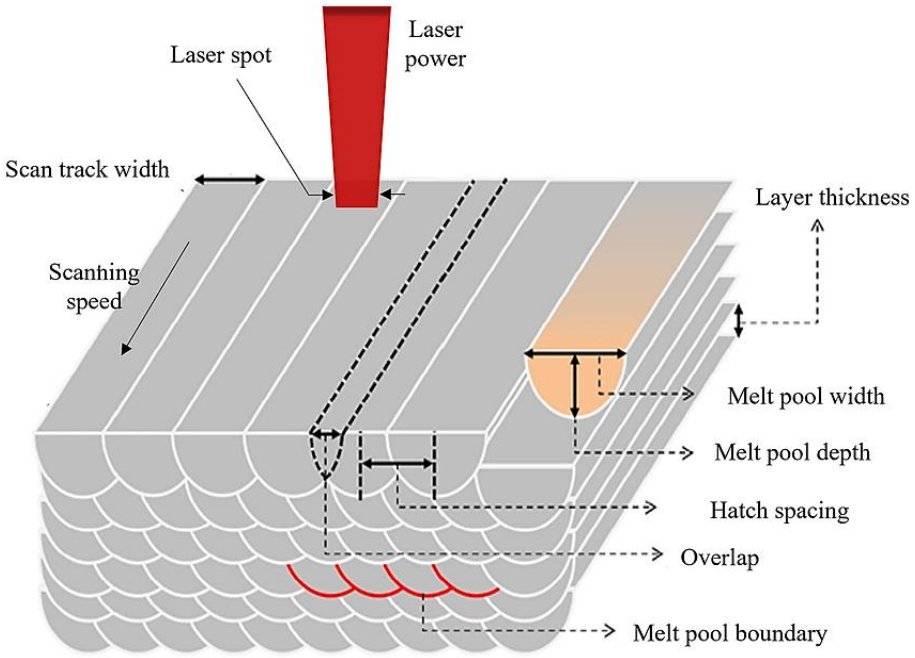

Figure 2-2 - Interaction of the main processing parameters of L-PBF [5].

Table 2-1 - Classification of L-PBF manufacturing process parameters.

Machine-Based	**Post-Treatment**
Predefined: • Laser properties • Baseplate heating* • Laser spot size* • Protective gas environment*	Predefined: • Stress relief & support removal Variable: • Heat treatment • Hot isostatic pressing • Mechanical surface treatment
Process-Based	**Material-Based**
Predefined: • Supports quantity & geometry Variable: • Laser power • Layer thickness • Scanning speed • Hatch spacing • Building orientation • Scanning pattern	Predefined: • Powder alloy composition • Powder particle density • Material thermal conductivity • Material melting point • Powder size & geometry • Powder pre-heating*

Note:

- ** Parameters can be predefined and variable depending on the facility.*

Sectors such as aerospace, automotive, medical, energy, power generation, tooling, and industrial goods increasingly recognise L-PBF's potential to produce intricately designed, high-performance components, with several cases demonstrating successful achievement.

Figure 2-3 - Additively manufactured fuel nozzle tip for LEAP aircraft engines [6].

2.1.1 L-PBF Manufacturing Challenges and Considerations

To fully understand the concepts and principles of L-PBF AM, it is essential to grasp the processes involved in creating a 3D object. The interaction between the parameters, as shown in Figure 2-2, contributes to the complexity and challenges of L-PBF manufacturing, which encompasses multiple aspects of physics. However, many believe that four key parameters stand out: layer thickness, laser power, scan speed, and hatch spacing. While variations in all parameters can make it challenging for researchers to comprehend and predict the process's outcomes, starting with these four factors can provide some understanding. Furthermore, insights from previous studies indicate that using these four parameters in conjunction can be effective, especially when it has been established that the variations in parameters are non-linear and complicate the ability to make accurate predictions [2], [7].

The standard variable called bulk energy density has been adopted and was developed to quantify and study the relationship of the key variable parameters. The bulk energy density, also known as volumetric energy density, is defined by Equation 2.1.

$$E = \frac{P}{hvL} \qquad \text{Equation 2.1}$$

Where:

- E is the bulk energy density
- P is the laser power
- h is the hatch spacing,
- v is the scanning speed, and
- L is the layer thickness.

The bulk energy quantifies how much energy is provided at a specific time to a particular volume of powder on the build platform [7]. This ratio is essential since it can help determine optimum parameter sets using a single value. The effects of properties on produced parts, particularly on physical and mechanical features, are defined and controlled at the laser interaction zone [2], [8].

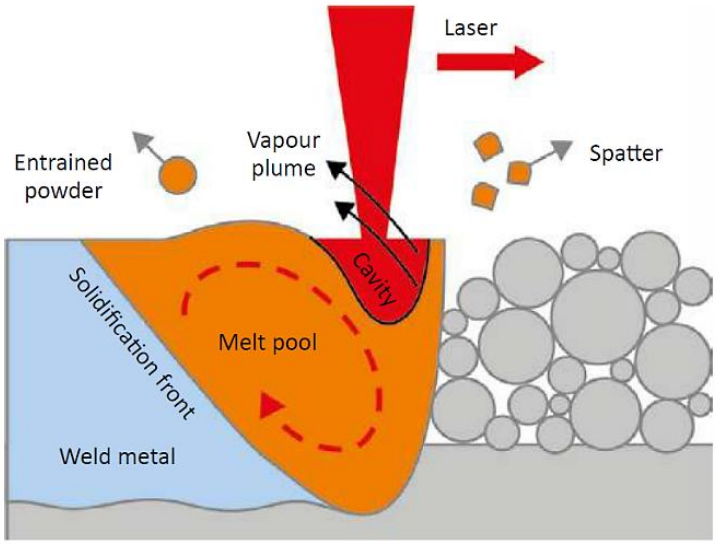

Figure 2-4 - Cross-sectional representation of an optimal laser interaction zone [8].

In an article published in the 2018 edition of METAL AM, Marc Saunders, the director of Global Solutions Centres at Renishaw plc, discusses how to determine the correct parameters for various materials and machines to achieve optimal melt pool dynamics, which ensures consistent results in AM builds [8]. The melt pool needs adequate depth and width to melt and fuse metal powder particles and bond with the previous layer and the surrounding powder or track. This concept is illustrated in Figure 2-4 and Figure 2-5 showing a stable laser interaction zone area and a plot of laser power versus scanning speed at a specific layer thickness, respectively. The definition of an operating window is crucial for achieving high part density. Scanning too fast at low laser power can prevent proper melting and fusion of the powder, causing lack of fusion (LoF) defects. Conversely, using too much laser energy at slow scanning rates can lead to overheating, deep melt pools, gas entrapment, and porosity. Pushing both parameters to their limits can cause instability, resulting in issues like spattering, humping, or balling [2]. As illustrated in the plot, hatch spacing is an essential factor to consider, as it affects the melt pool similarly to the scanning speed. Moreover, the size, temperature, and direction of the melt pool formation significantly influence the bonding quality and heat transfer rates (conduction and dissipation) in the heat-affected zone (HAZ). This operating window represents the ideal balance of parameters to achieve optimal part density, a primary concern of the manufacturing process.

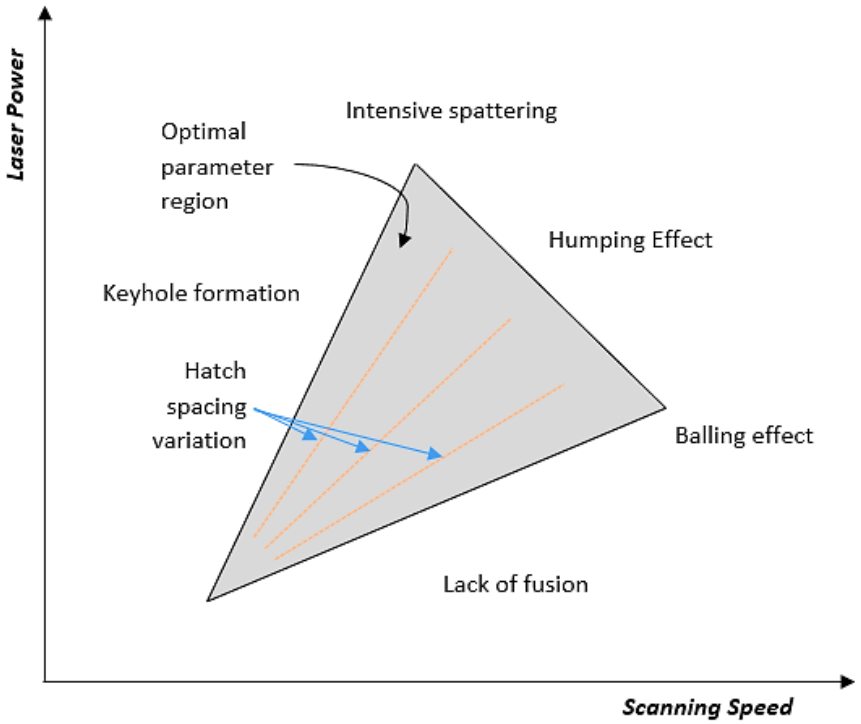

Figure 2-5 - Plot showing the operating window map [8].

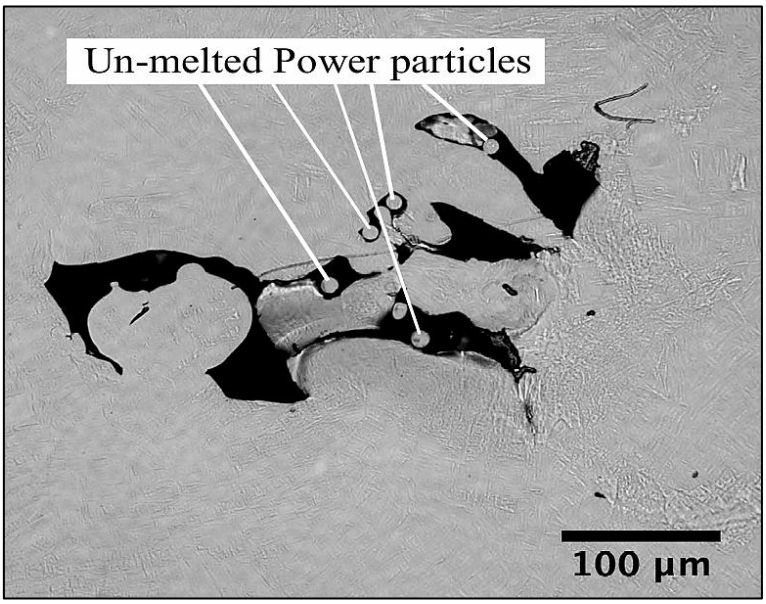

Figure 2-6 - Lack of Fusion in L-PBF produced Ti-6Al-4V with unmelted particles [9].

There are additional specificities that manufacturers consider when producing L-PBF parts for mechanically performing applications. Due to the similar nature of a moving heat source, challenges in L-PBF AM are often compared to welding [10]. Apart from producing defect-free parts, such as voids (microporosity), factors such as impurities, inclusions, inhomogeneities, internal cracks, and second-phase particles can significantly affect the ductility and workability of metals. The fracture-critical properties and fracture mechanisms of the parts produced are also crucial [11]. Crack propagation in AM parts is a concern and should be investigated whether it occurs either along grain boundaries (intergranular) or through grains (transgranular) [12]. One of the primary considerations for this involves the microstructural structure. Observations from previous work on the high cooling rates inherent to L-PBF AM of Ti-6Al-4V alloys, for example, have revealed inherent columnar grain growth. This configuration of elongated grains of non-equilibrium α′ (instead of α) within a β matrix along the direction of the build is created, which yields parts with high hardness and strength but anisotropic characteristics and low ductility. Such characteristics are sometimes undesirable, mainly where loading is not applied in any specific orientation, and a minimum mechanical requirement for elongation at fracture is required [2].

Figure 2-7 - The microstructure of Ti-6Al-4V produced by L-PBF [13].

When producing mechanically robust parts, it is also very important to consider the residual stresses (RS) associated with L-PBF AM. These stresses significantly influence the properties of the final product. The moving heat source creates transient conditions that impact microstructural quality and introduce residual stresses. These RS can lead to solidification cracking, particularly in the fusion zones [7]. Such issues can cause warping or deformation, presenting challenges that impede the consistency of the produced parts and highlighting the necessity for post-processing [12].

As it can be observed, especially with manufacturing defects, the certification path can be quite complex. Understanding the type and origin of defects is paramount to achieving the required robustness for manufacturers to establish L-PBF as a reliable technique [7]. However, the certification and qualification processes can be costly, presenting challenges to the widespread adoption of AM. Standards like ISO 9001 and SAE AS9100 outline the steps necessary to achieve the desired outcomes [14], [15]. Testing is not just a one-time effort at the beginning of the design phase; it is an ongoing requirement that continues throughout the development of the final product. In aerospace applications adherence to additional technical standards such as NASA 6030 [16] is also crucial, often causing the expenses associated with achieving these standards to surpass the forecasted budget [17].

Therefore, the L-PBF manufacturing process can be portrayed as a double-edged sword. Besides its incredible versatility, a lot of considerations need to be made. One of the most challenging aspects is to be able to establish a universal approach to the process. Nevertheless, the procedures of establishing qualification for L-PBF-produced parts are very similar to conventional manufacturing methods where product and process requirements, methods used, and process sensitivity are looked into to ensure repeatable results are obtained [12].

This chapter focuses on the mechanical characteristics and their determination. However, understanding these characteristics relies on the other aspects discussed, as will be demonstrated later in the chapter.

2.2 Commercial Integration of L-PBF AM

The complex nature of L-PBF AM presents challenges, such as inconsistencies in parts that have yet to be resolved [7]. That is why design engineers rely on qualification and certification procedures to ensure the safe application of such parts. However, it is essential to clearly understand the terms ‘qualification’ and ‘certification’ to avoid any confusion. Qualification refers to the internal process of demonstrating that all manufacturing process elements can meet specific requirements before regular production begins. In contrast, certification provides documented evidence that the manufacturing process complies with the technical standards applicable to its intended industry [18]. Qualification involves ensuring that a part is manufactured to meet a specific strength requirement by pinpointing the conditions and characteristics that influence it. On the other hand, certification relies on strength testing reports conducted under standardised methods and conditions on actual components, helping to ascertain whether the part is suitable for an intended use. The two concepts are, however, interconnected, as improvements in one often hinge on the other, creating a collaborative relationship between them.

In the aerospace industry, stringent regulations make the qualification and certification of parts complex. Aerospace applications demand a unique blend of essential properties, yet many components often fall short of these critical requirements. However, advancements in materials and manufacturing techniques are transforming how aircraft are designed, built, and operated, resulting in lighter, stronger, more cost-effective, and more durable aircraft. Because safety is a top priority, aviation authorities like the Federal Aviation Administration (FAA) or the EASA have established strict regulations focusing on damage tolerance of vital structural components. These regulations not only enhance safety but also spark innovation in engineering, creating a ripple effect that influences other industries [19].

2.2.1 Establishing Control Protocols

To effectively manage all aspects of metal AM, Richard Russell et al. [12] emphasised in their work the importance of regulatory guidelines from various international organisations, which serve as roadmaps for parts certification. The National Institute of Standards and Technology (NIST) and National Aeronautics and Space Administration (NASA) have identified four essential quality and control (Q&C) requirements for the aeronautical field: (1) Closed-loop process control, (2) Standardised guidelines, (3) Shared databases, and (4) Protocols that ensure parts are reproducible [12]. The guidelines are set by regulatory bodies (EASA & FAA) in the United States to establish testing procedures for material properties based on certification standards set by organisations such as the American Society for Testing and Materials (ASTM) and the International Organisation for Standardisation (ISO). The aerospace industry adheres to these standards and may employ specialised testing methods when standardised procedures are unavailable [19]. An advisory circular issued by the FAA, the US Department of Transportation, outlines the requirements for ensuring compliance with federal powder bed fusion (PBF) parts regulations [20]. Recently, GE Aerospace, a leading provider of jet and turboprop engines, received the FAA's approval to use compressor inlet temperature sensor housings in its GE90 jet engines [12], [21].

Currently, 17% of aircraft parts fail due to fabrication imperfections. Proper process certification can only help achieve a robust manufacturing process, which requires thorough testing of manufactured parts using a building block approach [10], [20]. This is discussed in section 2.2.2. Understanding the root causes of failures that degrade part performance involves the following steps:

- Laboratory investigations that collect data as evidence.
- Fracture mechanics and failure analysis that use material properties obtained from testing to derive insights and relationships.
- Categorising failures based on various issues such as distortions, deformations, fractures, corrosion, and wear.

2.2.2 Laboratory Testing for Documentation

Structural failures can occur in various ways when a material can no longer withstand the stresses applied to it, with one of the primary forms being fractures. A fracture arises when too much stress is applied to a specific area, causing the material to break. Also, due to imperfections in the material, the strains encountered under stress may deviate from what was anticipated. These strains can vary in magnitude and direction, potentially leading to the failure of the material. Laboratory investigations are essential to systematically identify the root causes of these fractures. The explanation and classification of failure types can be done by analysing the material behaviour at the fracture surfaces. Once we categorise the failures, appropriate prevention methods can be implemented to mitigate their impact. This is why conducting fracture testing on materials to obtain their mechanical properties may produce results that differ from those seen in uniaxial tension or planar bending tests [10] [11].

Testing procedures are organised into specific categories of the building block, as shown in Figure 2-8. Testing begins with small sample coupons and progresses to actual components. As the testing moves from coupons to entire components, the number of tests required decreases, but the associated costs increase significantly. Generic specimens are primarily used to gather data for developing a database, and most of the testing will support future applications in the aerospace industry [19]. Key considerations for testing L-PBF AM parts for aerospace applications are: [12]

1. Levels of defects
2. Microstructure forms
3. Mechanical Properties
4. Part Surface Quality
5. Post Processing requirements
6. Cost Considerations

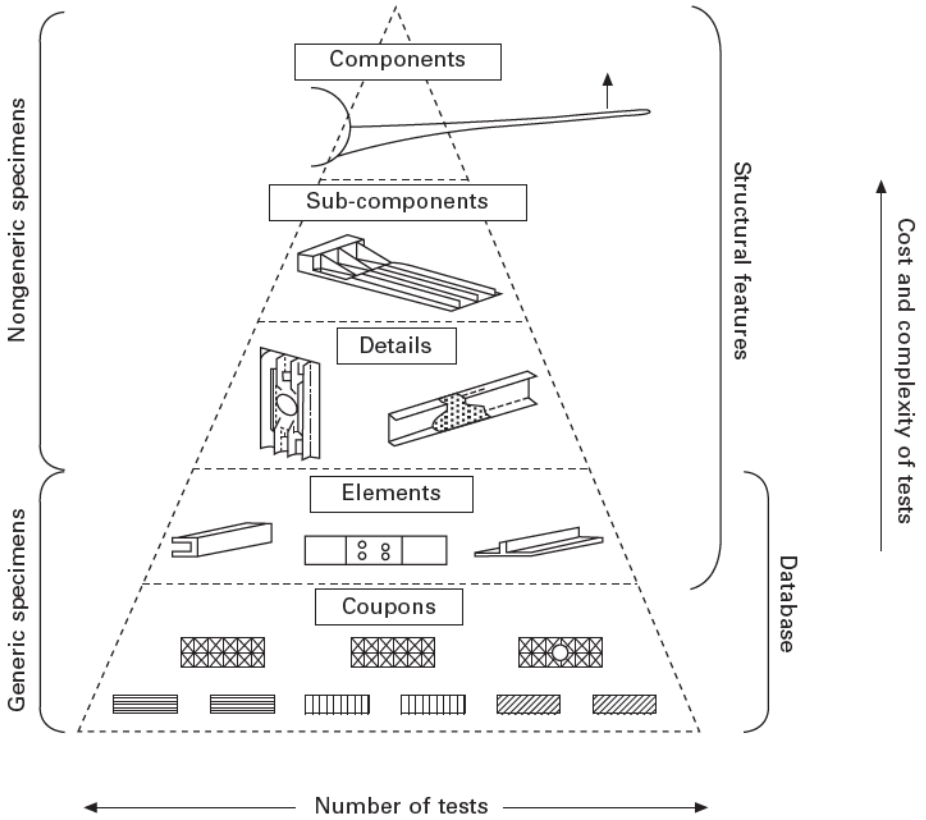

Figure 2-8 - The testing pyramid showcasing the certification pathway [19].

The coupon tests are conducted under standardised conditions that outline specific parameters, including sample size and loading rate. Organisations like the ASTM establish these testing conditions. There are two main categories of coupon tests: quantitative and qualitative. Quantitative tests yield data suitable for design and certification purposes, with examples including tension, compression, and creep tests. In contrast, qualitative tests provide results intended solely for comparison. For instance, tests like hardness and Charpy impact assessments offer a straightforward "go/no-go" evaluation of materials. Certification testing at the coupon level focuses on measuring material properties under various load conditions [19].

2.3 L-PBF of Ti-6Al-4V Alloy

The use of titanium alloys in L-PBF is significant, comprising about a third of all metals employed in AM. The static properties of AM Titanium parts have been reported to be comparable to those of traditional wrought products. They have excellent mechanical properties, such as high-temperature specific strength, good fracture resistance, low specific gravity, and excellent corrosion resistance [7]. Since the 1950s, the aerospace sector has utilised titanium for military and commercial aircraft, accounting for 25-30% of the weight in modern jets. Titanium's high utilisation in aerospace is due to its key advantage of performing well in heavily loaded applications, especially where space is at a premium. However, growth in this area has been somewhat sluggish, primarily due to the high costs associated with manufacturing and machining [19]. As a result, there is a strong push to advance the field of AM for titanium components. Ti-6Al-4V is one of the most widely used titanium alloys, representing nearly half the market.

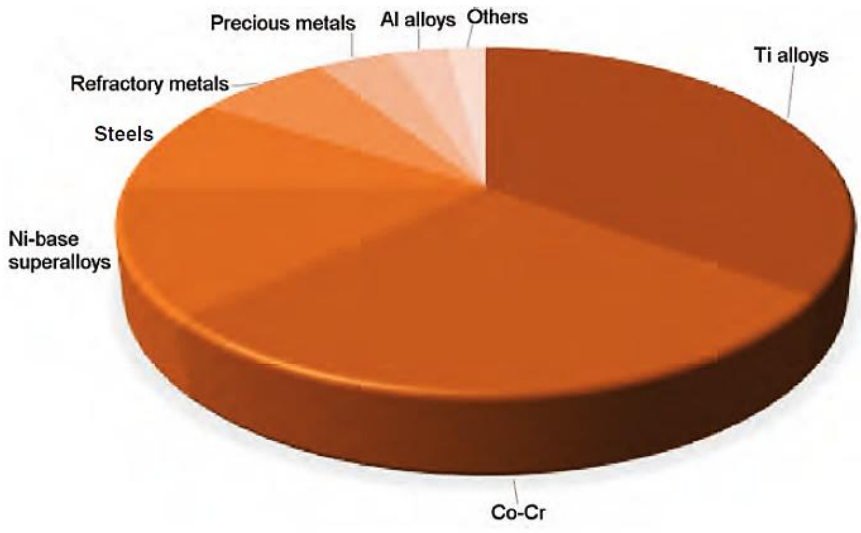

Figure 2-9 – Illustrative distribution of metals used in additive manufacturing [7].

2.3.1 Ti-6Al-4V Alloy

Titanium exists in two crystallographic forms. The alpha (α) phase, with a hexagonal close-packed (hcp) crystal structure and the beta (β) phase, in a body-centred cubic (bcc) crystal structure [22]. By alloying titanium alloys, alterations to the microstructural configuration can be made, thus altering its properties. Ti-6Al-4V is a two-phase, α + β alloy with an allotropic behaviour. Aluminium and Vanadium serve as alpha and beta stabilizers, controlling the transformation of the crystal structure from α + β at room temperature to all β through heating. The alloy's microstructure can vary significantly based on its processing history, cooling temperature, and cooling strategy [22], [23].

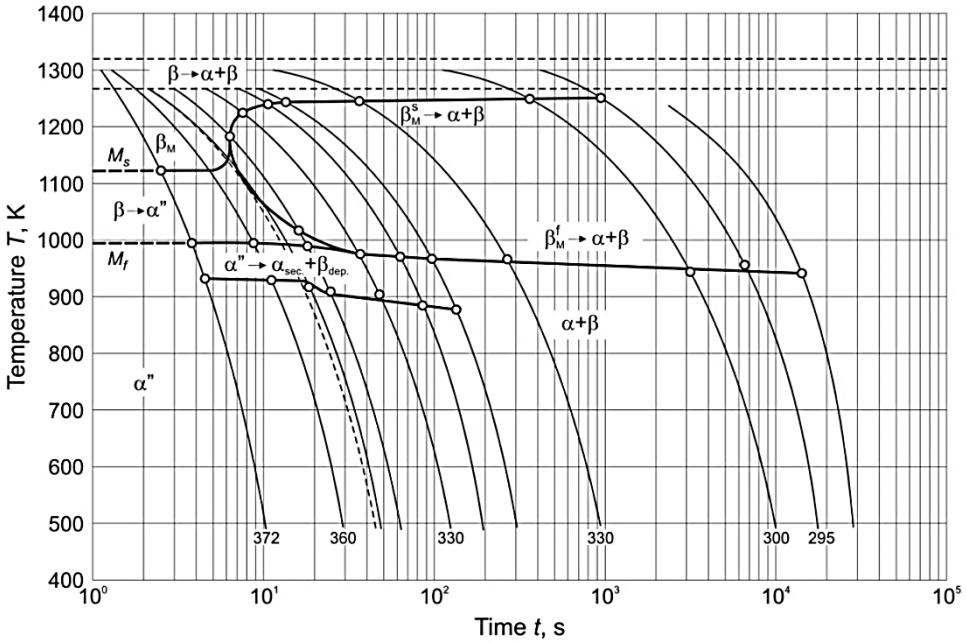

Figure 2-10 - CCT diagram for Ti-6Al-4V alloy from above T_β [24].

When cooling occurs from above the beta transus temperature, T_β, the continuous cooling transformation (CCT) diagram in Figure 2-10 provides an understanding of the expected phases. At high cooling rates, diffusional transformation occurs, where equiaxed α grain with β grain boundaries form a fully equiaxed microstructure. On the other hand, low cooling rates promote stable growth of α laths within prior β phases, resulting in fully lamellar microstructures. Intermediate cooling causes a microstructural structure known as bimodal, where both equiaxed and lamellar α are formed [23], [24].

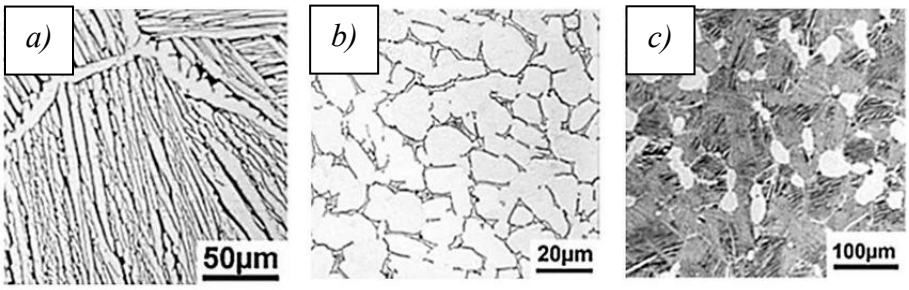

Figure 2-11 - α+β titanium alloy microstructure [25].
(a) Fully Lamellar, (b) Fully Equiaxed, (c) Bimodal.

In the above microstructural illustrations, the alpha (α) phase appears in light patches, and the beta (β) phase is in the dark regions. However, in L-PBF additive manufacturing, the cooling rates are significantly higher, leading to a complete transformation of the β phase into martensitic microstructural phases known as α′. This transformation results in a body-centred tetragonal (bct) structure. As previously demonstrated in Figure 2-7, the α′ martensitic phase develops within the columnar β structure. The α′ phase looks like an intersecting fine needle-like pattern, as shown in Figure 2-12.

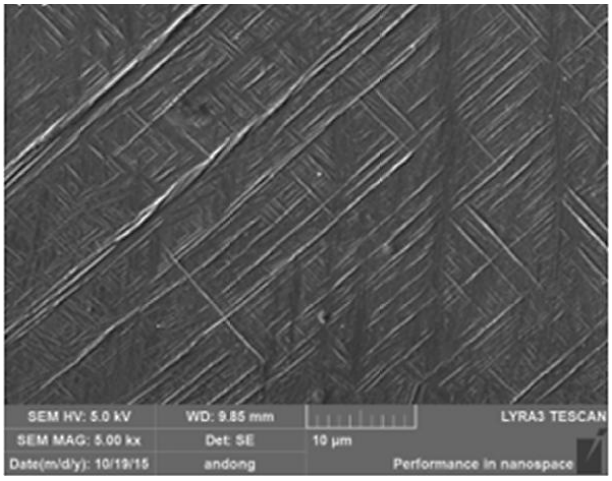

Figure 2-12 - SEM micrograph of As-Built L-PBF Ti-6Al-4V [26].

Various perspectives regarding the microstructural characteristics of Ti-6Al-4V produced through L-PBF technology exist. While certain desirable features, such as high strength and hardness, there are also significant drawbacks, including low ductility and poor fracture properties. Additionally, the directional configuration of the microstructure is an important factor to consider. Key aspects include the columnar grain structure (the arrangement of elongated grains in a column-like formation), the configuration type (lamellar or rotated), and the direction of growth (influenced by temperature gradients during solidification). These factors are particularly crucial when examining the anisotropic characteristics of the alloy.

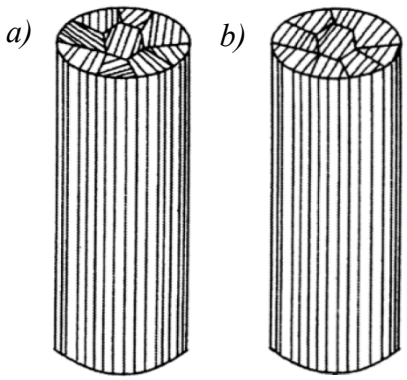

Figure 2-13 - Schematic representation of directional solidification [23].
(a) rotation of each columnar grain. (b) lamellar orientation of the columnar grain.

2.3.2 Documented Work

The study of L-PBF of Ti-6Al-4V has progressed for several decades, leading to substantial advancements in this area. These investigations have clarified many key elements concerning the interplay between the manufacturing process and the material properties. Researchers have primarily focused on optimisation, striving to minimise undesirable factors while maintaining or even enhancing the desirable qualities of the materials. Despite the remarkable progress, the aim remains the successful commercialisation of parts produced through L-PBF AM. Achieving this goal requires a thorough understanding of the research efforts that shape the properties of the resulting parts. However, it has been observed that these properties are influenced by certain inherent features of the manufacturing process, irrespective of the facility involved. Consequently, the need to study these features' underlying causes is also examined. This work categorises the exploration of previous studies into the three main aspects, as shown Figure 2-14.

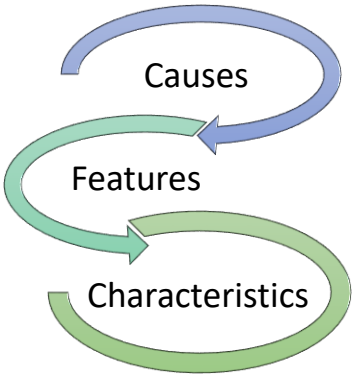

Figure 2-14 - Cyclical flowchart of the three key categories under examination.

The term "characteristics" is used here instead of "properties" because the emphasis is on the descriptive features that define L-PBF products. Additionally, due to the wide range of possibilities, the focus has been narrowed to specific aspects. Table 2-2 and Table 2-3 are summarising previous research findings on feature causes and their effects.

Table 2-2 - Summary of the causes of features of Ti-6Al-4V parts produced by L-PBF.

Feature	Cause	References
Density & imperfections	Melt pool characteristics	[27], [28], [29], [30], [31], [32], [33], [34], [35], [36], [37]
	Powder material	[32]
	Heating & cooling cycles	[38]
	Built strategy	[39]
Residual stresses	Melt pool characteristics	[27], [38], [40]
	Cooling rate & direction	[9], [35], [38], [40], [41], [42]
	Heating & cooling cycles	[9], [38], [43]
	Built strategy	[40], [44], [45], [46]
Microstructural structure	Heat affected zone	[9], [32], [34], [35], [47]
	Melt pool characteristics	[13], [27], [31]
	Cooling rate & direction	[27], [28], [29], [31], [34], [35], [36], [46], [47], [48], [49], [50], [51]
	Built strategy	[26], [31], [39], [49], [51], [52], [53], [54], [55], [56], [57], [58], [59]
Surface integrity	Melt pool characteristics	[27], [31], [33]
	Powder material	[35]
	Built strategy	[12], [53]

- *The Build strategy includes the built orientation, scanning pattern, print dimensions, powder characteristics and built environment.*

Table 2-3 - Summary of effects of features on characteristics of L-PBF Ti-6Al-4V parts.

Characteristic	Feature	References
Strength: • Tensile • Impact • Bending • Creep • Fatigue	Density & imperfections	[27], [28], [29], [30], [31], [33], [34], [35], [49], [53], [54], [56], [57], [58], [60], [61], [62], [63]
	Residual stresses	[35], [38], [46], [59], [61], [64], [65]
	Microstructural Structure	[9], [26], [31], [33], [34], [35], [36], [39], [43], [46], [47], [49], [51], [52], [53], [54], [56], [59], [61], [63], [64], [65], [66], [67], [68], [69]
	Surface integrity	[12], [31], [34], [35], [49], [59]
Ductility	Microstructural Structure	[9], [30], [51], [53], [56], [61], [66], [67], [68]
	Density & imperfections	[60]
Fracture mechanics: • Initiation • Propagation	Microstructural Structure	[30], [35], [53], [55], [58], [59], [64], [67], [68]
	Density & imperfections	[26], [28], [30], [55], [56], [57], [58], [59], [60], [63], [64], [67]
Microhardness	Microstructural structure	[33], [49], [56], [57], [62], [64], [68], [70]
	Density & imperfections	[33], [34]

Examining previous research has provided valuable insights into the causes and various features and their influence on part characteristics. One notable observation is that recurring themes consistently emerge despite many studies addressing different aspects. However, a significant gap remains: the objective linking of identified causes - primarily occurring during the manufacturing and post-processing phases - to the resulting characteristic features. In addition, it is essential to clearly define the influence of these individual features while establishing connections between them and their source of variation. Achieving all this in one study would ensure that few aspects are overlooked, ultimately leading to a comprehensive understanding of the subject and open possibilities for developing empirical relationships.

With an understanding now established and elements categorised in the summary of past works, a more focused and strategic approach can be made in the testing process of L-PBF manufactured Ti-6Al-4V alloy. This work can now progress by considering the underlying causes of these features during manufacturing, highlighting and attempting to modify them during post-processing, and ensuring that the goal of creating optimum characteristics for mechanically reliable components that excel in their intended applications is achieved.

2.3.3 Post-Processing

Post-processing in L-PBF typically involves a series of steps aimed at overcoming the challenges observed in 2.3.2 related to this manufacturing technology. Post-processing has considerable implications for parts produced using L-PBF and is a reality of the manufacturing process that needs to be admitted. A survey revealed that pre- and post-manufacturing processing can constitute up to 40% of the total expenses of L-PBF AM [2]. Although lead time delays and increased costs reduce the buy-to-fly ratio, optimism remains high regarding process improvements through innovation [12]. While traditional post-processing methods generally include heat treatment and surface machining, several other enhancement techniques have proven effective. Table 2-4 summarises the treatments commonly utilised in this context.

Table 2-4 - Main post-processing employed on L-PBF-produced parts

Traditional Post-Processing		**Others**
Heat Treatment	**Surface Machining**	
Stress Relieving	Electrical Discharge Machining	Abrasive Blasting (Sandblasting, etc.)
Annealing	CNC Machining (Milling, Turning, etc.)	Shot Peening
Hot Isostatic Pressing	Mechanical Polishing (Grinding, Honing, etc.)	Laser Shock Peening
	Chemical Polishing (Electropolishing, Acid Etching, etc.)	Tribofinishing

Altering parts' physical and mechanical characteristics by stress relieving and annealing typically include reduction of internal RS and/or microstructural modifications. Hot isostatic pressing (HIP) addresses issues such as porosity and ductility. Additionally, surface machining is commonly performed to achieve specific surface textures required for intended applications. Other processes have also been employed with the same intention as the previous two. The main objective of these processes has always been to obtain physical, mechanical, and functional characteristics that closely resemble those of traditionally wrought materials.

Stress relief can reduce RS in L-PBF AM parts, but selecting the right conditions is crucial to avoid microstructure changes [38], [46]. This selection helps prevent deformation or cracking when removing parts from the baseplate, preserving mechanical integrity. Research by [59] shows that stress relief enhances cycles to failure in vertical specimens while decreasing cyclic fatigue in horizontal ones. Also, an increase of 20% in energy absorption was observed in stress-relieved Charpy impact specimens by [26]. Additionally, [62] observed that stress relieving Ti-6Al-4V did not affect the material's porosity and microhardness, but HIPping improved fatigue performance and lowered microhardness. Works by [28], [71], demonstrated that HIP post-processing effectively reduced or closed existing pores. Furthermore, the impact of HIP processing on the absorbed Charpy energy in the samples was also studied, and improvements were observed [54]. HIP and annealing treatments typically alter the acicular α′ martensitic structure of as-built Ti-6Al-4V into lamellar, equiaxed, or bimodal forms based on processing conditions [67]. Manufacturers often use annealing to improve ductility, but this was found to reduce the ultimate tensile strength (UTS) and yield strength (YS) of parts, [31], [55], [59] due to the transition to a basket-weave α + β lamellar structure [61]. Research by [69] also showed that fractured surfaces indicated a shift from brittle quasi-cleavage failure to a more ductile fracture mechanism.

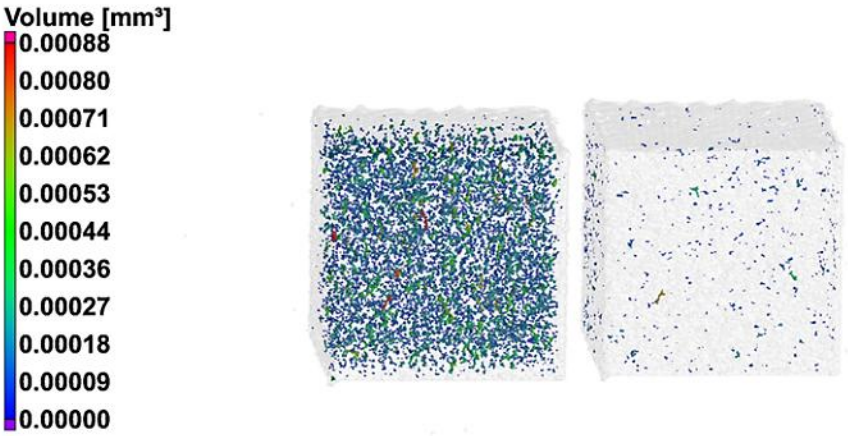

Figure 2-15 - LoF pores from large hatch spacing were closed using HIP [71].

Achieving the correct surface finish in parts also remains a significant challenge. While optimal part features are desired, they often produce subpar surface finishes. Factors influencing surface characteristics include part design and manufacturing strategies, which face limitations like the stair-step effect due to layer thickness. Surface roughness is also impacted by powder adherence and the upskin or downskin angles of the part surfaces [72]. To address these issues, manufacturers often utilise surface treatments such as milling, polishing, blasting, chemical etching and laser polishing/remelting [12]. Surface roughness is a critical factor that significantly affects fatigue failures. Surface defects can serve as stress concentrators, compromising fatigue life, particularly in load-bearing applications such as aerospace [73], [74]. Therefore, effective surface treatment is essential. Proper surface polishing can also alter residual stresses and consequently influence the fatigue characteristics to a level comparable to wrought materials [75].

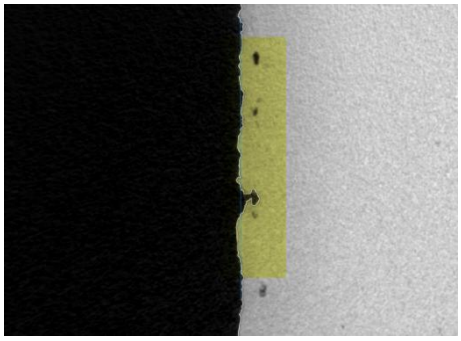

Figure 2-16 - Open connected sub-surface pore influencing surface integrity [76].

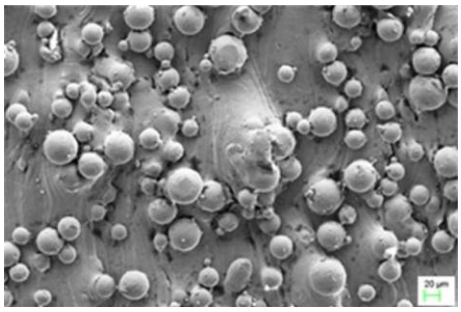

Figure 2-17 - SEM Image of surface topography of As-built Ti-6Al-4V [75].

Traditional surface machining can, however, be challenging for complex shapes, leading to alternative methods like shot peening, blasting, or laser shock peening. The additional advantage of using these techniques is not only to modify surface profiles but also to affect other characteristics. A study by [75] who investigated the interactions between as-built, post-processed HIPped, traditionally machined, and surface-treated materials, concluded that surface smoothness affects performance more than residual stress. Blasting, for instance, yielded better residual stress shifts than conventional machining on the Ti-6Al-4V parts but did not do so well in improving the roughness. On the other hand, samples that have been tribofinished provided the best improvement in surface finish and were found to yield better fatigue performance. Laser shock peening, on the other hand, was found to cause a nearly uniform strain distribution on the treated surface and also brought slight changes to the surface roughness [77], [78]. The ideal scenario would, however, be to obtain a smooth finish with induced compressive residual stresses.

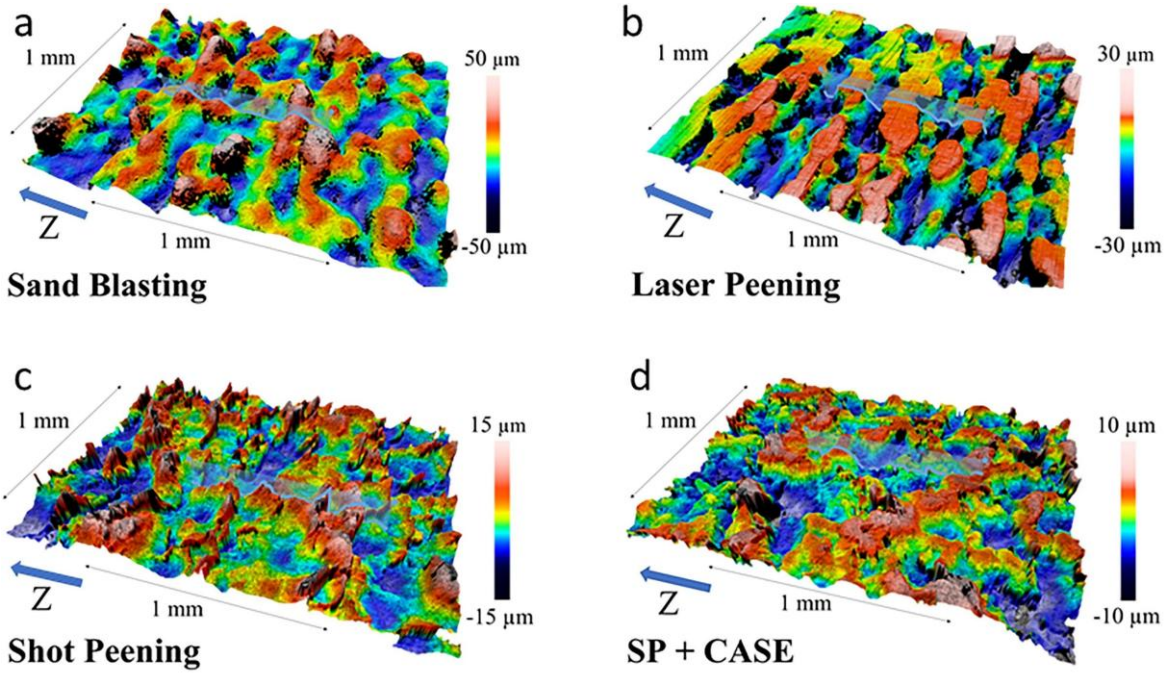

Figure 2-18 - Surface profiles of L-PBF Ti-6Al-4V with various treatments [77]. (a) Sand Blasting, (b) Laser Shock Peening, (c) Shot Peening, (d) Shot Peening + Chemical Assisted Surface Enhancement.

2.3.4 Key Insights and Way Forward

It is well established that as-built Ti-6Al-4V samples demonstrate impressive mechanical strength and hardness. However, they frequently suffer from low ductility and a poor surface finish, adversely affecting their mechanical performance. This issue stems mainly from the unique microstructure that forms during the manufacturing process, compounded by challenges related to density and imperfections or surface conditions that can act as weak points, ultimately leading to material failure. Furthermore, tensile residual stresses generated during cooling also pose a significant concern. Collectively, these factors can significantly influence the material's fracture mechanics. On the positive side, post-processing techniques have been extensively researched and have shown encouraging results in enhancing these properties. Although the strategies employed have flaws, they have produced satisfactory outcomes. Given this backdrop, it was established that the emphasis would need to be on producing samples that specifically target the defined features instead of merely aiming for general desirable characteristics, as these features ultimately determine the properties of the parts. Subsequently, post-processing can be utilised to refine and adjust these features into more favourable ones, allowing the part to achieve its intended performance. This approach provides the most effective pathway for leveraging L-PBF AM of Ti-6Al-4V.

2.4 LSP of L-PBF Ti-6Al-4V Alloy

To enhance the possibilities of commercialising this manufacturing technique, researchers have been adamant that the post-processing of parts produced by L-PBF is vital. However, the various traditional thermal post-processing techniques that mainly aim to alter the part density, microstructure and internal residual stresses without much improving poor surface characteristics of L-PBF-produced parts can become very strenuous, costly and time-consuming. The idea of using Laser Shock Peening (LSP) as a mechanical post-processing is considered in this work. The advancement of the LSP technology has been as promising as L-PBF manufacturing. Using LSP to modify surface and subsurface characteristics can be vital in altering the mechanical properties of parts produced with the aspiration of producing repeatable results.

2.4.1 About LSP

LSP is a surface treatment invented in the 1960s. In this process, a high-energy laser beam is directed onto a metallic material with a pulse duration of nanoseconds. This action generates a shock wave from the formation of a confined plasma. Typically, the confinement medium is either distilled water or glass, which directs the shock wave to propagate within the material. This phenomenon has been shown to enhance the fatigue properties of materials by creating compressive residual stress along the same direction of tensile extension obtained parallel to the surface. There are two types of LSP: one with a coating and one without [79].

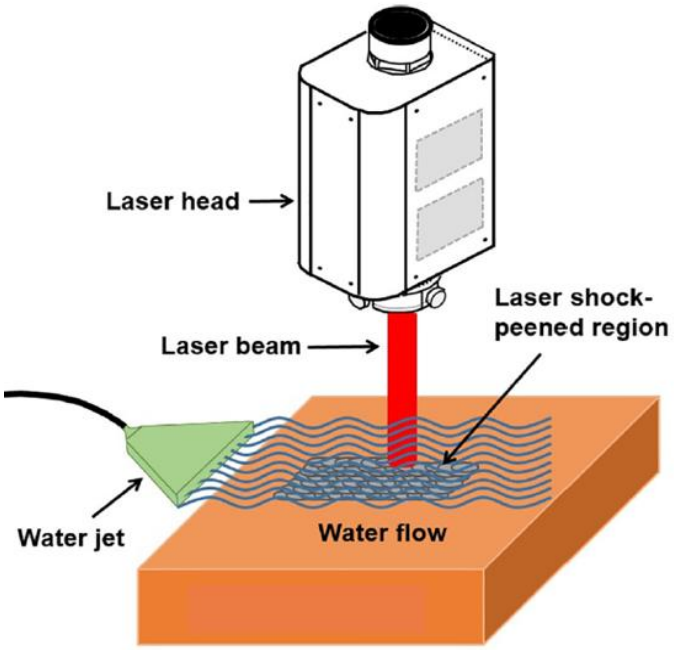

Figure 2-19 - Schematic diagram of Laser Shock Peening without Coating [80].

Table 2-5 - Some of the main LSP facilities around the world.

Facility/Company	Country
Toshiba	Japan
CSIR	South Africa
Universidad Politecnica de Madrid	Spain
Helmholtz-Zentrum Gaeltacht	Germany
HiLASE	Czech Republic
Metal Improvement Company	USA
CNRS	France

The parameters of a LSP system can be categorised into three main types and are summarised in Table 2-6 below:

1. **System Parameters**: These characteristics are inherent to the laser system and are difficult to change.
2. **Control Parameters**: These can be adjusted independently and impact the processing outcomes.
3. **Interaction Parameters**: These were developed through mathematical relationships between the system and control parameters.

Table 2-6 - Categorisation of the main LSP processing parameters

System Parameters	Control Parameters	Interaction Parameters
Laser Type (Nd:YAG)	Pulse Density (N_p)	Power Intensity (PI)
Pulse Duration	Laser Energy	Coverage (C_v)
Pulse Frequency	Spot Size (SS)	% Overlap
Spot Shape (round)	Peening Pattern	

Similarly to the L-PBF manufacturing process, LSP processing parameters are often characterised using interaction parameters. Interaction parameters are widely used to facilitate comparative analysis across studies performed on multiple facilities. Typically, researchers combine three key relevant parameters: Spot Size, Power Intensity, and any pulse density metric. The pulse density metric itself measures the number of spots per unit area (spots/mm^2). However, it is not commonly used because of the variations in the laser spot characteristics (shape and area) and the peening area characteristics. Therefore, the interaction parameters related to the pulse density metric (Coverage or % Overlap) are often employed. The coverage gives the total number of spots on the treated surface area. The % Overlap, on the other hand, is a dimensionless parameter that indicates the amount of overlay the spots have on the neighbouring spot. Both parameters provide insight into the extent of spot coverage during peening.

While Spot Size is an inherent laser characteristic, Power Intensity (PI), Coverage (C_v) and % Overlap can be defined as follows:

$$PI = \frac{Laser\ Energy}{Pulse\ Length\ \times SS^2} \quad \text{Equation 2.2}$$

- *The laser energy in Joules can be varied, with a pulse length in nanoseconds and a fixed spot size (SS).*

$$C_v = N_p\ \times \frac{\pi}{4} \times\ SS^2 \quad \text{Equation 2.3}$$

$$\%\ Overlap = 1 - \frac{SS}{\sqrt{N_p}} \quad \text{Equation 2.4}$$

- *Interaction parameters that depend on the pulse density (Np) and the spot size (SS).*

Different facilities use lasers with varying wavelengths, impacting their interaction with materials. The most common wavelengths are 1064 nm (infrared) and 532 nm (visible green). The 532 nm laser offers good surface absorption and efficient plasma generation, resulting in strong shockwaves and high residual stresses at the surface. In contrast, the 1064 nm laser penetrates deeper and causes less heat buildup but generates lower surface stress levels while significantly affecting the subsurface. When the intended use of LSP is for surface treatment, the 532 nm laser is often more effective, especially where high power intensities that can enhance residual stress induction can be used. A study of both laser wavelengths with relatively close power intensities by Cesar A. Reynoso-Garcia et al. [81] indicated that the high plasma generated by the 532nm laser vaporises and melts the surface material, leading to hardening and forming an oxide layer. However, a much more significant compressive residual stress at a higher depth is observed in samples peened with the 1064 nm laser.

2.4.2 LSP's Effectiveness and Outcomes

LSP has been used for aerospace applications to refurbish conventionally manufactured components such as turbine blades, rotors, discs, gear shafts, bearings, and fastener holes [79]. LSP is used mainly to increase the lifetime of components. For L-PBF AM, the goal is a bit different. In addition to increasing the lifespan by inducing compressive residual stresses, the LSP of L-PBF AM parts alters manufacturing features inherent to the manufacturing process. LSP targets the concerns of poor surface properties, typical microstructures, and physical properties to define a promising new route [82].

Observations have highlighted that surface characteristics significantly influence the mechanical properties of Ti-6Al-4V parts produced through L-PBF. Previous studies on the LSP of L-PBF produced parts have drawn promising conclusions regarding these surface characteristics, documenting notable morphological and topographical changes. Additionally, the formation of an oxide layer composed of TiO_2 and Al_2O_3 has been reported [83]. The surface modifications are believed to result from plastic deformations induced by LSP ablation, which affects both the surface and subsurface layers [84]. Notably, research focusing on the cross-sections of these surfaces indicates that the enhancements in additively manufactured Ti-6Al-4V components are mainly attributable to the smoothing of surface valleys, which involves a reduction in the height difference between peaks and valleys, regardless of their specific locations on the surface as shown in Figure 2-20 [78].

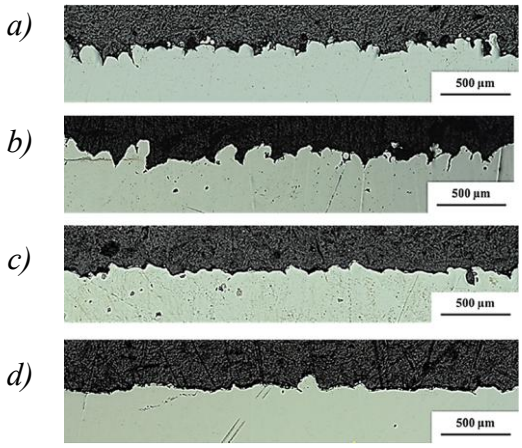

Figure 2-20 - Cross-section of downskin and upskin surfaces of Ti-6Al-4V [78]. (a), (b) before LSP, (c), (d) after LSP.

While tensile residual stresses in manufactured components may not substantially prevent failure mechanisms, their existence can significantly affect the part's lifespan. Generally regarded as undesirable, these tensile stresses can adversely impact a component's performance, particularly regarding its fatigue characteristics. Extensive research has delved into the effects of LSP processing, which aims to create advantageous residual stress profiles. Studies have shown that LSP remarkably effectively transforms tensile residual stresses in additively manufactured Ti-6Al-4V components into compressive stresses. This transformation occurs regardless of the orientation of the components under analysis, highlighting the versatility and effectiveness of this innovative treatment in enhancing the durability of critical components [83], [85], [86]. Additionally, in components produced through suboptimal manufacturing processes, LSP consistently established enhanced compressive residual stresses across the subsurface, altering the part's density and hardness properties [78].

Investigations into LSP's influence found that the process did not significantly change the microstructure at the treated surface or across the cross-section of the treated samples. Nevertheless, due to the plastic deformations previously discussed and the potential densification of the areas near the subsurface, an increase in microhardness was observed in these parts following LSP treatment [79], [82], [83]. Additionally, a study by [78] highlighted an increase in fatigue life in samples produced using suboptimal parameters. This suggests that addressing imperfections can enhance the strength of the components. This observation supports the notion that defects at the surface or sub-surface regions may substantially impact performance more than the residual stresses present. Conversely, other research focusing on Ultimate Tensile Strength did not report any significant changes. A study has examined the effects of LSP treatment on L-PBF-built Ti-6Al-4V components after undergoing stress relief at 820°C for 4 hours. These studies observed a slight change in microstructure, transitioning from elongated grain structures (which were somewhat thicker than those in the as-built condition) to a partially mixed structure of equiaxed and lath-type grains. This change results from dynamic recrystallisation that occurs during the LSP process. Furthermore, the same study discovered that using high power intensities from a 532 nm laser led to more significant improvements in hardness and indicated improved impact performance of Ti-6Al-4V parts [87].

2.5 Assessment of L-PBF Ti-6Al-4V Parts

Having explored the product characteristics yielded by the L-PBF process of Ti-6Al-4V and the impacts of LSP post-processing, systematic part property evaluation needs to be done. The evaluation should thoroughly document the parts' composition, structure, and external influences. When designing components for aerospace applications, it is crucial to consider a wide range of assessment tests, ensuring all aspects are considered to guarantee reproducibility and reliability. Although there may be significant differences in the uniformity of parts produced by L-PBF compared to those made using traditional manufacturing methods, the testing protocols remain similar. Below are the key physical test methods for AM parts that design engineers should consider to ensure optimal performance [88].

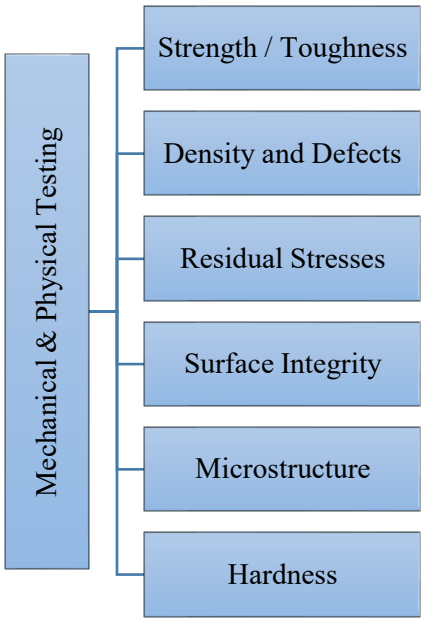

Figure 2-21 - Main testing aspects that require consideration.

Examining and testing the materials' mechanical and physical properties must be carried out according to standards set by reputable organisations and established practices. These tests aim to identify failure behaviours, which can occur in three forms: fracture, fatigue, and creep. Understanding these behaviours helps counteract them or help engineers design accordingly [10].

A component fails when it cannot perform as expected under specific conditions, with fracture being a standard failure mode. Fracture mechanics gained prominence during World War II due to the need to understand impact fractures in aerospace components [89]. Fractography, on the other hand, emerged as a distinct engineering field in the Metals Handbook, Vol. 12 of 1974, following a 1944 Annual Convention [90]. Fracture mechanics and fractography are often linked to mechanical testing. Fracture mechanics examines the relationships between loads, geometry, and material properties that can lead to fractures, focusing on fracture resistance from a macroscopic perspective. On the other hand, fractography is particularly effective in offering an even broader practical assessment of fracture behaviour. Fractography examines the fracture process and the fractured surface's characteristics [89]. It enables engineers to describe and characterise crack initiation and propagation without getting too detailed about the specifics of the crack failure. Key features like fibrous marks, radial marks, and beach marks help trace fracture origins, while attributes such as chevron marks and crack branching provide insights into crack propagation [10]. Fractures typically follow inter-granular (along grain boundaries) or trans-granular (through grains) paths. Imperfections in L-PBF additive manufacturing summarised in Table 2-7 often lead to localised stress concentrators, influencing how fractures initiate and spread. Changes in surface texture typically accompany fractures, highlighting potential root causes in this manufacturing method [90].

Table 2-7 - Summary of discontinuities causing fracture in L-PBF parts [90].

Stress concentrator / Discontinuity	**Origin**	**Method of Identification / Appearance**
Laps, Seams or Cold Shuts	Unstable melt pool	Low Magnification: Visible gaps
Cracks or Incomplete fusion	Lack of energy density	Moderate Magnification: Intergranular texture
Inclusions	Improper machine and material parameters	High Magnification: Fatigue-looking cracks
Porosity	Improper process parameters	Low magnification: Visible pores
Segregation	High thermal Gradients	High Magnification: Both brittle & ductile appearance
Unfavourable grain flow	Improper process parameters	Low magnification: Woody texture

2.6 Charpy Impact Toughness of L-PBF Ti-6Al-4V Alloy

The pendulum-type impact test, developed by the Frenchman Georges Charpy in 1905, involves dynamic loading and was designed to simulate significant strain rates [11]. The effect of strain rates is an important aspect of mechanical testing. The strain rate mimics those that failed components are subjected to, ranging from low (creep failure) to very high (shock loading). Charpy Impact tests have been classified as a testing method generating moderately high strain rates (10^2 /s) [90]. The energy absorbed during impact tests indicates a material's toughness, with tougher materials absorbing more energy than brittle ones. While these tests allow for comparing impact toughness among materials, the results obtained are qualitative and cannot aid in determining intrinsic fracture toughness. However, they provide a simple and cost-effective means of screening materials for toughness properties [19].

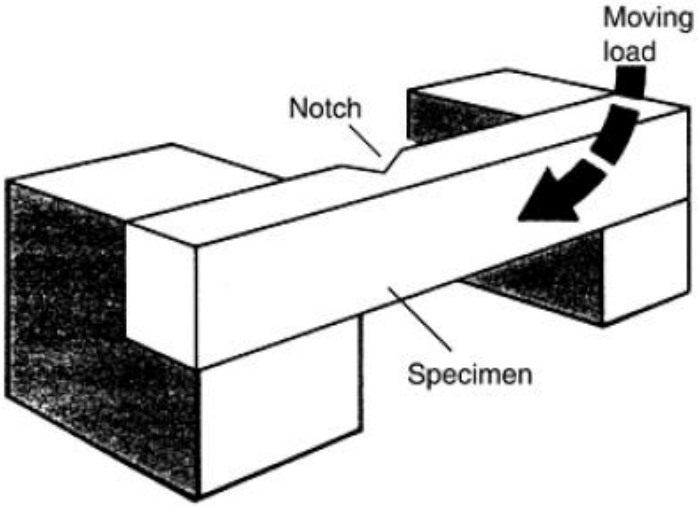

Figure 2-22 - Basic configuration setup of the Charpy Testing [11].

The basic concept of this test method involves a 3-point loading system, in which the specimen is held at both ends, resembling a simple beam as shown in Figure 2-22. During the test, the sample is struck on the unnotched side. The difference between the height from which the pendulum falls and the height it rises to, along with considerations of energy losses, allows us to calculate the specimen's absorbed energy [11].

2.6.1 Test Variations

The fundamental principle of utilising a swinging arm to break a sample and measuring the energies before and after impact is to determine the absorbed energies. The test, however, has several variations. One variation pertains to the specimen size; different standards allow flexibility to accommodate other types of samples, especially when full-sized samples are unavailable. Another variation involves the type of notch geometry used, which can differ based on the characteristics of the materials being tested. However, the most used notch geometry is the V-notch. This is because it allows for testing a wide range of materials with various properties and is practical, as it can be consistently produced more quickly than the other types. Additionally, variations can arise in the test equipment employed. Different geometries of the striker and anvils may be used depending on the specific test standard. However, these variations can generally be standardised based on mathematical relationships that have been developed. These relationships simplify the testing process for organisations, providing greater freedom in the types of tests that can be conducted.

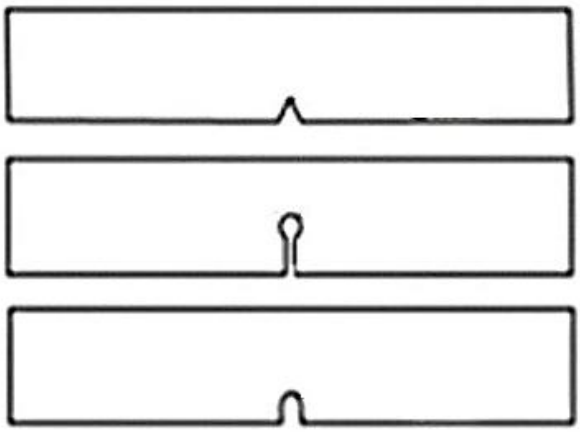

Figure 2-23 - Charpy specimens notch types.
(a) V-notch, (b) Keyhole notch, (c) U-notch.

Research conducted by the NIST has examined and confirmed the effectiveness of using sub-sized and miniature specimens with comparable results to standard specimens [91]. This approach is considered a valuable alternative when the material is limited or samples are inherently small [91]. Table 2-8 provides a summary of the sample dimensions and the associated acceptable standards.

Table 2-8 - Summary of Charpy Specimen sizes [92], [93], [94], [95], [96], [97].

Type	Size (mm)	Standard
Standard Size	10 × 10 × 55	ASTM E23, ISO 148-1, EN 10045-1, GB/T 229
Sub-Size	10 × 7.5 × 55, 10 × 5 × 55, 10 × 2.5 × 55	ASTM E23, ISO 148-1, JIS Z 2242, EN 10045-1, GB/T 229
Miniature Size	4.83 × 4.83 × 24.13	ASTM E2248

Miniature or sub-sized specimens for Charpy impact tests are becoming more widely accepted. A key reason for this growing acceptance is cost efficiency. Research has demonstrated a strong correlation between the results of miniaturised or sub-sized samples and those of standard samples. The reduced material requirements - whether for manufacturing new samples or preparing them from existing pieces or previously tested standard specimens - give these smaller samples a distinct advantage. For example, the MCVN specimen was initially specifically designed to be made from broken pieces of standard samples, showcasing its practical benefits. It is important to note that miniaturised and sub-sized samples are different. Miniaturised samples are scaled-down versions of standard specimens governed by the standard ASTM E2248 [92]. The main goal of these samples is to achieve a testing method that maintains the same ratio of stress fields as in the standard samples. In contrast, sub-sized samples have different aspect ratios, and their correlation to the results of standard samples is determined only by mathematical relationships [91], [93], [98].

2.6.2 Impact Mechanics

Understanding how materials absorb energy upon impact is crucial, as it provides insights into their ability to withstand catastrophic failure. Charpy tests simulate moderately high strain rate impacts and serve as an effective method for assessing the toughness of a material. It is important to note that the toughness derived from conventional monotonic loading stress-strain curves differs fundamentally from that obtained through impact loading, resulting in two distinct toughness values that should not be directly compared. In the context of L-PBF, the specific characteristics of the produced components render impact toughness a more relevant assessment methodology. Compared to traditional toughness evaluations, this approach more effectively highlights both the advantages and disadvantages related to microstructures, defects, and residual stresses of AM parts. Numerous studies have explored this issue, including investigations focused on Ti-6Al-4V testing at room temperature, which are summarised in Table 2-9.

Notes on Table 2-9:

- *The summary of absorbed impact energy (toughness) below presents values obtained from mentions in studies or interpreted from graphs and charts. Any evaluated absorbed energy value, whether derived from a chart or converted to Joules from another unit, has been calculated accurately.*
- *The abbreviations in the table are as follows:*
  - *L-PBF - Laser Powder Bed Fusion,*
  - *EBM - Electron Beam Melting,*
  - *DMLS - Direct Metal Laser Sintering,*
  - *AB - As-Built,*
  - *SR - Stress Relieved,*
  - *HT - Heat Treated,*
  - *HIP - Hot Isostatically Pressed,*
  - *LSP - Laser Shock Peened,*
  - *UP - Notch cut upskin on horizontal samples,*
  - *LO - Notch cut downskin on horizontal sample,*
  - *LT30 - Layer thickness at 30 µm,*
  - *LT60 - Layer thickness at 60 µm,*
  - *P-Ω% - The percentage of porosity at the Ω level.*

Table 2-9 - Summary of Charpy impact results of Ti-6Al-4V at room temperature.

Sample Tested Condition	Sample Size	Absorbed Energy (J)	Reference
Additively Manufactured			
L-PBF + AB + Vertical L-PBF + SR + Vertical	Standard	4.77 10.35	[46]
DMLS + AB + UP DMLS + AB + LO DMLS + SR + UP DMLS + SR + LO	Standard	14.0 15.0 16.5 17.5	[99]
L-PBF + AB + Vertical L-PBF + HT + Vertical L-PBF + LSP + Vertical	Standard	4.0 10.0 9.0	[87]
L-PBF + AB + Vertical EBM + AB + Vertical	Standard	15.0 16.0	[64]
L-PBF + HT + Vertical + Printed Notch L-PBF + HT + Vertical + Wire cut Notch L-PBF + HT + UP + Printed Notch L-PBF + HT + UP + Wire cut Notch	Standard	38.0 38.0 33.0 41.0	[100]
L-PBF + AB + Horizontal + LT30 + P-0% L-PBF + AB + Horizontal + LT30 + P-14% L-PBF + AB + Horizontal + LT60 + P-0% L-PBF + AB + Horizontal + LT60 + P-4%	Standard	35.0 3.0 30.0 11.0	[60]
L-PBF + AB + Vertical L-PBF + SR + Vertical	Sub-Sized	6.0 7.3	[26]
EBM + AB + Horizontal EBM + AB + Vertical EBM + HIPped + Horizontal EBM + HIPped + Vertical	Miniaturised	13.06 14.46 18.90 25.90	[54]
L-PBF + AB + Horizontal + Printed Notch L-PBF + AB + Vertical + Printed Notch L-PBF + HIP + Horizontal + Printed Notch L-PBF + HIP + Vertical + Printed Notch L-PBF + AB + Horizontal + Machined Notch L-PBF + AB + Vertical + Machined Notch L-PBF + HIP + Horizontal + Machined Notch L-PBF + HIP + Vertical + Machined Notch	Miniaturised	3.79 4.96 5.29 6.02 4.48 5.33 6.00 8.77	[52]
Conventionally Manufactured			
Equiaxed microstructure Bimodal microstructure Lamellar microstructure Coarse lamellar microstructure	Standard	50.0 85.0 60.0 63.0	[67]
Wrought + Vertical	Standard	35.0	[64]
Wrought + Along Rolling Direction Wrought + Along Rolling Direction	Miniaturised	4.99 5.0	[52]

There is a significant difference between the readings obtained from standard samples and those obtained from their miniaturised versions. This might be due to the changes in the sample dimension, which resulted in some fundamental changes to the test equipment that need to be considered. However, we can draw useful conclusions when comparing AM miniature samples to conventionally manufactured ones. In most cases, the results from the AM samples demonstrate superior impact toughness values, marking a substantial improvement in material performance, unless affected by poor characteristics. Note that the miniature sample readings from wrought materials in Table 2-9 are certified values from the NIST agency and are considered reference standard values.

2.6.3 Fractography

Fractographic assessment is carried out to complement the absorbed energies obtained from Charpy impact tests and consists of three steps. First, the fracture type is determined, i.e., ductile or brittle. Second, the fracture mechanism is identified, which includes factors such as overload or fatigue. Third, fractographic analysis is carried out to classify the fracture based on the micro-mechanisms observed [89]. While the first step is usually straightforward, determining the other two requires some analytical work. Fracture examinations are performed in three main steps: visual examination, light microscopy, and scanning electron microscopy. The first two can be termed Macrography, which uses macroscopic analysis techniques, and the third as Micrography, which uses microscopic analysis [10].

Table 2-10 - Descriptive summary of the main fracture types [89].

Ductile fractures	Brittle fractures
It occurs under tension when a material can no longer support the load and begins to deform uniformly. It is characterised by void nucleation and growth, resulting in dimples or craters on the fracture surface.	**Cleavage** The direct rupture of atomic bonds, resulting in smooth, shiny cleavage plane facets with no plastic deformation, often displaying river-like patterns due to interconnected cleavage planes.
	Quasi-Cleavage Similar to cleavage with coarser and rougher river marks due to stress triaxility.
	Pseudo-Cleavage It features distinct slip lines around a polished cracked surface like cleavage from fatigue failures.
	Decohesive Grain boundary decohesion leads to fractures with a grainy appearance. These fractures may exhibit pitting, micro-cavities, or slip marks.

The macroscopic examination allows the researcher to understand the kind of fracture by looking at the general appearance and looking for deformations. This examination firstly consists of visually examining the fractured surface to analyse whether any plastic deformations (ductile fracture) or otherwise (brittle fracture) occurred. A brittle fracture is a sudden material failure that can cause a quick breakdown under heavy loads. On the other hand, ductile fracture occurs slowly and involves bending or deforming at the crack's edge. The surface texture is also observed as it allows the determination of the type of fracture crack propagation based on the surface texture. A secondary assessment is then made using a light stereomicroscope to observe whether the fracture regions can be discerned. The advantage of using a stereomicroscope lies in the depth perception that it can provide [10], [19], [89], [90].

Figure 2-24 - Appearance of fractures in different types of Charpy samples [101].

In addition to macroscopic examinations, SEM is used in microscopic analysis, enabling the researcher to reach a higher depth of field. SEM images enable researchers to obtain structural and compositional data that helps in fractographic analysis. The main image types generated by SEM examination are the Secondary Electrons (SE) and Backscattered Electrons (BSE). The fracture modes are identified by looking at features such as dimples for ductile, cleavage or fatigue that showcase typical brittle transgranular fractures or decohesive ruptures showing intergranular brittle fractures [10], [89], [90].

Microscopic analysis by [26] of as-built specimens revealed a stair-step effect, while the heat-treated specimen exhibited more curved features in the region of fracture initiation, as shown in Figure 2-25. Both specimen types showed brittle fracture, irrespective of stress relief. However, findings indicate that prior β grain boundaries alleviated by the stress relief have less impact on crack propagation. Another study by [54], who used MCVN samples identified two major aspects in the fractographic images: internal pores and ridges. This confirms that porosity affects fracture behaviour. The ridges were found to be parallel to the build direction, which may be attributed to a mixed-mode fracture phenomenon when localised plastic deformation takes place along specific grain orientations.

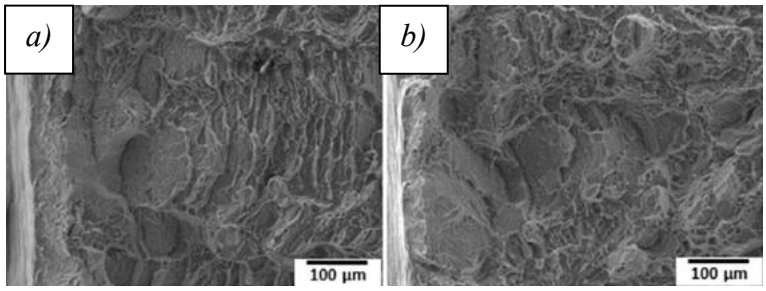

Figure 2-25 - SEM Fractographic images at crack initiation region [26].
(a) stair-step on the AB sample, (b) curved features on the heat-treated sample.

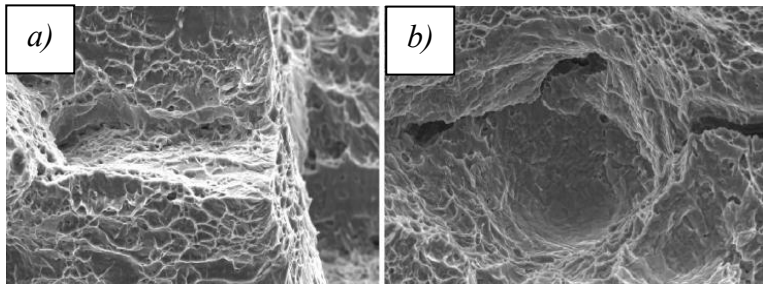

Figure 2-26 - SEM fractographic images of MCVN fractured samples surface [54].
(a) Ridges observed on horizontal samples, (b) Internal pores on As-built samples.

2.7 Summary

The investigation into the foundation of the research topic has provided insight into the pathway to certification. The nature of tests at all levels has also been thoroughly described. The understanding from previous work has been documented, revealing the connections between causes, features, and characteristics relevant to the subject matter. The variations in part features from a manufacturing perspective have been identified, along with the influential features related to the part characteristics. The subsequent sections have been structured to provide clear definitions of the goals and targets, as well as the methods employed to achieve these objectives. It also delves into the elaboration of the main characteristics testing, as well as the detailed aspects of testing ancillary features. This approach facilitates a deeper understanding and provides substance to explanations of the tested characteristic.

Chapter 3. Aim and Objectives

3.1 Research Question

Can Ti-6Al-4V parts built by laser powder bed fusion additive manufacturing and laser shock peened, be effectively qualified using a preliminary assessment test method, such as the Miniaturised Charpy V-Notch impact testing, and do the highlighted features provide substantial evidence to support the obtained performance results?

3.2 Research Aim

The aim of this work is to assess the Miniaturised Charpy V-Notch impact test as a screening method for qualifying Laser Powder Bed Fusion-built and laser shock-peened Ti-6Al-4V parts for aerospace applications, while validating their performance through prominent features.

3.3 Research Objectives

- Establish a framework for conducting Miniaturised Charpy V-Notch impact tests, with a setup and operating procedures that comply with international standards and can produce accurate, reliable, and consistent results.
- Evaluate the variation of MCVN impact toughness test results and correlate it to the determined fundamental building features identified in L-PBF of Ti-6Al-4V parts.
- Assess the measurable differences in MCVN test results between LSPeened samples and unpeened samples, and to determine the sensitivity of the test method.
- Analyse the fractured surfaces of the MCVN test samples to identify and understand the underlying failure mechanisms and factors that contributed to failure.
- Correlate the recorded absorbed impact energies, the determined building features and the possible identified causes observed from underlying failure mechanisms and formulate scientific reasoning.
- Develop empirical relationships based on the significant influencing aspects of the results obtained.

Chapter 4. Methods and Techniques

This chapter presents the framework of this research work, detailing the entire experimentation strategy and work plan based on established standards, procedures, prior research, and credible literature sources. The work plan begins by outlining the testing plan, including the concepts and reasoning behind the experimental design and the primary types of data analysis that will be conducted to assess the MCVN test results. Following this, the methodology for manufacturing samples and the post-processing steps taken to obtain suitable samples for testing are explained. The various methods and techniques are thoroughly described to ensure proper preparation for MCVN and ancillary testing to achieve reliable and repeatable results.

4.1 Experimental Approach

The importance and application of a proper experimental approach in engineering is to effectively evaluate and compare configurations, consider alternatives, select parameters for robust design, outline key parameters, and develop new products. In the case of this work and the targets set in Chapter 3, achieving the goals starts with the proper definition of the experimental strategy. Experiment planning and execution are essential, especially when seeking to obtain analytic data and formulate objective conclusions [102]. Adopting an iterative approach to the MCVN tests was deemed adequate for gaining a broad perspective while addressing challenges related to reducing variability. The summary of the testing roadmap is illustrated in Figure 4-1.

The ASM Handbook on Failure Analysis and Prevention [10] categorises failure analysis into three stages, reflecting the testing process outline:

1. The first step involves collecting data from prior work and conducting preliminary tests. This process continues iteratively until satisfactory results are obtained to inform the main experiment.
2. The second step focuses on identifying important samples and conducting main experiments to help draw clear conclusions.
3. The third step includes testing and evaluating the root cause of part failures and previously identified part features via ancillary testing.

In this research work, the initial MCVN testing continued until acceptable results were obtained, serving two important purposes: it established the groundwork for the testing process and facilitated the refinement of both the equipment and the experimental design for sample manufacturing. Modifications to the apparatus were made due to the unique nature of the MCVN test method. Section 4.4 elaborates more on this aspect. The preliminary tests meticulously evaluated the outcomes and developed a well-informed strategy for moving forward through the iterative process. This evaluation was guided by determining the smallest measurable increment that the testing method could reliably detect, while ensuring that the largest possible span of the experimental design space was explored.

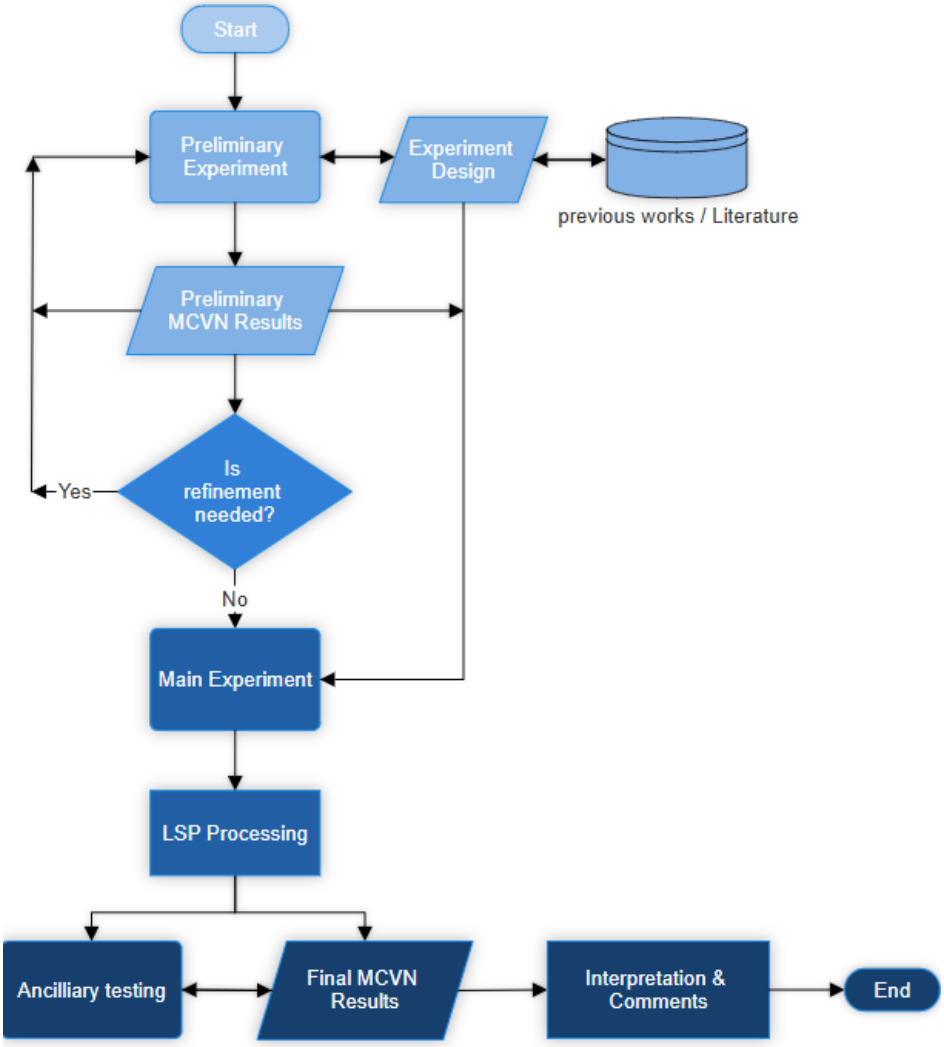

Figure 4-1 - Outline of the adopted experimental approach.

This approach is regarded as both efficient and highly optimised in terms of time and resources. Similar to the qualification and certification processes for L-PBF parts in the aerospace sector, this work adopts the principles of the testing pyramid to ensure a comprehensive evaluation that leads to superior results. After the initial phase, the next step involved refining the experimental design space by selecting key samples that represented significant conditions for the main experiment. These experiments were designed to generate essential data for identifying trends, validating assumptions, and analysing process behaviour. The subsequent final step involved performing LSP post-processing and conducting ancillary tests on previously identified features, which examined the properties of the parts that influence their characteristics. This final layer not only supports the main findings but also contributes to a comprehensive understanding of the entire process.

4.2 Experimental Design and Conditions

4.2.1 Computational Pre-Assessment – Simufact Additive

The literature review section has thoroughly discussed how part features define specific characteristics, and it identified four factors that influence these features:

1. Melt pool characteristics
2. Powder material properties
3. Heating and cooling cycles
4. Build strategy

Recall that the primary concern of L-PBF AM is the variability in process output. This variability is the root cause of many issues elaborated in section 2.3, and the motivation behind this work, is to advocate for a method to qualify parts through MCVN testing. Among the four factors, variation in melt pool characteristics is the most preferred option, as it is the only common cause that significantly impacts all the part features previously identified in Table 2-2. The bulk energy density metric influences the melt pool, which is defined by laser power, scanning speed, layer thickness, and hatch spacing. Preliminary simulations were conducted using the Simufact Additive software, enabling the observation of variability in real-life L-PBF processes and a controlled assessment of their effects on part quality and consistency. The impact on the melt pool and, consequently, the resulting part features were observed. The simulations also allowed for the observation of underlying issues affecting part quality, such as residual stress accumulation and the influence of block placement on the build platform, which in turn affected thermal gradients and stress distribution.

4.2.2 Process Parameter Variation

For experimentation purposes, it is essential to introduce variability in the manufacturing process in a controlled manner. Typically, the material's supplier provides parameters for bulk energy density, having conducted thorough testing to determine the most effective settings for their powders. These parameters are selected based on optimal product output and manufacturing time efficiency. From a business perspective, minimising post-processing and reducing production lead times are crucial factors that manufacturers strive to achieve. However, when intentional variations to these parameters are contemplated, the operating window map described in section 2.1.1 offers insights into the potential defects that may arise.

The lack of fusion (LoF) defect, which is often considered manageable, is a flaw that, if induced, allows the manufacturer to have complete control over the extent of the faults. Two primary methods to achieve LoF are utilising high scanning speeds with low laser power or maintaining consistent scanning speeds and power while varying only the hatch spacing. It is important to note that for all these variations, the layer thickness - a key parameter of bulk energy density - remains constant, as this parameter primarily depends on the particle size of the powder material used.

An experimental design known as One Factor at a Time (OFAT) was selected for this work, focusing on the variation of hatch spacing. The approach is easy to implement, allowing the unambiguous attribution of aspects observed on the produced parts to a single cause. Along with the chosen refinement strategy, OFAT is believed to be a complementary experimental approach. Its simplicity in implementation is expected to yield insightful conclusions.

The second variation is, of course, the LSP post-processing. However, this post-processing was only carried out on samples during the main experimental work. This is because obtaining reliable data regarding the sensitivity of MCVN based on one-factor variation was considered more important at the preliminary testing phase than introducing another factor. Details about the strategies and implementations are provided in Section 4.6.

4.3 Data Analysis Strategy

Some key concepts are essential before using any statistical approach to experimental analysis. First, it is important to clearly understand what is being studied and how the data will be collected. The primary purpose of using statistical analysis is to render results objective rather than judgmental. However, it is important to note that statistical analysis does not prove that a factor has any effect; instead, it provides reliability and validity to observations. A statistical hypothesis is a statement about the parameters of a probability distribution. The P-value at a significance level (α-value) indicates the likelihood of obtaining the observed statistic if the null hypothesis (H_0) is true. It helps gauge evidence against H_0 and shows the smallest significance level for rejecting it. It is important, however, to understand that statistical hypothesis analysis, when used with other tools, can provide more sound conclusions with a better understanding of the experimental situation. Graphical representations such as histograms and bar charts are tools often used to assist in the analysis of experiments. While they allow the experimenter to showcase the data's general tendency and distribution spread, they can be inaccurate and unreliable with small data sets. Another powerful representation of data is the use of box and whisker plots. This allows comparisons to be quickly made between data sets as it consists of a series of metrics that give insightful information on an experiment [102].

Data obtained from MCVN tests was presented and handled using three distinct methods. The chosen methods were intended to provide a comprehensive and holistic understanding in a layered fashion from various perspectives. Once all results were obtained, the MCVN absorbed energy and the other determined aspects were analysed and represented through regression models. The following subsections briefly explain the concepts of these analyses, emphasising their essential role. They also discuss the methods and what insights they provide.

4.3.1 Descriptive Analysis

The comparison of mean values is a practical and straightforward approach to summarise data, enabling easy identification of central trends and patterns. This method allows for a quick visualisation of key metrics through simple graphical representations, making it accessible for various analyses. However, a significant drawback of relying solely on mean comparisons is that it overlooks the nuances and variations that may exist within the data. Such variations can provide essential insights, and without considering them, the analysis may miss critical details that contribute to a deeper understanding of the dataset.

4.3.2 Explanatory Data Analysis (EDS)

Box and whisker plots serve as highly effective visual tools for representing data sets clearly and intuitively. These plots allow a straightforward comparison of the data's central tendency and variability. By highlighting quartile regions, they provide insight into the distribution of data points, making it easier to see where most values lie and how they spread across the range. This graphical representation simplifies understanding complex data sets and facilitates quick assessments of medians, ranges, and potential outliers.

4.3.3 Inferential Analysis

The analysis of variance (ANOVA) is a powerful statistical method that plays a crucial role in enhancing the depth of analysis and delivering solid statistical evidence to back up potential conclusions. Typically used with hypothesis testing, ANOVA ensures high objectivity in the conclusions drawn, mainly from final data sets. Much like EDS, this method accounts for the variability inherent in data sets, allowing researchers to derive definitive conclusions even when data noise and inconsistencies are present. This robustness makes ANOVA invaluable for uncovering meaningful insights from complex data, especially final experimental sets.

4.4 MCVN Impact Toughness Testing

4.4.1 Test Method

This work focuses on two specific standards: ASTM E23, which covers Notch Bar Impact Testing of Metallic Materials, and ASTM E2248, which pertains to Impact Testing of Miniature Charpy V-notch Specimens. The first standard outlines the significance of notch bar impact testing for metals. The second standard expands upon the first by introducing modifications that accommodate testing smaller samples. In short, ASTM E2248 is a standard that adopts the principles of the standard Charpy testing described in ASTM E23 for miniaturised sample testing. The scope of both test methods is summarised in Table 4-1.

Table 4-1 - Summary of the scope that ASTM test standards provide [92], [93].

ASTM E23	ASTM E2248
Requirements for standard tests on: • The test equipment • The test procedures • The Equipment verification procedure	Description for MCVN tests on: • The apparatus modifications • The inspection procedure • The calibration requirements

The dimensions of miniature samples and key features of the equipment are scaled down from standard Charpy V-notch to ensure that the stress fields are preserved. However, it is the user's responsibility to compare data of standard and miniature tests, and this comparison should be done with caution.

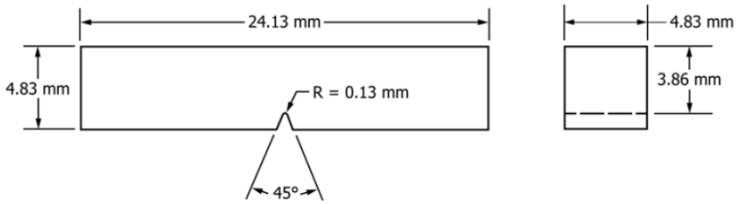

Figure 4-2 - Miniaturised Charpy V-notch sample dimensions [92].

4.4.2 Equipment and Procedures

Table 4-1 indicates that specific modifications must be made to the apparatus for MCVN tests to be successfully conducted. A summary of the background work that was undertaken is provided in Sections 4.4.2.1 and 4.4.2.2.

4.4.2.1 Apparatus Modifications

The pendulum-type Charpy impact tester found in the materials lab at the University of the Witwatersrand is from the German company FRANK-PTI. Its impact head, anvils, and supports were designed based on old test standards that could not be retrieved. The equipment was modified accordingly to conform to the new ASTM test standards. The crucial parts of the apparatus to be modified are the pendulum head (including the striker), anvils, and support geometry.

Figure 4-3 - The Charpy impact tester of the material labs at Wits.

Table 4-2 - Dimension comparisons of standard and MCVN tests setup [92], [93].

Description	Standard Dimensions	MCVN Dimensions
Span between anvils	40 mm	19.3 mm
Anvil radius	1 mm	0.48 mm
Anvil angle	80°	80°
Anvil support angle	90°	90°
Striker radius	8 mm or 2 mm	3.86 mm or 0.96 mm
Striker angles	30°	30°
Anvil Surface finish	0.1 µm	0.1 µm

A modification report containing the new designs for the impact head, the anvils, and the support was prepared and is attached in Annex 1 – Charpy Impact Tester - Modifications Report. The designs were made according to the existing equipment geometry and characteristics. This was done so the part modifications can be fitted properly and shall not be considered generic solutions to any apparatus. Care was taken not to alter too many things that might have unwanted effects, such as increased energy losses. For example, sleeve-like designs that mount on existing anvils and supports were made. The modifications report also includes the design of a centring jig. This tool was made to facilitate the testing exercise as it would ensure that the new anvils and supports are correctly spaced and centred with the striker.

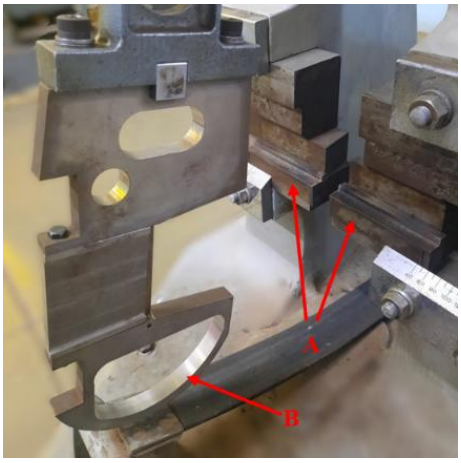

Figure 4-4 - Photo of the new anvils and supports (A), the updated impact head (B).

Figure 4-5 - Centring jig designed for the new anvils.

Table 4-3 - Main criteria respected when designing and making the modifications.

Criteria	Comment
The pendulum's centre of mass coincides with the percussion's centre.	Design requirement of ASTM E23
The striker portion of the impact head that passes between the anvils is between 10 mm and 18 mm thick.	Recommendation from BS EN ISO 148-1:2016
The angle between the striker's line of contact and the horizontal axis of the test piece is 90° ± 2°.	Design requirement of ASTM E23
Case hardening of key components, such as the striker, anvils, and support, to avoid breakage when hard materials are tested.	Performed by the Carburising process
The striker position is within 2.5 mm from the test specimen when the pendulum hangs freely.	Design requirement of ASTM E23
Impact velocities yielded are within the recommended range by having the pendulum head to the correct mass.	Design requirement of ASTM E2248
Considerations were made for specimen clearance in the design of the anvils.	Design requirement of ASTM E2248
The notches of the test specimens are within 0.25 mm of the midpoint between the anvils. (Due to the centring jig)	Design requirement of ASTM E23

4.4.2.2 Apparatus Verification and Calibration

The ASTM E23 standard recommends verifying and calibrating the apparatus following the modifications. The verifications, which are subdivided into direct and indirect, consider several aspects.

Direct verifications focus on inspecting the equipment and assessing key elements of the apparatus setup. These key elements involve measuring and calculating specific metrics by performing certain manoeuvres. The verification process is completed once the evaluations are confirmed to fall within the specified limits. The Charpy impact tester's range capacity and energy losses are among the main aspects determined in direct verifications.

Indirect verifications focus on confirming that the absorbed energy variation from testing reference samples with known impact energies using a modified setup is within the recommended range. This exercise uses reference samples of three energy levels: low, medium and high, which are defined by the test standard. However, indirect verifications are done after the scale of the MCVN test setup has been adjusted. The process involves using mathematical relationships to correlate determined absorbed energy values from MCVN tests with absorbed energies from standard samples that should have similar Charpy energy measurements. Only then can indirect verifications be done by comparing the adjusted readings to the reference absorbed energy readings, ensuring the variations are within range.

The verification report, attached to Annex 2 - Charpy Impact Tester - Calibration Report, explains how all the above-mentioned values are determined and the calculation methods. Each aspect of both the direct and indirect verifications is thoroughly documented. Additionally, the report includes information on whether the determined metrics of both direct and indirect verifications fall within the acceptable range prescribed within the standards for the results to be deemed valid. Table 4-4 and Table 4-5 summarise and outline some aspects that were adhered to for the test results to be acceptable.

Table 4-4 - Key requirement for machine suitability for MCVN tests [92].

Criteria	ASTM Std / Section
The capability of the equipment to break the specimen in one blow while retaining over 80% of its initial potential energy.	E2248 - Section 6.1
Achievable measurements with a resolution of 0.1 J or better.	E2248 - Section 6.1
Alignment of the specimen's centreline with the pendulum's strike centre.	E2248 - Section 6.2
The pendulum's impact velocity at the centre of the strike is within range.	E2248 - Section 6.3

Table 4-5 - Key requirements for Direct and Indirect verifications [93].

Criteria	ASTM Std / Section
The equipment level and pendulum rotation axis are within range, and the machine is securely fastened to requirements.	E23 - A1.1, A2.2.2, A2.2.5 & A2.2.6
The analogue scale shows measurements in degrees that can be estimated accurately.	E23 - A1.2
Frictional losses in the analogue scale are compensated, minimising errors in the indicating device.	E23 - A1.2.1
The percentage of friction and windage loss is within the range.	E23 - 9.1.1.3
The percentage of total losses to the range capacity during testing is to be within acceptable limits.	E23 - A1.3
The pendulum’s transverse play at the striker when a transverse force of a certain magnitude is applied at the centre of the strike is within range.	E23 - A1.5
The pendulum’s impact velocity at the centre of strike is within range.	E23 - A1.6
The pendulum’s release mechanism operates smoothly without any hard initial push, delay, or side vibrations.	E23 - A1.8 E23 A2.2.4
The striker position is perpendicular to the specimen's longitudinal axis and parallel to the face of a square specimen.	E23 - A1.10.3
The absolute and percentage differences between determined and certified specimens are within range.	E23 A2.4.1

The calibration and verification process are critical foundations for MCVN testing, underscoring the importance of the methodology's accuracy and precision. The modifications report and the verification report function interdependently, as any adjustments made to the modifications report can significantly impact the calculations detailed in the verification report. After all established criteria are satisfactorily met and confirmed through comprehensive reports, one can proceed to MCVN testing.

4.4.2.3 Testing Protocols

Following a standard operating procedure (SoP) is essential before testing to ensure that the obtained test results are consistent and reliable. The steps of the SoP are as follows:

1. All equipment parts are correctly verified and secured, and the moving parts can safely and freely operate across their entire range of motion.
2. Using the centring jig, the distance between the anvils and supports is adjusted, and the striker position is ensured to be precisely in the middle.
3. The pendulum from the latch position and allow it to swing between 50 to 100 times. This helps ensure that the joint bearing is loose and moving freely.
4. Before conducting any tests, the analogue scale needs to be initialised. From the latched position, allow the pendulum to make one free swing. Then, adjust the dial guide until the pointer indicates 0°. It’s important to ensure that after each swing, the pointer is put back to the same initial position as performed during verification.
5. The pendulum arm is secured in the latched position ready for testing.
6. The guard panels on the sides of the equipment are adjusted to prevent the small broken sample halves from flying away.
7. Once all the above conditions are met, the sample can be placed using the centring jig to ensure it is centred. MCVN samples can then be tested, and angular readings can be noted.

For this specific work, at least 3 samples were Charpy impact tested to get an average absorbed energy reading.

4.5 L-PBF Manufacturing

4.5.1 L-PBF facility

When evaluating L-PBF facilities, key factors to consider are reliability, efficiency, and resolution. Companies are refining the process, but success hinges on understanding the interaction of all relevant factors specific to each setup. The HYRAX metal 3D printer is an advanced piece of equipment created by the South African company Aditiv Solutions and is used for L-PBF AM in this work. Its versatility makes it particularly effective in producing medium to large components, making it an excellent choice for academic and research and development (R&D) applications. Equipped with a cutting-edge 400 W laser optical system and a Ø200 mm × 300 mm build volume, this printer can efficiently manufacture parts from various materials, including steel, titanium, aluminium, nickel, and cobalt-chrome [103].

Figure 4-6 - The HYRAX metal 3D printer [103].

4.5.2 Manufacturing Parameters and Conditions

The selection of manufacturing parameters is generally governed by the powder material used. This is determined by obtaining an equilibrium to generate a stable melt pool to fuse the powder sufficiently, which is also very dependent on the volume of the material (i.e. layer thickness). Research indicates that AM techniques like L-PBF yield improved surface finish and mechanical properties when thin layers of fine powder are used [4]. However, the particle size (and size distribution) is generally outside the manufacturer's control.

This study manufactured MCVN samples using Grade 5 Ti-6Al4V powders from Advanced Powders & Coatings (AP&C) [104].

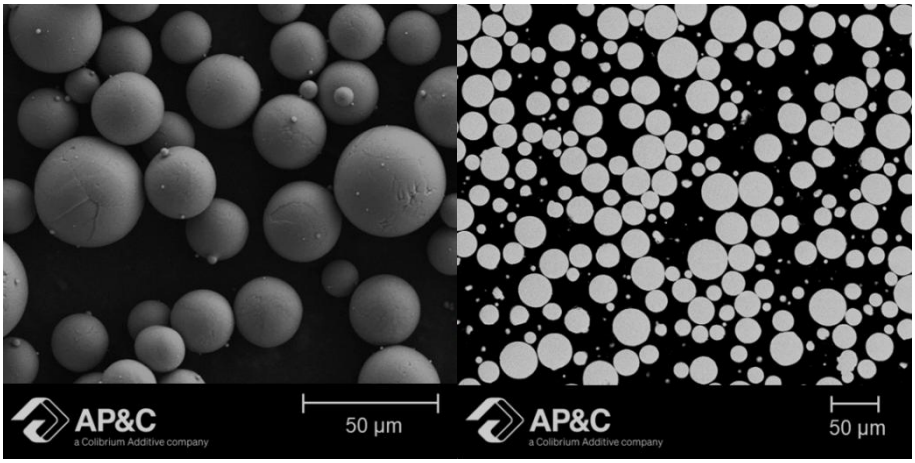

Figure 4-7 - SEM and metallographic image of the powder material from AP&C [104].

The Ti-6Al-4V material powder used has been manufactured through the proprietary APATM Plasma Atomisation process, featuring a particle size distribution of 15-45 µm. This is the smallest distribution size produced by the company, suitable for L-PBF AM. The powders are spherical, exhibiting virtually no entrapped porosities, and are sieved to meet the specifications set forth by customers [104].

Blocks were printed from which the MCVN samples were prepared. The dimensions of these blocks were explicitly designed to account for material loss during sample preparation. Additionally, the design included allowances for the clamping of the material, which was needed throughout the sample preparation.

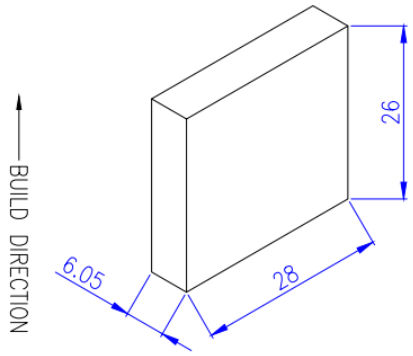

Figure 4-8 - Dimensions (in mm) of printed blocks

However, when designing the printing blocks for the samples, the primary consideration remained the orientation in which the samples would be prepared. The main aspects that significantly depend on the build orientation are the microstructure, residual stresses, and the shape or orientation of LoF defects. In this work, the horizontal build orientation was preferred, as it was believed to yield a lack of fracture resistance capabilities, based on the anticipated part features. These expected features stemmed from the chosen experimental design and were deemed suitable for assessment by MCVN impact tests. Due to the microstructural characteristic of martensitic α′ within the columnar prior β grains along the build direction, the transverse direction was considered more favourable for crack propagation. With the limited number of grain boundary obstacles, failure by intergranular or cleavage fractures along β grain boundaries is more common. Furthermore, as noted in past research, the tensile residual stresses inherent to the L-PBF process tend to be higher along the scanning vector lines. In the case of horizontal MCVN samples, this orientation represents a plane perpendicular to the direction of fracture propagation, creating another disadvantage to crack propagation. Finally, the variation in hatch spacing leading to LoF defects is more pronounced in horizontal samples. The melt pool for single tracks being correctly optimised will ensure adequate bonding to the previous layer but may not provide sufficient bonding between adjacent layers.

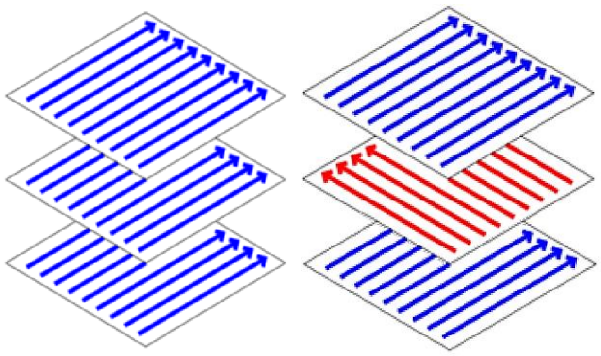

Figure 4-9 - Representation of scanning variations: alternating and unidirectional.

The scanning strategy is another process-based parameter that significantly influences the mitigation of adverse effects associated with temperature cycles and residual stress fields in L-PBF builds. Common strategies include meander, chessboard, stripe, and island scanning. Additionally, the variation of scanning patterns across successive layers plays a crucial role, particularly regarding whether each layer's scanning direction is altered. Research has indicated that residual stress components are highest in the scanning track direction, regardless of the pattern employed. Numerous studies have suggested that alternating the scanning pattern between layers can effectively balance and reduce the buildup of residual stress in the builds. Considering the machine capabilities and results observed in prior work, the meander alternating layer scanning strategy (-30°, 0°, 30°) was considered appropriate [105], [106].

4.5.3 Post Manufacturing – Stress Relieving

After what has been observed from previous works in section 2.3.3 and after conducting the exploratory trial run simulations, it was decided that samples would be stress-relieved post-manufacturing. This was made because the printing blocks designed were relatively small and prone to unwanted deformations or cracks. Because Charpy samples for mechanical testing heavily depend on uniformity in size and features resulting from the manufacturing process, this step was considered very important.

There are multiple ways to relieve stress in L-PBF Ti-6Al-4V, as residual stresses from the additive manufacturing process can vary based on build parameters and geometry. Variations exist in temperature, hold time, atmosphere, and cooling rate, often tailored to strike a balance between stress reduction and microstructure stability, as well as mechanical properties. Specific information about the method is detailed in standards like the AMS 2801D [107]. The two most common stress-relieving methods are low temperature (593-600°C for 2-4 hours, followed by air cooling) and mid-temperature (650-670°C for 3-5 hours, followed by air or furnace cooling). These processes are typically performed in either a vacuum, with an inert gas (e.g., argon), or in air to prevent oxidation. The goal is to reduce residual stresses without significantly altering the martensitic or fine microstructure from L-PBF. In this work, the guidelines on mid-temperature heat treatment from the ASM Handbook, Volume 4, were followed and are detailed in section 5.1 [7], [108].

4.5.4 Post Manufacturing - Sample Preparation

Following the stress relief, samples were prepared from the blocks. An EDM wire cutter, equipped with a 0.2 mm thick zinc-coated brass wire and operating at a cut speed of approximately 2 mm/min, was used to separate the blocks from the base plate. Subsequently, using the same equipment, a slightly oversized profile of the MCVN was cut out to ensure that the notch was centred and uniform on each sample. A face milling process was carried out before cutting the individual samples. Given the oversized profile cuts, this step is intended to achieve the required surface finish on both the front and rear sides of each MCVN sample, while also meeting the sample thickness specifications. A final EDM wire-cutting operation was performed to separate the samples individually. The Laser Peening faces, as labelled Figure 4-10, derived from the last cut, were lightly polished using silicon carbide paper of grit 320 to ensure a smoother and more uniform surface, with an average S_a value of around 0.1 µm, as specified in ASTM E2248.

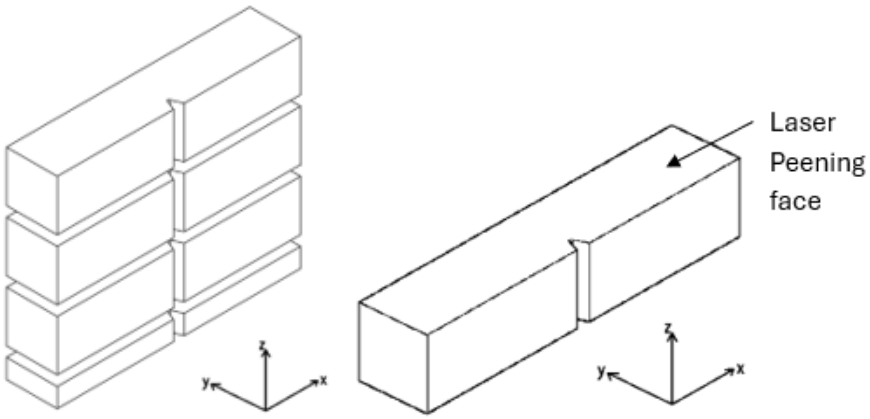

Figure 4-10 - MCVN sample orientation prepared from printed blocks.

4.6 LSP Processing

4.6.1 LSP Facility

The Laser Shock Peening (LSP) facility at the Council for Scientific and Industrial Research (CSIR) National Laser Centre (NLC) is equipped with two lasers: a 1064 nm laser and a 532 nm laser. For this research project, peening was conducted using the 532 nm laser, commonly called "green" light laser. The Spectra Quanta-Ray PRO270 Q-Switched Nd:YAG laser is designed to generate high-energy laser pulses of ~ 2 ns [109].

Figure 4-11 - Illustration of the Spectra Quanta Ray laser [109].

4.6.2 Processing Strategy and Conditions

The initial step involves identifying the peening parameters that will be used for processing the MCVN Ti-6Al-4V samples. As previously mentioned, the LSP in this study will be defined by three fundamental parameters: Power Intensity, Spot Size, and % Overlap. Given titanium's reputation for being challenging to machine, the decision was made to employ high power intensities for the peening process. This aligns with multiple recommendations from research specialists at the CSIR and observations from prior studies on the topic. Additional insights regarding the pulse density metric indicate that high overlap yields more uniform and effective results. Furthermore, it has been noted that using small spot diameters, along with high overlap, produces more significant residual stresses in the near-surface region [81], [83], [86].

The challenge for processing MCVN samples was to secure them on the CNC platform during processing. Thus, a sample-holding jig was designed to keep the individual samples in place while the jig was clamped onto the platform. The jig is constructed from mild steel, and further design details are available in Annex 3 – Sample Holding Jig Design for LSP of this report.

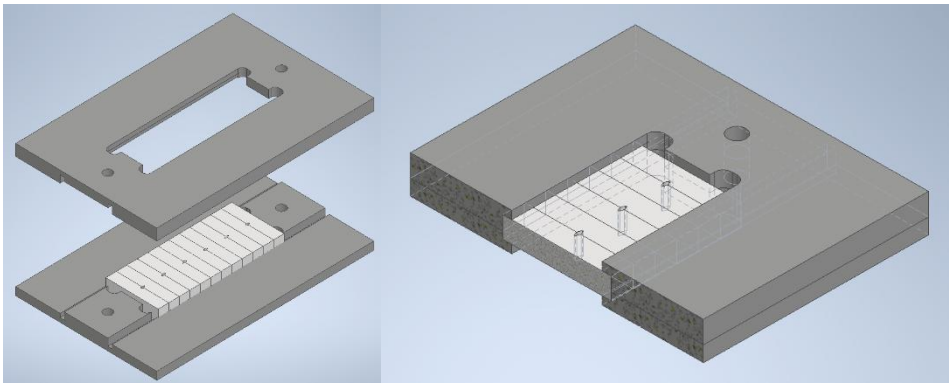

Figure 4-12 - Designed jig model showcasing clamping of samples for LSP.

Peening was conducted on the sides of the MCVN samples to mitigate defects (surface and subsurface) and induce beneficial compressive residual stresses, thereby enhancing the strength of the test piece against impact loading. The middle section of the sample was peened over a total length of 12 mm, centred around the notch, covering the entire thickness of the sample. This approach was chosen because peening the central portion was deemed sufficient; this area experiences the most stress and is where cracking typically occurs.

Additionally, two aspects were considered when selecting the peening scan strategy: (1) the magnitude of the induced residual stresses at a specific location on the peened component and (2) the direction of the major induced stresses relative to the scanning direction. Studies indicate that significant compressive residual stresses are more effectively induced on the surface and subsurface close to the front edges, where scanning begins [110], [111]. Moreover, works, like Wang et al. [112], observed that while the residual stresses induced in a single pass were significant in the scanning direction, they were even more pronounced in the stepping direction. However, when peening the MCVN samples using the raster pattern strategy, which is the most prevalent approach for peening, it was not feasible to maximise the advantages of both aspects simultaneously. Consequently, the decision was made to use the same peening procedure as in Ruschau et al. [113], who found that the maximum surface residual stresses induced by LSP to counter fatigue crack growth were approximately 1 mm to 5 mm from the front edge, which is relatively similar to what we aim to achieve in our MCVN samples. The notch side of the sample was therefore chosen as the front edge during the peening process, which, unfortunately, meant that the scanning step would be perpendicular to the optimal orientation for mitigating crack propagation.

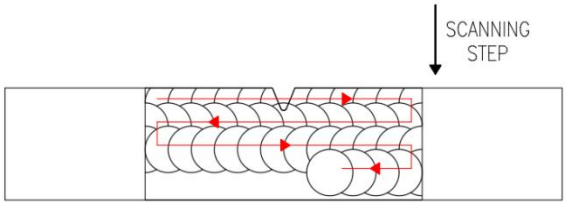

Figure 4-13 - A representation of the LSP processing pattern is on the MCVN sample.

4.7 Ancillary Testing

In Chapter 2, the assessment methods of the L-PBF AM process were examined, and several key factors contributing to the stagnation of technology development were identified. Although strength and toughness are the primary metrics of importance, it is crucial to analyse additional parameters that influence these properties. Gaining insight into these factors and correlating them with mechanical performance can enhance our understanding of the manufacturing process.

Recall, the essential features to be examined include:

1. Fractography,
2. Density and Defects,
3. Surface Integrity,
4. Internal Residual Stresses,
5. Metallography, and
6. Hardness.

The following sections will systematically explore these features in detail by addressing the testing setups, procedures, and key considerations. They will also outline their relation to standard practices or established testing protocols. This comprehensive examination also describes the overall experimental process. It highlights the critical factors considered during the experimental work to ensure that relevant data is obtained to qualify and quantify the effects on the performance of parts manufactured through L-PBF.

Note:
- *Ancillary testing was only performed for the main experimental samples.*
- *The specific details of the testing metrics are elaborated in sections 4.7.1 to 4.7.5.*

4.7.1 Fractured Surface Fractography

The three steps detailed in the literature review on fractographic analysis require specific tools and equipment, which are summarised in Table 4-6.

Table 4-6 – Necessary tools/equipment for fractographic analysis.

Examination	Tool / Equipment
Visual	Magnifying glass, Digital camera
Low magnification	Optical Stereomicroscope, Digital Camera
Microscopic	Scanning Electron Microscope

4.7.1.1 Testing Facilities

Visual features were captured using a standard high-resolution camera. Optical stereomicroscopy was performed in the materials lab at the School of MIA Engineering, while scanning electron microscopy was conducted on the TESCAN VEGA3 at the Microscopy and Microanalysis Unit (MMU) at Wits University.

Figure 4-14 - The TESCAN VEGA3 SEM facility at the MMU [114].

4.7.1.2 Test Procedures

After impact testing, the fractured halves were carefully collected and, if necessary, cleaned with compressed air. They were then safely stored in a dry container, with precautions taken to avoid damage or contamination of the fractured surfaces. Proper storage was considered crucial when SEM analysis could not be performed within a few hours after the fracture. An airtight container was used to prevent excessive oxidation of the fractured surfaces. Once MCVN testing had concluded, the samples were prepared for macroscopic analysis, during which images were captured using a camera and a stereomicroscope. Following this, SEM analysis was conducted.

In microscopic analysis, mainly when light and electron microscopes were used, two key aspects had to be considered: 1. the areas to be examined, and 2. the features of interest. The ASTM E23 standard briefly explains the different regions that should be observed on the fractured surface as shown below. The level of magnification was determined by the observed features, ranging from very low to magnifications in the x1000.

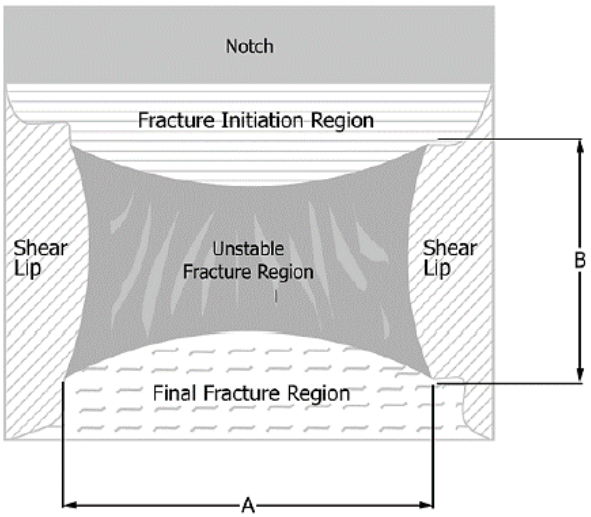

Figure 4-15 - Areas on a stable fractured surface of a Charpy V-Notch specimen [93].

Note:

- *Dimensions A and B are measurements taken when a stable fracture occurs, resulting in visible regions. Their purpose is to analyse the appearance of shear fractures.*

4.7.1.3 Fracture Data Handling

Fracture analysis at all levels was characterised by observing and appreciating features, which were then described and interpreted based on previous findings and existing literature [115]. Due to the intentional variation in hatch spacing and the expectation of highly porous surfaces, fractures originating from localised inhomogeneities or defects within the material, such as inclusions, microcracks, and voids, were given particular attention [11].

The analysis of fractured surfaces was considered delicate, especially when attempts were made to understand fracture mechanisms and intrinsic factors [89]. The sequence of examination was as follows:

1. Understanding of the overall geometry and orientation of the fracture plane.
2. Deducing the type of fracture.
3. Observing the roughness and texture of the fracture surface.
4. Identification of secondary cracks, if present.
5. Pointing out patterns and features.
6. Relating the features of the fractured surface to the other determined attributes.

After the analysis, links were established between the fractographic observations and the absorbed impact energy values.

4.7.2 Micro Computed Tomography (microCT)

The test standard ASTM E1441 outlines the general principles of X-ray microCT. This examination method was utilised to reconstruct radiographic images using computers. The process was employed to generate 3D graphics by triangulating each point in the plane from many different directions [116]. This technique proved ideal because of its non-destructive nature. It permitted the MCVN impact testing to be conducted on the same samples following the CT scans.

4.7.2.1 Testing Facility

The porosity testing for this work was carried out using the cone-beam, Comet Xylon FF20 micro-CT scanner located at the National Metrology Institute of South Africa (NMISA) at the CSIR.

Figure 4-16 - The Comet Xylon FF20 CT machine [117].

4.7.2.2 Test Procedures

Once the samples were ready for testing, they were mounted on the fixation table. They were secured with non-conductive adhesive tape to prevent slight movements during scanning. The machine was switched on and warmed up with the test specimen inside. The settings for Ti-6Al-4V testing, including the X-ray voltage and current, were adjusted accordingly by trial and error for the initial scan. The values used are specified in the section 5.5.2 and ensured that the optimal resolution of readings could be recorded. The same parameters were maintained for subsequent scans to ensure uniform measurements. These parameters, including voxel resolution, rotation steps, and the number of desired projections, were chosen to obtain the highest-resolution images for more accurate analysis.

4.7.2.3 Porosity Data Handling

Following the scanning and the data obtained, the processing phase was initiated. This step was deemed crucial, as even minor errors could lead to significant repercussions on the values of the results. The software Volume Graphics VGStudioMax 3.1 [118] was used to handle the scanned data. First, the data was cleaned up by removing any noise picked up during the scan. The following task involved defining the regions of interest (ROIs). This included outlining the total volume of the scanned part, identifying the boundaries of voids and pores, and determining the regions of the material. In some cases, manual definitions were necessary. A final verification was conducted using slices of the samples in all three orientations to ensure nothing was overlooked. Once satisfaction was achieved with the definitions of the regions, the data was processed, and the equipment defined the porosity through automatic arithmetic operations applied to the defined regions of interest.

4.7.2.4 Surface Integrity Data Handling

The surface characteristics were also determined from the same data set obtained during micro-CT scanning using the same Volume Graphics software. This method was preferred due to the small size of the samples. With an anticipated significant roughness average (R_a) value, the concern was insufficient material for selecting an adequate evaluation length. Expected surface defects, even after machining and/or polishing, were expected to cause a high surface roughness average.

The micro-CT evaluation process of surface integrity is detailed in the work carried out by Du Plessis et al. [76]. A region of interest (ROI) was again defined, encompassing the surface in question, along with a portion just outside and a little inside the sample. Following this, a mesh was created based on random points clicked on the material's surface. The mesh's purpose was to trace the surface's peaks and valleys. Subsequently, the data regarding the deviations of the mesh from the region of interest were extracted, and the average surface roughness (Sa) value was calculated through further processing.

4.7.3 X-Ray Diffraction (XRD)

The X-ray diffraction (XRD) technique is governed by the test standard ASTM E915 [116]. Its rapidity and accuracy make it an effective identifier of stresses in the small MCVN samples [10]. The analysis was based on the atomic spacing at the specimen's surface. The spacing shifts, derived from diffracted X-ray peaks determined by Bragg's law, enabled the determination of residual stresses.

4.7.3.1 Testing Facility

The residual stress determinations in this work were carried out on the iXRD combo from Proto at the Centre for Innovation through Engineering (eNtsa) of Nelson Mandela University (NMU).

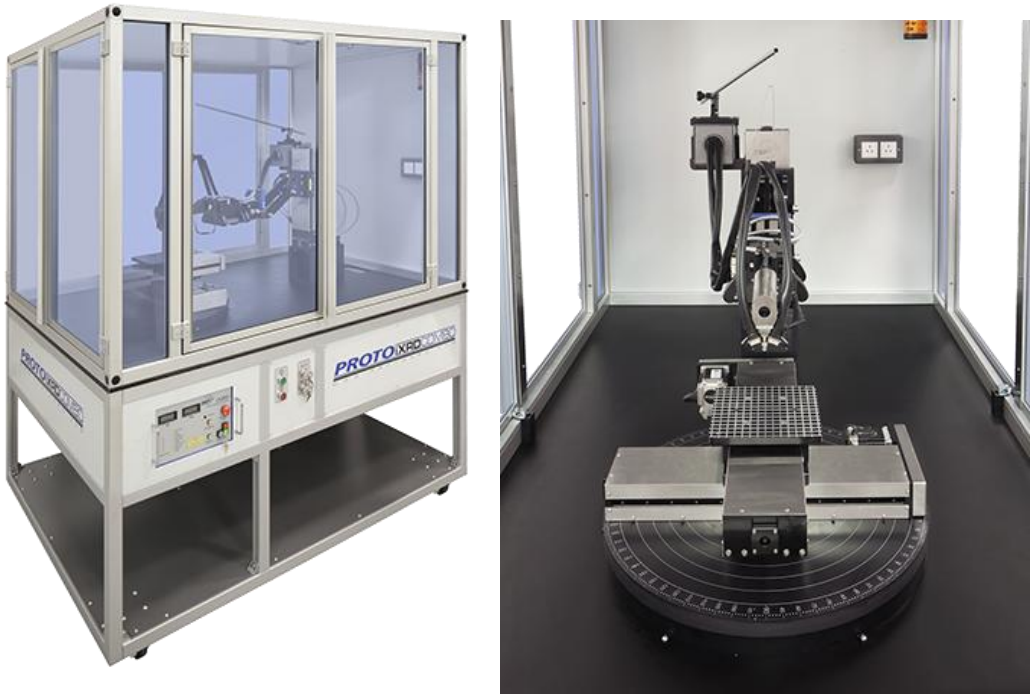

Figure 4-17 - The Proto iXRD combo [119].

4.7.3.2 Test Procedures

Samples were prepared and sent for analysis. The samples were clamped and aligned correctly to ensure that the appropriate region of each sample was evaluated. Before testing, key parameters such as the aperture size, exposure times, number of exposures, X-ray source, Bragg angles and tilting angles, amongst others, were set. Larger aperture sizes provide a higher resolution. However, due to the small geometry of the samples, appropriate apertures were chosen accordingly. The exposure times and number of exposures were also critical factors, as they influence the type of signal captured. Given the high atomic number of Ti-6Al-4V, a high-energy X-ray source was required for testing. The samples' material also dictated the Bragg angle and the tilting angle to be used.

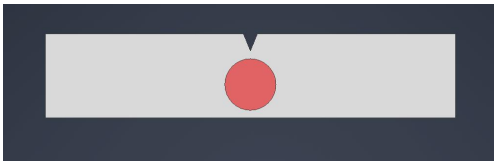

Figure 4-18 - The region where evaluation was carried out.

4.7.3.3 Residual Stresses Data Handling

The stress values were recorded straight from the equipment and were calculated using ASTM E915 principles. The main aspects of the triaxial test results, including the major and minor principal stresses, were analysed. The direction of the principal stresses was also recorded, as this data was crucial for making analytical observations.

4.7.4 Metallography

Metallography can be carried out using low-magnification and high-magnification microscopy. Low-magnification microscopy serves as the primary and most critical examination step in metallography. High-magnification microscopy offers precise, detailed assessments and facilitates the determination of the material's composition and phases [10], [23].

Table 4-7 - Type of microscope used for magnification level.

Magnification	Microscope type
Low level magnification	Optical Microscope
High level magnification	Scanning Electron Microscope

4.7.4.1 Testing Facilities

Grinding and polishing of samples were conducted using LaboSystem equipment from Struers in the metallography lab at School of CHMT Engineering. Low-magnification microscopy was performed on the Motic B1 trinocular optical microscope in the materials lab at the School of MIA Engineering, and high-magnification microscopy was conducted using the same equipment, the TESCAN VEGA3, shown in Figure 4-14 at the Microscopy and Microanalysis Unit (MMU) at Wits University.

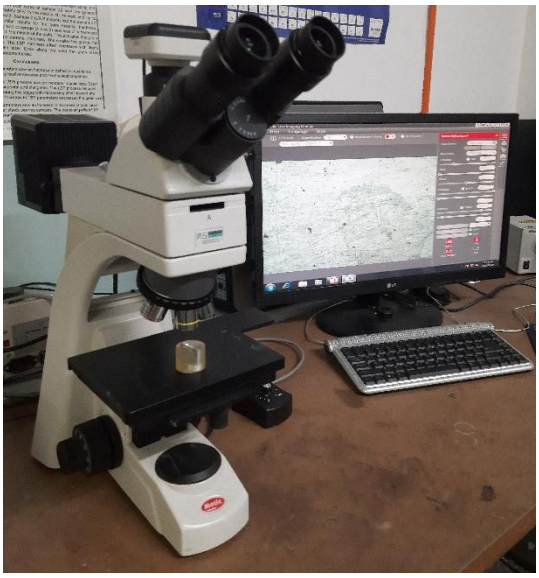

Figure 4-19 - The Motic B1 trinocular optical microscope - MIA Materials Lab, Wits.

4.7.4.2 Test Procedures

Metallographic preparation and determinations were conducted according to the standard procedures outlined in the ASM Handbook - Metallography and Microstructures, Volume 9 [23]. Given the components' anisotropic nature, observations in at least two directions were necessary to properly analyse the specific features associated with the L-PBF additive manufacturing of Ti-6Al-4V. Figure 4-20 below illustrates the sectioned planes that were investigated.

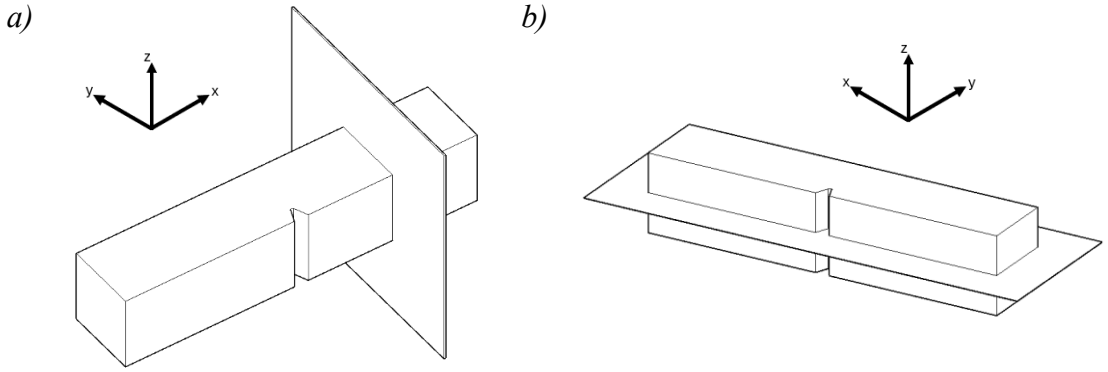

Figure 4-20 - Metallographic planes investigated: (a) YZ direction, (b) XY direction

These two planes were selected based on their relative orientation with the fracture propagation path. This selection is justified as it enables the identification of the mode of fracture propagation and understanding whether the LSP post-processing affects the microstructural aspects and, ultimately, the fracture mechanism [10].

The fractured surfaces were mounded in moulds using an appropriate resin. Grinding and polishing were performed until satisfaction was achieved. The samples were etched with Kroll's reagent to reveal microstructural features.

Table 4-8 - Kroll's microetchant composition [23].

Product	**Quantity (mL)**
Distilled Water	100
Nitric Acid (65 %)	2 - 6
Hydrofluoric Acid (40 %)	1 - 3

4.7.4.3 Microscopic Data Handling

Qualitative and quantitative analyses were conducted on metallographic microscopic images of metallographs. The examination process begins with light microscopy before advancing to higher magnifications, as most microstructural features are effectively observed and identified using this initial technique. Optical Microscopy (OM) establishes the relationship between microstructural grains and their boundaries with the fracture paths. It was also employed to evaluate whether undesirable microstructural conditions, resulting from the material's quality, poor manufacturing processes, post-manufacturing treatments, or stress-relieving heat treatment, have influenced fracture behaviour. In addition to analysing grain features, geometrical dimensions of grains can also be quantitatively assessed. Conversely, Electron Microscopy (EM) is recognised as an excellent complementary tool to Optical Microscopy (OM), as it provides a greater depth of field. High-magnification images were produced that facilitated the determination of material composition and phases. Furthermore, the SEM facility, which was equipped with an Energy-Dispersive X-ray Spectroscopy (EDS) probe, enabled quantitative analysis of chemical composition with a lateral resolution of one micrometre and a typical depth resolution of a few tenths of a micrometre [10], [23].

4.7.5 Microindentation Hardness

The hardness property provides reliable and quantitative insights into other mechanical properties. Although many techniques exist for measuring the hardness of a metallic component, indentation testing remains the most popular due to its simplicity and cost-effectiveness. This testing method evaluates how well a material can withstand plastic deformation, ultimately assessing its resistance to permanent indentation [10], [11], [19].

The test standards governing microindentation testing are ASTM E384 and E92. These standards encompass tests conducted using Knoop and Vickers indenters. While the testing principle is the same for both methods, the geometry of the indenters and the analysis techniques differ slightly [120], [121].

4.7.5.1 Testing Facility

Samples in this work were tested using the Falcon 500G2 hardness tester from INNOVATEST, found in the metrology laboratory of the School of MIA Engineering at Wits University. The equipment was equipped with a Vickers indenter.

Figure 4-21 - The Falcon 500G2, with a Vickers micro indenter [122].

4.7.5.2 Test Procedures

Microindentation hardness testing was conducted on the same samples prepared for metallographic analysis. Initially, one of the primary purposes of this test was to assess the influence of LSP on hardness and to determine any correlations with the observed absorbed energies. The evaluation focused on the YZ direction, as illustrated in Figure 4-20. A trial-and-error approach was adopted to establish the two critical input parameters for the testing: applied force and dwell time, despite the numerous recommendations found in existing literature. This iterative method was necessary because of variations in materials and manufacturing processes across different works. Achieving precise measurements using the light microscope fitted on the equipment was essential before settling on consistent parameters for all tests. Indentations were made across the samples' cross-section, (on the subsurface of the peening face) reaching a depth considered reasonable and likely to be affected by the LSP post-processing. At least five indents were performed for each depth level, ensuring they were evenly spaced as recommended in testing practices.

4.7.5.3 Microhardness – Vickers (HV) Data Handling

Once the test setup had been confirmed, with the appropriate force and dwell times, data collection was straightforward. Indentations were made and observed under a light microscope. The procedure followed was that all the indents for a particular depth were done together and saved as one test. The equipment software automatically drew crosshair lines across the corners of the indent; however, they were manually adjusted, when necessary, until satisfied. The software automatically calculated the Vickers Hardness (HV) values following the standard test method, and a test certificate, containing information about the tests, was extracted for analysis.

Chapter 5. Testing and Evaluation

This chapter details the experimental work conducted, summarising the activities carried out in the workshop and laboratory. It outlines the parameters, conditions, and results of various activities undertaken. Additionally, it addresses specific tasks encountered during laboratory testing or data processing. Observations derived from the results, mainly those illustrated graphically, are discussed. The chapter also includes a statistical analysis of the main experiment's MCVN results to support the discussions in the later stages of the research.

Note:

- *This section provides a summary of the results obtained. Due to the large amount of material collected and the complexity involved in interpretation, the data presented has been simplified. It is primarily presented through graphs and visual illustrations to enhance clarity. For further information and to explore the raw data, please refer to Appendices one to seven section.*

5.1 MCVN sample Fabrication and Preparation

The manufacturing parameters used for the AP&C powder material on the Hyrax machine from Aditiv Solutions, located at the CSIR, are summarised in Table 5-1.

Table 5-1 - Summary of parameters used for L-PBF printing

Parameter	Value
Laser Power	360W
Scanning Speed	2.3 m/s
Scanning Pattern	Back and forth, (-30, 0,30)
Beam Diameter (Spot size)	90 µm
Inert gas	Argon
Baseplate Heating	No – unavailable on equipment
Powder Material	AP&C Ti-6Al-4V grade 23
Layer thickness	40 µm
Hatch Spacing	Varied

Note:

- *Contour scanning was not conducted because the printed blocks are designed to be oversized, with MCVN samples to be cut out using EDM wire cutting.*
- *The staggered orientation strategy of the printed blocks was used to prevent contamination from unfused particles in neighbouring blocks.*

The hatch spacing for manufacturing preliminary samples was based on data from previous projects that provided density information. This data pertains to samples made using the same machine and powder material supplied by the manufacturing company. Hatch parameters for the final set were, on the other hand, selected based on the results of the preliminary tests and corresponded to the minimum variation, which will provide a noticeable trend in the decrease in the absorbed energies recorded. The summarised values of hatch spacing used are presented in Table 5-2.

Table 5-2 - Summary of hatch spacing values used in sample manufacturing.

	Set 1	Set 2	Final Set
Hatch Spacing Value (µm)	72	72	72
	172	92	132
	202	112	142
	-	-	152
	-	-	162
	-	-	172

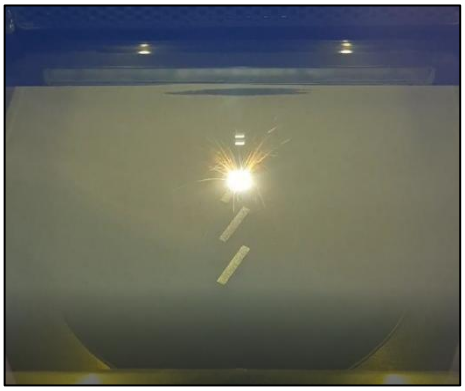

Figure 5-1 - Manufacturing of blocks for preliminary testing.

Figure 5-2 - Powder removal from the build chamber.

After the blocks, measuring 6.05 × 28 × 26 mm, were printed and before being removed from the baseplate, they were sent to be stress-relieved (SR) at the local company Metal Heart in Johannesburg [123]. The stress-relieving conditions for Ti-6Al-4V without altering the part's microstructure were as follows: heated to 650°C for 3 hours in a vacuum, followed by air cooling to room temperature [108].

Figure 5-3 - Manufactured blocks on the baseplate for the final experiment.

Figure 5-4 - EDM wire cutting of printed blocks from the base plate.

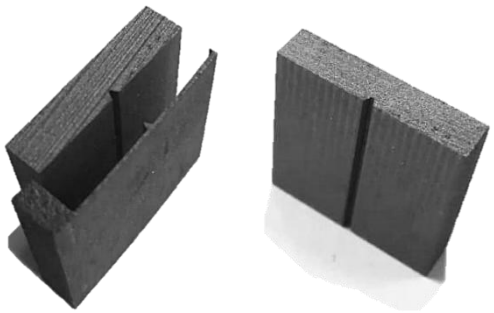

Figure 5-5 - Oversized MCVN samples profile cut out of the manufactured block.

After the oversized profiles were cut, a face milling operation was performed to remove excess material and achieve a smooth surface finish. Measurements before the operation indicated that an expected surface layer of approximately 0.1 to 0.2 mm had to be removed for all the blocks. This operation took place in the workshop of the School of MIA Engineering, utilising a micro grain carbide end mill tool bit, with the machine parameters summarised in Table 5-3 below.

Table 5-3 - Face milling machine parameters used on printed blocks.

Parameter	Value
Feed Rate	80 mm/min
Tool Speed	800 rev/min
Depth of Cut	0.05 mm

Following the milling operation, samples were cut and polished to be ready for testing as elaborated in Chapter 4.

5.2 Preliminary Assessment – 1st Set

The first set of samples was manufactured with varied hatch spacing, as summarised in Table 5-2. The results of the MCVN tests that were conducted are shown in Table 5-4.

Table 5-4 - Results Summary of the 1st test set.

Sample Description	Absorbed Energy Reading (J)			Mean Absorbed Energy (J)
	1	2	3	
72 µm Hatch	14.82	11.40	12.00	12.74
172 µm Hatch	5.35	4.85	4.13	4.78
202 µm Hatch	3.19	3.89	3.65	3.58

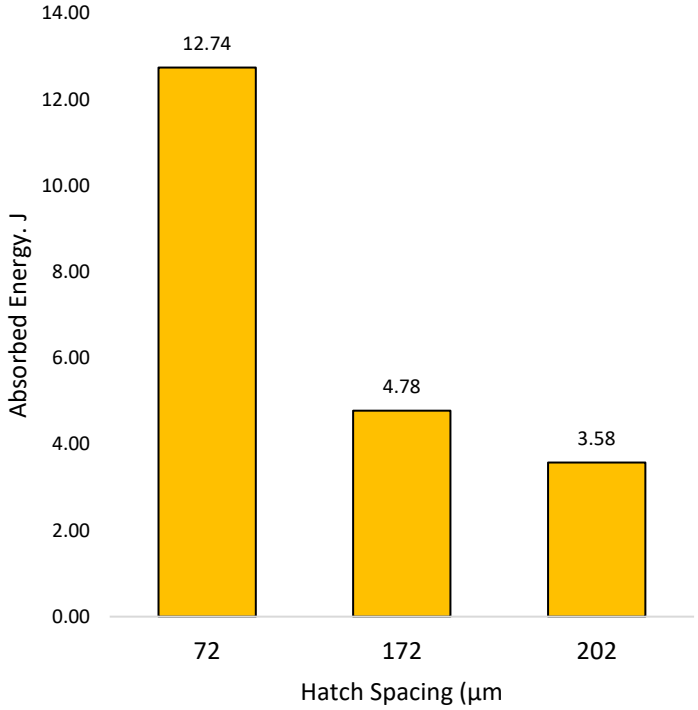

Figure 5-6 - Mean absorbed energy, 1st Set.

.

Table 5-5 - Summary Statistics of the 1st test set.

Sample Description	Key Descriptive Statistics				
	Minimum	Q1	Q2	Q3	Maximum
72 µm Hatch	11.40	11.70	12.00	13.41	14.82
172 µm Hatch	4.13	4.49	4.85	5.10	5.35
202 µm Hatch	3.19	3.42	3.65	3.77	3.89

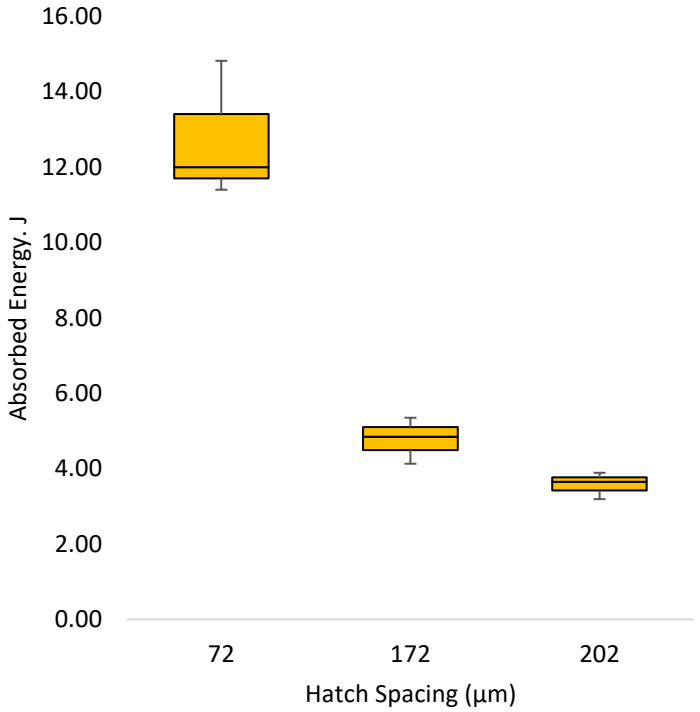

Figure 5-7 - Explanatory Results, 1st Set.

Observations:

1. Figure 5-6 suggests a trend of decreasing absorbed energy values as the hatch spacing increases.
2. A sharp drop is observed in the absorbed value energies between the 72µm hatch spacing, considered the "ideal" condition, and the increased values of hatch spacing.
3. The box and whisker plot of Figure 5-7 reflects a similar pattern to the mean values obtained, confirming the significant change in absorbed energy recorded.
4. The first sample with 72µm hatch spacing shows a broader spread of whiskers and more significant variability in absorbed energy values compared to the 172µm and 202µm samples with smaller interquartile ranges, indicating more clustered absorbed energy values.

5.3 Focused Exploration – 2nd Set

The hatch spacing variation window for the second test set was significantly minimised. The MCVN test results summary of samples with varied hatch spacing in Table 5-2 is illustrated in Table 5-6.

Table 5-6 - Results Summary of the 2nd test set

Sample Description	Absorbed Energy Reading (J)			Mean Absorbed Energy (J)
	1	2	3	
72 µm Hatch	12.31	14.82	13.23	13.45
92 µm Hatch	13.23	12.31	12.92	12.82
112 µm Hatch	13.55	12.92	12.61	13.03

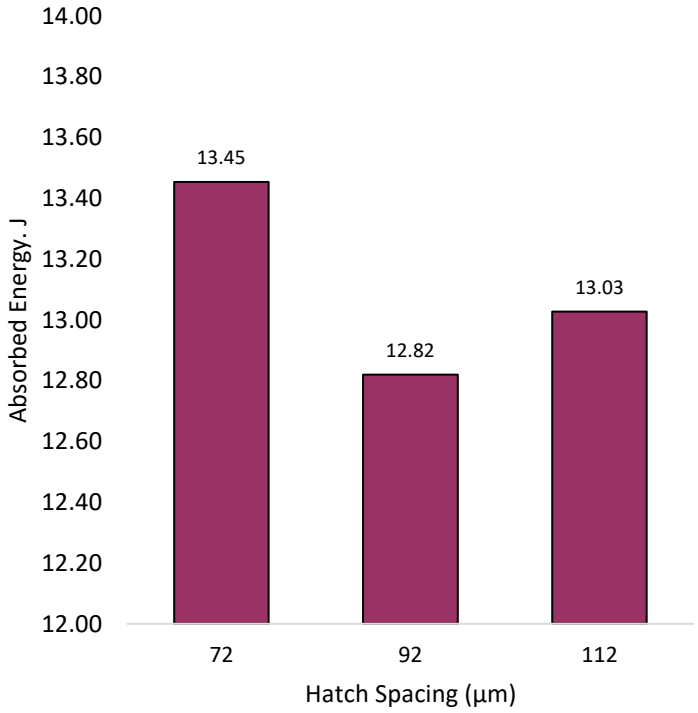

Figure 5-8 - Mean absorbed energy, 2nd Set.

Table 5-7 - Summary statistics of the 2nd test set

Sample Description	Key Descriptive Statistics				
	Minimum	Q1	Q2	Q3	Maximum
72 µm Hatch	12.31	12.77	13.23	14.03	14.82
92 µm Hatch	12.31	12.62	12.92	13.08	13.23
112 µm Hatch	12.61	12.77	12.92	13.24	13.55

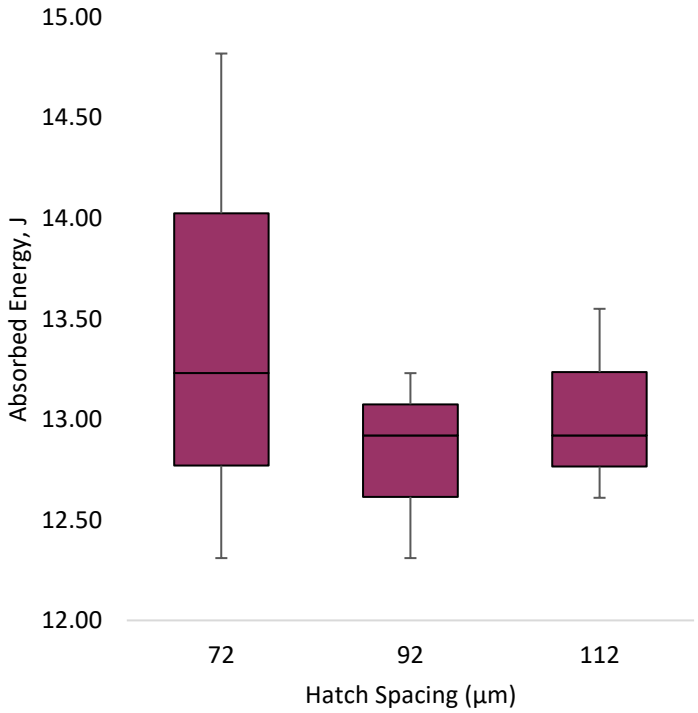

Figure 5-9 - Explanatory Results, 2nd Set.

1. From Figure 5-8, the first sample set with hatch spacing of 72 µm still performs better than the 92 µm and 112 µm samples.
2. There is, however, not much quantitative difference between the mean of the 72µm, 92µm and 112µm hatch spacing sample sets.
3. The box and whisker plot of Figure 5-9 provides a better understanding of the results. The variability and spread of the 72µm hatch spacing sample set are much more significant than those of the other two samples, covering the variability and spread of the other two sample sets. Thus, the slight differences observed in the mean values can be considered insignificant.

5.4 Main Experiment - Final Set

Following the first two experiments, a final set of hatch spacing values was developed to manufacture samples for the main experiment. This time, six hatch spacing levels were chosen to observe trends. The hatch spacing was varied from 72 µm to 172 µm, where a significant difference in absorbed energies was observed. Additionally, 3 levels of hatch spacing, low (72 µm), intermediate (142 µm), and large (172 µm), were selected for LSP post-processing. The LSP processing parameters are summarised in Table 5-8 below:

Table 5-8 - Summary of LSP processing parameters

Parameter (Unit)	Value
Power Intensity (GW/cm²)	15
Spot Size (mm)	1
% Overlap	60

The power intensity used was relatively high, with a moderate overlapping rate. The spot size was adjusted by moving the CNC platform. Concerns about ablation compromising V-notches led to a test scan on dummy samples with putty-filled grooves, which worked effectively. This putty was applied to the MCVN samples to preserve the V-notches and ensure uniformity. After the peening process, both stress-relieved (SR) and stress-relieved + Laser shock peening (SR+LSP) samples were ready for MCVN testing.

Figure 5-10 - LSP of MCVN samples held in jig.

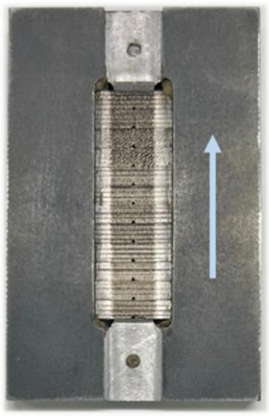

Figure 5-11 - LSPeened samples showing more oxidation with increased hatch spacing.

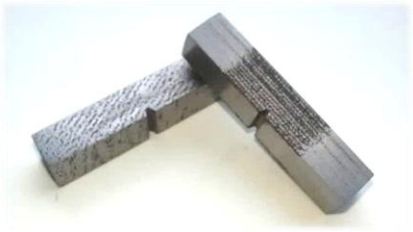

Figure 5-12 - SR and SR+LSP samples ready for testing.

5.4.1 Stress Relieved (SR) Samples

Below is a summary of the final MCVN test results for SR samples with varied hatch parameters indicated in Table 5-2.

Table 5-9 - Results Summary of the 3rd test set.

Sample Description	Absorbed Energy Reading (J)			Mean Absorbed Energy (J)
	1	2	3	
72 µm Hatch	11.10	15.80	12.31	13.07
132 µm Hatch	8.24	6.63	8.80	7.89
142 µm Hatch	7.69	7.43	7.16	7.43
152 µm Hatch	6.89	7.69	6.63	7.07
162 µm Hatch	6.37	6.63	6.11	6.37
172 µm Hatch	4.61	5.10	5.35	5.02

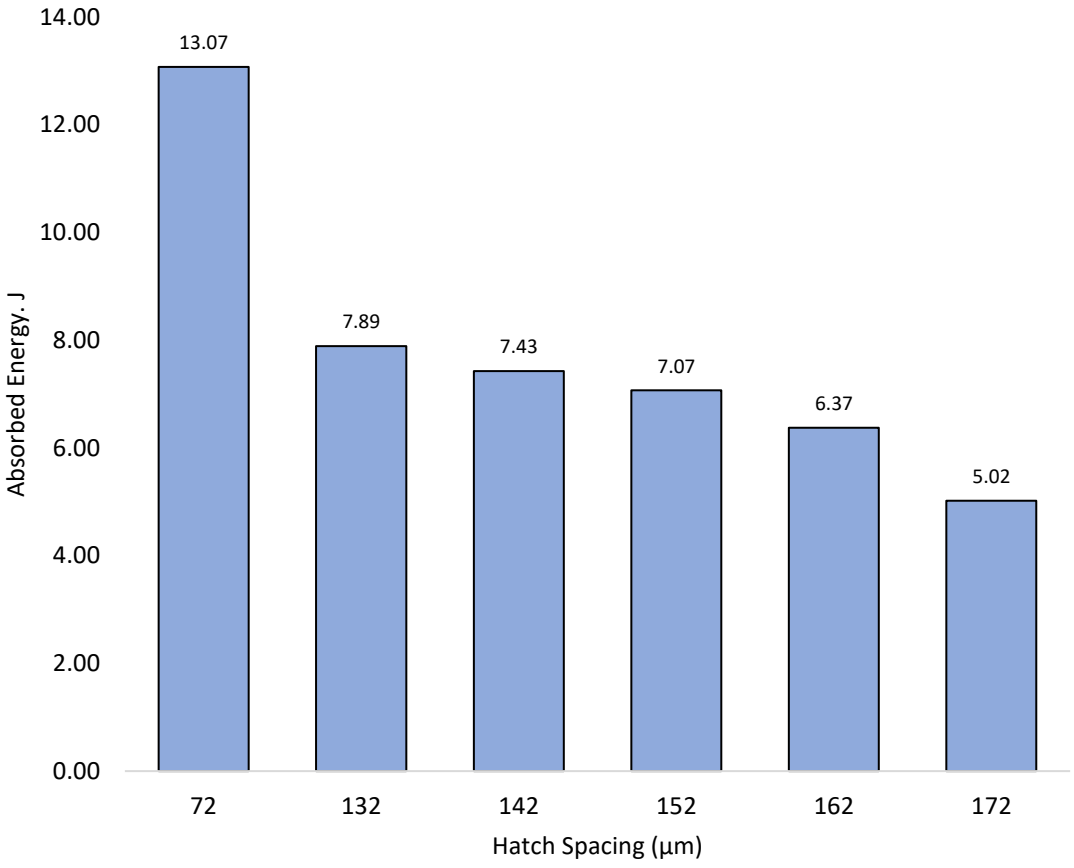

Figure 5-13 - Mean absorbed energy of SR samples, Final Set.

Table 5-10 - Summary statistics of the final SR test set.

Sample Description	Key Descriptive Statistics				
	Minimum	Q1	Q2	Q3	Maximum
72 µm Hatch	11.10	11.71	12.31	14.06	15.80
132 µm Hatch	6.63	7.44	8.24	8.52	8.80
142 µm Hatch	7.16	7.30	7.43	7.56	7.69
152 µm Hatch	6.63	6.76	6.89	7.29	7.69
162 µm Hatch	6.11	6.24	6.37	6.50	6.63
172 µm Hatch	4.61	4.86	5.10	5.23	5.35

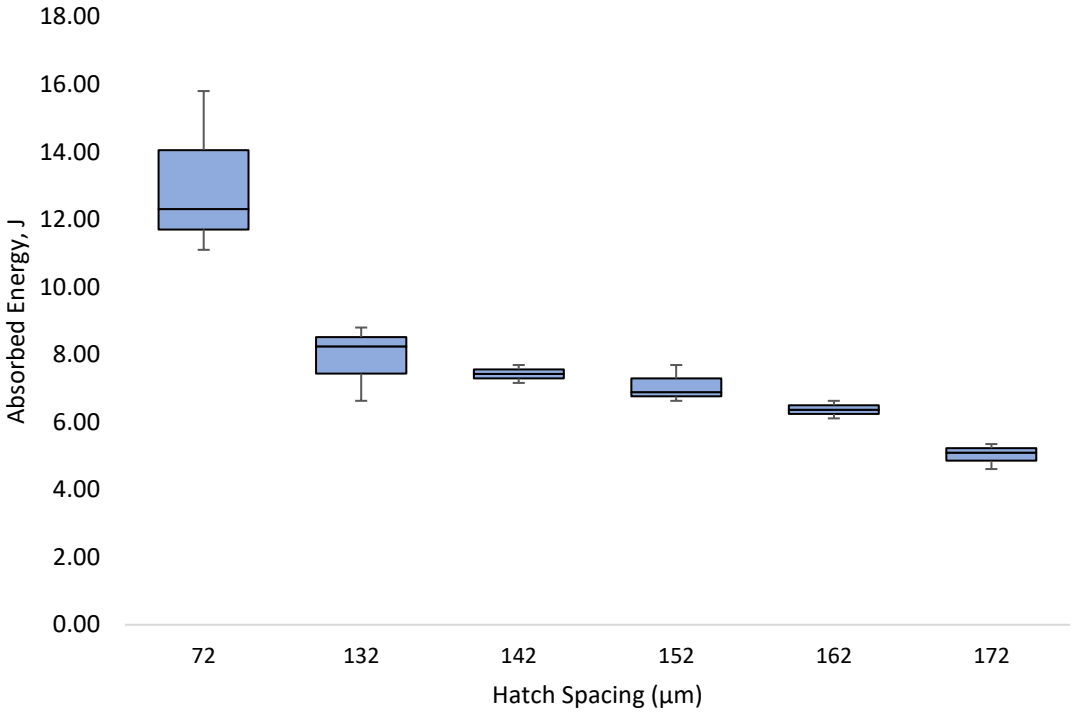

Figure 5-14 - Explanatory Results of SR samples, Final Set.

1. The expected decreasing trend in absorbed energies can be observed in Figure 5-13. The "ideal" parameter sample significantly outperforms the other sample sets.
2. Figure 5-14 also shows the anticipated decreasing trend in absorbed energies.
3. Another recurring observation is the spread of absorbed energy values for the samples with a hatch spacing of 72 µm, which is consistent across all three test sets. As the hatch spacing used in manufacturing the samples increases, the failure of the samples seems to become more straightforward.

5.4.2 Laser Shock Peened Samples

LSP was carried out on the sample sets as demonstrated in Figure 5-10 and Figure 5-11. The test results for LSPeened samples from the MCVN tests are summarised in Table 5-11.

Table 5-11 - Results Summary of the Laser Shock Peened test set.

Sample Description	Absorbed Energy Reading (J)			Mean Absorbed Energy (J)
	1	2	3	
72 µm Hatch	12.31	14.18	13.23	13.24
142 µm Hatch	11.70	10.81	8.80	10.44
172 µm Hatch	6.37	5.86	5.60	5.94

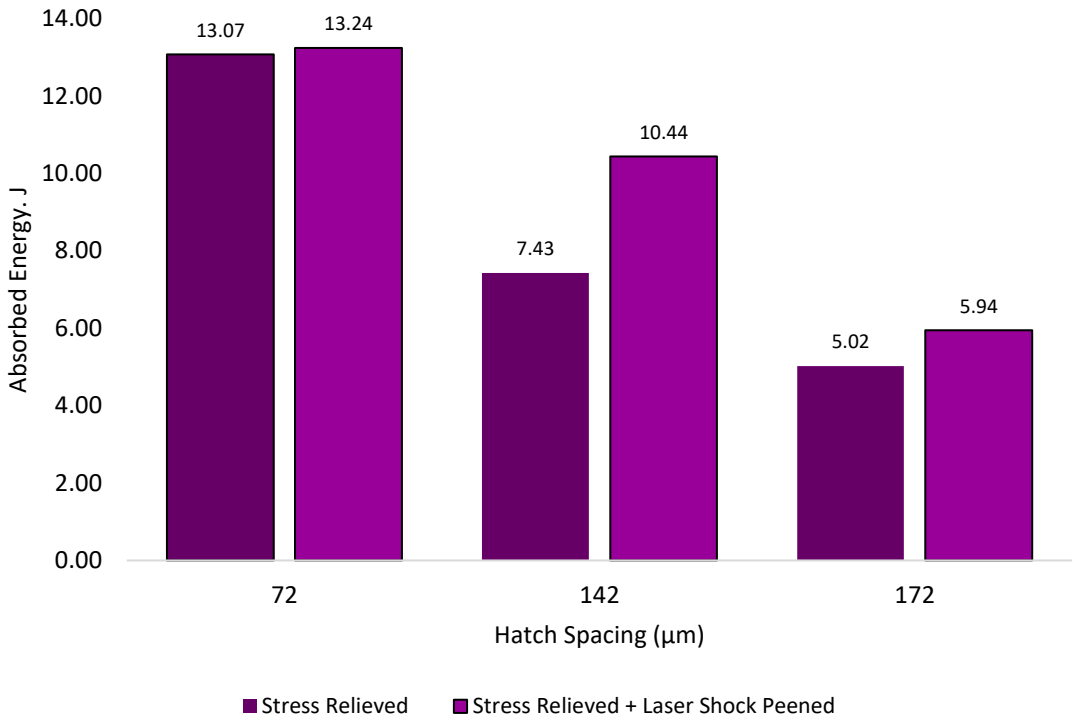

Figure 5-15 - Mean absorbed energy, Comparison - Unpeened and Peened samples.

Table 5-12 - Summary statistics of the final LSP test set.

Sample Description	Key Descriptive Statistics				
	Minimum	Q1	Q2	Q3	Maximum
72 µm Hatch	12.31	12.77	13.23	13.71	14.18
142 µm Hatch	8.80	9.81	10.81	11.26	11.70
172 µm Hatch	5.60	5.73	5.86	6.12	6.37

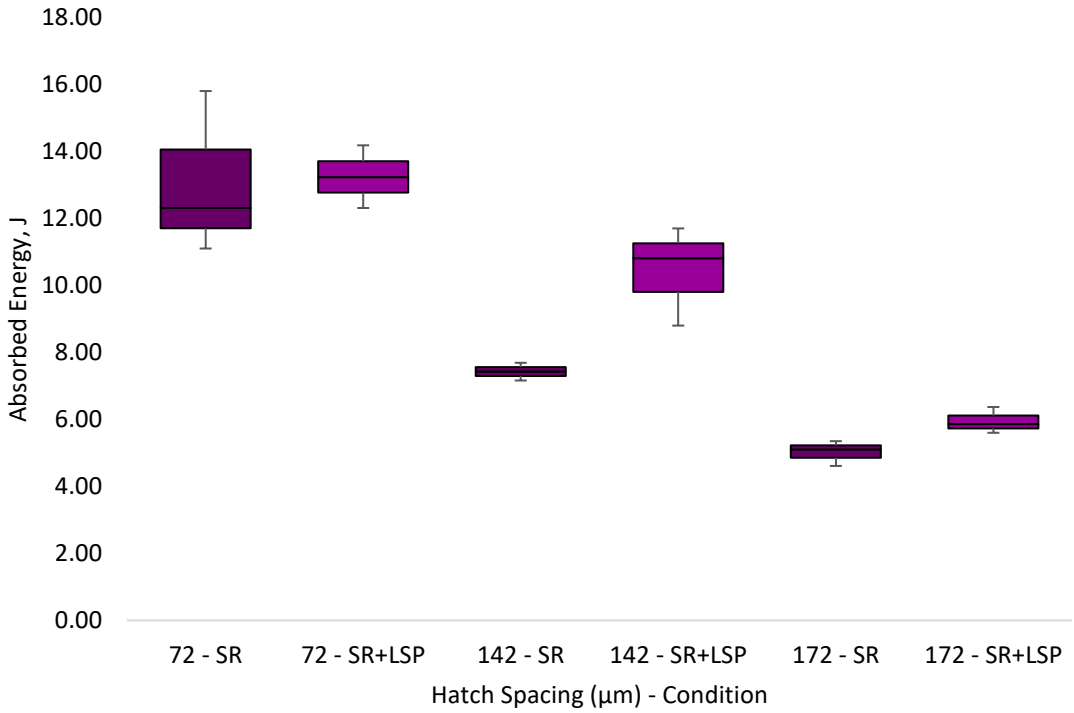

Figure 5-16 - Explanatory Results, Comparison - Unpeened and Peened samples.

1. The sample set across all three levels of hatch spacing demonstrated a slight improvement in the recorded absorbed energies.
2. From Figure 5-15, the most improved sample set is the 142 µm hatch spacing.
3. The box and whisker plots indicate significant differences at 142 µm and 172 µm hatch spacing samples but not at 72 µm hatch spacing samples.
4. The variability in the absorbed energies of samples with a 72 µm hatch spacing decreased after LSP processing, indicating that LSP made the absorbed energy at which failures occur more consistent.

5.4.3 Statistical Evaluation

ANOVA is conducted at a 5% significance level to statistically assess the effects of the variations on MCVN absorbed impact energies in the experimental run, summarised in Table 5-13 below. The following effects are investigated:

1. Variation of hatch spacing,
2. LSP post-processing on parts,
3. The engagement between LSP post-processing and hatch spacing variations.

Table 5-13 - Representation of experimental run for Analysis of Variance

Expt. number	Hatch Spacing, µm	Condition	Absorbed Energy Reading (J)		
			1	2	3
1	72	SR	11.1	15.8	12.31
2	72	SR+LSP	12.31	14.18	13.23
3	142	SR	7.69	7.43	7.16
4	142	SR+LSP	11.7	10.81	8.8
5	172	SR	4.61	5.1	5.35
6	172	SR+LSP	6.37	5.86	5.6

A null hypothesis and an alternate hypothesis are formulated and are as follows:

Hatch Spacing Variation	
$H_0 = \mu_1 = \mu_2 = \mu_3$ $H_1 = \mu_1 \neq \mu_2 \neq \mu_3$	μ_1, μ_2, & μ_3 are the population means of absorbed energy at varied hatch spacing.

Sample Condition	
$H_0 = \mu_1 = \mu_2$ $H_1 \neq \mu_1 \neq \mu_2$	μ_1 & μ_2 are the population means of absorbed energy at varied post-processing conditions.

For both scenarios, the null hypothesis H_0 indicates no significant difference between the means, while the alternative hypothesis H_1 means that at least one of the group means is significantly different.

Table 5-14 - Two Factor Analysis of Variance with Replication

SUMMARY	***72 µm Hatch***	***142 µm Hatch***	***172 µm Hatch***	***Total***
Condition - SR				
Count	3	3	3	9
Sum	39.21	22.28	15.06	76.55
Average	13.07	7.43	5.02	8.51
Variance	5.96	0.07	0.14	14.35
Condition - SR+LSP				
Count	3	3	3	9
Sum	39.21	22.28	15.06	76.55
Average	13.07	7.43	5.02	8.51
Variance	5.96	0.07	0.14	14.35
Total				
Count	6	6	6	
Sum	78.93	53.59	32.89	
Average	13.16	8.93	5.48	
Variance	2.74	3.63	0.37	

ANOVA						
Source of Variation	*SS*	*df*	*MS*	*F*	*P-value*	*F crit*
Condition	8.42	1	8.42	5.37	0.04	4.75
Hatch Spacing	177.24	2	88.62	56.55	0.00	3.89
Interaction	6.49	2	3.25	2.07	0.17	3.89
Error	18.80	12	1.57			
Total	210.96	17				

From the ANOVA Table 5-14, the following deductions can be made:

1. In comparing the sample conditions of SR and SR+LSP, the computed F-value is 5.37, which exceeds the critical F-value of 4.75. This suggests that the change in population mean of absorbed energy is statistically distinct from the group variations observed. Furthermore, the P-value is 0.04, below the threshold of $\alpha = 0.05$. This provides substantial evidence to reject the null hypothesis H_0, indicating that the factor effect of LSP post-processing is significant.
2. Similar to the sample condition and as visually illustrated by Figure 5-13 and Figure 5-14, the comparisons of hatch spacing reveal that $F = 56.55$, comfortably exceeding the value $F_{crit} = 3.89$. Also, the P-value is 0, below the significance level of $\alpha = 0.05$. Consequently, there is very strong statistical evidence to reject the null hypothesis H_0, concluding that the effect of hatch spacing variation on absorbed energies is significant.
3. The interaction between the sample condition and the hatch spacing variation showcased an interesting outcome. The statistical $F = 2.07 < F_{crit} = 3.89$ indicates insignificant interaction between sample condition and hatch spacing variation. The P-value of 0.17, greater than $\alpha = 0.05$, further supports the failure to reject the null hypothesis H_0. The direct comparison made between sample conditions and hatch spacing at different levels in Figure 5-16 demonstrates the positive effects of LSP. However, it is important to clarify that the magnitude of these effects resulting from whichever hatch spacing is independent of the sample condition. This means that both factors contribute **independently** to the samples' absorbed energy changes.
4. The Mean Square Error (MSE) of 1.57 is relatively low, which indicates that the results obtained for sample condition and hatch spacing variation are reliable.

5.5 Principal Characteristics – Findings

The following section delves into the ancillary testing methodologies outlined in Chapter 4, which were employed to further investigate and support the findings from the MCVN tests. This comprehensive analysis examines the different aspects and aims to provide a deeper understanding of the factors influencing the performance of MCVN samples.

5.5.1 Fractography

5.5.1.1 Low Magnification – Visual and Optical Microscopic Examination

The macrography procedure was followed, during which pictures were taken at low magnification. The main challenge encountered in this process was the attainment of optimal lighting. Several trials were conducted, revealing that the best photographs for visual examination were obtained under natural lighting, providing a better representation of surface features. In the case of stereomicroscopy, particularly for the slanted fractures, getting a good focus was also found to be challenging.

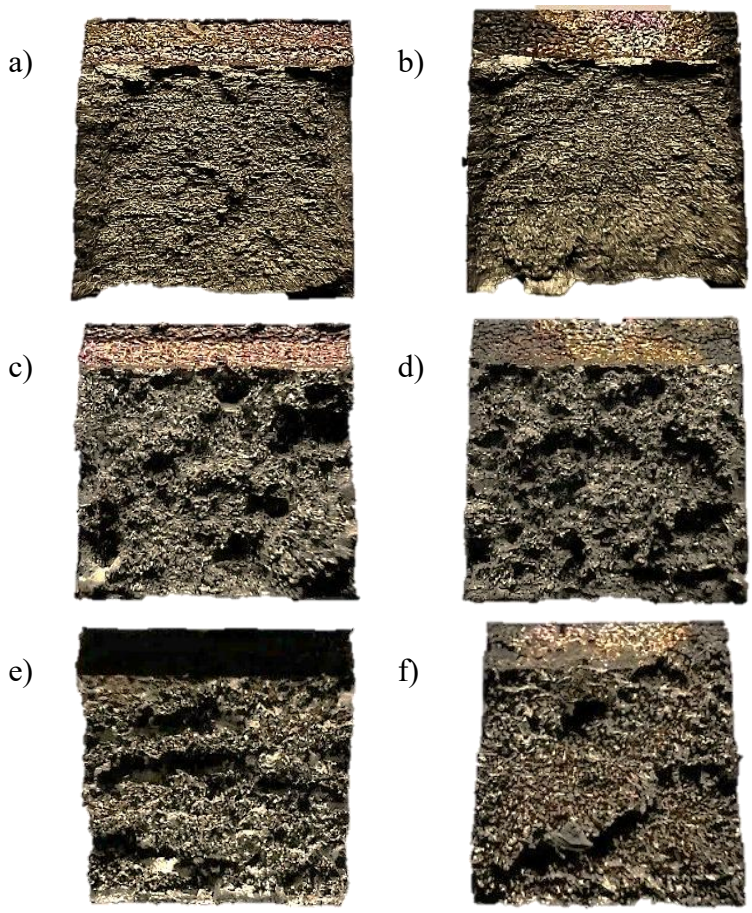

Figure 5-17 - Visual appearance of fractured surfaces, SR & SR+LSP. (a)(b) 72 µm hatch, (c)(d) 142 µm hatch, (e)(f) 172 µm hatch.

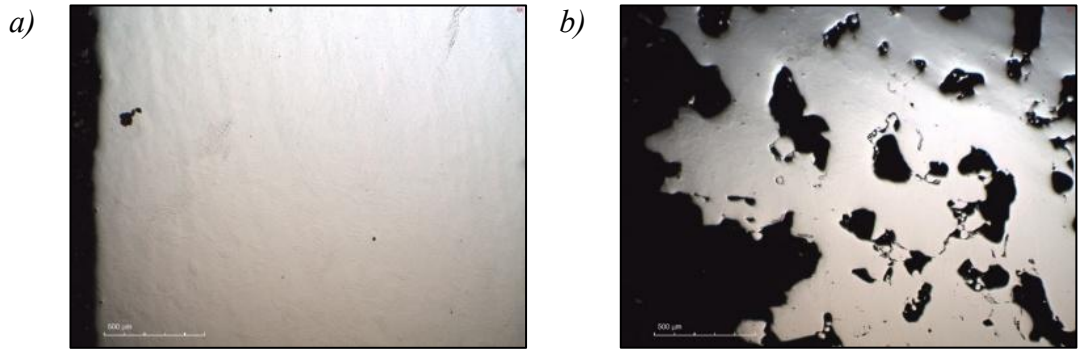

Figure 5-18 - Cross-section of the fractured surface at the unstable crack region. (a) 72 µm Hatch SR sample, (b) 172 µm Hatch SR sample.

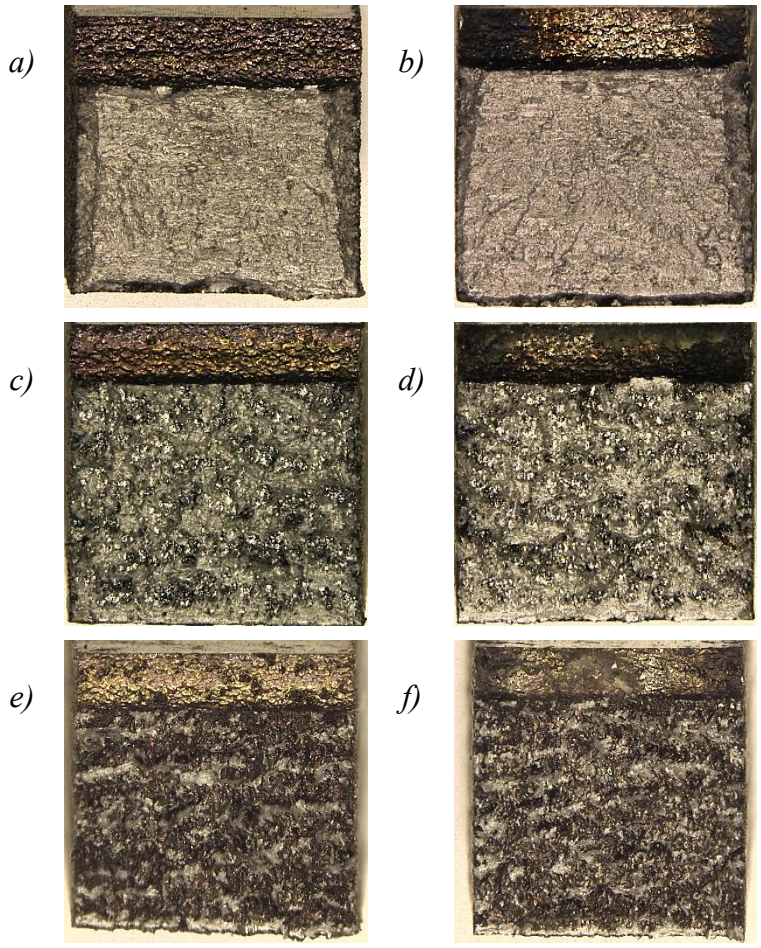

Figure 5-19 - Stereo-microscopic image of fractured surfaces, SR and SR+LSP. (a)(b) 72 µm hatch sample, (c)(d) 142 µm hatch sample, (e)(f) 172 µm hatch sample.

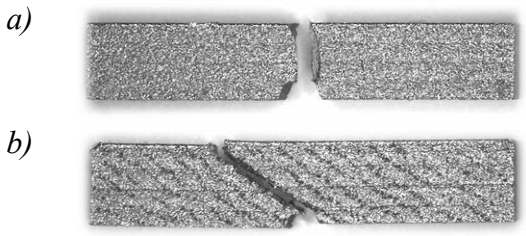

Figure 5-20 - Side sample appearance. (a) 72 µm hatch SR, (b) 132 µm hatch SR.

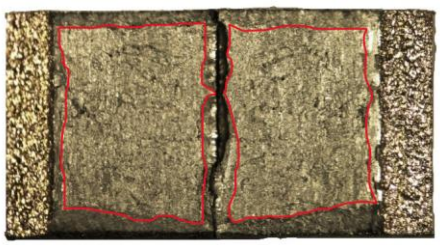

Figure 5-21 – 72 µm hatch spacing SR sample - defined unstable fracture region.

The main observations are:

1. No significant plastic deformations, such as lateral expansion or fracture shear lip, are observed, indicating a brittle fracture.
2. The sample manufactured with low hatch spacing, considered ideal manufacturing parameters, has a noticeably smoother fracture surface appearance than the 142 µm and 172 µm hatch spacing samples, which nearly have a 'woody' fracture appearance.
3. The cross-sectional view in Figure 5-18 indicates that the rough fracture surface is due to significant void defects.
4. The stereomicroscopic image provided additional details not visible in the visual examination, specifically the observable fracture regions highlighted in Figure 5-21 of the 72 µm hatch spacing samples.
5. The side appearance of fractured samples revealed that in samples manufactured using large hatch spacings, if the fracture origin, the notch, was aligned with one of the Lack of Fusion regions in the direction of the scanning strategy, the crack followed that path.

5.5.1.2 High Magnification - Electron Microscopic Examination

Due to the observations made in the previous section, where fracture regions were identified exclusively for the 72 µm hatch spacing sample, this section will focus solely on the unstable crack region (UCR) to ensure consistency. However, SEM fractography was also conducted on the fracture initiation and final fracture regions. In instances where the boundaries of these zones were not visually discernible, regions, approximately defined, were observed. Fractographic images were captured for all samples at magnifications of x100, x600, and x1500. When specific features warranted further analysis, images at a magnification of x3000 were also obtained. Only a selection of these images is presented in this section; for additional imaging, please refer to Appendix 2.

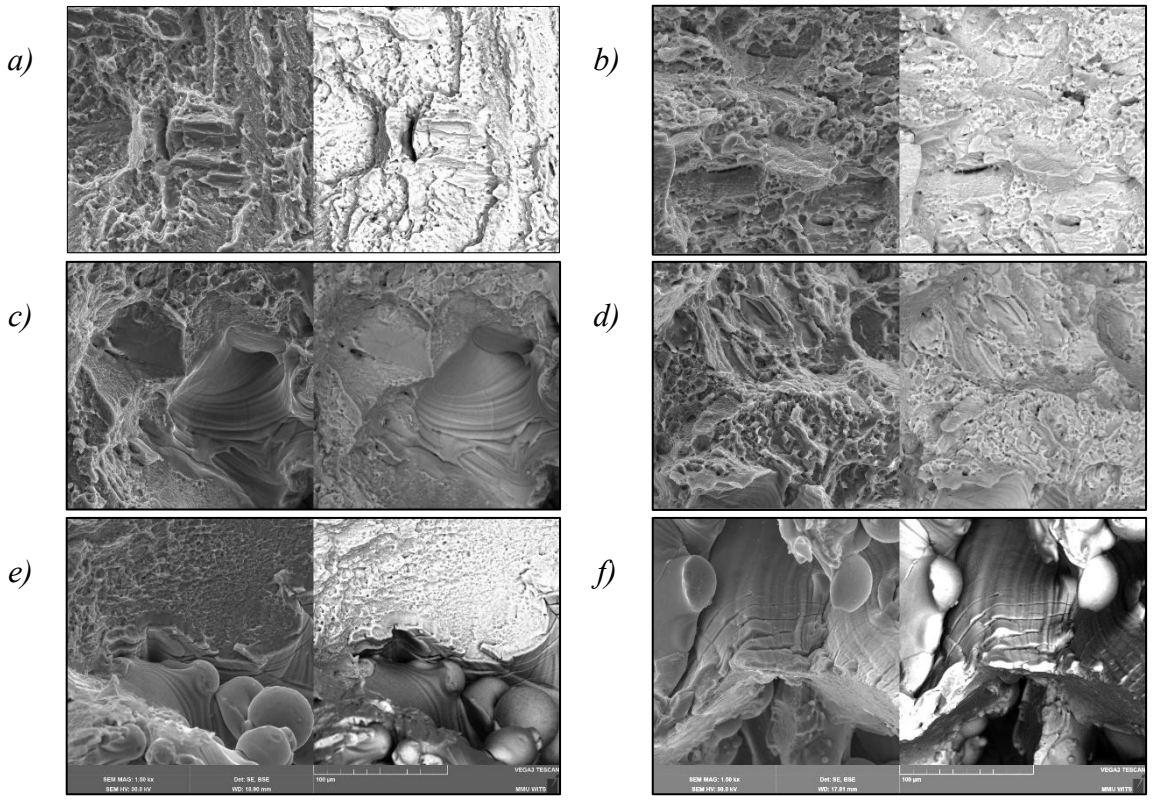

Figure 5-22 - SEM images of the unstable fracture region - ×1500, SR & SR+LSP. (a)(b) 72 µm hatch spacing, (c)(d) 142 µm hatch spacing, (e)(f) 172 µm hatch spacing.

The main findings are as follows:

1. Three main types of fractures can be observed on the fractured surfaces. The first type is general quasi-cleavage fracture, present in all samples. This type of fracture is more evident in the samples with a 72 µm hatch spacing, as they contain fewer voids. The second type consists of sections that exhibit shear rupture, which are found at strategic locations. They are observed to increase in samples produced with larger hatch spacings. The third type is mainly observed in samples built with 172 µm hatch, where random spots appear to have suffered from ductile fracture.
2. Besides the evident presence of LoF voids, the samples also contained tiny circular pores visible as dots on the fractured surface.
3. In the samples with hatch spacings of 142 µm and 172 µm, unmelted powder particles, which serve as inclusions, were visible.
4. In the samples where the larger particles have not melted properly, as shown in Figure 5-22 (c), fractures by what is suspected to be shear occurred, and the shear lips were also visible.
5. The areas resembling ductile fracture surfaces are mainly located at the boundary of the fused scanned vector line, and the unfused LoF regions and may suggest that some parts have mixed-mode fracture surfaces or intergranular fracture paths.
6. Secondary cracks were observed in the samples produced with a hatch spacing of 172 µm. These features can be seen in Figure 5-22 (e) and (f), in regions between two scan tracks. The regions concerned are the properly melted and fused area and a lack of fusion area, where unfused particles are present.

5.5.2 Porosity and Imperfections

A trial process determined parameter selection for micro-CT scans to achieve optimal analysis results. The summarised parameters are displayed in Table 5-15 below. Data analysis is conducted using two software programs: Dragonfly Imaging and Volume Graphics.

Table 5-15 - Micro CT scanning parameters.

Parameter	Description/Value
Tube Voltage (kV)	175
Tube current (µm)	145
Scan Method	Cone beam stop and go.
Number of Projections	3600
Resolution x-axis (mm)	0.01609285
Resolution y-axis (mm)	0.01609285
Resolution z-axis (mm)	0.01609285
Voxel Count	7637476392

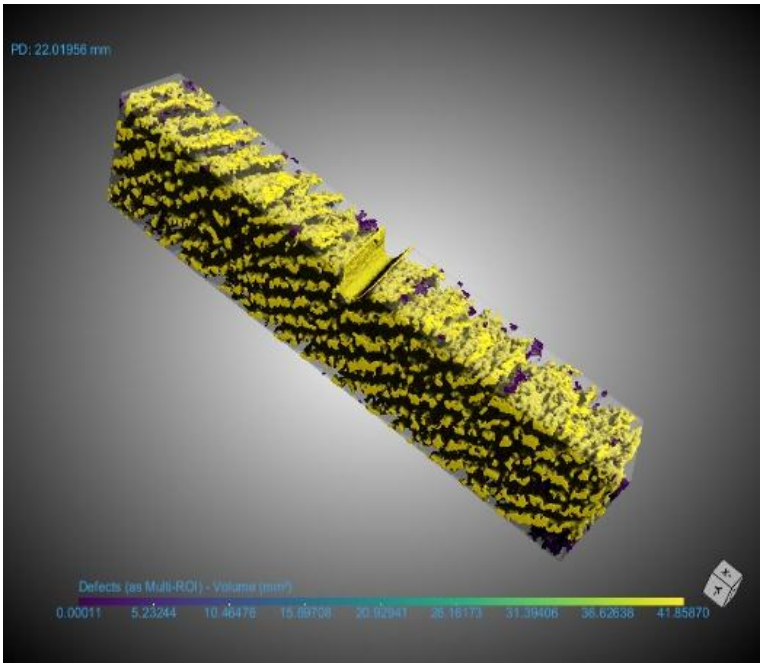

Figure 5-23 -Micro CT image showing voids in the 172µm hatch SR sample.

The scanned 3D image undergoes processing to determine the sample's percentage porosity. Slices of the sample scan are analysed from three different orientations to identify the material and the voids, ensuring that any overlapping or unclear areas are removed to maintain accuracy. Once the regions are defined, the analysis continues by subtracting the identified regions to determine the volume of the void areas.

The results obtained from the micro-CT scans are summarised in Table 5-16 below.

Table 5-16 - Percentage Porosity Results.

Sample Description	Condition	% Porosity
72 µm Hatch	SR	0.22318
	SR+LSP	0.12164
172 µm Hatch	SR	4.14902
	SR+LSP	3.94636
202 µm Hatch	SR	24.52962
	SR+LSP	17.20649

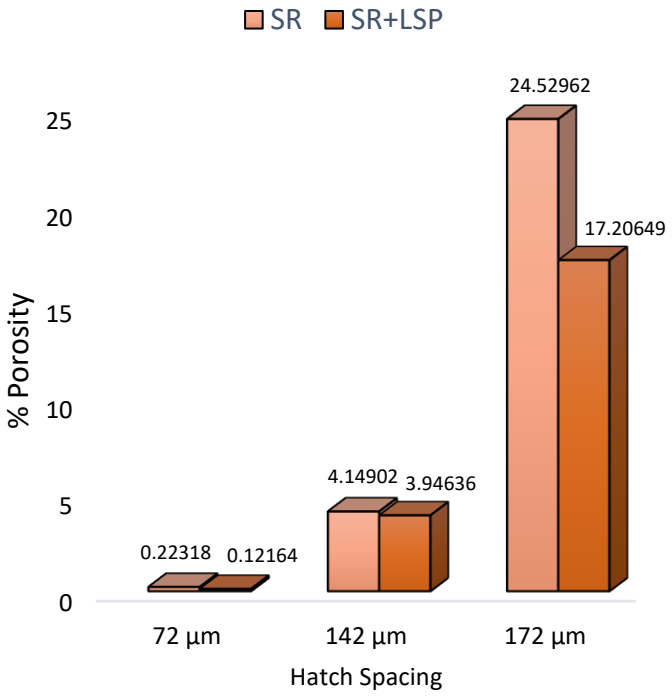

Figure 5-24 - Percentage Porosity Results.

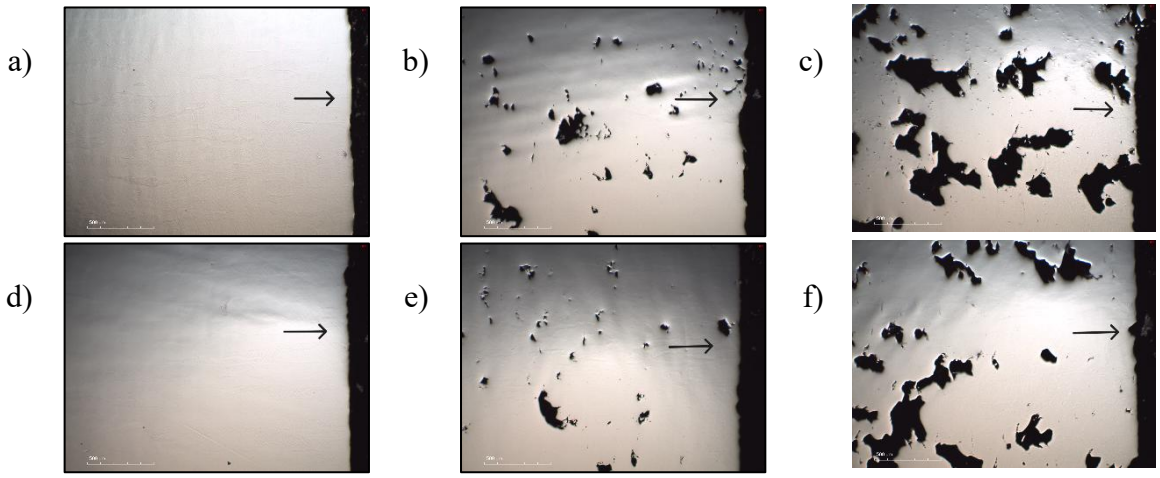

Figure 5-25 - Cross-section of MCVN samples with peened face indicated by arrow. (a)-(c) SR 72 µm, 142 µm & 172 µm, (d)-(f) SR+LSP 72 µm, 142 µm & 172 µm samples.

In-depth analysis was carried out using the scanned micro-CT data, including analysing the distribution and sphericity of the void volumes. However, this process could only be made with the 72 µm and 142µm hatch spacings. The reason is that for the 172 µm hatch spacing sample, the voids were found to be interconnected as shown Figure 5-26.

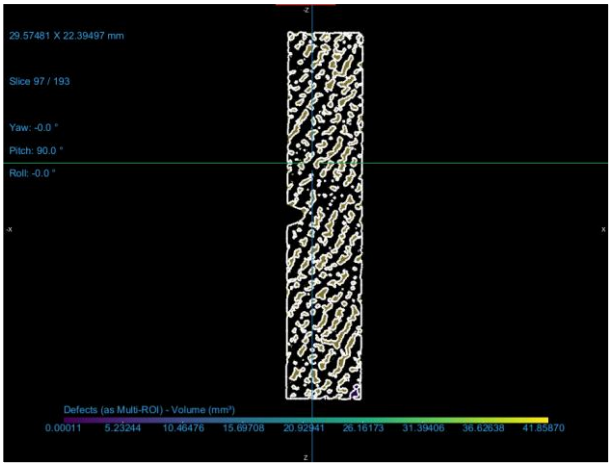

Figure 5-26 - Sliced image of 172 µm SR sample across its profile.

5.5.2.1 Volume Distribution

Void sizes significantly influence the material's structure and mechanical properties. Figure 5-28 below summarises the findings.

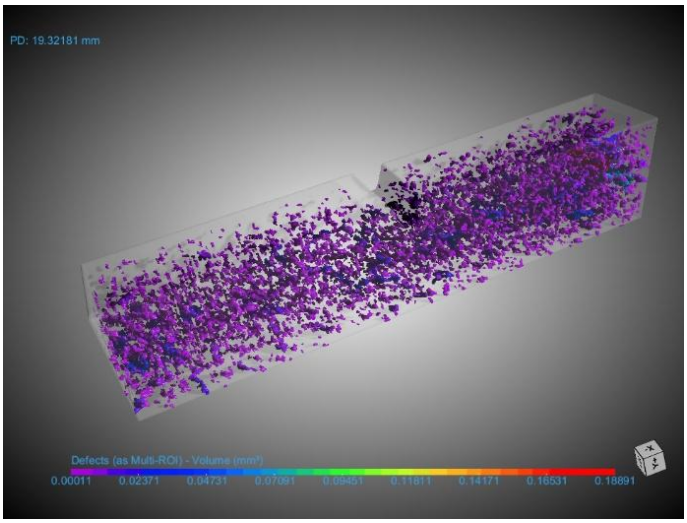

Figure 5-27 - Volume distribution of pores and voids in 142 µm hatch SR sample.

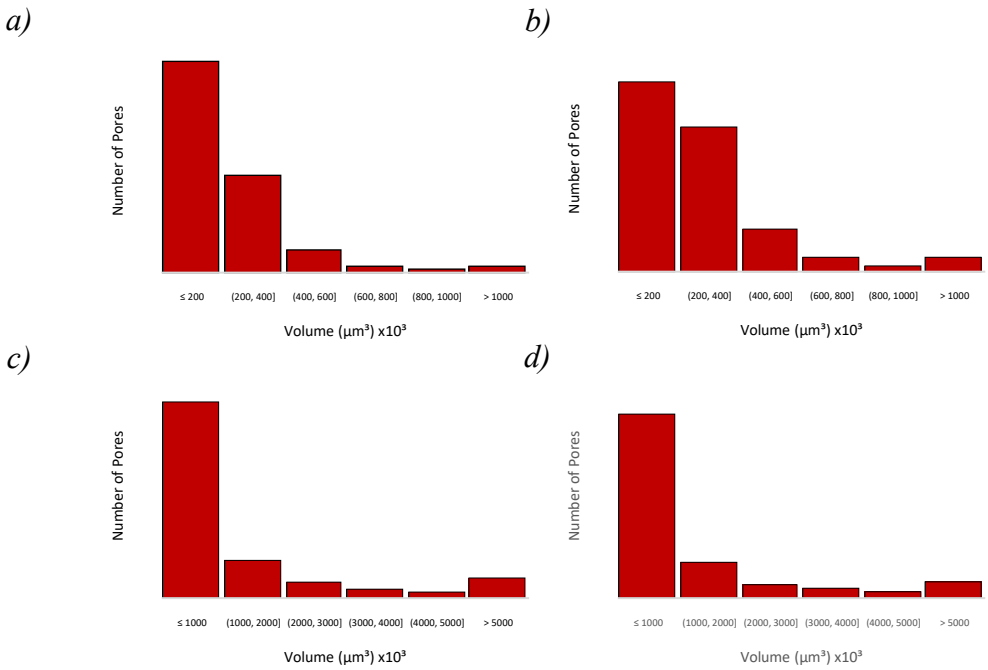

Figure 5-28 - Volume distribution of pores and voids.
(a)(b) 72 µm hatch SR & SR+LSP, (c)(d) 142 µm hatch SR & SR+LSP.

5.5.2.2 Sphericity Distribution

LoF defects are known to be irregularly shaped, which makes them undesirable since their behaviours are unpredictable. Figure 5-30 shows the pore sphericity distribution.

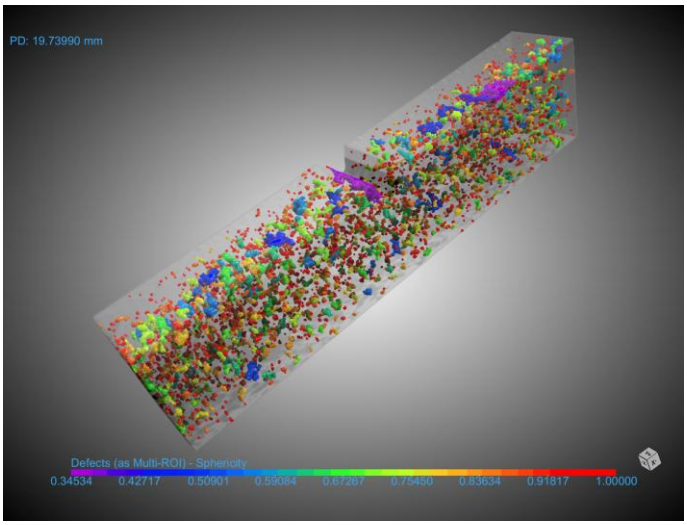

Figure 5-29 - Sphericity of pores and voids in 142 µm hatch SR+LSP sample.

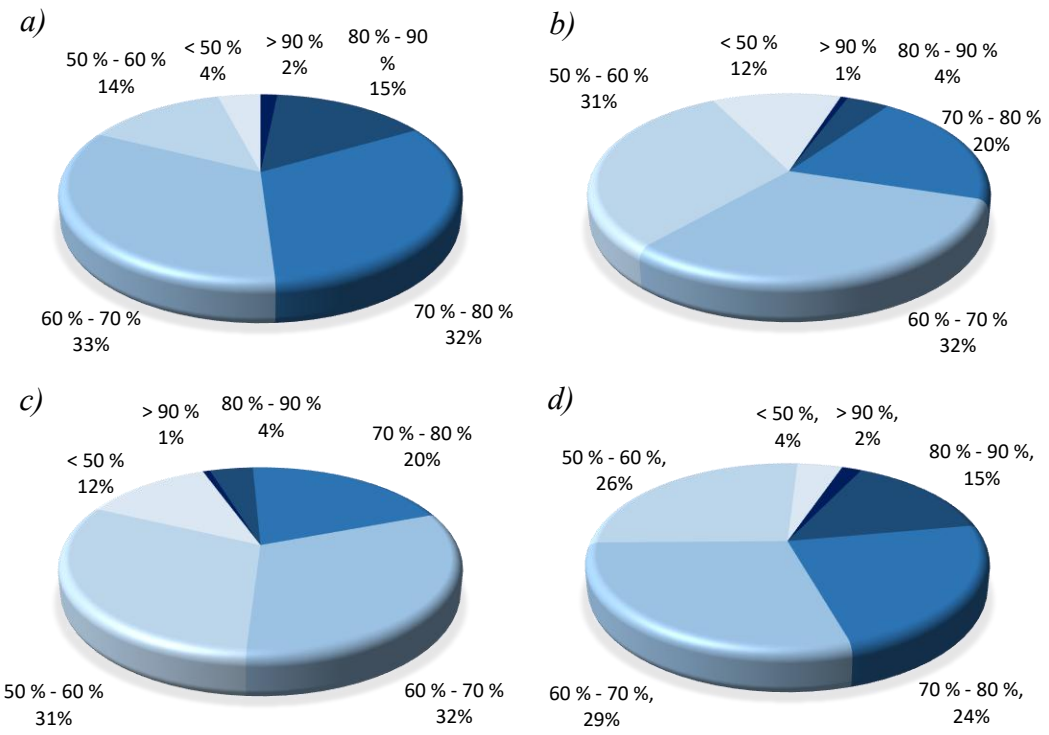

Figure 5-30 - Pores and voids sphericity distribution.
(a)(b) 72 µm hatch SR & SR+LSP, (c)(d) 142 µm hatch SR & SR+LSP.

The key insights gathered are:

1. The increase in lack of fusion (LoF) porosity is evident as shown in Figure 5-24, when the hatch spacings are increased. There is a significant jump from the samples built with a hatch of 142 µm to those built with a hatch of 172 µm.
2. Laser shock peening has improved the conditions regarding surface and subsurface voids created by the increased hatch spacing parameter, effectively closing them. Cross-sectional microscopic observations, as illustrated in Figure 5-25 provide a visual representation of this improvement.
3. The samples printed with the 'ideal' parameter set demonstrated decent results with low porosity levels. The volume distribution indicates that nearly 80% of the pores were smaller than 400 μm^3.
4. The volume distribution data indicates that LoF pores are much larger than tiny, gas-entrapped pores as the volume data revealed for the 142 µm hatch spacing sample.
5. Sphericity data on the pores indicate that a third of the voids were consistent with being 60-70% spherical for all the samples.

5.5.3 Surface Roughness

Data extraction for surface averages was slightly more complicated than anticipated. The extracted data included height differences between the mesh and RoI boundary and peak/valley surface areas. Specific height ranges had to be defined for accuracy, balancing omitting smaller features and overlooking deeper defects. Data was extracted in 5-micron increments from 0 to 35 microns, with additional processing to prevent duplication.

Table 5-17 – Surface Average results.

Sample Description	Condition	S_a (µm)
72 µm Hatch	SR	5.855
	SR+LSP	4.591
172 µm Hatch	SR	13.833
	SR+LSP	6.304
202 µm Hatch	SR	20.642
	SR+LSP	10.435

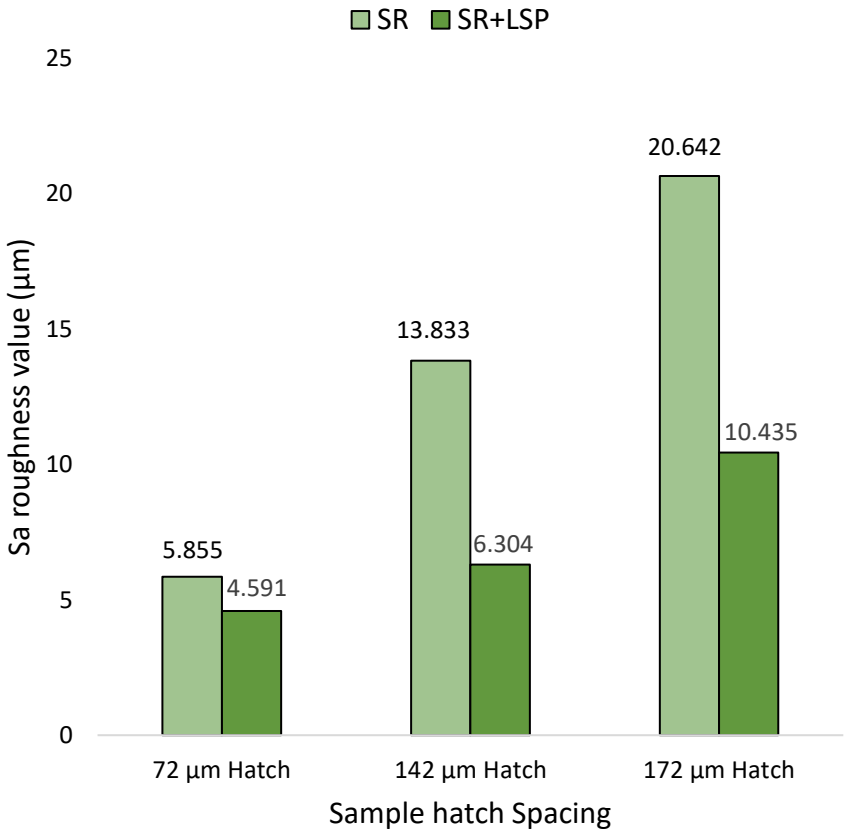

Figure 5-31 - Representation of S_a values.

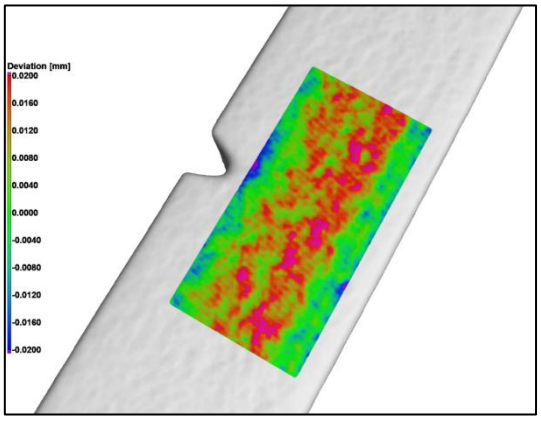

Figure 5-32 - 72 µm hatch spacing SR+LSPeened sample surface map.

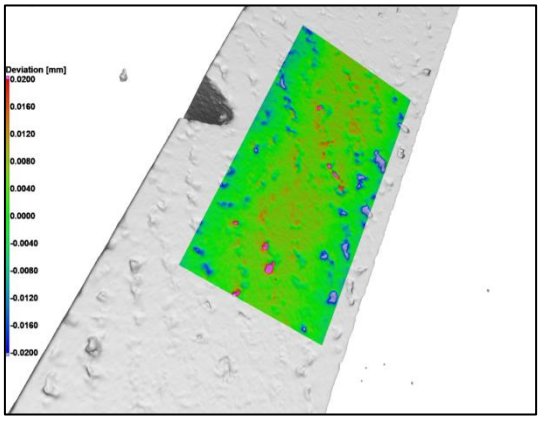

Figure 5-33 - 172 µm hatch spacing SR+LSPeened sample surface map.

Note:

- *Recall that samples have been machined and lightly ground using silicon carbide paper grit 320.*

The observations are presented below:

1. Although the polishing process was applied, increasing the hatch spacing led to more significant surface voids, resulting in higher surface average values.
2. The LSP process, previously shown in section 5.5.2 provided a slight improvement, as the surface-confined ablation has closed some surface LoF pores.

5.5.4 Residual Stresses

Residual stresses were measured in two phases. The first phase involved measuring the surface residual stresses as-is, meaning the samples were tested in the same state as they were prepared for MCVN. However, the results were unexpected, prompting a second and final set of tests. In this phase, the samples were mounted in resin and electropolished to a depth of some microns before repeating the XRD tests. This approach yielded more comprehensive data. The information and details of the testing parameters presented in this section pertain to the second set of measurements.

Table 5-18 - XRD test parameters.

Parameter	Description/Value
X-Ray Source	Cu
Aperture Size (mm)	3
Voltage (kV)	25
Current (mA)	4
Filters	Ni
Bragg Angle (°)	139.69
Exposure Time (s)	7
Number of Exposures	10
β osc (°)	3

Parameters were chosen to achieve the best and most thorough results, following the recommendations outlined in the National Measurement Good Practice Guide No. 52 by the National Physics Laboratory [124].

The samples for the second testing set were electropolished to a depth of up to a few microns, reaching a maximum of 40 μm. It was challenging to achieve an exact depth for all the samples because the electropolishing process is quite aggressive and typically takes just a matter of seconds. The graphical representation of the major principal stress is denoted by σ_1, while the minor principal stress is represented by σ_2.

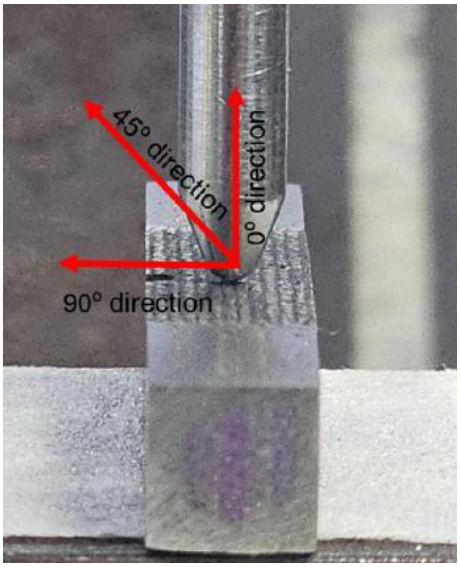

Figure 5-34 - Sample positioning under focus stub indicating measurement axes

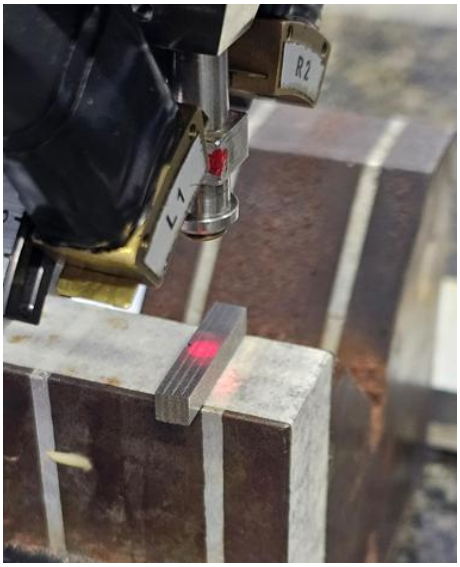

Figure 5-35 - XRD surface measurement on MCVN Sample

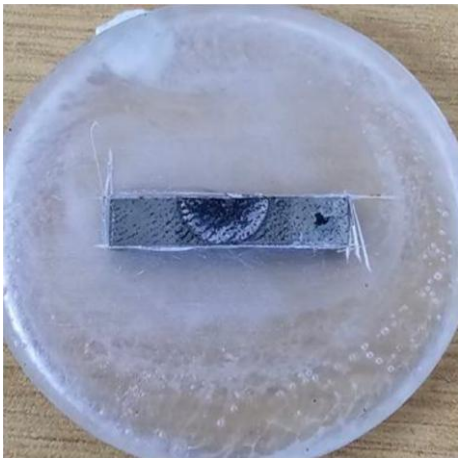

Figure 5-36 - 172 µm SR+LSP sample mounted for electropolishing.

Table 5-19 - Recorded residual stresses for the two test sets.

Sample - Condition	Surface – Phase 1		Sub-Surface – Phase 2	
	σ_1 (MPa)	σ_2 (MPa)	σ_1 (MPa)	σ_2 (MPa)
72 µm Hatch - SR	-106.09	-318.89	107.72	78.34
72 µm Hatch – SR+LSP	124.61	-93.55	-505.52	-585.11
142 µm Hatch - SR	538.13	283.27	93.20	39.14
142 µm Hatch – SR+LSP	-47.49	-205.85	-460.31	-572.03
172 µm Hatch - SR	-175.30	-290.97	36.68	10.82
172 µm Hatch – SR+LSP	66.28	-25.52	-205.91	-345.40

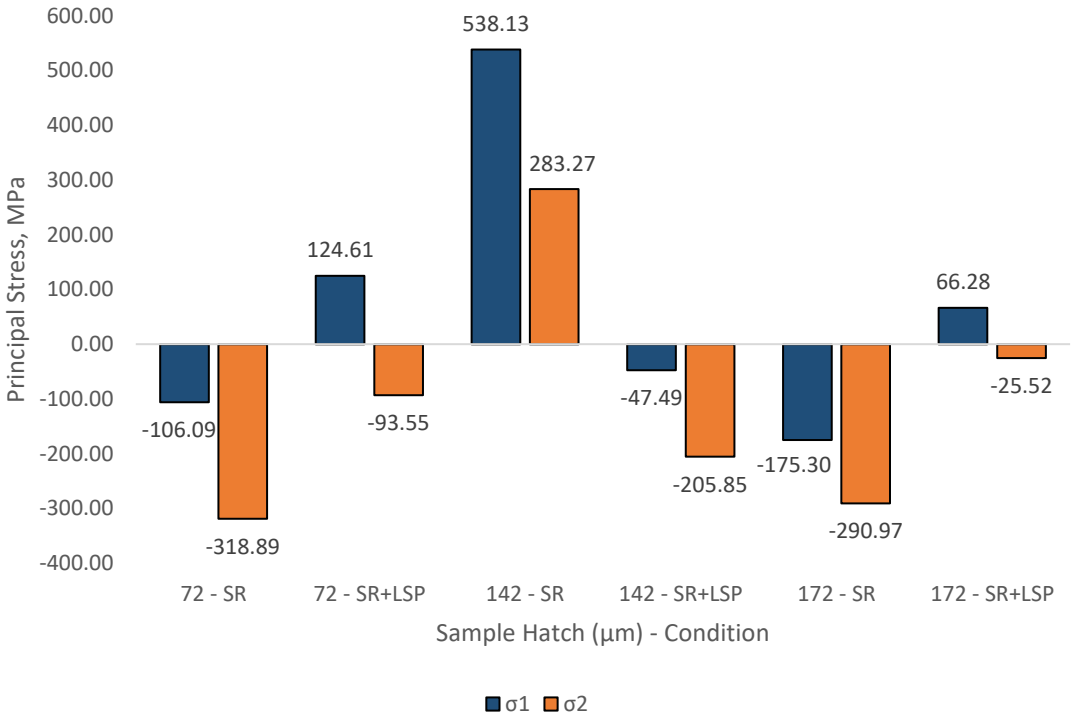

Figure 5-37 - Plot of measured residual stresses at surface level.

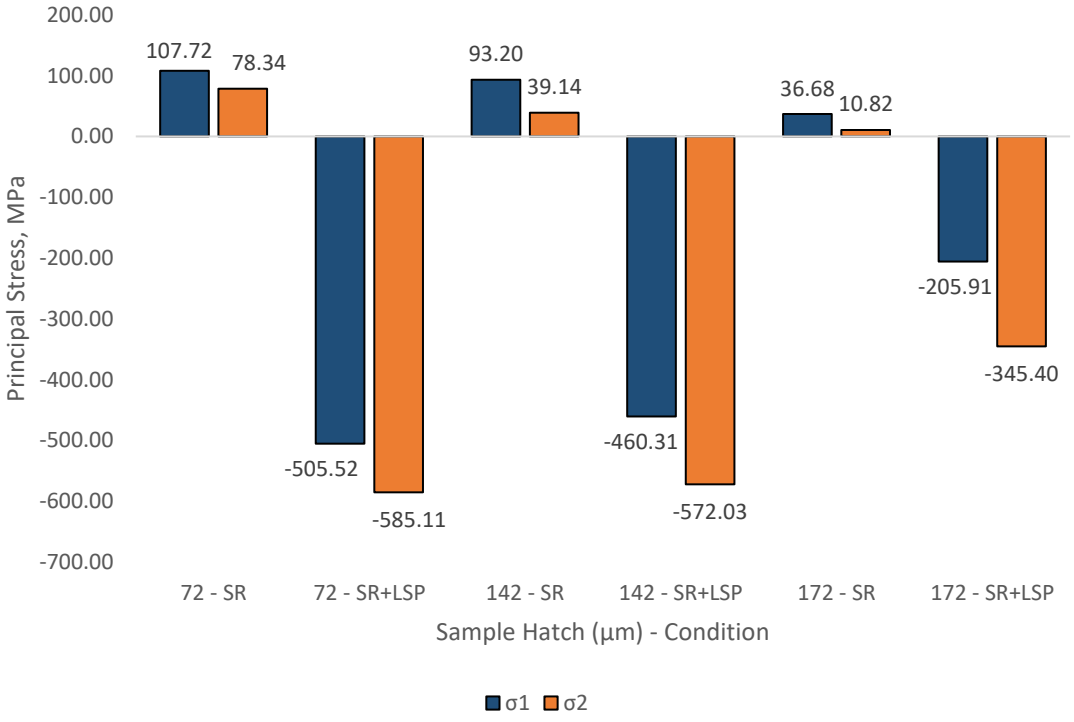

Figure 5-38 - Plot of measured residual stresses at the subsurface level.

However, the principal stresses obtained from the test were in different orientations and are specified in Table 5-20. They were not aligned with the critical direction of concern, which is perpendicular to crack growth. By examining Figure 5-34 and Figure 5-39 it was evident that the components of the main principal stresses, σ_1, needed to be transformed to a 90° orientation, which corresponds to the x-direction of the samples. This transformation would provide a more precise insight since the resolved components of the major principal stresses would now be oriented in the critical direction defined. These values determine the magnitude of the principal stresses in the direction influencing the crack propagation. The stress resolution was performed using the stress transformation Equation 5.1 and Equation 5.2 and the values of the transformed major and minor principal stresses were denoted as σ_x and σ_y, respectively.

However, the readings obtained from testing indicated the direction from the 0° reference, which is represented by α. Therefore, the transformation requires a counterclockwise rotation of the principal stresses by an angle θ, where θ = 90 - α.

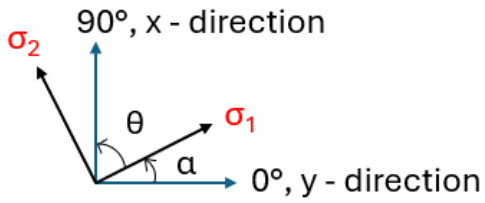

Figure 5-39 - Measured principal stresses direction.

$$\sigma_x = \frac{\sigma_1 + \sigma_2}{2} + \frac{\sigma_1 - \sigma_2}{2}\cos 2\theta + \tau_{12}\sin 2\theta \qquad \text{Equation 5.1}$$

$$\sigma_y = \frac{\sigma_1 + \sigma_2}{2} - \frac{\sigma_1 - \sigma_2}{2}\cos 2\theta - \tau_{12}\sin 2\theta \qquad \text{Equation 5.2}$$

Table 5-20 - Summary of transformed residual stresses.

Sample - Condition	Max Shear (MPa)	Direction (°)	Transformed Principal Stresses, (MPa)	
	T_{12}	α	σ_x	σ_y
72 µm Hatch - SR	14.69	-59.8	87.5	98.5
72 µm Hatch – SR + LSP	39.79	36.1	-519.6	-571.1
142 µm Hatch - SR	27.03	65.0	104.3	28.1
142 µm Hatch – SR + LSP	55.86	-59.1	-539.0	-493.3
172 µm Hatch - SR	12.93	-53.9	15.4	32.1
172 µm Hatch – SR + LSP	69.75	50.0	-194.8	-356.5

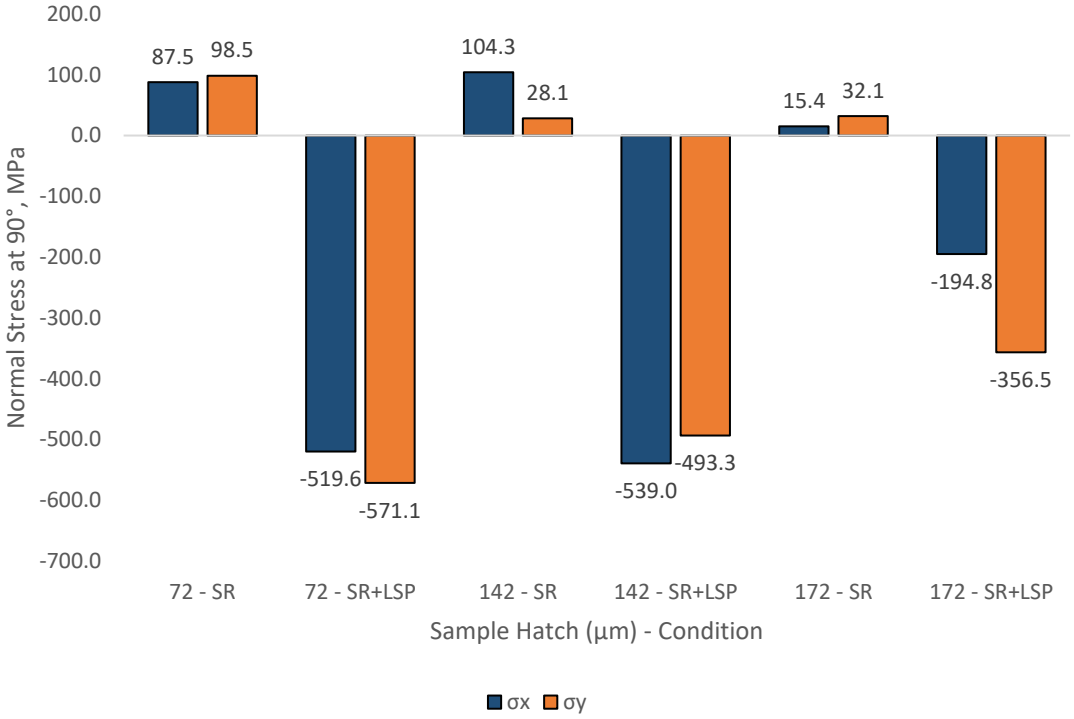

Figure 5-40 - Plot of transformed subsurface residual stresses.

The findings of the XRD residual stress measurement are as follows:

1. The initial results showed considerable variation, with no discernible trend or pattern. This was assumed to be due to surface processing during sample preparation and the visible oxide layer formed on the LSPeened samples.
2. Electropolishing and assessment of the residual stress (RS) in the subsurface region produced anticipated results, showing low tensile residual stress in the stress-relieved samples. This stress was attributed to the cutting, machining and polishing during the sample preparation process and resulted in a shift to compressive residual stress after LSP treatment.
3. LSP's effect on the 172 µm hatch spacing sample is less than on the other two, as the induced compressive residual stresses are higher in those samples.
4. The transformed principal stress values perpendicular to crack propagation reveal that the 142 µm hatch spacing exhibits a higher level of major compressive principal stresses.
5. While determining the transformed stresses, an observation was made regarding the directions of the principal stresses obtained from the testing. The range of these directions varied significantly, from ~ -60° to 65°. Notably, this led to the unusual finding that the magnitudes of the major principal stresses were lower than those of the minor principal stresses in the 72 µm and 172 µm hatch spacing SR and 142 µm hatch spacing SR+LSP samples.

5.5.5 Microstructure and Crystallography

The standard systematic method of grinding, polishing, and etching was used. Grinding was performed using silicon carbide paper with grits of 320, 600, 1000, 1500, and 2000. A force of 25 N was applied at a speed of 200 rpm for 30 to 60 seconds, with frequent checks under a microscope to ensure the desired surface finish was achieved before moving on to the next grit. Polishing was conducted with the same machine settings, using a suspension of 0.05 µm. The etching times for the samples were determined through trial and error, as not all samples were etched at the same rate.

5.5.5.1 Qualitative Findings

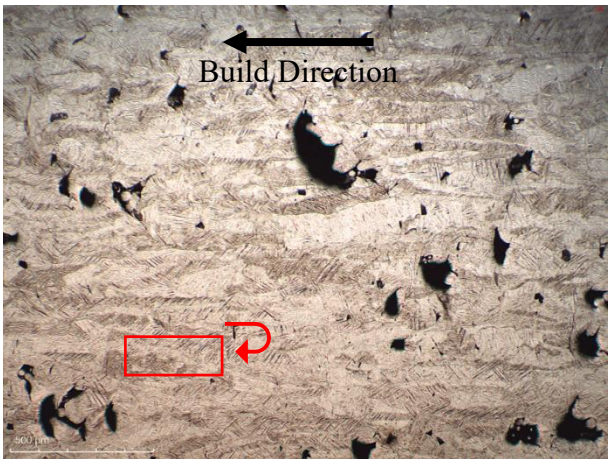

Figure 5-41 - UCR region of 142 µm hatch spacing SR+LSP sample in the YZ plane.

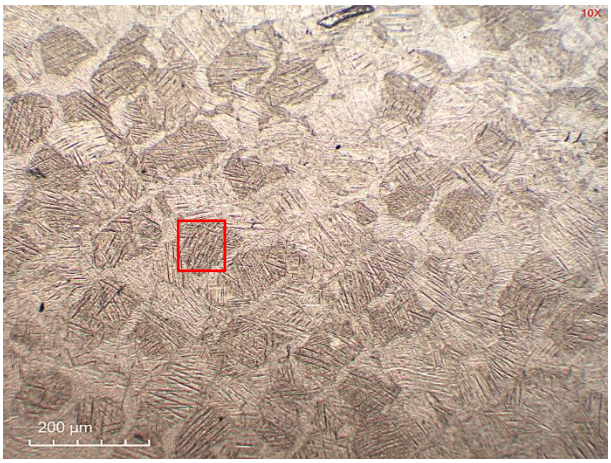

Figure 5-42 - 72 µm hatch spacing SR sample in the XY plane at the UCR region.

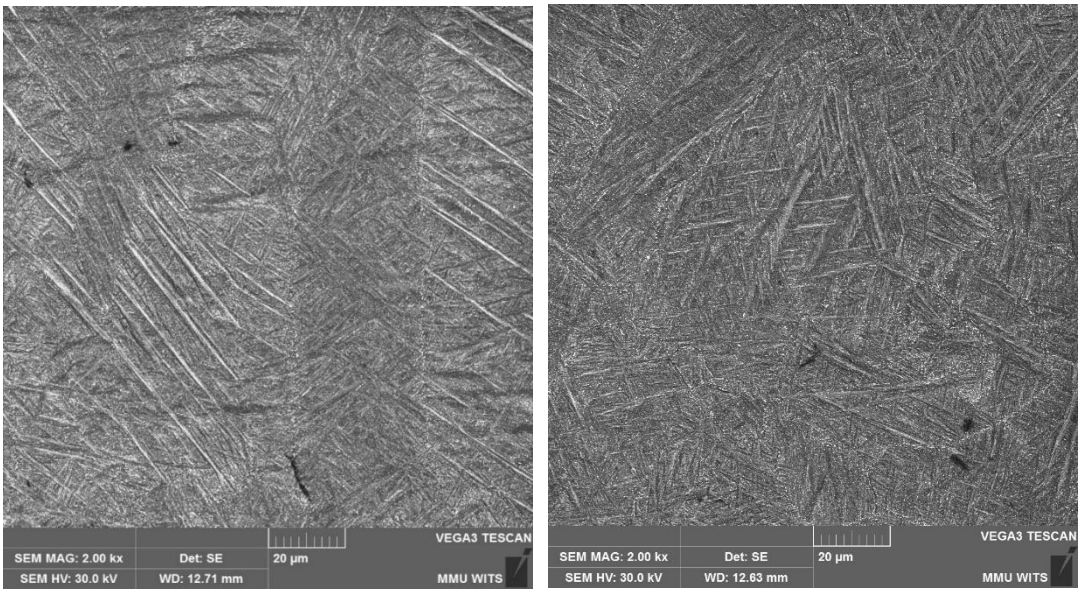

Figure 5-43, 5-44 - Highlighted region of interest in Figure 5-41 & Figure 5-42.

The metallographic observations are as follows:

1. All samples in the YZ plane, regardless of the hatch spacing and post-processing, exhibit acicular martensitic alpha (α′) within columnar β grains aligned with the build direction.
2. In the XY plane, the martensitic alpha α’ in all the samples is observed to be in grains with a chessboard-like appearance.
3. Regions of the α phase were also observed in both orientations.
4. The samples' microstructure, mostly the grain shape, showed no noticeable changes after the laser shock peening treatment.
5. Higher magnification SEM images in both the XY and YZ planes show the presence of primary, secondary, and tertiary α′, categorised by size.
6. The columnar grain in Figure 5-43 shows that the primary α′ crystals have the same crystallographic orientation within their specific β grains.

5.5.5.2 Quantitative Findings

Following the interesting aspects of the microstructural grain structure in the XY plane, it was wondered whether the change in hatch spacing and LSP post processing influences their size. Using the software that operates the camera on the microscope, which can obtain quantitative data on the grains, it was decided to investigate whether any possible trends or patterns existed. The outlines of the grains were roughly traced manually to obtain their areas. The recorded mean grain areas are summarised in Figure 5-46.

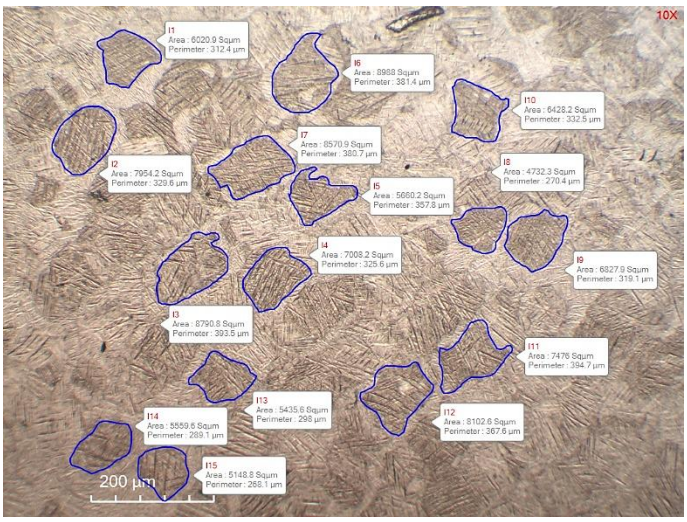

Figure 5-45 - Measurements of the grain dimensions from Figure 5-42.

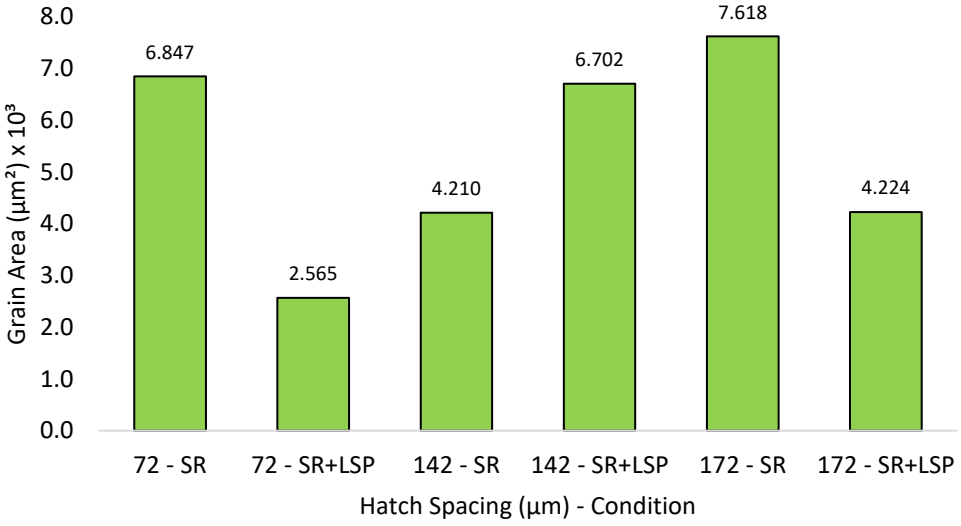

Figure 5-46 - Mean grain size area measured.

5.5.5.3 Energy-Dispersive X-Ray Spectroscopy

The electron microscope used for metallography was equipped with a Bruker XFlash 7 Quantax EDS detector, which enabled spectroscopy to gather information on the material's composition. However, the data analysis was made using a comparative approach to compare the readings of samples.

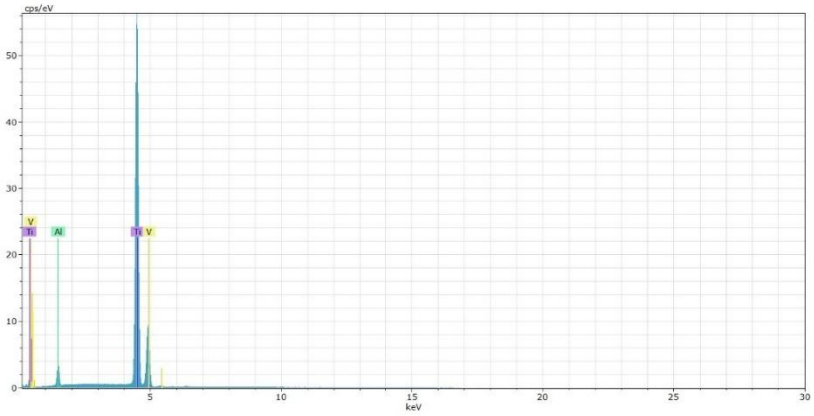

Figure 5-47 - EDS spectrum of 172 µm hatch SR+LSP sample

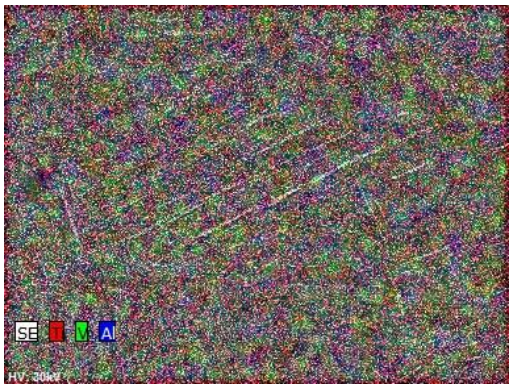

Figure 5-48 - Image map of the EDS spectrum illustrated in Figure 5-47.

Table 5-21 - Summary of spectrum results for all samples.

Sample	Normalised weight %			
	O	Al	Ti	V
72 AB	32.58	2.44	41.40	23.58
72 LSP	32.99	2.55	42.08	22.38
142 AB	33.13	2.40	42.56	21.92
142 LSP	33.32	2.48	42.84	21.35
172 AB	33.44	2.42	43.35	19.87
172 LSP	33.83	2.52	43.81	19.83

The findings of the Quantitative metallography are:

1. No clear trend is observed regarding the effects of variations in hatch spacing on the grain size. While a reduction in grain size can be observed for the 72 µm and the 172 µm hatch spacing samples post-LSP, there is not much substance that can be given to it. This is because the 172 µm hatch samples had so many voids that caused discontinuities in the grains, making the reliability of the results questionable. Instead, significant variability in grain sizes within the same samples has been noted, which does not provide substance for further investigations.
2. The EDS spectra demonstrated the expected components of Ti-6Al-4V. However, high levels of oxygen were recorded. This can be attributed to titanium's high reactivity; instant oxidation occurred when a thin layer of material was removed via etching and exposed to air.

5.5.6 Microhardness

The tests were conducted in accordance with the standard operating procedure manual for the equipment and using the parameters outlined in the table below.

Table 5-22 - Key microindentation test parameters.

Parameter	Value
Applied Force (kgf)	0.3
Dwell time (s)	10

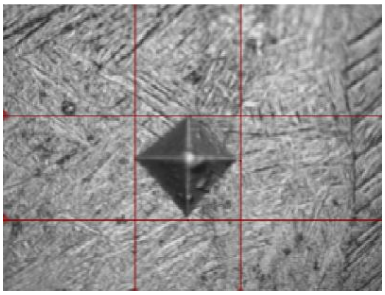

Figure 5-49 - $HV_{0.3}$ reading on the SR+LSP, 72 µm Hatch spacing sample.

Table 5-23 - Summary of the mean $HV_{0.3}$ values at different depths.

DEPTH (mm)	72-SR	72-SR+LSP	142-SR	142-SR+LSP	172-SR	172-SR+LSP
0.2	401.14	411.752	413.034	386.494	401.084	374.314
0.4	395.326	428.556	418.378	375.32	395.036	398.338
0.8	394.522	409.004	412.728	372.884	397.908	393.736
1	384.798	394.228	418.56	375.512	399.82	396.762
1.2	397.38	416.236	402.902	373.614	384.482	389.954

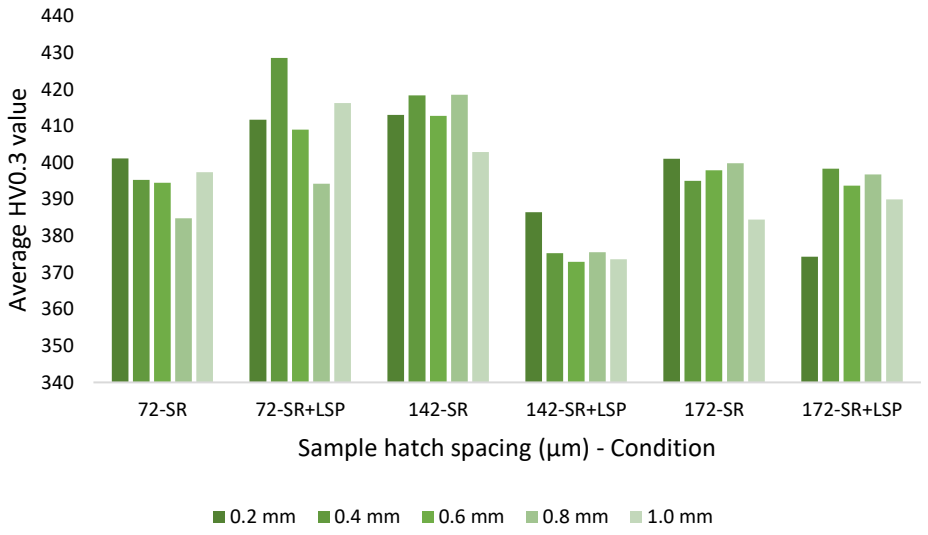

Figure 5-50 - Mean $HV_{0.3}$ values at varying depths from the peened surface.

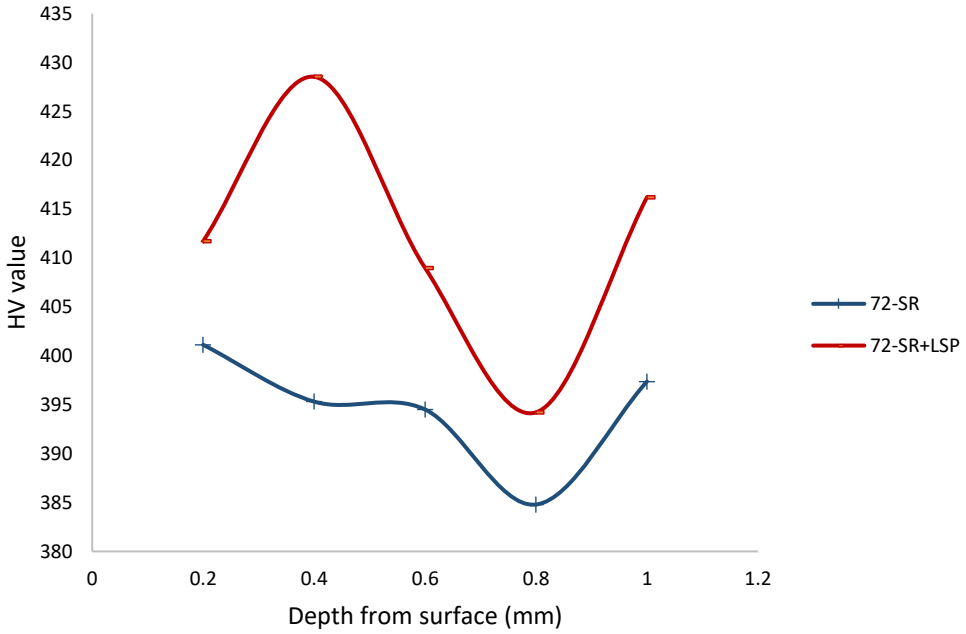

Figure 5-51 - Average $HV_{0.3}$ values of samples generated by the 'ideal' parameter set.

The observations from the test results are as follows:

1. No apparent trend was identified from the mean $HV_{0.3}$ values at several depths in both sample conditions.
2. After LSP, a general increase in microhardness was observed only in the samples with 72 µm hatch spacing.
3. In peened samples, $HV_{0.3}$ values decreased at the subsurface level (0.2 mm) as the hatch spacing increased.
4. The 142 µm and 172 µm hatch spacing results were inconsistent. It is important to note that the guidelines for spacing the indents were followed per ASTM E384. However, caution was necessary due to the presence of voids, which meant that spacing needed to account for both adjacent dents and voids.
5. The average $HV_{0.3}$ values for the 72 µm hatch spacings showed a significant increase at a depth of 0.4 mm from the peened surface.

Chapter 6. Analysis and Discussions

The literature review, specifically section 2.3.2, elaborated on why it is essential to integrate all relevant aspects to develop empirical relationships that can accurately predict part features. While the experimentation and results section enabled us to obtain insightful information on the causes of part features and characteristics, establishing a connection between the causes, features, and characteristics of the part is now crucial for further advancement.

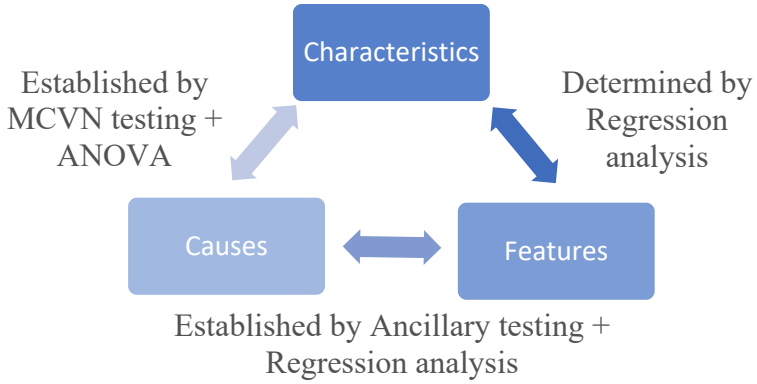

Figure 6-1 - The closed-loop relationship.

This section aimed to identify the influential aspects of the work and their impact on measured quantities. It also determined the statistical significance. Discussions were conducted to link the quantitative data to other qualitative aspects recorded, providing a more insightful description of the situation. Finally, the findings were compared with previous research work to determine correlations and assess whether their conclusions were aligned with the findings.

Note:

- *This chapter focuses only on analysing and discussing the results of the main experiment.*

6.1 Regression Analysis

Attempting to construct a model relationship can be an intriguing method for relating the MCVN absorbed energies to the features of the parts identified for outcome prediction. Linear regression analysis is an exceptionally prevalent choice due to its simplicity and favourable results in predicting outcomes and determining significance [102].

A linear regression model with response variable y and independent variables x can be modelled as follows:

$$y = \beta_0 + \beta_i x_i + \beta_j x_j + \varepsilon \qquad \text{Equation 6.1}$$

Where:

- β_0 *is the intercept,*
- β_i *and* β_j *represent the expected change in the response variable for a one-unit increase in their respective predictors, keeping other predictors constant,*
- ε *is the error term.*

Applying linear regression in engineering design is considered an asset, as many relationships tend to be linear over a limited range. It facilitates quick and straightforward approximations, which design engineers appreciate, as it eliminates the need for extensive and complex data simulations. Regression analysis also indicates the statistical significance of developed relationships and whether they can be considered relevant outside the context of this work.

In this work, linear regressions were conducted in two phases: (1) analysing the part features based on varied parameters and (2) assessing the MCVN absorbed energies with these part features, as shown in Figure 6-1. However, we recall that, from the MCVN tests and the ANOVA analysis in 5.4.3, the varied parameters, in our case, the hatch spacing and post-processing, affected MCVN results independently. Therefore, hatch spacing and post-processing effects were studied separately to achieve accurate correlations.

The two phases' simple regression analysis was carried out in Excel, and the results, with their ANOVA table, are found in Appendix Eight – Regression Analysis. Table 6-1 below summarises the two values of concern: the coefficient of determination (R^2) and the regression models' significance F (p-value) at a 95% confidence interval.

Table 6-1 - Summary of key statistical values from regression analysis.

Sample Condition: SR					
Feature as a function of Hatch			**MCVN as a function of Feature**		
Feature	**R^2**	**P-value**	**Feature**	**R^2**	**P-value**
Porosity	0.572440	0.453721	Porosity	0.680537	0.382410
S_a	0.915749	0.187483	Sa	0.967067	0.116173
RS	0.254756	0.663182	RS	0.357684	0.591872
HV0.3	0.108737	0.786069	HV	0.049354	0.857380
GS	0.014990	0.921860	GS	0.000115	0.993170
Sample Condition: SR+LSP					
Feature as a function of Hatch			**MCVN as a function of Feature**		
Feature	**R^2**	**P-value**	**Feature**	**R^2**	**P-value**
Porosity	0.739516	0.340988	Porosity	0.969436	0.111872
S_a	0.801755	0.293768	Sa	0.989722	0.064652
RS	0.484489	0.509876	RS	0.817790	0.280761
HV0.3	0.999219	0.017792	HV	0.893800	0.211323
GS	0.353567	0.594609	GS	0.074730	0.823725

When the experimental results were divided into two groups (one with SR samples only and the other with SR+LSP samples) and analysed separately, the number of observations in each analysis was reduced by half. This is not ideal when establishing empirical relationships, especially when the sample size is relatively low.

In Table 6-1, the values of R^2 that show at least 80% of the dependent variable can be explained by the independent variable are highlighted in green. Also, the only p-value observed to be less than 0.05, indicating statistical significance, is highlighted in yellow.

The first significant observation from this work is that nearly all the established relationships are statistically insignificant, with one notable exception. However, even that single exception appears inconsistent and may reflect random fluctuations in the data. The small sample size used in the analysis is a primary contributing factor to this issue. As a result, the observed trends, even those indicating strong correlations, should be regarded as preliminary indicators, paving the way for further investigation.

Given that this study is a foundational exploration into the qualification of L-PBF additive manufacturing (AM) samples, such statistical outcomes are entirely acceptable. While this may not be ideal from a theoretical standpoint, having a high p-value is not uncommon in practical scenarios and is a natural part of the design process that does not necessarily invalidate findings [125]. With this understanding, discussions can be engaged, particularly regarding trends that exhibited promising R^2 values, to explore how these insights can align with future research efforts.

The regression analysis provided coefficients β_0 and β_1, which can be utilised in this work as predictive metrics. However, it is important to note that these results do not guarantee applicability in all situations or contexts. The following section presents the regression models that exhibit strong correlations. Plots showcasing the coefficients within the range explored by the experiment were analysed. It is important to note that extrapolation beyond this range was avoided since the models have proven to be potentially unrepresentative.

Table 6-2 - Summary of coefficients of regression relationships with high R^2.

Sample Condition - SR	**β_0**	**β_1**
MCVN as a function of Hatch Spacing	18.866	-0.0805
S_a as a function of Hatch Spacing	-4.8097	0.1419
MCVN absorbed energy as a function of S_a	15.8862	-0.5490
Sample Condition – SR+LSP	**β_0**	**β_1**
MCVN as a function of Hatch Spacing	18.514	-0.0672
MCVN absorbed energy as a function of % Porosity	12.7397	-0.4042
S_a as a function of Hatch Spacing	0.3653	0.0524
MCVN absorbed energy as a function of S_a	18.5397	-1.2189
MCVN absorbed energy as a function of RS	2.6815	-0.0172
HV0.3 as a function of Hatch Spacing	438.7146	-0.3720
MCVN absorbed energy as a function of HV0.3	-61.3524	0.1822

6.2 Analytical Discussions

The results obtained from the MCVN tests showed that hatch spacing significantly impacted the recorded absorbed energies for both sample conditions tested. The effect of hatch spacing variation and LSP post-processing, as well as porosity influence on the mechanical behaviour, is illustrated in Figure 6-2 and Figure 6-3.

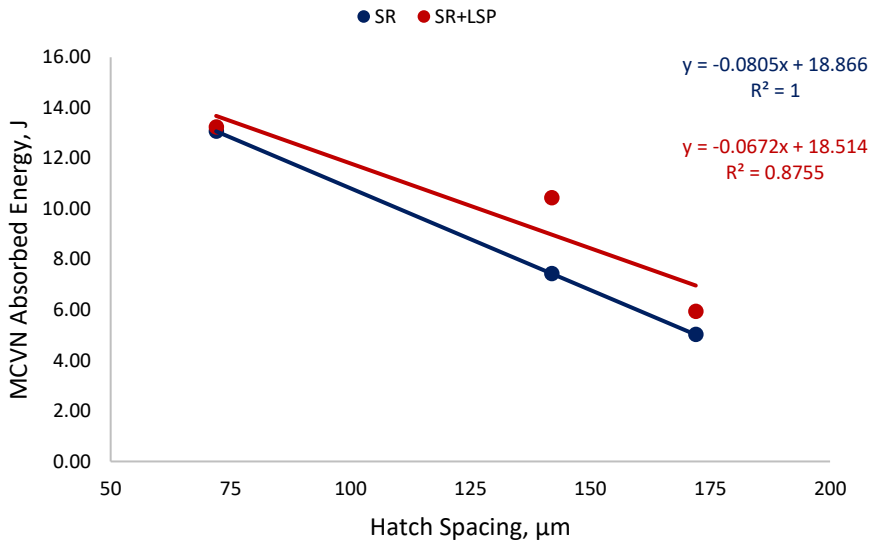

Figure 6-2 - Hatch spacing variation effects on MCVN absorbed energy.

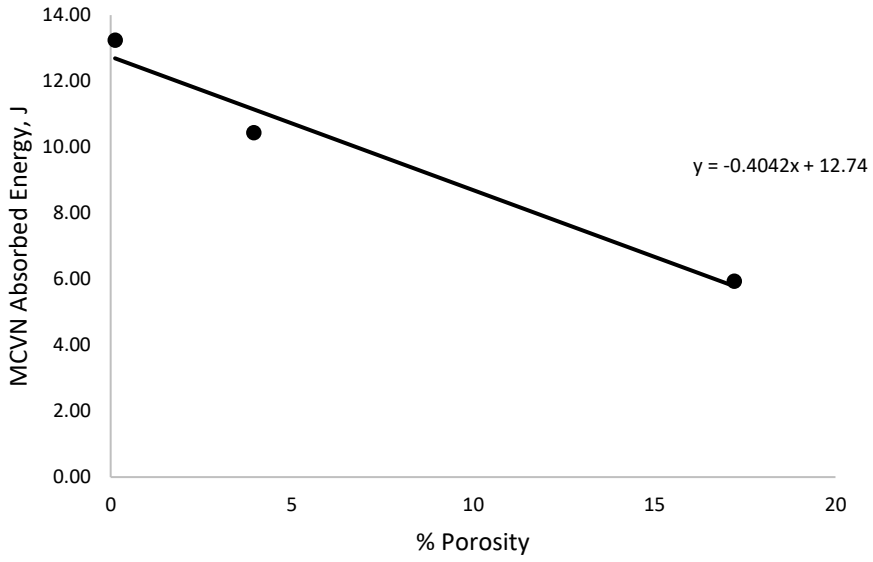

Figure 6-3 - Porosity variation effect on MCVN absorbed energy of SR+LSP samples.

The 72 µm hatch spacing samples recorded absorbed energies comparable to standard NIST reference samples, confirming the magnitudes of absorbed energies obtained are relevant [52]. When analysing the percentage porosity alongside MCVN absorbed energy results, two primary factors are essential: the number of pores within the part and their size distribution. The micro-CT results demonstrated an increase in both factors with higher hatch spacing values. The fractography results confirm these results, with deeper voids observed on the fractured surfaces of samples manufactured using higher hatch spacings (red arrows in Figure 6-4) explaining the inhomogeneity of the samples. However, the fracture type was also seen to evolve with this change. The cleavage planes observed in samples featuring an ideal hatch spacing of 72 µm were relatively large and consistent. This fracture type diminished as the number of voids increased, resulting in findings like those reported by Ji et al. [27], where fractures began stemming from the aggregation of microvoids. Subsequent cross-sectional metallographic images of the fractured surfaces supported this theory. Additionally, a significant number of unmelted particles were found on the fractured surfaces of samples with higher hatch spacings. As noted by Gong et al. [29], despite these unmelted particles contributing to density, their effect on the strength of the test pieces was minimal [30], [31], [32], [37], [38].

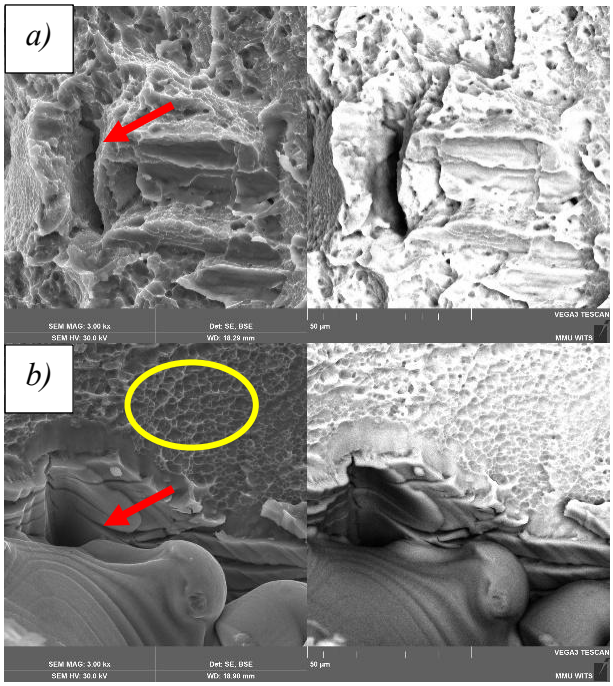

Figure 6-4 - Fractured surface of SR samples at ×3000 magnification. (a) 72 µm, (b) 172 µm.

Interesting observations on the fractured surface of samples also reveal the quasi-cleavage facets, indicating that the general fracture type is transgranular. However, features resembling ductile fractures were increasingly noted as the hatch spacing used in manufacturing increased (circled in yellow in Figure 6-4). Since macrographic examinations did not reveal any signs of ductile fracture, it was more reasonable to classify these dimples as brittle intergranular fractures. The origin of these intergranular fractures, which are weaker than transgranular fractures, occurred because the gaps allowed for the expansion and contraction of material near the lack of fusion (LoF) regions during the heating cycles of the build process, resulting in thermal stresses build-up at the boundaries of those grains and ultimately weakening them [28], [31]. Furthermore, the metallographic structures of AM Ti-6Al-4V, known for their relatively high hardness and reduced ductility, could further explain the observed fracture features and the eventual fracture path [29], [51], [59].

Microstructural evaluations focused on two primary aspects: grain characteristics - such as size, shape, and orientation - and phase structure [31]. The metallographic results for both SR and SR+LSP samples align with findings from other studies. No noticeable difference was spotted in the microstructural characteristics post-LSP. The microstructure observed in both orientations for both sample conditions is characterised by acicular martensitic α′ and β phases. This results from a rapid cooling process that does not allow sufficient time for vanadium (V) to diffuse out of the β phase. Consequently, a diffusionless transformation occurs directly into the α′ phase [32], [46], [47], [53]. However, as noted by Xie et al. [51], different orientations experience varying heating cycles and cooling rates. Fine acicular α′ grains were observed within columnar prior β grains in the YZ direction. This structure resulted from the epitaxial growth due to remelting each scanned layer's previous surface [26], [28], [46], [51], [55], [58]. Conversely, in the XY direction, a chessboard pattern of α′ grains was noted, similar to what has been reported in previous studies [55]. This crystallographic plane is of particular concern in this study, as it is the side where fracture crack propagation occurs.[49], [54]

An interesting observation was made regarding the hierarchical structure of the α′ phase, which consisted of primary, secondary, and tertiary levels. The primary α′ phase was formed through rapid cooling, while subsequent heating and cooling cycles involving less severe cooling rates gave rise to the secondary and tertiary phases. Notably, the primary α′ phase resulted in an aligned configuration, whereas the secondary and tertiary phases exhibit more random orientations. The presence of α phases was also noted, resulting from the decomposition of the α′ phase [46]. The observed chessboard pattern of hard α′ and ductile α grains within β boundaries can also help explain the occurrence of quasi-cleavage brittle fractures. When a crack reached a primary β grain boundary separating the hard and brittle α′ and softer and more ductile α, the direction of propagation changed [49], [56], [59].

Furthermore, the variation in hatch spacing was found to have no impact on the microstructure configuration, and this observation is supported by Gong et al. [29]. However, minor variations were noted, which were consistent with previous studies. When the hatch spacing was set to 72 µm, a good texture with a relatively high number of columnar grains and chessboard patterns (depending on orientation) was observed. However, as the hatch spacing increased, the texture deteriorated because the grains became discontinuous due to LoF pores [13], [27]. Moreover, no significant change in average grain size was recorded. This is understandable, as grain size is primarily affected by the melt pool geometry, which is mainly influenced by the laser power, scan speed, and layer thickness - parameters that influence the dynamics of a single track. For instance, Mukalay et al. [31], observed changes in grain size when the scanning speed was varied.

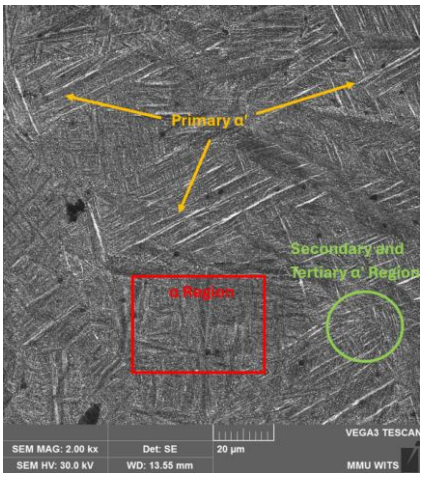

Figure 6-5 - SEM image of the 172 SR+LSP sample in the XY plane.

The Lack of fusion pores on the surface, which results from high hatch spacing, significantly contributed to the observed poor average surface roughness (S_a) values. A study by Ji et al. [27] indicated that when hatch spacings exceed the width of individual tracks, surface roughness tends to increase rapidly. The trend lines in Figure 6-6 show that the surface defects increase due to greater hatch spacing. However, improvements were achieved through laser shock peening (LSP) and became more pronounced as the S_a value increased. Previous studies have attributed the enhancement in surface quality achieved through LSP to two main factors. Some researchers state that surface ablation causes the melting of a very thin material layer, and upon solidification, some inherent features of L-PBF additive manufacturing are mitigated [83], [84], [126]. Others suggest that the change in morphology results from the uniform distribution of strain induced by shock waves, which causes plastic deformation [127], [128]. Although this study could involve a mix of both factors, the elevated laser power intensities employed during the LSP post-processing suggest that the first aspect is more likely to have occurred.

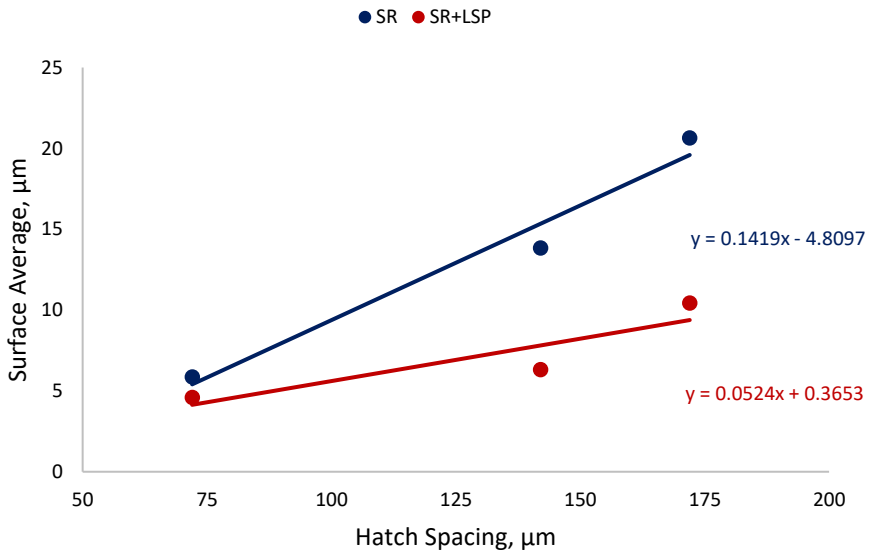

Figure 6-6 - Hatch spacing variation effects on S_a values.

Examination of the effects of Sa values on the MCVN absorbed energy aligns with what many studies have reported: poor surface roughness led to stress concentration points, such as sharp valleys and crack initiation. These points amplify the magnitude of the applied stresses, and performing LSP improves that aspect. Samples showed more impact toughness before fracturing when Sa values decreased [31], [59], [73] [49], [78]. The trend line in Figure 6-7 indicates that the LSP line of best fit is steeper, suggesting that while LSP post-processing is beneficial, there is a threshold beyond which absorbed energy may remain low even at lower Sa values due to other factors, such as porosity, overriding its effects.

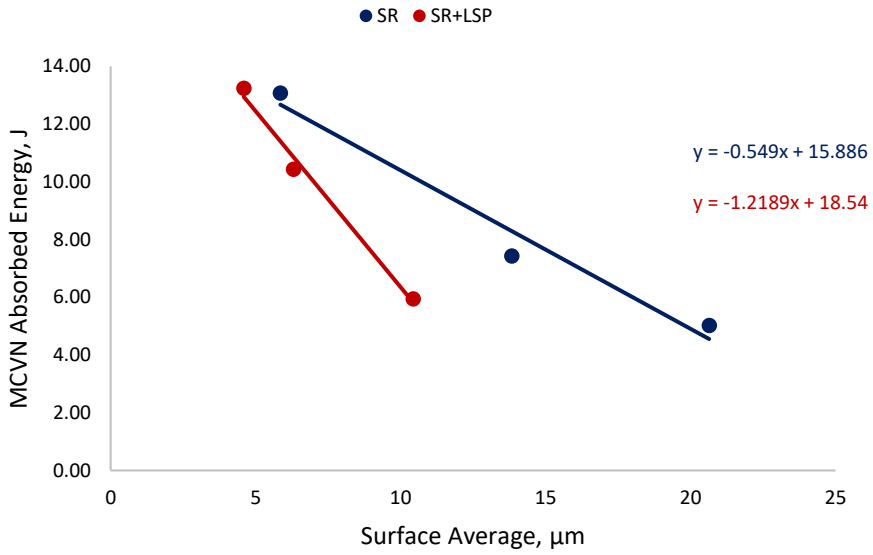

Figure 6-7 - The variation effect of S_a on the MCVN absorbed energy.

It is well-established that the main factors influencing residual stresses revolve around energy density and scanning patterns, which are crucial in defining the cooling rates [31], [38], [41], [42]. The directions of anisotropic residual stresses observed at the subsurface level were very random across all the samples. Depending on geometry and manufacturing orientation, these stresses significantly impact a part's mechanical properties [38], [59]. However, research indicates that these stresses tend to be higher in the direction perpendicular to the scanning process [45]. The transformation of major principal stresses in a specific orientation relative to the crack propagation was deemed necessary. The only major other characteristic that changes and could impact the residual stresses when doing so is the microstructural structure. However, previous studies have shown that it appears to have little effect on residual stresses [40].

An important aspect to consider was addressed by a study by Ji et al. [27], who indicated that increasing hatch spacing can alter residual stresses. Although tensile residual stresses can negatively impact mechanical performance, the stress-relieving process performed meant that they could not be considered in the analysis [43], [46], [53], [59], [61], [78], [87]. The microscopic fractographic analysis of MCVN samples showed an interestingly increasing number of secondary cracks as hatch spacing increased in the samples, as illustrated in Figure 6-8. A major cause could be the stress buildup, which may have been high at the lack of fusion (LoF) regions observed between scan tracks. Due to the part's low structural density, it is plausible that the material experienced significant contraction upon solidification. Previous works have elaborated that in areas next to the LoF regions, higher localised stresses were experienced during MCVN testing [30], [31], [38].

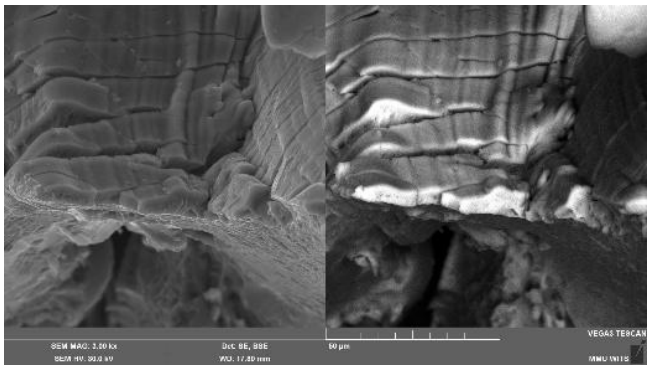

Figure 6-8 - Fractured surface of SR+LSP 172 µm sample at ×3000 magnification.

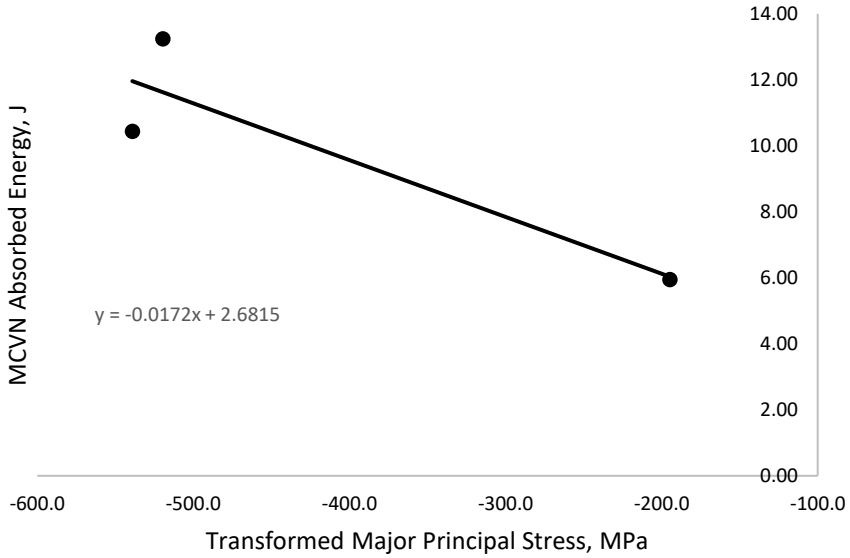

Figure 6-9 - CRS variation effect on the MCVN absorbed energy of SR+LSP samples.

The results suggest that the enhancement of residual stresses observed after LSP significantly improved the components' impact toughness by promoting deep and stable compressive residual stresses [73], [84], [127]. The trend line formulated in Figure 6-9 showcases the results of post-LSP processing, showing induced compressive stresses yielding significant improvement in MCVN absorbed energies. Previous research has shown similar outcomes: components produced using L-PBF often display considerable tensile residual stresses, which are effectively mitigated in the near-surface region following LSP treatment, irrespective of orientation [78], [83], [85], [86], [87], [128]. Additionally, in line with findings concerning Sa values, the sample with a hatch spacing of 142 µm demonstrated the most substantial enhancement in its ability to absorb impact energy. This improvement is due to samples with a hatch spacing of 172 µm falling short in other areas, such as porosity and surface roughness, which hindered them from capitalising on the process's full advantages.

The influences relating to microhardness results obtained were analysed and the significant finding is that the hardness of materials produced through L-PBF AM is comparable to, or even exceeds, that of wrought alloys, largely due to the presence of α′ phase [56], [64], [70]. With the microstructural assessments revealing consistent results across all samples, no major impact on microhardness values was observed, with the exception for the 142 SR+LSP sample. The presence of finer primary and secondary α′ phases - resulted in minimal variation across the sample depths. Findings reported in Figure 6-10, show the structural density of the components, affected by pore defects caused by hatch spacing variations, influencing the recorded hardness values. These results are in line with and confirmed by previous findings [32], [49], [56], [57].

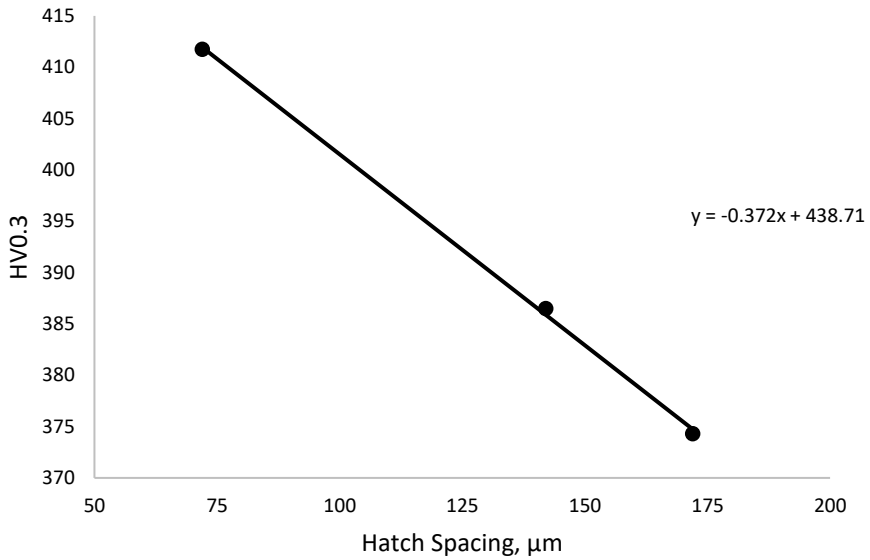

Figure 6-10 - Hatch spacing effects on $HV_{0.3}$ at 0.2 mm depth in SR+LSP samples.

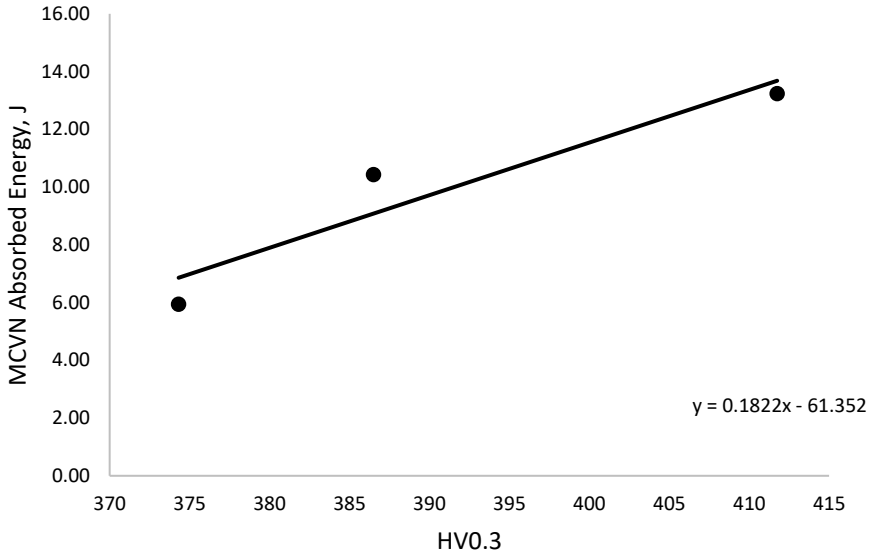

Figure 6-11 - $HV_{0.3}$ effects at 0.2 mm depth on absorbed energy in SR+LSP samples.

Among the few trends discerned, the values of $HV_{0.3}$ of LSP samples at subsurface level were analysed. Figure 6-11 illustrates that $HV_{0.3}$ values at the depth of 0.2 mm showed an increasing pattern, resulting in improved impact toughness. These results align with previous works that indicate maximum hardness is typically found at the surface and tends to decrease with greater depth [81], [82], [83], [87], [126], [128]. These findings are, however, relevant only to LSPeened samples. The observations can be explained similarly to how surface roughness analysis (S_a) was done. One possible reason for the increased hardness is plastic deformation, which enhances the density and hardening of the material in that area [43], [85]. A second factor could involve LSP surface ablation's rapid melting and cooling [81]. Additionally, it is worth considering the attribution of this increase to the surface oxide layer that forms during the LSP process, impacting the $HV_{0.3}$ values [81], [83], [90].

Chapter 7. Conclusions

This section elaborates on the main aspects of the project. It summarises the motivation behind the work undertaken and the type of tasks performed, guided by the objectives set at the beginning to ensure a focused approach. It also outlines the underlying concepts throughout the work, leading to meaningful results. A clear illustration of the results' direction is also summarised, paving the way for future exploration and application.

The issue presented was related to the inconsistencies that were observed in parts produced by L-PBF AM. Furthermore, certain specific features were exhibited by the products, which were key in defining the characteristics of the part that needed to be considered during the design process. When considerations were made regarding the application of L-PBF AM in the aeronautical context, the challenges were pronounced. The rigorous testing and certification protocols that were mandated by the industry necessitated a clearly defined pathway for engineers to navigate toward achieving the final objective. Within this framework, a significant focus was placed on the preliminary testing of mechanical properties.

The study focused on a variant of the Charpy-absorbed energy test, known as miniaturised Charpy V-Notch testing, which was assessed for its efficiency in evaluating the L-PBF manufacturing of Ti-6Al-4V. The effects of mechanical post-processing via LSP were also evaluated. The results were analysed alongside key features identified as influential to the impact toughness property. Due to its uncommon usage, the setup of the MCVN test method had to be developed. It involved modifying and calibrating the equipment according to standard practices and assessing the sensitivity of the test setup. Samples were created using hatch spacing parameters ranging from 80% (20% Overlap) “ideal parameter” to 225% of the laser spot diameter, which was followed by a reduction of 80% to 125% for the second set. Based on these findings, an iterative process allowed for adjustments, recalibrations, and verifications, paving the way for the final set of tests.

The final testing experiment was focused on varying the hatch spacing distance between 80% and 191% of the spot size centres. This alteration negatively impacted the volumetric energy density, affecting the recorded values of MCVN absorbed energy. Additionally, samples that underwent LSP post-processing were evaluated and were found to show an enhancement in the MCVN absorbed energy values across all hatch settings - low, medium, and high - within the manufactured range. It is important to highlight that the MCVN absorbed energy values obtained for the optimal parameter set were comparable to those of standard test specimens of renowned organisations such as NIST, as summarised in Table 2-9, underscoring these results' reliability. Inferential analysis revealed that hatch spacing variations and LSP post-processing significantly influenced the recorded MCVN energy values, although their effects were unrelated.

The fractographic analysis revealed that the fracture type was brittle, with no signs of deformation observed. Attention was drawn to the fracture surface topography, which was noted to vary from smooth to very rough as the hatch spacing was increased. Microscopic analysis indicated that quasi-cleavage fracture characteristics primarily dominated the fractured surface. Such fracture type was attributed to the directional change of crack propagation upon reaching a grain boundary. Microstructural evaluations that were carried out perpendicular to the direction of crack propagation exhibited colonies of primary, secondary, and tertiary α′ phases alongside some α phase, all positioned within β boundaries in a chessboard-like pattern. The other orientation exhibited a columnar microstructure of the same phases, oriented towards the building direction. Additionally, shear striations and ductile-looking fracture facets were observed on the fracture surface of samples produced by the larger hatch distances. The features were noted in areas of lack of fusion voids and around unmelted particles.

The localised smooth shear faces observed on the fractured surfaces corresponded with the microCT high % porosity measurements. Large, irregular, interconnected voids in the high hatch spacing settings were identified. Due to the irregular shape of these voids and the minimal material available for load-bearing in those areas, significant stress concentrations occurred. This led to localised shear surfaces characterised by visible shear bands. The voids, also present on the samples' surfaces, significantly influenced the measured energy

absorption values. The determined Sa values indicated that the surface voids became increasingly deeper, acting as stress concentrators during the impact loading to which the samples were subjected. In contrast, the ductile appearance of the fracture type was attributed to intergranular brittle fracture due to stress build-up. XRD tests, however, revealed very low tensile residual stresses. It is important to recall that these tests were conducted after a stress-relieving process, and the observed tensile stresses were primarily linked to the sample preparation itself.

The XRD test results provided insight into a key reason for the increased energy absorbed by MCVN after LSP processing. Due to the oxide layer formed during the confined surface ablation, subsurface investigations were performed and revealed that compressive residual stresses were induced, which helped counteract crack propagation. Additionally, the energy absorption of MCVN was enhanced due to the reduction in surface and subsurface voids, which decreased porosity and lessened the surface roughness (Sa). Furthermore, it is believed that the remelting and rapid solidification caused by the high laser power intensities of LSP, as well as the plastic deformations and the presence of the oxide layer, also contributed to a slight increase in the microhardness ($HV_{0.3}$) values observed in the cross-section and the near-surface region of the peened samples.

Throughout the assessment process, various key elements have been examined, yielding valuable insights. The study reveals that the MCVN impact testing method serves as an effective means of evaluating the mechanical performance of these parts, providing a trustworthy preliminary assessment tool. The prominent features, such as LSP-induced compressive residual stresses, reduced porosity, and modified fracture surface characteristics, offer strong evidence that reinforces the performance results obtained. Notably, the increased MCVN absorbed energy values across all hatch spacing settings, combined with the diminished surface roughness observed after LSP, establish the effectiveness of this method. These findings highlight the potential of MCVN testing for qualifying L-PBF-manufactured Ti-6Al-4V parts within the aerospace sector, instilling confidence in future efforts to refine this approach and move toward commercialisation.

Chapter 8. Further Work

This research has yielded several significant findings; however, like any study, there are always elements that, upon completion, one might wish had been approached differently or done additionally. The following is a list of recommendations that, if implemented, could enhance our understanding and further reinforce the conclusions drawn in this work.

1. Conduct the same experimental procedures and tests with other materials to observe if similar results emerge. Of course, the magnitudes and exact values will differ, but an investigation of whether the trends, behaviours, and tendencies align could make the method generic.

2. Instead of just focusing on the LoF property, investigate other potential defects that L-PBF AM can yield and test whether MCVN testing can discern between samples having different levels of that defect.

3. Investigate using the same testing methods and techniques, but this time, focus on an optimisation strategy. This approach will allow for analysis from a different perspective, enabling the identification of individual parameters and knowing at which level they have a greater impact on the results. Additionally, it will help identify the parameter settings that yield the best outcomes.

Testing an additional mechanical property, such as tensile strength, bending, creep, or fatigue, and observing how these properties vary with our different parameters and the qualitative Charpy impact test results. Since these parameters are more common and better suited for qualification, they can help bridge another gap by attempting to establish a relationship.

Chapter 9. Contributions and Extra Activities

The research outputs listed below provide an overview of the key contributions resulting from this work and a parallel LSP research study. Each contribution reflects either direct implications of the study or advancements influenced by the central themes explored. Relevant abstracts and awards related to this work are listed in Annex 4 – Abstracts and Awards for further context.

- A. Chundunsing, C. Polese, T. Strydom, *Characterisation of Laser Powder Bed Fusion, As-Built, and Laser Shocked Peened Ti6Al4V by Miniaturised Charpy Impact Toughness*, 15th African Laser Centre Student Workshop 18-20 November 2024, Stellenbosch, South Africa. Exceptional Presentation Award.
- N. Shonhai, A.N.N. Chundunsing, C. Polese, L.A. Cornish, H. Ramasawmy *Corrosion Behaviour of Conventional Aeronautical Aluminium Alloy 7075 Processed by Laser Shock Peening without Coating*, Aeronautical Society of South Africa Conference, 27-28 July 2023, Pretoria, South Africa. https://www.aessa.org.za/conference/.
- N. Shonhai, A.N.N. Chundunsing, C. Polese, L.A. Cornish, H. Ramasawmy, *Investigation of Corrosion Behaviour of Aeronautical Aluminium Alloy 7075 Processed by Laser Shock Peening without Coating*, 8th ICLPRP, 22-27 October 2023, Gyeongju, Korea. (Accepted for Oral, moved to Poster A097). https://www.iclprp2023.org/. Best Poster Award. DOI: 10.13140/RG.2.2.10874.88000.

The intricacies of the laser powder bed fusion additive manufacturing process were studied using Simufact Additive software, which was shared between the University of the Witwatersrand (Wits University) and the Central University of Technology (CUT) by Dr Lehlohonolo Francis Monaheng, Lecturer in the Department of Mechanical and Mechatronics Engineering at CUT. An online course and tutorials were completed to gain a better understanding of the relationships and effects of parameter variation.

References and Bibliography

[1] European Union Aviation Safety Agency, ‘Certification Memorandum Additive Manufacturing’. May 06, 2024. [Online]. Available: https://www.easa.europa.eu/sites/default/files/dfu/cm-s-008_issue_04_-_for_consultation_0.pdf

[2] I. Yadroitsev and I. Yadroitsava, *Fundamentals of Laser Powder bed Fusion*. Elsevier, 2021.

[3] ASTM International, *Additive manufacturing - General principles - Fundamentals and vocabulary*, ISO/ASTM 52900, 2021.

[4] J. Pelleg, *Additive and Traditionally Manufactured Components*. Elsevier, 2020.

[5] A. Cunha, A. Marques, M. Rodrigues da Silva, and F. Bartolomeu, ‘Laser powder bed fusion of the steels used in the plastic injection mould industry: a review of the influence of processing parameters on the final properties’, *The International Journal of Advanced Manufacturing Technology*, vol. 121, no. 7–8, pp. 1–33, Aug. 2022.

[6] ‘Manufacturing Milestone: 30,000 Additive Fuel Nozzles | GE Aerospace News’. Accessed: Feb. 03, 2025. [Online]. Available: https://www.geaerospace.com/news/articles/manufacturing/manufacturing-milestone-30000-additive-fuel-nozzles

[7] ASM International, *Additive Manufacturing Processes*, vol. 24.

[8] M. Saunders, ‘How process parameters drive successful metal AM part production’, *Inovar Communications Ltd.*, vol. 4, no. 2, pp. 127–135, 2018.

[9] Q. Liu, J. Elambasseril, S. Sun, M. Leary, M. Brandt, and P. K. Sharp, ‘The Effect of Manufacturing Defects on The Fatigue Behaviour of Ti-6Al 4V Specimens Fabricated Using Selective Laser Melting’, *Advanced Materials Research*, vol. 891–892, pp. 1519–1524, 2014.

[10] ASM International, *Failure Analysis and Prevention*, vol. 11.

[11] ASM International, *Mechanical Testing and Evaluation*, vol. 8.

[12] F. Froes and R. Boyer, *Additive Manufacturing for the Aerospace Industry*. Elsevier.

[13] D. F. Louw and P. G. H. Pistorius, 'The effect of scan speed and hatch distance on prior-beta grain size in laser powder bed fused Ti-6Al-4V', *The International Journal of Advanced Manufacturing Technology*, vol. 103, pp. 2277–2286, 2019, doi: https://doi.org/10.1007/s00170-019-03719-w.

[14] SAE, *Quality Systems - Aerospace*, 1999.

[15] ISO, *Quality management systems*, 9001, 2015.

[16] *Additive Manufacturing Requirements For Spaceflight Systems*, NASA-STD-6030. [Online]. Available: https://standards.nasa.gov/sites/default/files/standards/NASA/Baseline/0/2021-04-21_nasa-std-6030-approveddocx.pdf?

[17] R. Dalton-Taggart, 'Consolidation, competition, and the cost of certification: Insight from New York's AM Strategies 2024', vol. 10, no. 1, pp. 167–174.

[18] D. W. Gibbons and A. F. Van Der Merwe, 'A Conceptual Framework for The Certification of Laser Powder Bed Fusion Process Quality Management Systems for Aerospace Applications', *SAJIE*, vol. 32, no. 1, May 2021, doi: 10.7166/32-1-2342.

[19] A. P. Mouritz, *Introduction to aerospace materials*. WOODHEAD PUBLISHING, 2012.

[20] US Department of Transportation Federal Aviation Administration, 'Advisory Circular: Powder Bed Fusion Additive Manufacturing Process for Aircraft Engine Parts'. June 2023. [Online]. Available: https://www.faa.gov/documentLibrary/media/Advisory_Circular/AC_33.15-3.pdf?utm_source=chatgpt.com

[21] 'Accelerating Additive: GE 3D-Printed Metal Part Receives Air Force Airworthiness Qualification | GE Aerospace News'. Accessed: Jan. 28, 2025. [Online]. Available: https://www.geaerospace.com/news/articles/manufacturing-technology/accelerating-additive-ge-3d-printed-metal-part-receives-air-force

[22] ASM International, *Properties and Selection: Nonferrous Alloys and Special-Purpose materials*, vol. 2.

[23] ASM International, *Metallography And Microstructures*, vol. 9.

[24] J. Sieniawski and W. Ziaja, *Titanium Alloys Advances in Properties Control*. 2016.

[25] *Titanium*. in Engineering Materials, Processes. Berlin, Heidelberg: Springer Berlin Heidelberg, 2007. doi: 10.1007/978-3-540-73036-1.

[26] Y.-K. Kim, Y. K. KIM, J. H. YU, S. H. PARK, and M. C. KIM, 'Effect of Heat Treatment on Microstructure and Impact Toughness of Ti-6Al- 4V Manufactured by Selective Laser Melting Process', *Archives of Metallurgy and Materials*, pp. 1341–1346, 2017, doi: 10.1515/amm-2017-0205.

[27] L. Ji, S. Wang, C. Wang, and Y. Zhang, 'Effect of hatch space on morphology and tensile property of laser powder bed fusion of Ti6Al4V', *Optics and Laser Technology*, vol. 150, 2022, doi: https://doi.org/10.1016/j.optlastec.2022.107929.

[28] H. Shipley, D. McDonnell, M. Culleton, R. Lupoi, G. O'Donnell, and D. Trimble, 'Optimisation of process parameters to address fundamental challenges during selective laser melting of Ti-6Al-4V: A review', *International Journal of Machine Tools and Manufacture*, 2018, doi: 10.1016/j.ijmachtools.2018.01.003.

[29] H. Gong, K. Rafi, Gu, Hengfeng, G. D. J. Ramd, Starr, Thomas, and Stucker, Brent, 'Influence of defects on mechanical properties of Ti–6Al–4 V components produced by selective laser melting and electron beam melting', *Elsevier*, vol. 86, pp. 545–554, 2015, doi: http://dx.doi.org/10.1016/j.matdes.2015.07.147.

[30] N. R. Mathe, L. C. Tshabalala, S. Hoosain, L. Motibane, and A. Du Plessis, 'The effect of porosity on the mechanical properties of Ti-6Al-4V components manufactured by high-power selective laser melting', *The International Journal of Advanced Manufacturing Technology*, vol. 115, pp. 3589–3597, 2021, doi: https://doi.org/10.1007/s00170-021-07326-6.

[31] T. A. Mukalay, J. A. Trimble, K. Mpofu, and R. Muvunzi, 'A systematic review of process uncertainty in Ti6Al4V-selective laser melting', *CIRP Journal of Manufacturing Science and Technology*, vol. 36, pp. 185–212, 2022, doi: CIRP%20Journal%20of%20Manufacturing%20Science%20and%20Technology.

[32] J. Sun, Y. Yang, and W. Wang, 'Parametric optimization of selective laser melting for forming Ti6Al4V samples by Taguchi method', *Optics & Laser Technology*, vol. 49, pp. 118–124, 2013, doi: http://dx.doi.org/10.1016/j.optlastec.2012.12.002.

[33] M. A. Buhairi *et al.*, 'Review on volumetric energy density: influence on morphology and mechanical properties of Ti6Al4V manufactured via laser powder bed fusion', *Prog Addit Manuf*, vol. 8, no. 2, pp. 265–283, Apr. 2023, doi: 10.1007/s40964-022-00328-0.

[34] F. Bartolomeu, M. Gasik, F. S. Silva, and G. Miranda, 'Mechanical Properties of Ti6Al4V Fabricated by Laser Powder Bed Fusion: A Review Focused on the Processing

and Microstructural Parameters Influence on the Final Properties', *Metals*, vol. 12, no. 6, p. 986, June 2022, doi: 10.3390/met12060986.

[35] S. Cao, Y. Zou, C. V. S. Lim, and X. Wu, 'Review of laser powder bed fusion (LPBF) fabricated Ti-6Al-4V: process, post-process treatment, microstructure, and property', *gxjzz*, vol. 2, no. 2, p. 1, 2021, doi: 10.37188/lam.2021.020.

[36] J. Deng *et al.*, 'High power laser powder bed fusion of Ti6Al4V alloy: The control of defects, microstructure, and mechanical properties', *Journal of Materials Research and Technology*, vol. 33, pp. 4831–4843, Nov. 2024, doi: 10.1016/j.jmrt.2024.10.152.

[37] H. Gong, K. Rafi, H. Gu, T. Starr, and B. Stucker, 'Analysis of Defect Generation in Ti-6Al-4V Parts Made using Powder Bed Fusion Additive Manufacturing Processes', *Additive Manufacturing*, doi: 10.1016/j.addma.2014.08.002.

[38] L. J. Barlett and X. Li, 'An overview of residual stresses in metal powder bed fusion', *Additive Manufacturing*, no. 27, pp. 131–149, 2019, doi: https://doi.org/10.1016/j.addma.2019.02.020.

[39] P. Edwards and M. Ramulu, 'Effect of build direction on the fracture toughness and fatigue crack growth in selective laser melted Ti-6Al-4V', *Fatigue & Fracture of Engineering Material Structures*, vol. 38, 2015, doi: 10.1111/ffe.12303.

[40] N. C. Levkulich, S. L. Semiatin, J. E. Gockel, J. R. Middendorf, A. T. DeWald, and N. W. Klingbeil, 'The effect of process parameters on residual stress evolution and distortion in the laser powder bed fusion of Ti-6Al-4V', *Additive Manufacturing*, vol. 28, pp. 475–484, 2019.

[41] S. Chen, H. Gao, Y. Zhang, Q. Wu, Z. Gao, and X. Zhou, 'Review on residual stresses in metal additive manufacturing: formation mechanisms, parameter dependencies, prediction and control approaches', *Journal of materials research and technology*, vol. 17, pp. 2950–2974, 2022, doi: https://doi.org/10.1016/j.jmrt.2022.02.054.

[42] H. D. Nguyen *et al.*, 'A critical review on additive manufacturing of Ti-6Al-4V alloy: microstructure and mechanical properties', *Journal of Materials Research & Technology*, pp. 4641–4661, 2022, doi: https://doi.org/10.1016/j.jmrt.2022.04.055.

[43] Y. Eyzat, M. Chemkhi, Q. Portella, J. Gardan, J. Remond, and D. Retraint, 'Characterization and Mechanical Properties of As-Built SLM Yi-6Al-4V subjected to surface mechanicaal post-treatment', presented at the 52nd CIRP Conference on Manufacturing Systems, Elsevier, 2019, pp. 1225–1229. doi: 10.1016/j.procir.2019.03.298.

[44] A. M. Muiruri, M. Maringa, W. Du Preez, and L. Masu, 'Variation of Impact Toughness of As-built DMLS Ti6Al4V (ELI) Specimens with Temperature', *SAJIE*, vol. 29, no. 3, Nov. 2018, doi: 10.7166/29-3-2076.

[45] P. Mercelis and J.-P. Kruth, 'Residual stresses in selective laser sintering and selective laser melting', *Rapid Prototyping Journal*, 2006, doi: 10.1108/13552540610707013.

[46] Q. Gaillard, S. Cazottes, X. Boulnat, S. Dancette, and C. Desreyaud, 'Microstructure, texture and mechanical properties with raw surface states of Ti-6Al-4V parts built by L-PBF.', presented at the 6th CIRP Conference on Surface Integrity, Elsevier, 2022, pp. 698–703. doi: 10.1016/j.procir.2022.03.108.

[47] S. Chowdhury *et al.*, 'Laser powder bed fusion: a state-of-the-art review of the technology, materials, properties & defects, and numerical modelling', *Journal of Materials Research and Technology*, vol. 20, pp. 2109–2172, Sept. 2022, doi: 10.1016/j.jmrt.2022.07.121.

[48] R. Filip, K. Kubiak, W. Ziaja, and J. Sieniawski, 'The effect of microstructure on the mechanical properties of two-phase titanium alloys', *Materials Processing Technology*, vol. 133, pp. 84–89, 2003.

[49] A. D. Baghi, S. Nafisi, H. Reza, E.-H. Heike, and G. Reza, 'Experimental realisation of build orientation effects on the mechanical properties of truly as-built Ti-6Al-4V SLM parts', *Journal of Manufacturing Processes*, vol. 64, pp. 140–152, 2021, doi: https://doi.org/10.1016/j.jmapro.2021.01.027.

[50] W. E. Frazier, 'Metal Additive Manufacturing: A Review', *Journal of Materials engineering and Performance*, vol. 23, pp. 1917–1928, 2014, doi: https://doi.org/10.1007/s11665-014- 0958-z.

[51] Z. Xie, Y. Dai, X. Ou, S. Ni, and S. Min, 'Effects of selective laser melting build orientations on the microstructure and tensile performance of Ti–6Al–4V alloy', *Materials Science & Engineering A*, no. 776, 2020.

[52] E. Lucon and N. W. Hrabe, 'Instrumented impact tests on miniaturized Charpy specimens of additively manufactured (AM) Ti6Al4V', National Institute of Standards and Technology, NIST TN 1936, Sept. 2016. doi: 10.6028/NIST.TN.1936.

[53] M. Simonelli, Y. Y. Tse, and C. Tuck, 'Effect of the build orientation on the mechanical properties and fracture modes of SLM Ti-6Al-4V', *Materials Science & Engineering A*, pp. 1–11, 2014, doi: http://dx.doi.org/10.1016/j.msea.2014.07.086.

[54] N. Hrabe, R. White, and E. Lucon, ‘Effects of internal porosity and crystallographic texture on Charpy absorbed energy of electron beam melting titanium alloy (Ti-6Al-4V)’, *Materials Science & Engineering A*, vol. 742, pp. 269–277, 2019.

[55] V. Cain, L. Thijs, J. Van Humbeeck, B. Van Hooreweder, and R. Knutsen, ‘Crack propagation and fracture toughness of Ti6Al4V alloy produced byselective laser melting’, *Elsevier*, no. 5, pp. 68–76, 2015, doi: R.%20Knutsen.

[56] H. Eskandari *et al.*, ‘Microstructural characterization and mechanical properties of SLM-printed Ti–6Al–4V alloy: Effect of build orientation’, *Journal of Materials Research*, doi: 10.1557/s43578-021-00468-z.

[57] P. Hartunian and M. Eshraghi, ‘Effect of Build Orientation on the Microstructure and Mechanical Properties of Selective Laser-Melted Ti-6Al-4V Alloy’, *Journal of Manufacturing and Materials Processing*, 2018, doi: doi:10.3390/jmmp2040069.

[58] E. Yasa, J. Deckers, J.-P. Kruth, M. Rombouts, and J. Luyten, ‘Charpy impact testing of metallic selective laser melting parts’, *Virtual and Physical Prototyping*, 2013, doi: 10.1080/17452751003703894.

[59] I. Yadroitsev, P. Krakhmalev, I. Yadroitsava, and A. Du Plessis, ‘Qualification of Ti6Al4V ELI Alloy Produced by Laser Powder Bed Fusion for Biomedical Applications’, *JOM*, vol. 70, no. 3, pp. 372–377, Mar. 2018, doi: 10.1007/s11837-017-2655-5.

[60] W. H. Kan *et al.*, ‘The influence of porosity on Ti-6Al-4V parts fabricated by laser powder bed fusion in the pursuit of process efficiency’, *Int J Adv Manuf Technol*, vol. 119, no. 7–8, pp. 5417–5438, Apr. 2022, doi: 10.1007/s00170-021-08374-8.

[61] M. Losertová and V. Kubeš, ‘Microstructure and mechanical properties of selective laser melted Ti6Al4V alloy’, presented at the IOP Conference Series: Materials Science and Engineering, doi: 146.141.59.100%20on%2006/07/2022.

[62] N. Eshawish, S. Malinov, W. Sha, and P. Walls, ‘Microstructure and Mechanical Properties of Ti-6Al-4V Manufactured by Selective Laser Melting after Stress Relieving, Hot Isostatic Pressing Treatment, and Post-Heat Treatment’, *Journal of Materials engineering and Performance*, 2021, doi: https://doi.org/10.1007/s11665-021-05753-w.

[63] P. Krakhmalev, G. Fredriksson, I. Yadroitsava, N. Kazantseva, A. D. Plessis, and I. Yadroitsev, ‘Deformation Behavior and Microstructure of Ti6Al4V Manufactured by SLM’, *Physics Procedia*, vol. 83, pp. 778–788, 2016, doi: 10.1016/j.phpro.2016.08.080.

[64] M. Kazachenok, A. Panin, and S. Panin, ‘Impact toughness of Ti–6Al–4V parts fabricated by additive manufacturing’, presented at the AIP Conference Proceedings, 2019. doi: https://doi.org/10.1063/1.5132020.

[65] J. Tong, C. R. Bowen, J. Persson, and A. Plummer, ‘Mechanical properties of titanium-based Ti–6Al–4V alloys manufactured by powder bed additive manufacture’, *Materials Science and Technology*, vol. 33, no. 2, pp. 138–148, Jan. 2017, doi: 10.1080/02670836.2016.1172787.

[66] D. Kouprianoff and W. Du Preez, ‘Reducing time and cost of the heat treatment post-processing of additively manufactured Ti6Al4V’, *Materials Today Communications*, vol. 35, 2023.

[67] L. Lei, Y. Zhao, Q. Zhao, C. Wu, S. Huang, and W. Jia, ‘Impact toughness and deformation modes of Ti–6Al–4V alloy with different microstructures’, *Materials Science & Engineering A*, no. 801, 2021, doi: Materials%20Science%20&%20Engineering%20A.

[68] J. D. Kwon, Y. T. Bae, and S. J. Choi, ‘The effect of Microstructure on Mechanical Behaviour for Titanium Alloy (Ti-6Al-4V)’, *International Journal of Modern Physics B*, vol. 17, no. 8–9, pp. 1297–1303, 2003, doi: http://dx.doi.org/10.1142/S0217979203018909.

[69] X. Yan, S. Yue, J. Ge, C. Chen, R. Lupoi, and S. Yin, ‘Microstructural and mechanical optimization of selective laser melted Ti6Al4V lattices: Effect of hot isostatic pressing’, *Journal of Manufacturing Processes*, no. 77, pp. 151–162, 2022, doi: https://doi.org/10.1016/j.jmapro.2022.02.024.

[70] D. K. Do and P. Li, ‘The effect of laser energy input on the microstructure, physical and mechanical properties of Ti-6Al-4V alloys by selective laser melting’, vol. 11, no. 1, pp. 41–47, 2016, doi: 10.1080/17452759.2016.1142215.

[71] A. Du Plessis and E. Macdonald, ‘Hot isostatic pressing in metal additive manufacturing: X-ray tomography reveals details of pore closure’, *Additive Manufacturing*, vol. 34, p. 101191, Aug. 2020, doi: 10.1016/j.addma.2020.101191.

[72] ISO/ASTM International, *Additive manufacturing — Design — Part 1: Laser-based powder bed fusion of metals*, 2019.

[73] S. Moon *et al.*, ‘Impact of surface and pore characteristics on fatigue life of laser powder bed fusion Ti–6Al–4V alloy described by neural network models’, *Sci Rep*, vol. 11, no. 1, p. 20424, Oct. 2021, doi: 10.1038/s41598-021-99959-6.

[74] H. P. Miya, W. B. Du Preez, and L. F. Monaheng, 'High Cycle Fatigue Performance of Ti6al4v(Eli) Specimens Produced with Inherent Laser Powder Bed Fusion Surface Roughness', *SAJIE*, vol. 32, no. 3, pp. 248–257, 2021, doi: 10.7166/32-3-2659.

[75] A. M. Mancisidor *et al.*, 'Effect of Post-Processing Treatment on Fatigue Performance of Ti6Al4V Alloy Manufactured by Laser Powder Bed Fusion', *JMMP*, vol. 7, no. 4, p. 119, June 2023, doi: 10.3390/jmmp7040119.

[76] Anton Du Plessis *et al.*, 'Standard method for microCT-based additive manufacturing quality control 3: Surface roughness', *MethodsX*, vol. 5, pp. 1111–1116, 2018, doi: 10.1016/j.mex.2018.09.004.

[77] S. Aguado-Montero, C. Navarro, J. Vázquez, F. Lasagni, S. Slawik, and J. Domínguez, 'Fatigue behaviour of PBF additive manufactured TI6AL4V alloy after shot and laser peening', *International Journal of Fatigue*, vol. 154, p. 106536, Jan. 2022, doi: 10.1016/j.ijfatigue.2021.106536.

[78] K. Dyer, S. Ghadar, S. Zulić, D. Rostohar, E. Asadi, and R. Molaei, 'The Effect of Laser Shock Peening (LSP) on the Surface Roughness and Fatigue Behavior of Additively Manufactured Ti-6Al-4V Alloy', *Coatings*, vol. 14, no. 1, p. 110, Jan. 2024, doi: 10.3390/coatings14010110.

[79] K. Ding and L. Ye, *Laser Shock Peening*. 2006. Accessed: Oct. 09, 2024. [Online]. Available: https://shop.elsevier.com/books/laser-shock-peening/ding/978-1-85573-929-1

[80] C. Park, D. Jung, E.-J. Chun, S. Ahn, H. Jang, and Y.-J. Kim, 'Effect of laser shock peening without coating on fretting corrosion of copper contacts', *Applied Surface Science*, vol. 514, p. 145917, June 2020, doi: 10.1016/j.apsusc.2020.145917.

[81] Cesar A. Reynoso-Garcia *et al.*, 'Improving the Surface Properties of Ti6Al4V with Laser Shock Processing', *Int. Journ. of Peening Science and Technology*, vol. Vol. 1, pp. 119–136, 2018.

[82] N. Kalentics, K. Huang, M. Ortega Varela De Seijas, A. Burn, V. Romano, and R. E. Logé, 'Laser shock peening: A promising tool for tailoring metallic microstructures in selective laser melting', *Journal of Materials Processing Technology*, vol. 266, pp. 612–618, Apr. 2019, doi: 10.1016/j.jmatprotec.2018.11.024.

[83] T. Strydom, C. Polese, and D. Glaser, 'Laser shock peening of laser powder bed fusion produced Ti6Al4V for potential improvements to implant performance', *MATEC Web Conf.*, vol. 388, p. 10006, 2023, doi: 10.1051/matecconf/202338810006.

[84] M. Rozmus-Górnikowska, ‘Surface Modifications of a Ti6Al4V Alloy by a Laser Shock Processing’, presented at the Annual Conference of the Materials Research Society of Serbia, 2010.

[85] W. Guo *et al.*, ‘Laser shock peening of laser additive manufactured Ti6Al4V titanium alloy’, *Surface and Coatings Technology*, vol. 349, pp. 503–510, Sept. 2018, doi: 10.1016/j.surfcoat.2018.06.020.

[86] N. Kalentics, E. Boillat, P. Peyre, S. Ćirić-Kostić, N. Bogojević, and R. E. Logé, ‘Tailoring residual stress profile of Selective Laser Melted parts by Laser Shock Peening’, *Additive Manufacturing*, vol. 16, pp. 90–97, Aug. 2017, doi: 10.1016/j.addma.2017.05.008.

[87] I. Yeo, S. Bae, A. Amanov, and S. Jeong, ‘Effect of Laser Shock Peening on Properties of Heat-Treated Ti–6Al–4V Manufactured by Laser Powder Bed Fusion’, *Int. J. of Precis. Eng. and Manuf.-Green Tech.*, vol. 8, no. 4, pp. 1137–1150, July 2021, doi: 10.1007/s40684-020-00234-2.

[88] V. Agarwal, S. Jawade, S. Atre, and O. Kulkarni, ‘The role of mechanical testing in additive manufacturing: review’, *Mater. sci. eng., appl.*, vol. 1, no. 2, pp. 21–31, Dec. 2021, doi: 10.21595/msea.2021.22258.

[89] J. L. González-Velázquez, *Fractography and Failure Analysis*, vol. 3. Springer.

[90] ASM International, *Fractography*, vol. 12.

[91] E. Lucon, C. N. McCowan, and R. L. Santoyo, ‘Overview of NIST Activities on Sub-size and Miniaturized Charpy Specimens: Correlations with Full-Size Specimens and Verification Specimens for Small-Scale Pendulum Machines’, *Journal of Pressure Vessel Technology*.

[92] ASTM International, *Standard Test Method for Impact Testing of Miniaturized Charpy V-notch Specimens*, E2248, 2018.

[93] ASTM International, *Standard Test methods for Notched Bar Impact Testing of Metallic Materials*, E23, 2018.

[94] CEN, *Charpy impact test on metallic materials – Part 1: Test method.*, EN 10045.

[95] ISO, *Metallic materials — Charpy pendulum impact test*, 148–1, 2016.

[96] JIS, *Charpy pendulum impact test method for metallic materials*, Z 2242, 2023.

[97] SAC, *Charpy pendulum impact test method*, GB/T 229, 2020.

[98] E. Lucon, C. N. McCowan, and R. L. Santoyo, 'Overview of NIST Activities on Sub-size and Miniaturized Charpy Specimens: Correlations with Full-Size Specimens and Verification Specimens for Small-Scale Pendulum Machines', *Journal of Pressure Vessel Technology*.

[99] A. Muiruri, M. Maringa, W. Du Preez, and L. Masu, 'Effects of Stress-Relieving Heat Treatment on Impact Toughness of Direct Metal Laser Sintering (DMLS)-Produced Ti6Al4V (ELI) Parts', *JOM*, vol. 72, no. 3, pp. 1175–1185, Mar. 2020, doi: 10.1007/s11837-019-03862-5.

[100] L. F. Monaheng, W. B. Du Preez, and C. Polese, 'Towards Qualification in the Aviation Industry: Impact Toughness of Ti6Al4V(ELI) Specimens Produced through Laser Powder Bed Fusion Followed by Two-Stage Heat Treatment', *Metals*, vol. 11, no. 11, p. 1736, Oct. 2021, doi: 10.3390/met11111736.

[101] tec-science, 'Charpy impact test | tec-science'. Accessed: Jan. 30, 2025. [Online]. Available: https://www.tec-science.com/material-science/material-testing/charpy-impact-test/

[102] D. C. Montgomery, *Design and Analysis of Experiments*, Ninth. WILEY.

[103] 'Our Machines | Aditiv Solutions'. Accessed: Oct. 07, 2024. [Online]. Available: https://www.aditiv.co.za/our-machines/

[104] 'Ti-6al-4v Grade 5 Titanium Alloy | AP&C'. Accessed: Mar. 04, 2025. [Online]. Available: https://www.advancedpowders.com/powders/titanium-alloys/ti-6al-4v-grade-5

[105] Y. Li, K. Zhou, P. Tan, S. B. Tor, C. K. Chua, and K. F. Leong, 'Modeling temperature and residual stress fields in selective laser melting', *International Journal of Mechanical Sciences*, vol. 136, pp. 24–35, Feb. 2018, doi: 10.1016/j.ijmecsci.2017.12.001.

[106] I. Yadroitsev, I. Yadroitsava, A. Du Plessis, and E. MacDonald, *Fundamentals of Laser Powder bed Fusion*. Elsevier, 2021.

[107] SAE International, *Heat Treatment of Titanium Alloy Parts*, AMS2801D, Mar. 01, 2024.

[108] ASM International, *Heat Treating of Nonferrous Alloys*, vol. 4E.

[109] ‘Nd_Yag_Laser_Nanosecond_Laser_1064nm_1250mJ_Spectra_Physics-1462086952.pdf’. Accessed: Mar. 05, 2025. [Online]. Available: https://www.laserlabsource.com/files/pdfs/solidstatelasersource_com/product-305/Nd_Yag_Laser_Nanosecond_Laser_1064nm_1250mJ_Spectra_Physics-1462086952.pdf

[110] J. E. Rankin and M. R. Hill, ‘Measurement of Thickness-Average Residual Stress Near the Edge of a Thin Laser Peened Strip’, *Journal of Engineering Materials and Technology*, vol. 125, no. 3, pp. 283–293, July 2003, doi: 10.1115/1.1584481.

[111] P. R. Smith, M. J. Shepard, P. S. Prevéy Iii, and A. H. Clauer, ‘Effect of Power Density and Pulse Repetition on Laser Shock Peening of Ti-6AI-4V’, *Journal of Materials Engineering and Performance*, vol. 9, no. 1, pp. 33–37, Feb. 2000, doi: 10.1361/105994900770346259.

[112] Q. Wang, Y. Ge, J. Chen, T. Suzuki, Y. Sagisaka, and N. Ma, ‘Unraveling Residual Stress Distribution Characteristics of 6061-T6 Aluminum Alloy Induced by Laser Shock Peening’, *Materials*, vol. 17, no. 14, p. 3484, July 2024, doi: 10.3390/ma17143484.

[113] J. J. Ruschau, R. John, S. R. Thompson, and T. Nicholas, ‘Fatigue Crack Growth Rate Characteristics of Laser Shock Peened Ti-6Al-4V’, *Journal of Engineering Materials and Technology*, vol. 121, no. 3, pp. 321–329, July 1999, doi: 10.1115/1.2812381.

[114] Smartly-, ‘TESCAN VEGA’, TESCAN. Accessed: Oct. 25, 2024. [Online]. Available: https://www.tescan.com/product/sem-for-materials-science-tescan-vega/

[115] D. Hull, *Fractography: Observing, Measuring, and Interpreting Fracture Surface Topography*. Cambridge University Press.

[116] ASTM International, *Standard Guide for Computed Tomography (CT)*, E1441, 2019.

[117] ‘CT Metrology’, Comet YXLON. Accessed: Oct. 07, 2024. [Online]. Available: https://yxlon.comet.tech/en/technologies/ct-metrology

[118] ‘myVGL - Products - volumegraphics.com’. Accessed: Mar. 06, 2025. [Online]. Available: https://www.volumegraphics.com/en/products/myvgl.html

[119] ‘iXRD Portable Residual Stress Measurement Systems | Proto XRD’. Accessed: Mar. 10, 2025. [Online]. Available: https://www.protoxrd.com/products/residual-stress-measurement/ixrd-portable

[120] ASTM International, *Microindentation Hardness of Materials*, E384, 2022.

[121] ASTM International, *Vickers Hardness and Knoop Hardness of Metallic Materials*, E92, 2023.

[122] 'FALCON 500G2', INNOVATEST. Accessed: Nov. 13, 2024. [Online]. Available: https://www.innovatest-europe.com/products/falcon-500g2/

[123] 'Metal heart Additive Manufacturing', Metal Heart. Accessed: Sept. 08, 2024. [Online]. Available: https://metalheart.co.za/services/

[124] National Physics Laboratory, 'A NATIONAL MEASUREMENT GOOD PRACTICE GUIDE - Determination of Residual Stresses by X-ray Diffraction'. 2005.

[125] J. Cohen, *Statistical Power Analysis for the Behavioral Sciences*, 0 edn. Routledge, 2013. doi: 10.4324/9780203771587.

[126] E. Maawad, Y. Sano, L. Wagner, H.-G. Brokmeier, and Ch. Genzel, 'Investigation of laser shock peening effects on residual stress state and fatigue performance of titanium alloys', *Materials Science and Engineering: A*, vol. 536, pp. 82–91, Feb. 2012, doi: 10.1016/j.msea.2011.12.072.

[127] O. O. Ojo and E. Taban, 'Post-processing treatments–microstructure–performance interrelationship of metal additive manufactured aerospace alloys: A review', *Materials Science and Technology*, vol. 39, no. 1, pp. 1–41, Jan. 2023, doi: 10.1080/02670836.2022.2130530.

[128] G. Ranjith Kumar, G. Rajyalakshmi, S. Swaroop, S. Arul Xavier Stango, and U. Vijayalakshmi, 'Laser shock peening wavelength conditions for enhancing corrosion behaviour of titanium alloy in chloride environment', *J Braz. Soc. Mech. Sci. Eng.*, vol. 41, no. 3, p. 129, Mar. 2019, doi: 10.1007/s40430-019-1633-y.

Appendices

Appendix One – MCVN Results: Raw Data

1st Experimental Set

Condition: As-Built					
72 µm Hatch		172 µm Hatch		202 µm Hatch	
Angular Reading, °	Absorbed Energy, J	Angular Reading, °	Absorbed Energy, J	Angular Reading, °	Absorbed Energy, J
14.25	14.82	6.00	5.35	3.75	3.19
11.50	11.4	5.50	4.85	4.50	3.89
12.00	12	4.75	4.13	4.25	3.65

2nd Experimental Set

Condition: As-Built					
72 µm Hatch		92 µm Hatch		112 µm Hatch	
Angular Reading, °	Absorbed Energy, J	Angular Reading, °	Absorbed Energy, J	Angular Reading, °	Absorbed Energy, J
12.25	12.31	13.00	13.23	13.25	13.55
14.25	14.82	12.25	12.31	12.75	12.92
13.00	13.23	12.75	12.92	12.50	12.61

Note:

- The angular readings for the first set differ slightly from the second and final as further modifications were made to the Charpy impact tester head. However, the absorbed energies were recalculated and adjusted with thorough analysis, ensuring the validity of the results. Kindly Refer to Annex 1 – Charpy Impact Tester - Modifications Report and Annex 2 - Charpy Impact Tester - Calibration Report for further details.

Final Experimental Set

Condition: As-Built											
72 µm Hatch		**132 µm Hatch**		**142 µm Hatch**		**152 µm Hatch**		**162 µm Hatch**		**172 µm Hatch**	
Angular Reading, °	**Absorbed Energy, J**	**Angular Reading, °**	**Absorbed Energy, J**	**Angular Reading, °**	**Absorbed Energy, J**	**Angular Reading, °**	**Absorbed Energy, J**	**Angular Reading, °**	**Absorbed Energy, J**	**Angular Reading, °**	**Absorbed Energy, J**
11.25	11.1	8.75	8.24	8.25	7.69	7.5	6.89	7	6.37	5.25	4.61
15.00	15.8	7.25	6.63	8.00	7.43	8.25	7.69	7.25	6.63	5.75	5.1
12.25	12.31	9.25	8.8	7.75	7.16	7.25	6.63	6.75	6.11	6	5.35
Condition: Laser Shock Peened											
12.25	12.31	-	-	11.75	11.7	-	-	-	-	7.00	6.37
13.75	14.18	-	-	11.00	10.81	-	-	-	-	6.50	5.86
13.00	13.23	-	-	9.25	8.8	-	-	-	-	6.25	5.6

Appendix Two – Fractography

SEM Images: 72 SR

Fracture Initiation region

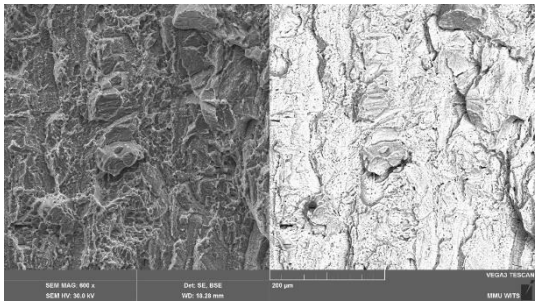

Unstable Crack Region

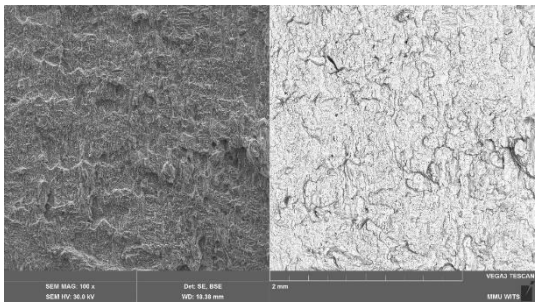

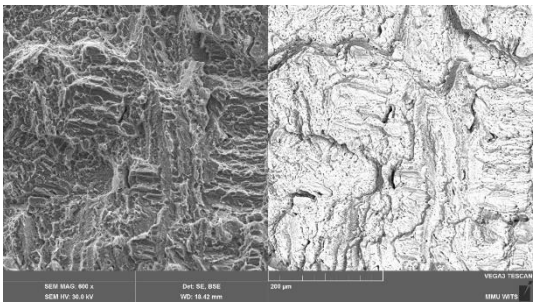

Final Fracture Region

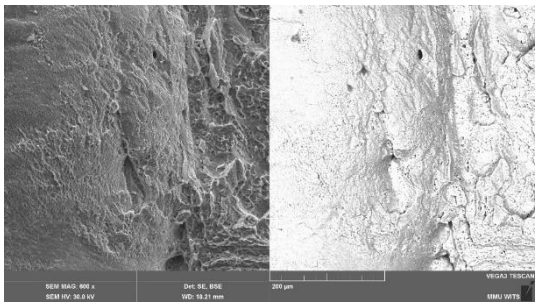

SEM Images: 72 SR+LSP

Fracture Initiation region

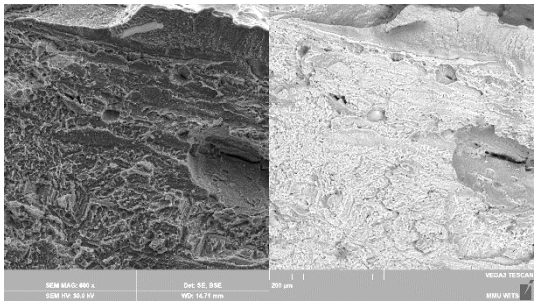

Unstable Crack Region

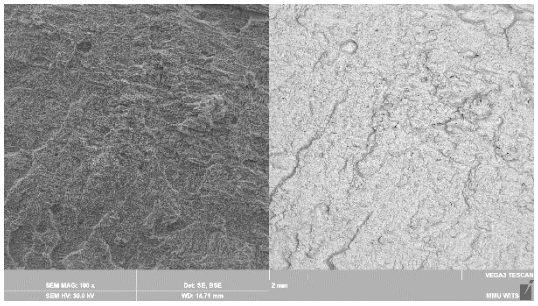

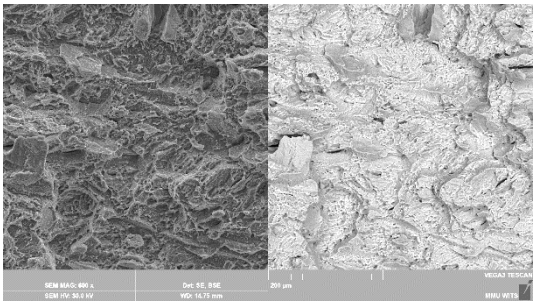

Final Fracture Region

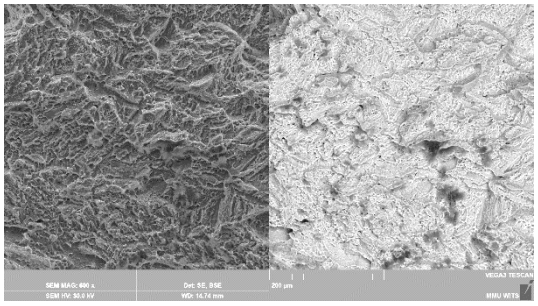

SEM Images: 142 SR

Fracture Initiation region

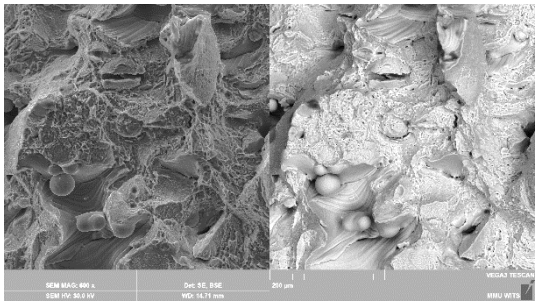

Unstable Crack Region

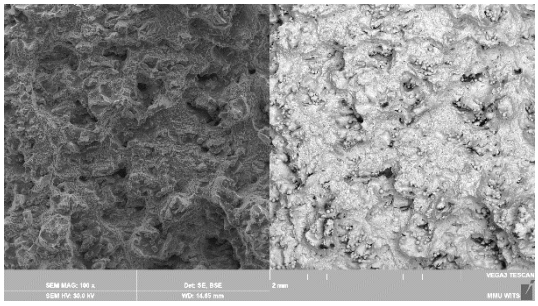

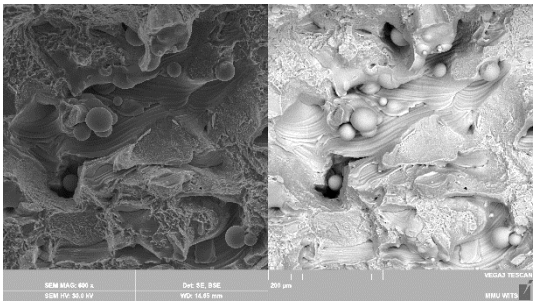

Final Fracture Region

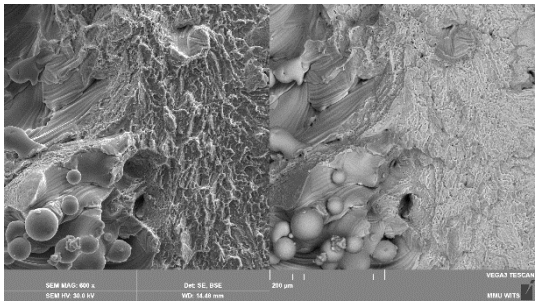

SEM Images: 142 SR+LSP

Fracture Initiation region

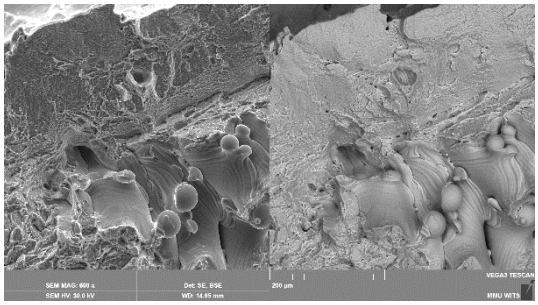

Unstable Crack Region

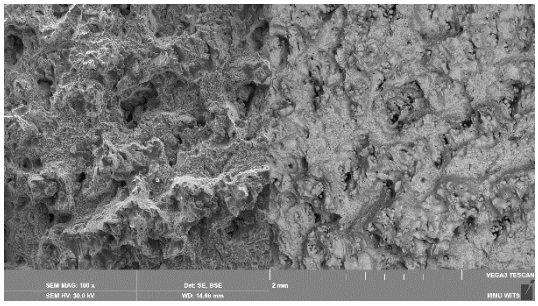

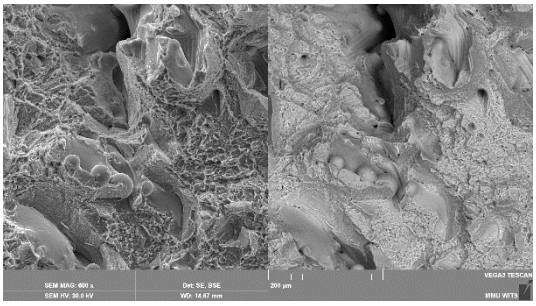

Final Fracture Region

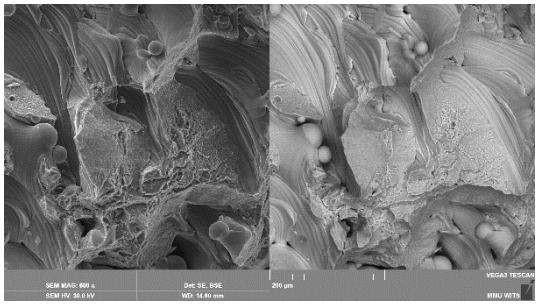

SEM Images: 172 SR

Fracture Initiation region

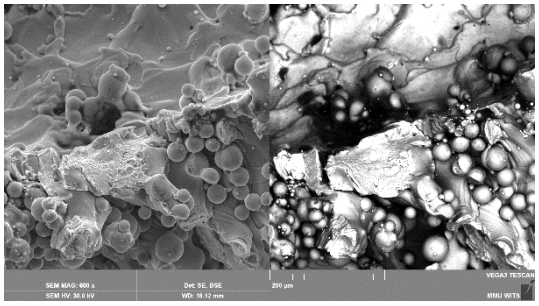

Unstable Crack Region

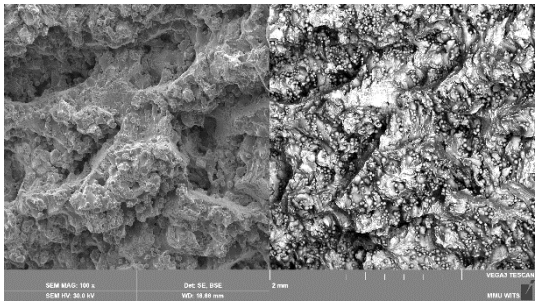

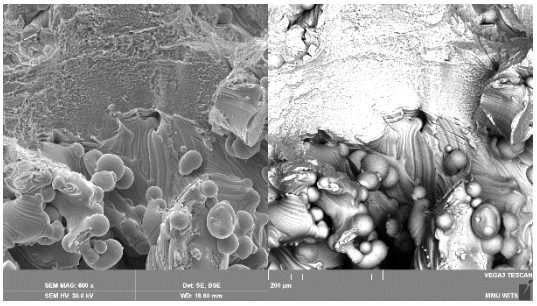

Final Fracture Region

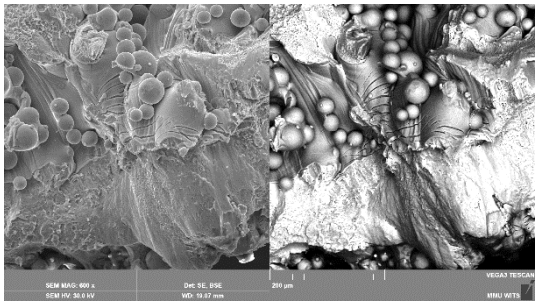

SEM Images: 172 SR+LSP

Fracture Initiation region

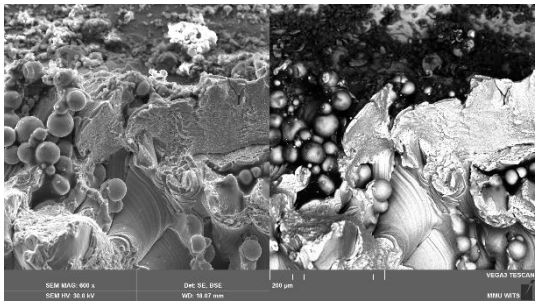

Unstable Crack Region

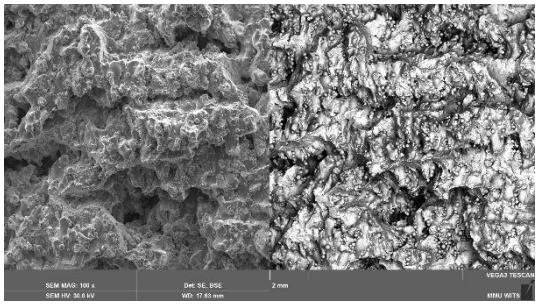

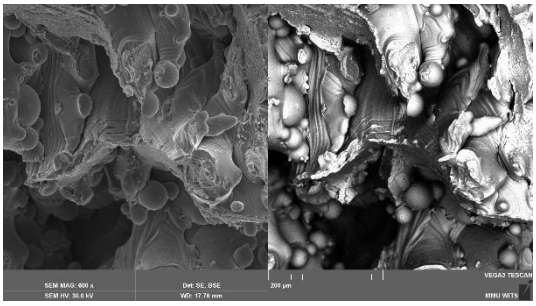

Final Fracture Region

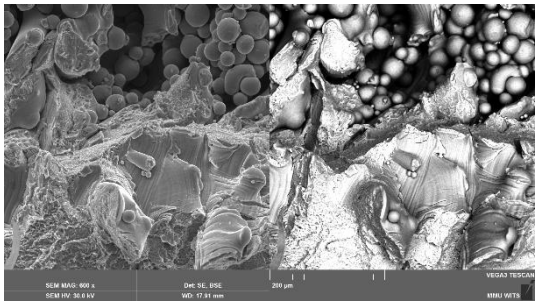

Cross-sectional Optical Images

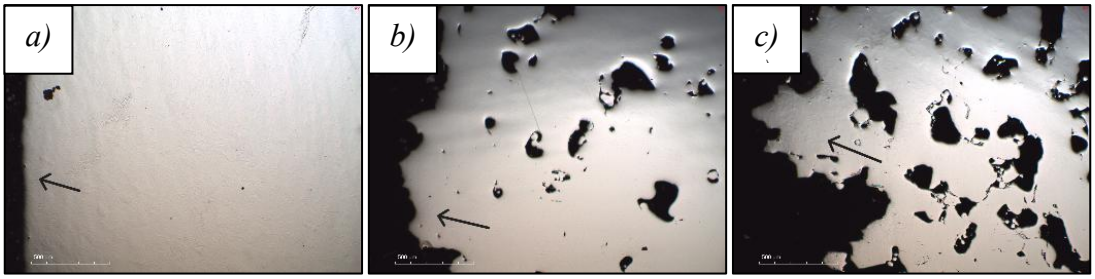

Cross-section view of SR fractured surfaces indicated by an arrow:
(a) 72 µm hatch, (b) 142 µm hatch and (c) 172 µm hatch.

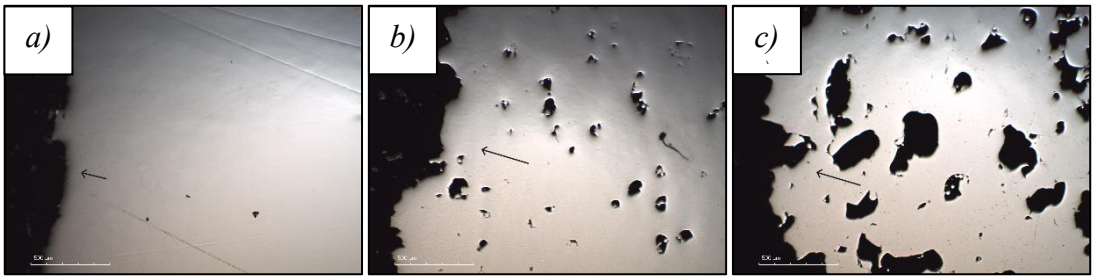

Cross-section view of SR+LSP fractured surfaces indicated by an arrow:
(a) 72 µm hatch, (b) 142 µm hatch and (c) 172 µm hatch.

Appendix Three – Porosity Results: Raw Data

Pore/Void: Region of Interest Definition

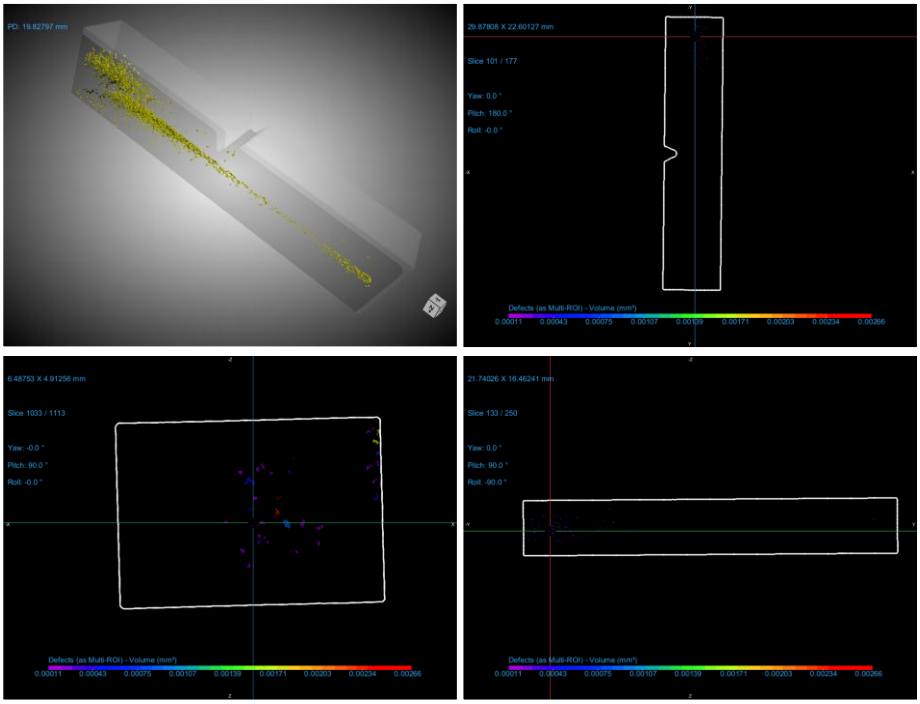

72 µm hatch spacing SR.

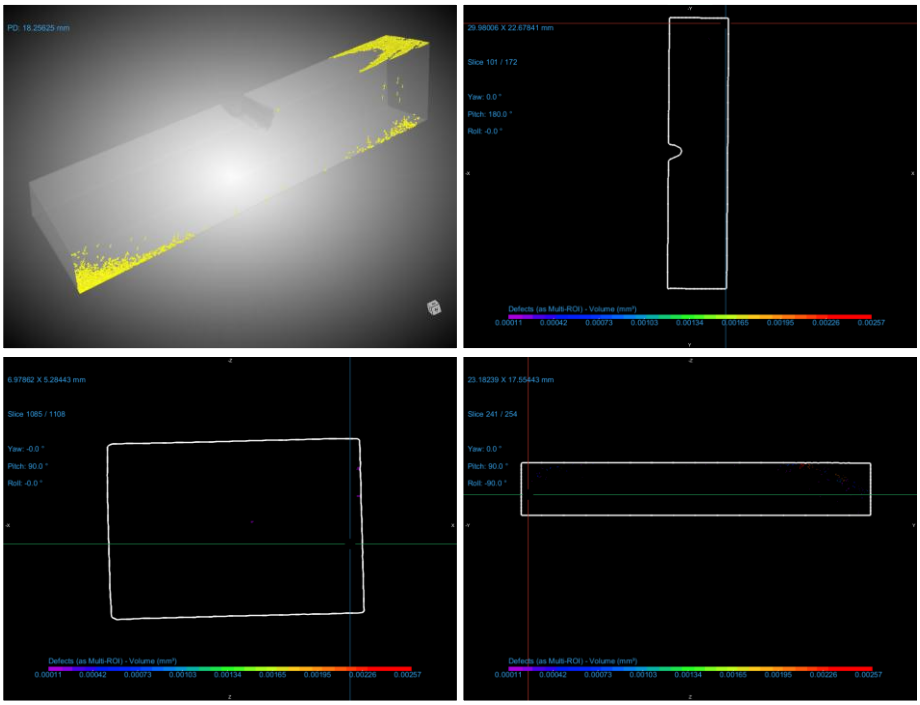

72 µm hatch spacing SR+LSP.

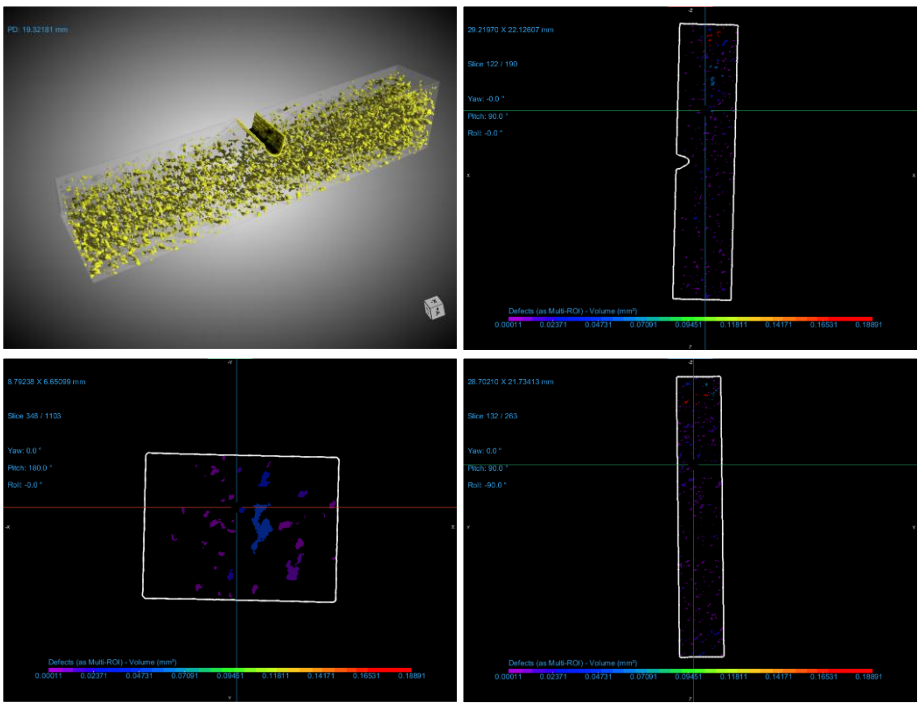

142 µm hatch spacing SR.

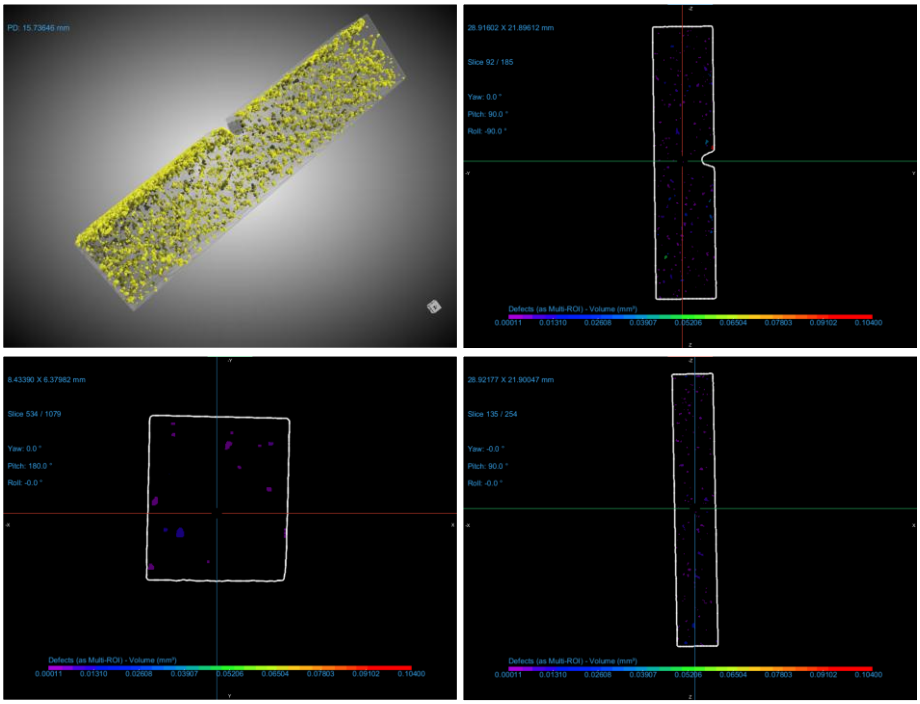

142 µm hatch spacing SR+LSP.

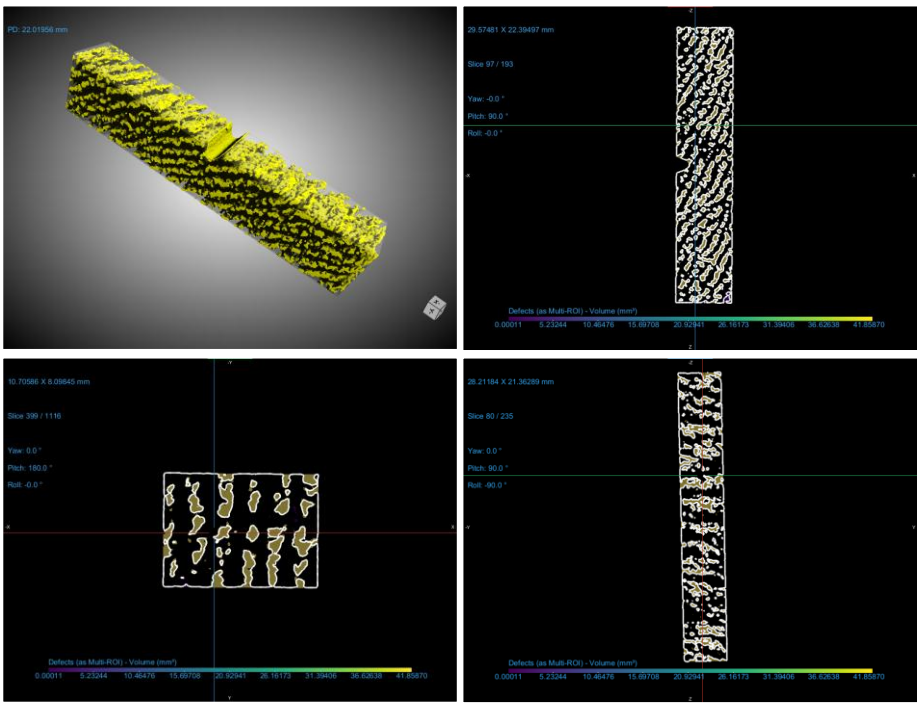

172 µm hatch spacing SR.

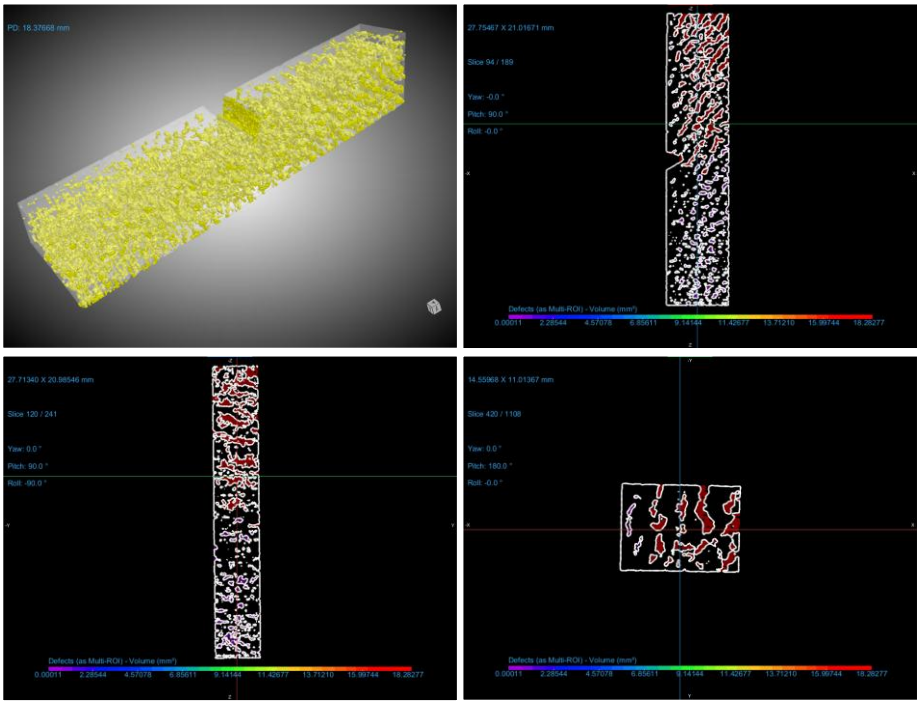

172 µm hatch spacing SR+LSP.

Pore/Void Volume Distribution

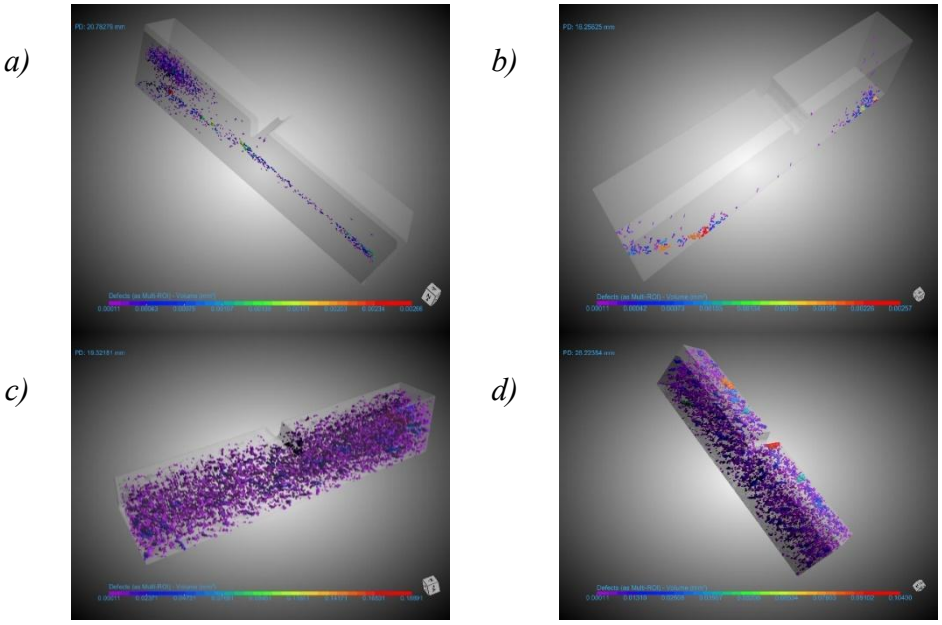

Micro CT Images illustrating the volume of pores and voids: (a)(b) 72 µm hatch SR & SR+LSP, (c)(d) 142 µm hatch SR & SR+LSP.

Pore/Void Sphericity Distribution

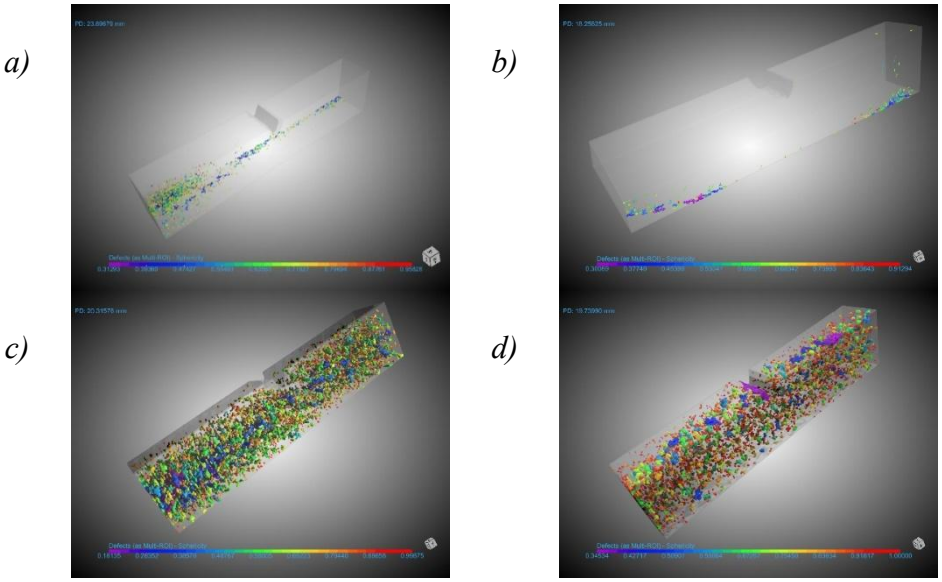

Micro CT Images illustrating the Sphericity of pores and voids: (a)(b) 72 µm hatch SR & SR+LSP, (c)(d) 142 µm hatch SR & SR+LSP.

Appendix Four – Surface Roughness

As-Built

a)

b)

c)

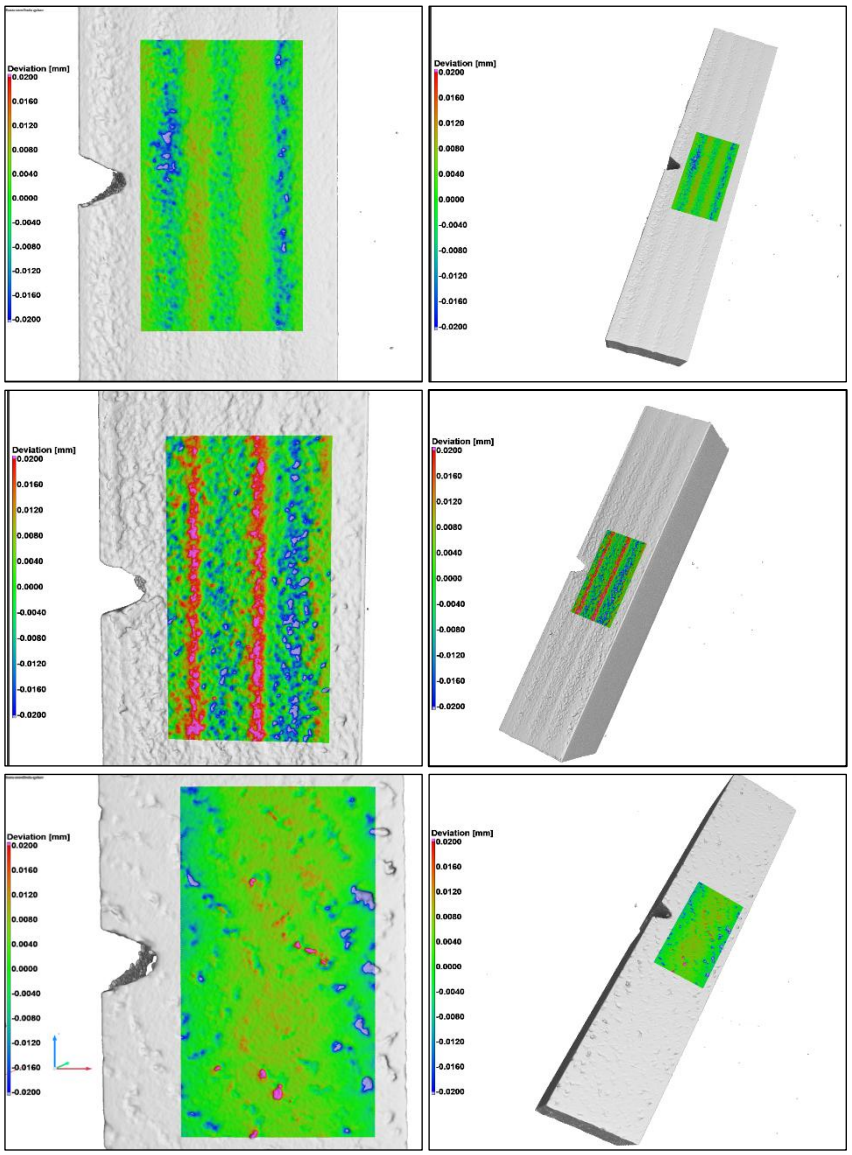

Surface mapping carried out on SR samples using Volume Graphics, VGStudioMax 3.1, from the micro CT scans: (a)72 µm hatch spacing, (b) 142 µm hatch spacing, (c) 172 µm hatch spacing.

Laser Shock Peened

a)

b)

c)

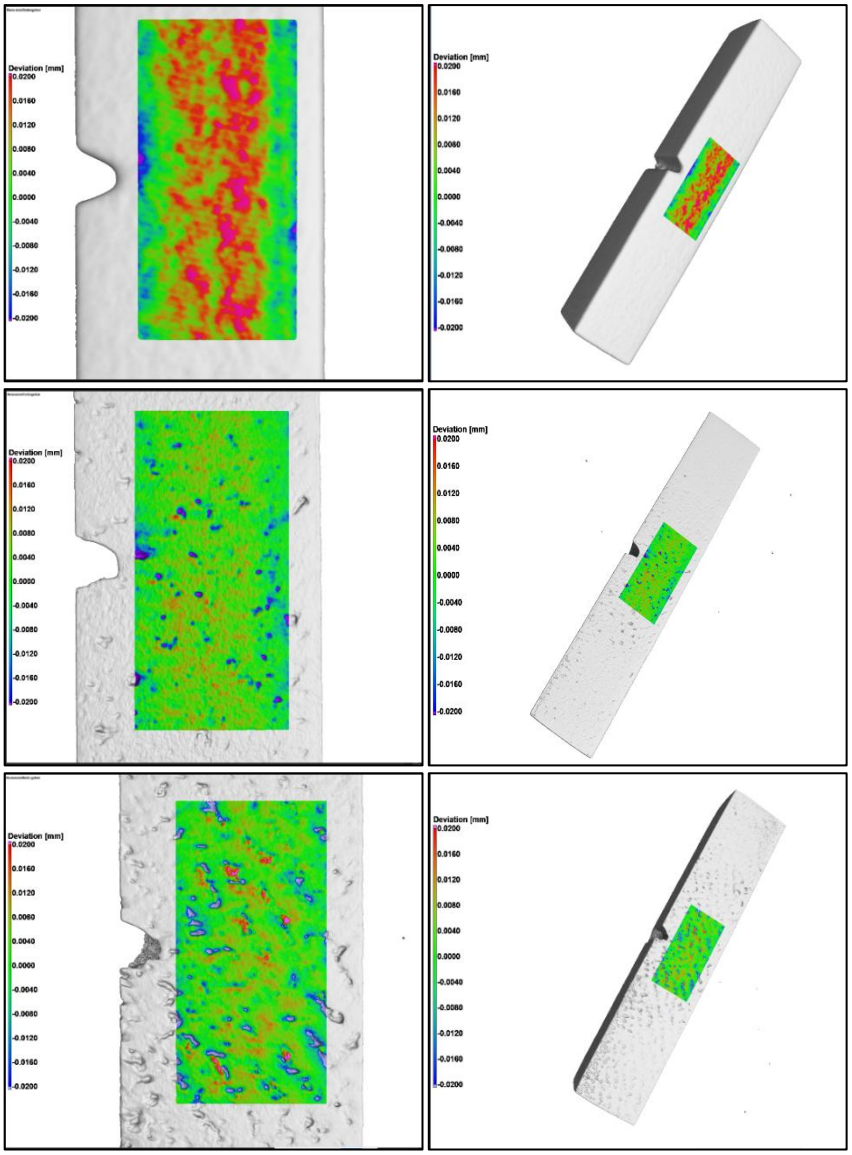

Surface mapping carried out on SR+LSPeened samples using Volume Graphics VGStudioMax 3.1, from the micro CT scans: (a)72 µm hatch spacing, (b) 142 µm hatch spacing, (c) 172 µm hatch spacing.

Appendix Five – Residual Stresses: Raw Data

Hatch Spacing (µm)	Sample	0°	45°	90°	Shear	σ1	σ2	Max Shear	Principal stress direction
					Values in MPa				
72	SR - As received	-243.4	-110.7	-181.5	101.8	-106.09	-318.89	106.40	53.5
	SR - Scouring Pad	-	-	-	-	-	-	-	-
	SR - Electropolished	85.8	80.3	100.3	-12.8	107.72	78.34	14.69	-59.8
	SR+LSP - As received	-70.8	82.2	101.9	66.7	124.61	-93.55	109.08	71.2
	SR+LSP - Scouring Pad	-224.0	-223.8	-170.6	-26.5	-159.63	-234.93	37.65	-67.6
	SR+LSP - Electropolished	-533.2	-507.4	-557.5	37.9	-505.52	-585.11	39.79	36.1
142	SR - As received	302.7	478.4	518.7	67.7	538.13	283.27	127.43	74.0
	SR - Scouring Pad	-	-	-	-	-	-	-	-
	SR - Electropolished	48.8	86.9	83.6	20.7	93.20	39.14	27.03	65.0
	SR+LSP - As received	-155.8	-53.1	-97.5	73.6	-47.49	-205.85	79.18	55.8
	SR+LSP - Scouring Pad	-268.7	-259.7	-257.5	3.4	-256.50	-269.67	6.59	74.3
	SR+LSP - Electropolished	-542.6	-565.4	-489.8	-49.2	-460.31	-572.03	55.86	-59.1
172	SR - As received	-231.3	-175.3	-234.9	57.8	-175.30	-290.97	57.83	44.1
	SR - Scouring Pad	-	-	-	-	-	-	-	-
	SR - Electropolished	19.8	11.4	27.7	-12.3	36.68	10.82	12.93	-53.9
	SR+LSP - As received	33.1	64.5	7.6	44.1	66.28	-25.52	45.90	36.9
	SR+LSP - Scouring Pad	-247.1	-230.8	-207.5	-3.5	-207.20	-247.37	20.08	-85.0
	SR+LSP - Electropolished	-287.8	-207.0	-263.5	68.7	-205.91	-345.40	69.75	50.0

Appendix Six – Metallography: Images

Optical Microscopy

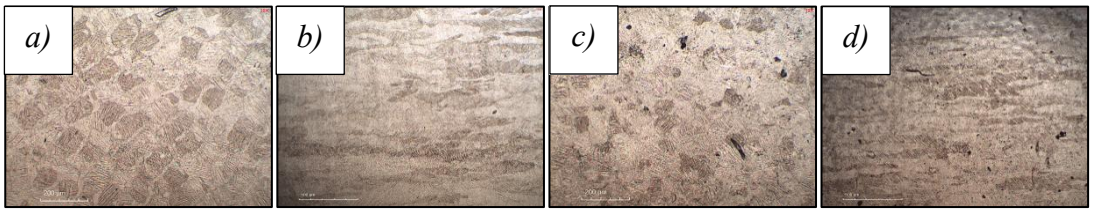

Optical Microscope images of etched 72 µm hatch samples in xy plane and yz planes: (a),(b) - microstructure of SR sample, (c),(d), microstructure of SR+LSP sample.

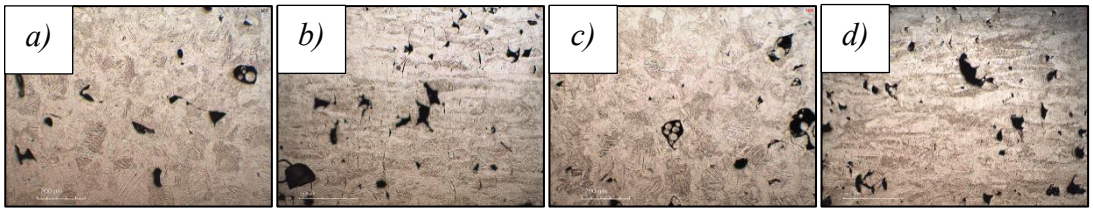

Optical Microscope images of etched 142 µm hatch samples in xy plane and yz planes: (a),(b) - microstructure of SR sample, (c),(d), microstructure of SR+LSP sample.

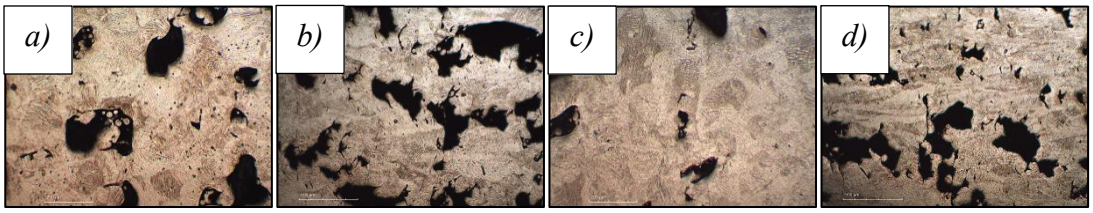

Optical Microscope images of etched 172 µm hatch samples in xy plane and yz planes: (a),(b) - microstructure of SR sample, (c),(d), microstructure of SR+LSP sample.

Grain Size measurement

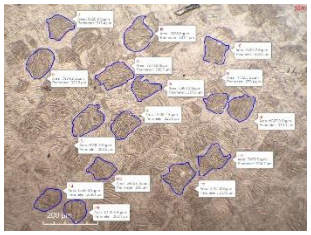

SR 72 µm Hatch

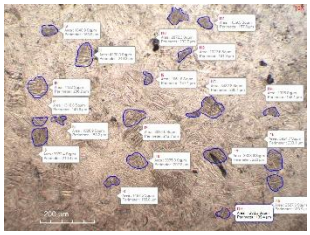

SR+LSP 72 µm Hatch

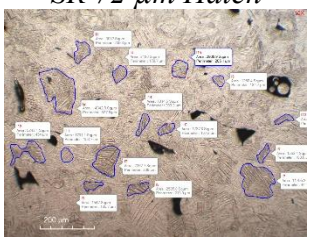

SR 142 µm Hatch

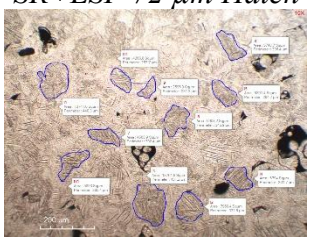

SR+LSP 142 µm Hatch

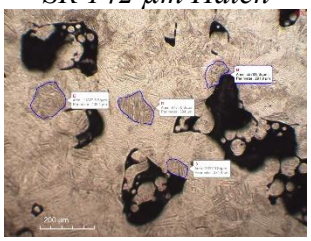

SR 172 µm Hatch

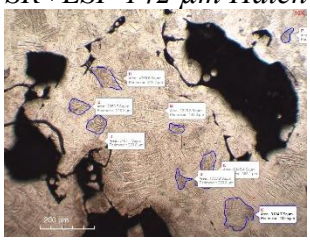

SR+LSP 172 µm Hatch

Note:

- *The images above depict measurement boundaries. Actual measurements were taken at various locations on the sample, with data recorded in a spreadsheet.*

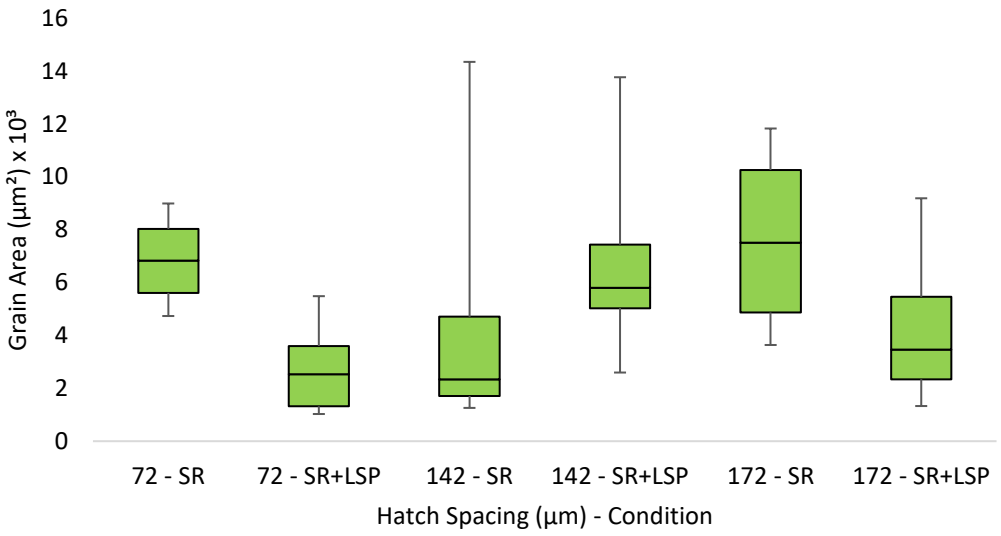

Variability in grain size for each sample.

Scanning Electron Microscopy

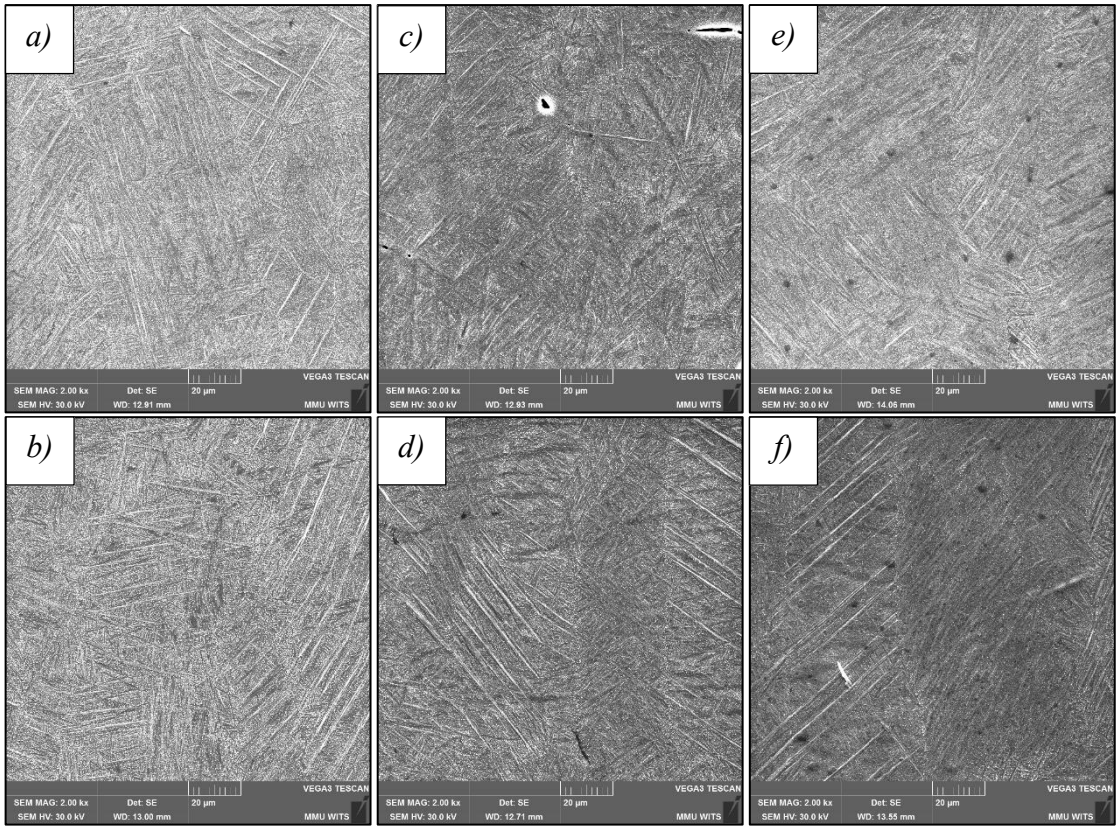

Scanning Electron Microscopy of etched, SR & SR+LSP samples in YZ plane respectively: (a),(b) 72 µm hatch spacing, (c),(d) 142 µm hatch spacing, (e),(f) 172 µm hatch spacing.

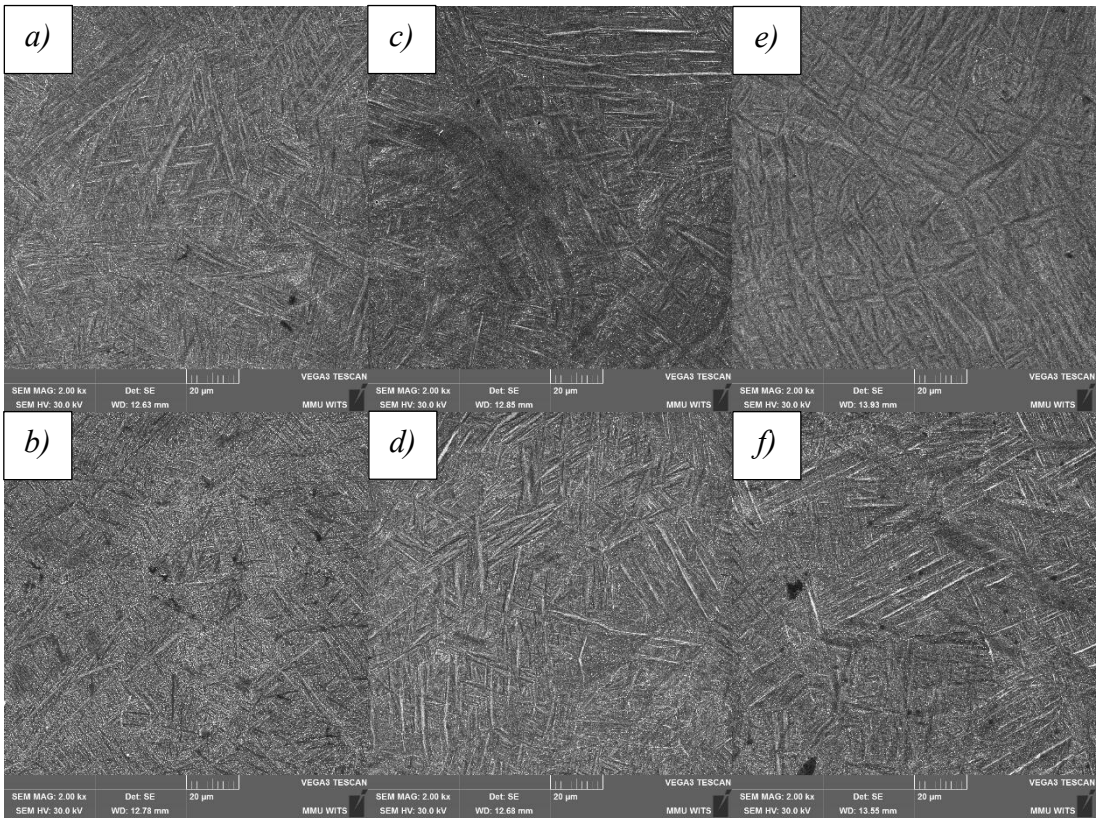

Scanning Electron Microscopy of etched, SR & SR+LSP samples in XY plane respectively: (a),(b) 72 µm hatch spacing, (c),(d) 142 µm hatch spacing, (e),(f) 172 µm hatch spacing.

Energy-Dispersive X-Ray Spectroscopy

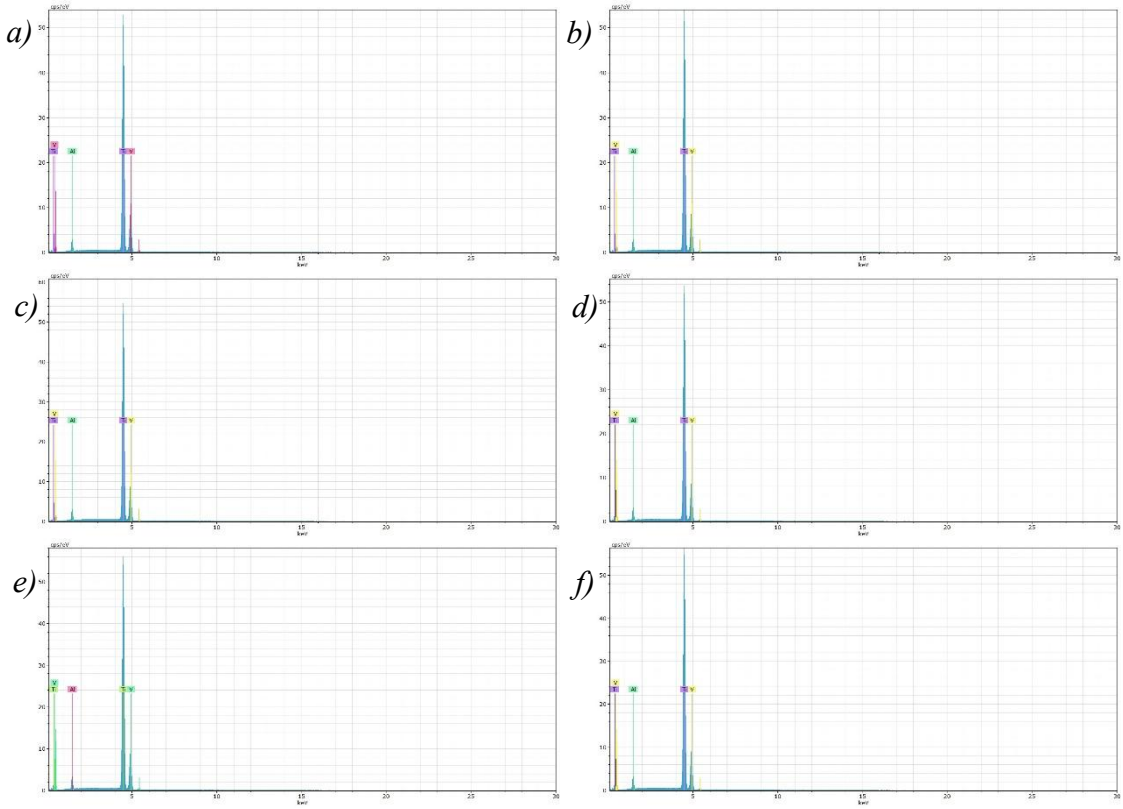

EDS spectrum of SR and SR+LSP samples respectively: (a),(b) 72 µm hatch sample, (c),(d) 142 µm hatch sample, (e),(f) 172 µm hatch sample.

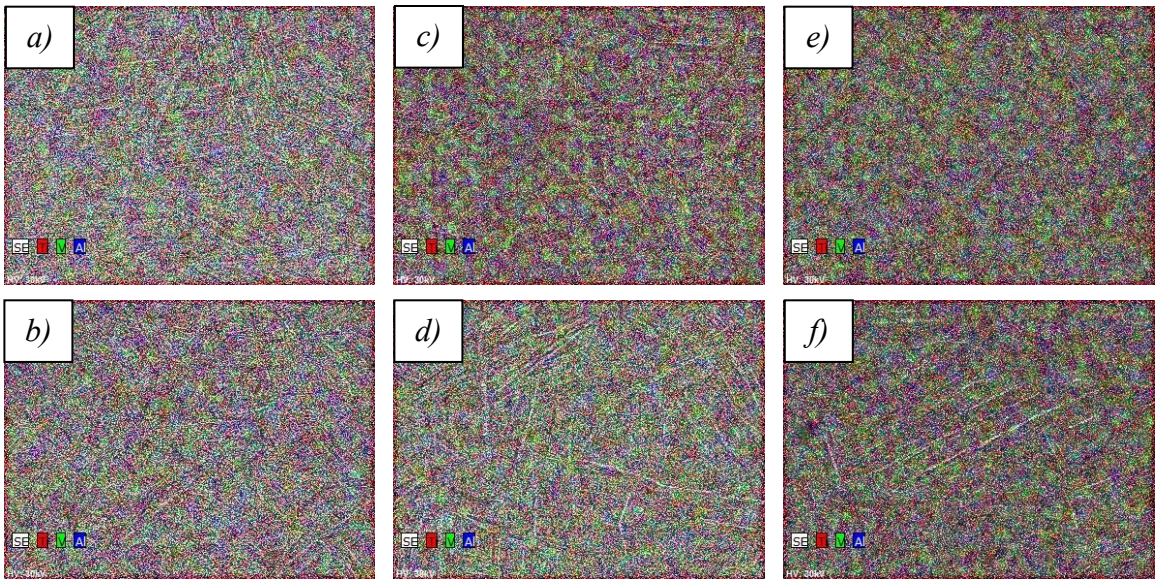

Illustrating the region of interests for corresponding spectrums of the above.

Appendix Seven – Microindentation: Data

Depth from surface (mm)	72-SR - HV value					Mean HV Value
	1	2	3	4	5	
0.2	427.65	374.51	406.08	407.44	390.02	401.14
0.4	423.99	347.52	408.78	400.61	395.73	395.326
0.8	424.43	397.05	349.47	394.76	406.9	394.522
1	411.12	316.9	403.22	395.29	397.46	384.798
1.2	409.76	373.71	402.43	400.56	400.44	397.38

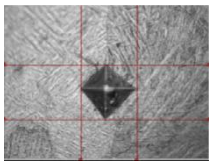
d1: 0.0364 mm
d2: 0.0358 mm

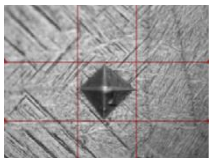
d1: 0.0384mm
d2: 0.0387mm

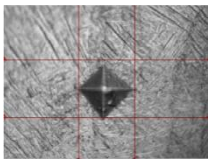
d1: 0.0364mm
d2: 0.0376mm

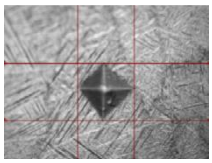
d1: 0.0366mm
d2: 0.0373mm

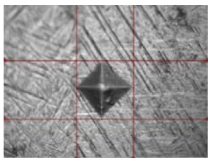
d1: 0.0372mm
d2: 0.0384mm

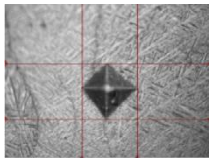
d1: 0.0361mm
d2: 0.0363mm

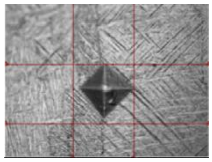
d1: 0.0399mm
d2: 0.0401mm

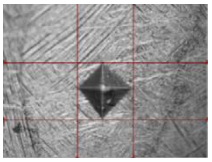
d1: 0.0365mm
d2: 0.0373mm

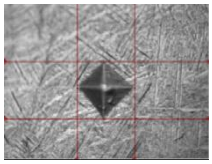
d1: 0.0375mm
d2: 0.0370mm

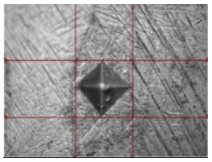
d1: 0.0376mm
d2: 0.0374mm

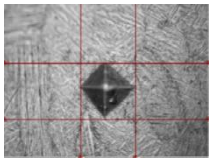
d1: 0.0357mm
d2: 0.0368mm

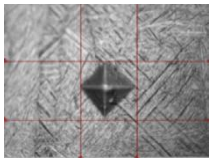
d1: 0.0365mm
d2: 0.0383mm

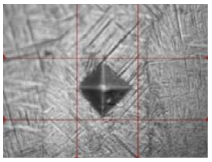
d1: 0.0399mm
d2: 0.0399mm

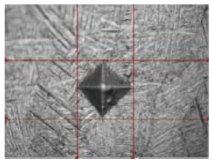
d1: 0.0367mm
d2: 0.0384mm

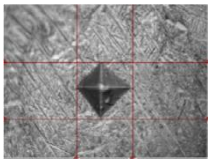
d1: 0.0367mm
d2: 0.0372mm

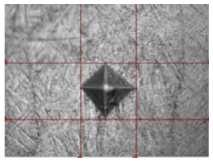
d1: 0.0362mm
d2: 0.0374mm

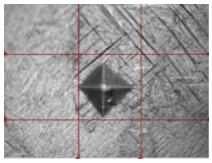
d1: 0.0409mm
d2: 0.0429mm

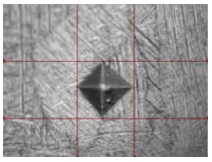
d1: 0.0370mm
d2: 0.0373mm

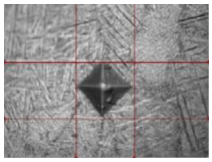
d1: 0.0379mm
d2: 0.0371mm

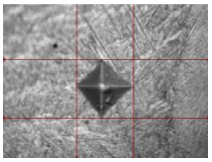
d1: 0.0368mm
d2: 0.0380mm

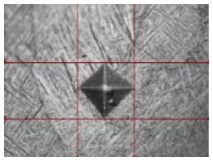
d1: 0.0370mm
d2: 0.0367mm

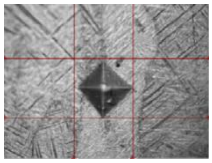
d1: 0.0384mm
d2: 0.0388mm

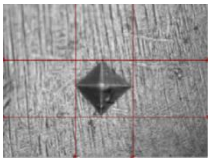
d1: 0.0374mm
d2: 0.0370mm

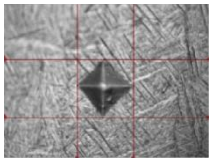
d1: 0.0365mm
d2: 0.0380mm

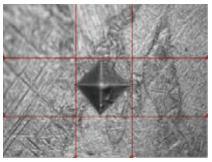
d1: 0.0367mm
d2: 0.0379mm

Depth from surface (mm)	72-SR+LSP - HV value					Mean HV Value
	1	2	3	4	5	
0.2	416.93	405.42	431.01	396.74	408.66	411.752
0.4	416.98	444.03	412.82	441.04	427.91	428.556
0.8	431.54	421.84	380.68	385.43	425.53	409.004
1	398.07	406.34	406.8	379.98	379.95	394.228
1.2	436.59	422.99	418.09	401.92	401.59	416.236

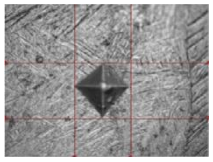
d1: 0.0366mm
d2: 0.0364mm

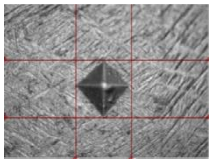
d1: 0.0364mm
d2: 0.0376mm

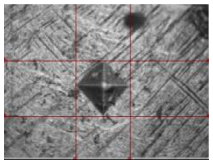
d1: 0.0354mm
d2: 0.0364mm

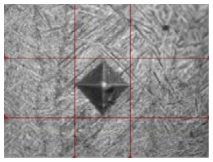
d1: 0.0362mm
d2: 0.0387mm

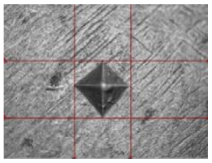
d1: 0.0367mm
d2: 0.0370mm

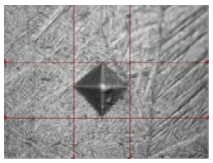
d1: 0.0367mm
d2: 0.0363mm

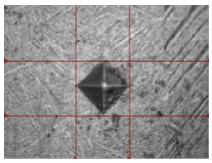
d1: 0.0351mm
d2: 0.0357mm

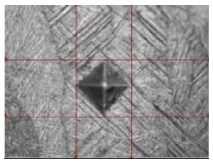
d1: 0.0361mm
d2: 0.0373mm

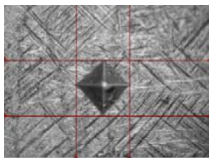
d1: 0.0347mm
d2: 0.0363mm

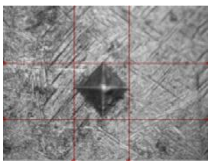
d1: 0.0358mm
d2: 0.0363mm

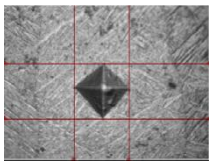
d1: 0.0357mm
d2: 0.0361mm

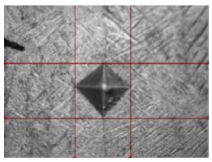
d1: 0.0365mm
d2: 0.0361mm

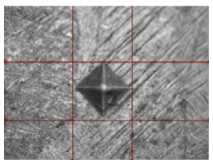
d1: 0.0386mm
d2: 0.0378mm

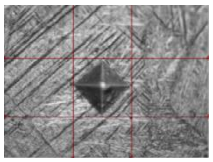
d1: 0.0379mm
d2: 0.0381mm

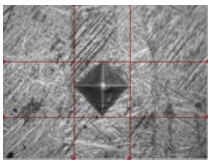
d1: 0.0364mm
d2: 0.0359mm

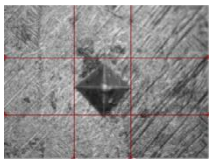
d1: 0.0372mm
d2: 0.0376mm

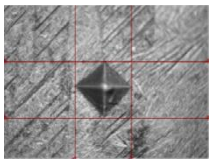
d1: 0.0369mm
d2: 0.0371mm

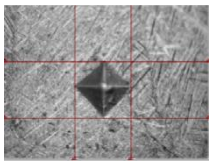
d1: 0.0368mm
d2: 0.0371mm

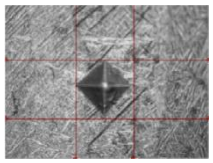
d1: 0.0381mm
d2: 0.0384mm

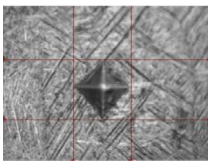
d1: 0.0375mm
d2: 0.0391mm

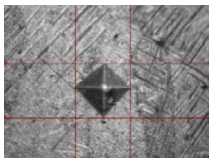
d1: 0.0358mm
d2: 0.0356mm

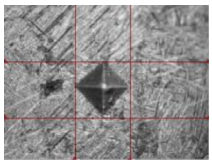
d1: 0.0360mm
d2: 0.0365mm

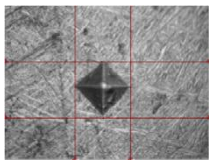
d1: 0.0363mm
d2: 0.0366mm

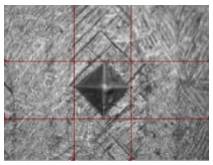
d1: 0.0369mm
d2: 0.0375mm

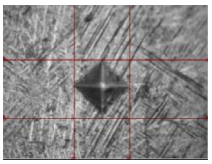
d1: 0.0362mm
d2: 0.0382mm

Depth from surface (mm)	142-SR - HV value					Mean HV Value
	1	2	3	4	5	
0.2	446.01	431.66	379.84	424.34	383.32	413.034
0.4	398.48	435.67	411.00	411.06	435.68	418.378
0.8	374.81	433.13	431.19	416.92	407.59	412.728
1	423.11	435.56	404.35	434.77	395.01	418.56
1.2	415.56	395.06	409.25	401.81	392.83	402.902

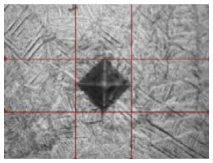
d1: 0.0363mm
d2: 0.0343mm

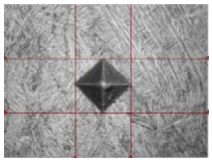
d1: 0.0363mm
d2: 0.0355mm

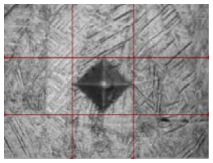
d1: 0.0395mm
d2: 0.0370mm

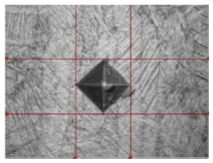
d1: 0.0362mm
d2: 0.0362mm

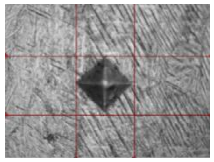
d1: 0.0379mm
d2: 0.0382mm

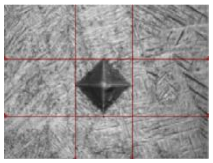
d1: 0.0374mm
d2: 0.0374mm

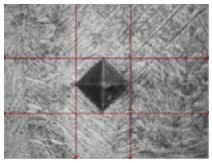
d1: 0.0356mm
d2: 0.0359mm

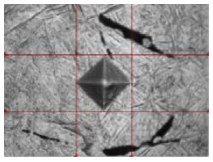
d1: 0.0363mm
d2: 0.0373mm

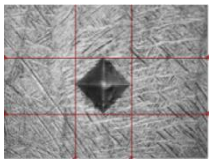
d1: 0.0368mm
d2: 0.0367mm

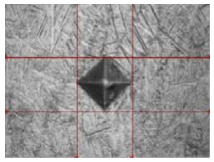
d1: 0.0360mm
d2: 0.0355mm

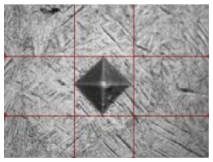
d1: 0.0384mm
d2: 0.0386mm

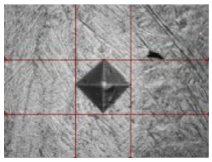
d1: 0.0361mm
d2: 0.0356mm

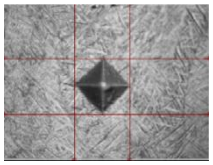
d1: 0.0359mm
d2: 0.0359mm

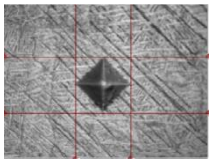
d1: 0.0361mm
d2: 0.0370mm

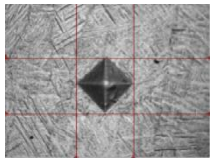
d1: 0.0375mm
d2: 0.0364mm

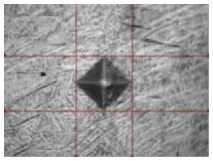
d1: 0.0365mm
d2: 0.0360mm

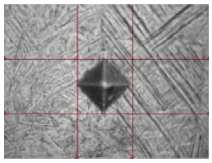
d1: 0.0359mm
d2: 0.0356mm

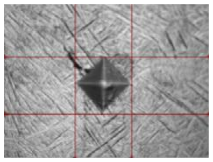
d1: 0.0368mm
d2: 0.0374mm

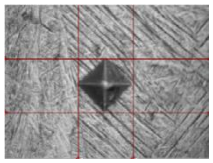
d1: 0.0358mm
d2: 0.0358mm

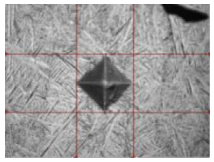
d1: 0.0371mm
d2: 0.0380mm

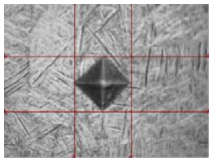
d1: 0.0371mm
d2: 0.0361mm

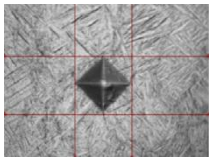
d1: 0.0372mm
d2: 0.0379mm

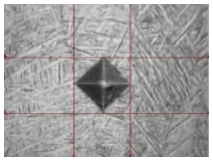
d1: 0.0369mm
d2: 0.0369mm

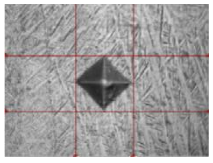
d1: 0.0377mm
d2: 0.0367mm

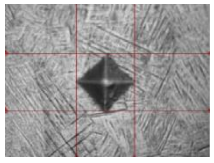
d1: 0.0379mm
d2: 0.0374mm

Depth from surface (mm)	142-SR+LSP - HV value					Mean HV Value
	1	2	3	4	5	
0.2	359.13	414.63	363.74	381.65	413.32	386.494
0.4	402.39	384.26	356.92	389.6	343.43	375.32
0.8	395	381.02	394.02	370.71	323.67	372.884
1	382.09	371.6	371.69	358.18	394	375.512
1.2	400.96	373.15	317.1	393.78	383.08	373.614

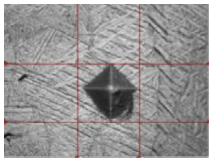
d1: 0.0405mm
d2: 0.0382mm

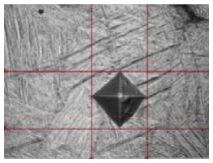
d1: 0.0361mm
d2: 0.0372mm

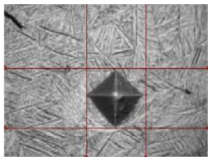
d1: 0.0387mm
d2: 0.0395mm

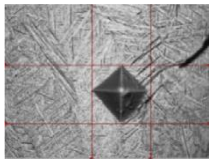
d1: 0.0384mm
d2: 0.0380mm

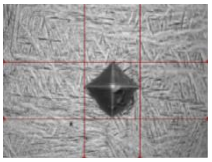
d1: 0.0362mm
d2: 0.0372mm

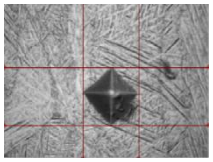
d1: 0.0364mm
d2: 0.0379mm

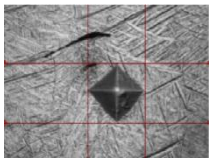
d1: 0.0373mm
d2: 0.0388mm

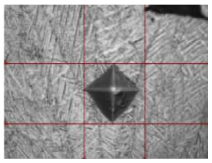
d1: 0.0397mm
d2: 0.0393mm

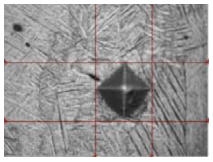
d1: 0.0371mm
d2: 0.0385mm

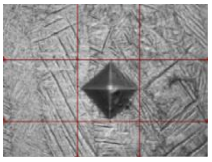
d1: 0.0405mm
d2: 0.0400mm

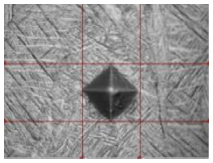
d1: 0.0375mm
d2: 0.0376mm

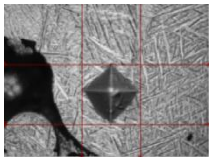
d1: 0.0380mm
d2: 0.0384mm

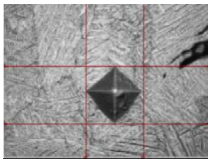
d1: 0.0375mm
d2: 0.0377mm

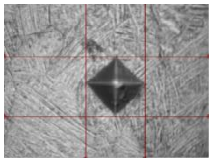
d1: 0.0385mm
d2: 0.0389mm

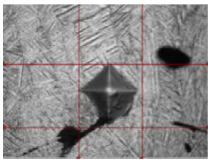
d1: 0.0416mm
d2: 0.0413mm

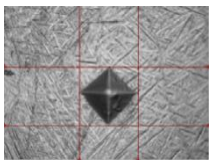
d1: 0.0382mm
d2: 0.0381mm

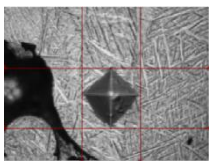
d1: 0.0381mm
d2: 0.0393mm

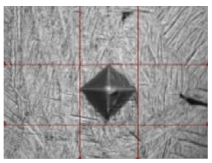
d1: 0.0379mm
d2: 0.0394mm

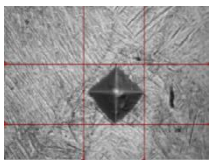
d1: 0.0396mm
d2: 0.0393mm

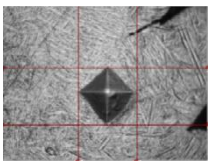
d1: 0.0381mm
d2: 0.0370mm

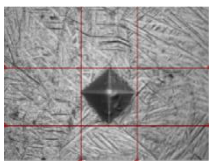
d1: 0.0367mm
d2: 0.0378mm

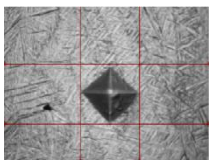
d1: 0.0382mm
d2: 0.0391mm

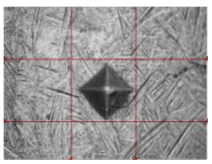
d1: 0.0426mm
d2: 0.0412mm

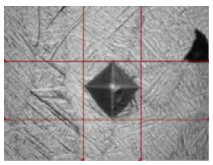
d1: 0.0374mm
d2: 0.0378mm

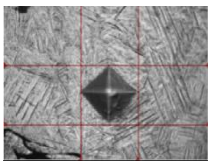
d1: 0.0376mm
d2: 0.0386mm

Depth from surface (mm)	172-SR - HV value					Mean HV Value
	1	2	3	4	5	
0.2	400.7	390.39	395.01	407.58	411.74	401.084
0.4	389.45	404.12	387.39	404.09	390.13	395.036
0.8	406.35	392.91	396.13	375.9	418.25	397.908
1	404.12	395.97	404.15	386.39	408.47	399.82
1.2	405.14	401.81	334.73	402.84	377.89	384.482

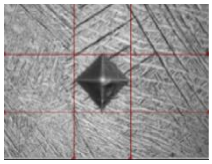
d1: 0.0367mm
d2: 0.0378mm

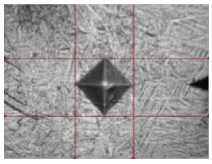
d1: 0.0380mm
d2: 0.0375mm

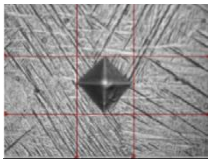
d1: 0.0373mm
d2: 0.0378mm

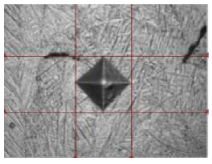
d1: 0.0368mm
d2: 0.0370mm

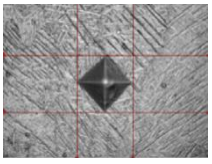
d1: 0.0362mm
d2: 0.0373mm

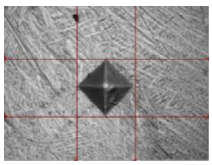
d1: 0.0381mm
d2: 0.0375mm

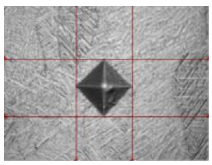
d1: 0.0375mm
d2: 0.0375mm

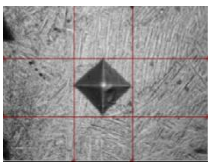
d1: 0.0380mm
d2: 0.0378mm

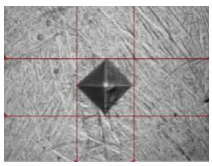
d1: 0.0372mm
d2: 0.0371mm

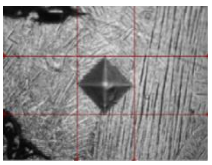
d1: 0.0374mm
d2: 0.0381mm

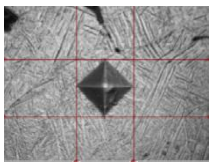
d1: 0.0370mm
d2: 0.0371mm

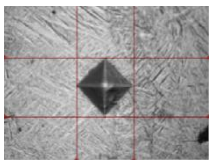
d1: 0.0372mm
d2: 0.0381mm

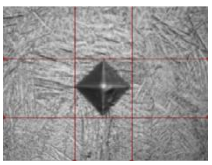
d1: 0.0370mm
d2: 0.0379mm

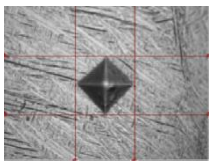
d1: 0.0388mm
d2: 0.0381mm

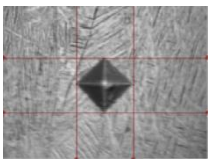
d1: 0.0371mm
d2: 0.0359mm

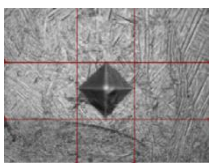
d1: 0.0373mm
d2: 0.0369mm

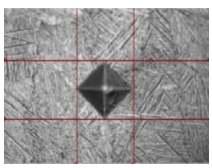
d1: 0.0368mm
d2: 0.0381mm

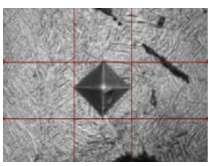
d1: 0.0374mm
d2: 0.0368mm

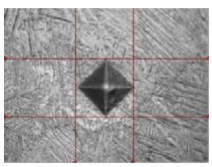
d1: 0.0379mm
d2: 0.0380mm

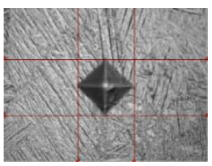
d1: 0.0370mm
d2: 0.0369mm

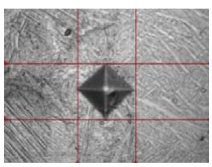
d1: 0.0377mm
d2: 0.0364mm

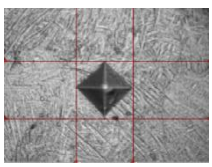
d1: 0.0371mm
d2: 0.0374mm

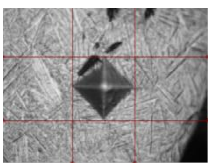
d1: 0.0403mm
d2: 0.0413mm

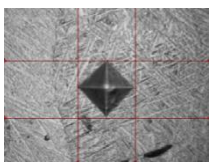
d1: 0.0372mm
d2: 0.0372mm

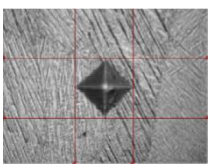
d1: 0.0379mm
d2: 0.0388mm

Depth from surface (mm)	172-SR+LSP - HV value					Mean HV Value
	1	2	3	4	5	
0.2	411.12	392.77	400.71	404.09	262.88	374.314
0.4	406.67	386.33	400.74	401.86	396.09	398.338
0.8	402.88	392.61	406.21	367.51	399.47	393.736
1	382.96	427.99	395.09	375.91	401.86	396.762
1.2	385.31	402.97	398.45	365.84	397.2	389.954

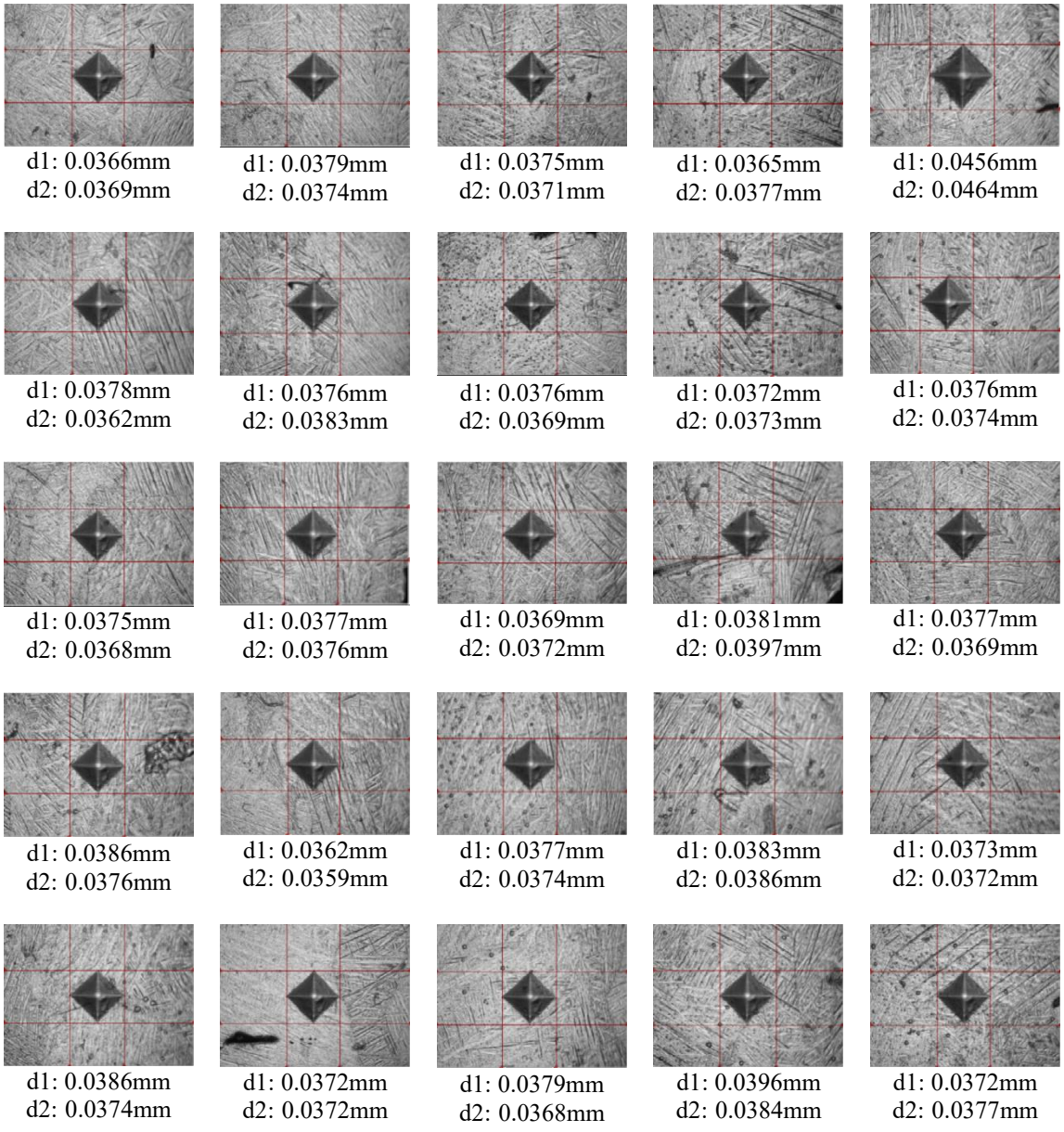

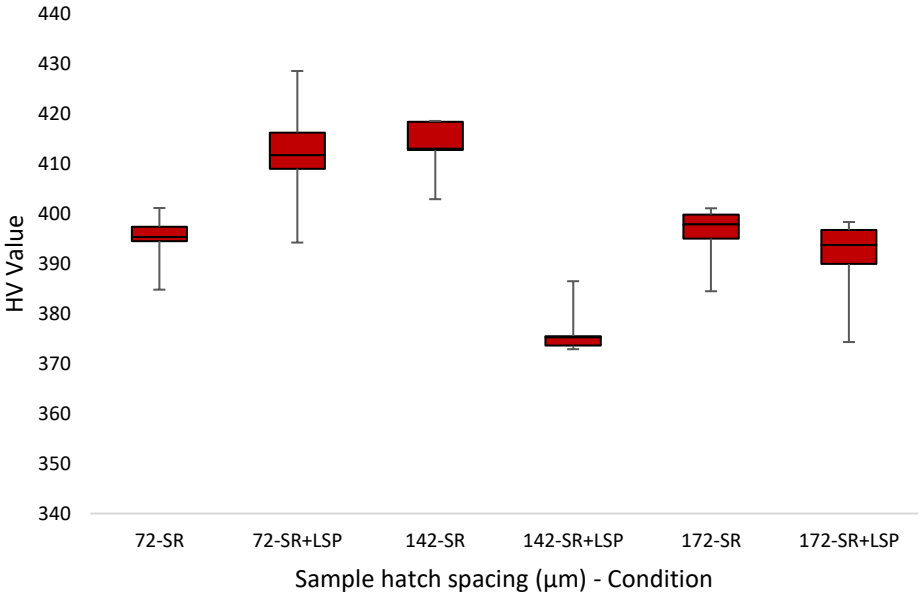

Explanatory box and whisker plot for HV values per sample.

Appendix Eight – Regression Analysis

Part Feature as a Function of Hatch Variation – SR Samples

Regression Statistics - % Porosity	
Multiple R	0.756597526
R Square	0.572439817
Adjusted R Square	0.144879633
Standard Error	12.06632622
Observations	3

ANOVA

	df	***SS***	***MS***	***F***	***Significance F***
Regression	1	194.9318053	194.9318053	1.338852024	0.453720505
Residual	1	145.5962286	145.5962286		
Total	2	340.5280338			

	Coefficients	***Standard Error***	***t Stat***	***P-value***
Intercept	-3.615981021	13.40371747	-0.269774488	0.83224965
Hatch, µm	0.120089919	0.103786355	1.157087734	0.453720505

Regression Statistics - S_a (µm)	
Multiple R	0.983601147
R Square	0.967471217
Adjusted R Square	0.934942433
Standard Error	1.88777788
Observations	3

ANOVA

	df	***SS***	***MS***	***F***	***Significance F***
Regression	1	105.9917393	105.9917393	29.74200439	0.115450852
Residual	1	3.563705323	3.563705323		
Total	2	109.5554447			

	Coefficients	***Standard Error***	***t Stat***	***P-value***
Intercept	-4.809662025	3.519938334	-1.366405195	0.402204799
Hatch, µm	0.141862658	0.026012553	5.453623051	0.115450852

Regression Statistics - RS (MPa)	
Multiple R	0.50473332
R Square	0.254755725
Adjusted R Square	-0.490488551
Standard Error	57.63809099
Observations	3

ANOVA

	df	*SS*	*MS*	*F*	*Significance F*
Regression	1	1135.649934	1135.649934	0.341841908	0.663181654
Residual	1	3322.149533	3322.149533		
Total	2	4457.799467			

	Coefficients	*Standard Error*	*t Stat*	*P-value*
Intercept	101.0444908	64.02650426	1.578166603	0.359558385
Hatch, µm	-0.289859433	0.495763771	-0.584672479	0.663181654

Regression Statistics - HV0.3	
Multiple R	0.329752514
R Square	0.10873672
Adjusted R Square	-0.78252656
Standard Error	9.189885241
Observations	3

ANOVA

	df	*SS*	*MS*	*F*	*Significance F*
Regression	1	10.30363325	10.30363325	0.122002917	0.786069391
Residual	1	84.45399075	84.45399075		
Total	2	94.757624			

	Coefficients	*Standard Error*	*t Stat*	*P-value*
Intercept	402.0397388	10.20846139	39.38299058	0.016161368
Hatch, µm	0.027609618	0.079045161	0.34928916	0.786069391

Regression Statistics - Grain Size (µm)	
Multiple R	0.122434638
R Square	0.014990241
Adjusted R Square	-0.970019519
Standard Error	2507.984722
Observations	3

ANOVA

	df	*SS*	*MS*	*F*	*Significance F*
Regression	1	95723.34035	95723.34035	0.015218368	0.921859629
Residual	1	6289987.365	6289987.365		
Total	2	6385710.705			

	Coefficients	*Standard Error*	*t Stat*	*P-value*
Intercept	6518.548994	2785.961362	2.339784422	0.257126326
Hatch, µm	-2.661179203	21.57198376	-0.123362748	0.921859629

Absorbed Energy as a function of part feature – SR Samples

Regression Statistics	
Multiple R	0.824946483
R Square	0.680536701
Adjusted R Square	0.361073401
Standard Error	3.302846309
Observations	3

ANOVA

	df	*SS*	*MS*	*F*	*Significance F*
Regression	1	23.23845811	23.23845811	2.130250022	0.382410378
Residual	1	10.90879374	10.90879374		
Total	2	34.14725185			

	Coefficients	*Standard Error*	*t Stat*	*P-value*
Intercept	11.02225386	2.57089803	4.287316623	0.14588093
% Porosity	-0.261232507	0.17898306	-1.459537605	0.382410378

Regression Statistics	
Multiple R	0.983395895
R Square	0.967067486
Adjusted R Square	0.934134973
Standard Error	1.0604503
Observations	3

ANOVA

	df	*SS*	*MS*	*F*	*Significance F*
Regression	1	33.02269701	33.02269701	29.36512818	0.11617311
Residual	1	1.12455484	1.12455484		
Total	2	34.14725185			

	Coefficients	*Standard Error*	*t Stat*	*P-value*
Intercept	15.88623348	1.493292643	10.63839265	0.059666403
Sa Value (µm)	-0.549021418	0.101314904	-5.418960065	0.11617311

Regression Statistics	
Multiple R	0.598066731
R Square	0.357683815
Adjusted R Square	-0.28463237
Standard Error	4.683303592
Observations	3

ANOVA

	df	*SS*	*MS*	*F*	*Significance F*
Regression	1	12.21391931	12.21391931	0.556865642	0.591871527
Residual	1	21.93333254	21.93333254		
Total	2	34.14725185			

	Coefficients	*Standard Error*	*t Stat*	*P-value*
Intercept	4.890501505	5.547907503	0.881503793	0.540041124
σ1’ (MPa)	0.052344042	0.070144245	0.746234308	0.591871527

Regression Statistics	
Multiple R	0.222158493
R Square	0.049354396
Adjusted R Square	-0.901291208
Standard Error	5.697537614
Observations	3

ANOVA

	df	*SS*	*MS*	*F*	*Significance F*
Regression	1	1.685316987	1.685316987	0.051916714	0.857379518
Residual	1	32.46193486	32.46193486		
Total	2	34.14725185			

	Coefficients	*Standard Error*	*t Stat*	*P-value*
Intercept	62.52883596	237.1205248	0.263700648	0.83585953
HV0.3 - 0.2mm	-0.133362497	0.58530215	-0.227852395	0.857379518

Regression Statistics	
Multiple R	0.010728717
R Square	0.000115105
Adjusted R Square	-0.999769789
Standard Error	5.843228673
Observations	3

ANOVA

	df	*SS*	*MS*	*F*	*Significance F*
Regression	1	0.003930532	0.003930532	0.000115119	0.993169756
Residual	1	34.14332132	34.14332132		
Total	2	34.14725185			

	Coefficients	*Standard Error*	*t Stat*	*P-value*
Intercept	8.351117021	14.78410196	0.564871444	0.67265706
Grain area µm²	2.48097E-05	0.002312322	0.010729334	0.993169756

Part Feature as a Function of Hatch Variation – SR+LSP Samples

Regression Statistics - % Porosity	
Multiple R	0.859951239
R Square	0.739516133
Adjusted R Square	0.479032267
Standard Error	6.471599951
Observations	3

ANOVA

	df	***SS***	***MS***	***F***	***Significance F***
Regression	1	118.9022708	118.9022708	2.83900935	0.340987684
Residual	1	41.88160592	41.88160592		
Total	2	160.7838767			

	Coefficients	***Standard Error***	***t Stat***	***P-value***
Intercept	-12.24123434	12.0669031	-1.014447057	0.495434417
Hatch, µm	0.150254386	0.089175129	1.684936008	0.340987684

Regression Statistics - S_a (µm)	
Multiple R	0.895407947
R Square	0.801755391
Adjusted R Square	0.603510781
Standard Error	1.89167611
Observations	3

ANOVA

	df	***SS***	***MS***	***F***	***Significance F***
Regression	1	14.47218349	14.47218349	4.044273352	0.293768029
Residual	1	3.578438506	3.578438506		
Total	2	18.050622			

	Coefficients	***Standard Error***	***t Stat***	***P-value***
Intercept	0.365260759	3.527206949	0.103555239	0.934308837
Hatch, µm	0.052420253	0.026066268	2.011037879	0.293768029

Regression Statistics - RS (MPa)	
Multiple R	0.696052154
R Square	0.484488601
Adjusted R Square	-0.031022798
Standard Error	196.34672
Observations	3

ANOVA

	df	*SS*	*MS*	*F*	*Significance F*
Regression	1	36232.02368	36232.02368	0.939821314	0.509876448
Residual	1	38552.03444	38552.03444		
Total	2	74784.05812			

	Coefficients	*Standard Error*	*t Stat*	*P-value*
Intercept	-755.2738608	366.1068147	-2.062987714	0.287344879
Hatch, µm	2.622879747	2.70555106	0.969443817	0.509876448

Regression Statistics - HV0.3	
Multiple R	0.999609471
R Square	0.999219095
Adjusted R Square	0.998438189
Standard Error	0.75466564
Observations	3

ANOVA

	df	*SS*	*MS*	*F*	*Significance F*
Regression	1	728.7380824	728.7380824	1279.564881	0.017792455
Residual	1	0.569520228	0.569520228		
Total	2	729.3076027			

	Coefficients	*Standard Error*	*t Stat*	*P-value*
Intercept	438.7145646	1.407144635	311.7764541	0.002041904
Hatch, µm	-0.371978481	0.010398882	-35.77100615	0.017792455

Regression Statistics - Grain Size (µm	
Multiple R	0.594615011
R Square	0.353567011
Adjusted R Square	-0.292865978
Standard Error	2367.352067
Observations	3

ANOVA

	df	*SS*	*MS*	*F*	*Significance F*
Regression	1	3065306.642	3065306.642	0.546950755	0.594608978
Residual	1	5604355.811	5604355.811		
Total	2	8669662.453			

	Coefficients	*Standard Error*	*t Stat*	*P-value*
Intercept	1393.281303	4414.149239	0.315639827	0.805358095
Hatch, µm	24.12509582	32.62082451	0.739561191	0.594608978

Absorbed Energy as a function of part feature – SR+LSP Samples

Regression Statistics	
Multiple R	0.984599506
R Square	0.969436187
Adjusted R Square	0.938872373
Standard Error	0.910042933
Observations	3

ANOVA

	df	*SS*	*MS*	*F*	*Significance F*
Regression	1	26.26851075	26.26851075	31.71843044	0.111871998
Residual	1	0.828178141	0.828178141		
Total	2	27.09668889			

	Coefficients	*Standard Error*	*t Stat*	*P-value*
Intercept	12.7397174	0.731500896	17.41586029	0.036513931
% Porosity	-0.404200157	0.071769618	-5.631911792	0.111871998

Regression Statistics	
Multiple R	0.994847654
R Square	0.989721855
Adjusted R Square	0.97944371
Standard Error	0.52773449
Observations	3

ANOVA

	df	*SS*	*MS*	*F*	*Significance F*
Regression	1	26.8181852	26.8181852	96.2938231	0.064652343
Residual	1	0.278503691	0.278503691		
Total	2	27.09668889			

	Coefficients	*Standard Error*	*t Stat*	*P-value*
Intercept	18.53972291	0.934240183	19.84470722	0.032052967
Sa Value (µm)	-1.218901487	0.12421367	-9.812941613	0.064652343

Regression Statistics	
Multiple R	0.9043176
R Square	0.817790321
Adjusted R Square	0.635580642
Standard Error	2.221998873
Observations	3

ANOVA

	df	*SS*	*MS*	*F*	*Significance F*
Regression	1	22.1594099	22.1594099	4.488182649	0.280760762
Residual	1	4.937278991	4.937278991		
Total	2	27.09668889			

	Coefficients	*Standard Error*	*t Stat*	*P-value*
Intercept	2.68150103	3.629035843	0.738901776	0.594880434
σ1' (Mpa)	-0.017213714	0.008125298	-2.118533136	0.280760762

Regression Statistics	
Multiple R	0.945410044
R Square	0.893800152
Adjusted R Square	0.787600304
Standard Error	1.696367955
Observations	3

ANOVA

	df	*SS*	*MS*	*F*	*Significance F*
Regression	1	24.21902465	24.21902465	8.416209345	0.211323232
Residual	1	2.877664238	2.877664238		
Total	2	27.09668889			

	Coefficients	*Standard Error*	*t Stat*	*P-value*
Intercept	-61.35237456	24.57105415	-2.496937013	0.242507127
HV0.3 - 0.2mm	0.182231292	0.062815192	2.901070379	0.211323232

Regression Statistics	
Multiple R	0.273367983
R Square	0.074730054
Adjusted R Square	-0.850539892
Standard Error	5.007170045
Observations	3

ANOVA

	df	*SS*	*MS*	*F*	*Significance F*
Regression	1	2.02493703	2.02493703	0.080765678	0.823724664
Residual	1	25.07175186	25.07175186		
Total	2	27.09668889			

	Coefficients	*Standard Error*	*t Stat*	*P-value*
Intercept	12.04685492	8.176177014	1.47340926	0.379607356
Grain area µm²	-0.000483287	0.001700557	-0.284193029	0.823724664

Annexes

Annex 1 – Charpy Impact Tester - Modifications Report

Pendulum Charpy Impact Tester Modifications Report

University of the Witwatersrand

School of Mechanical, Industrial and Aeronautical Engineering

This report is to showcase the modifications brought to the pendulum type Charpy impact tester in the MIA materials lab at the University of the Witwatersrand. The report details the adjustments made to parts of the equipment, aligned with standards ASTM E2248 and E23 to enable the testing of Miniaturized Charpy V-Notch samples.

Prepared By: Abhay Chundunsing

Date January 2024

The Charpy impact test is a standardized high-strain-rate test that determines the amount of energy a material absorbs during fracture. This test is critical for assessing material toughness and its ability to withstand sudden impacts. Traditionally governed by ASTM E23, the test involves a pendulum striking a notched sample supported on anvils, creating a well-defined stress field under impact.

Miniaturized Charpy V-Notch (MCVN) testing, governed by ASTM E2248, represents a more specialized application of Charpy impact testing. Unlike sub-sized specimens tested under ASTM E23, MCVN tests are designed to replicate the stress fields of standard Charpy testing on smaller samples using modified equipment geometry. This uncommon practice is primarily necessitated when standard-sized samples are unavailable, such as in materials research, limited sample extraction from components, or unique manufacturing scenarios. Consequently, the equipment is not readily available, and standard Charpy testers require significant modifications to meet ASTM E2248 specifications.

The existing Charpy impact testing machine, initially designed for ASTM E23 tests, cannot be directly utilized for MCVN testing without these modifications. This is due to geometry, energy requirements, and stress-field replication differences. To address this challenge, this report outlines a series of critical modifications to adapt the equipment, ensuring it can perform MCVN tests in accordance with ASTM E2248. The focus is on replicating the stress conditions of standard Charpy tests using miniaturized samples, ensuring accuracy and reliability.

This report details the design of the necessary modifications, focusing on three key components: the Charpy impact head, the anvils and supports, and a centering jig. Together, these changes enable the equipment to provide consistent and reliable results for MCVN testing. The following sections break down these modifications and their respective specification drawings, which are included in the document.

Charpy Impact Head

- Modified to reduce its scale and align the striking energy with MCVN requirements.
- Adapted to maintain the proper velocity and impact dynamics to replicate ASTM E2248 stress fields.

Anvils and Supports

- Redesigned to ensure precise sample positioning and alignment for miniaturized specimens.
- Adjusted geometry to maintain consistent contact and force distribution during testing.

Centering Jig

- Developed to guarantee uniform sample placement and notch alignment before each test.
- Includes adjustable features to accommodate various miniaturized sample sizes.

Each modification has been carefully evaluated to ensure compatibility with existing machine components while adhering to ASTM E2248 requirements. The subsequent sections of this report provide detailed descriptions and technical drawings to facilitate the implementation of these changes.

PART A
SCALE 1:1

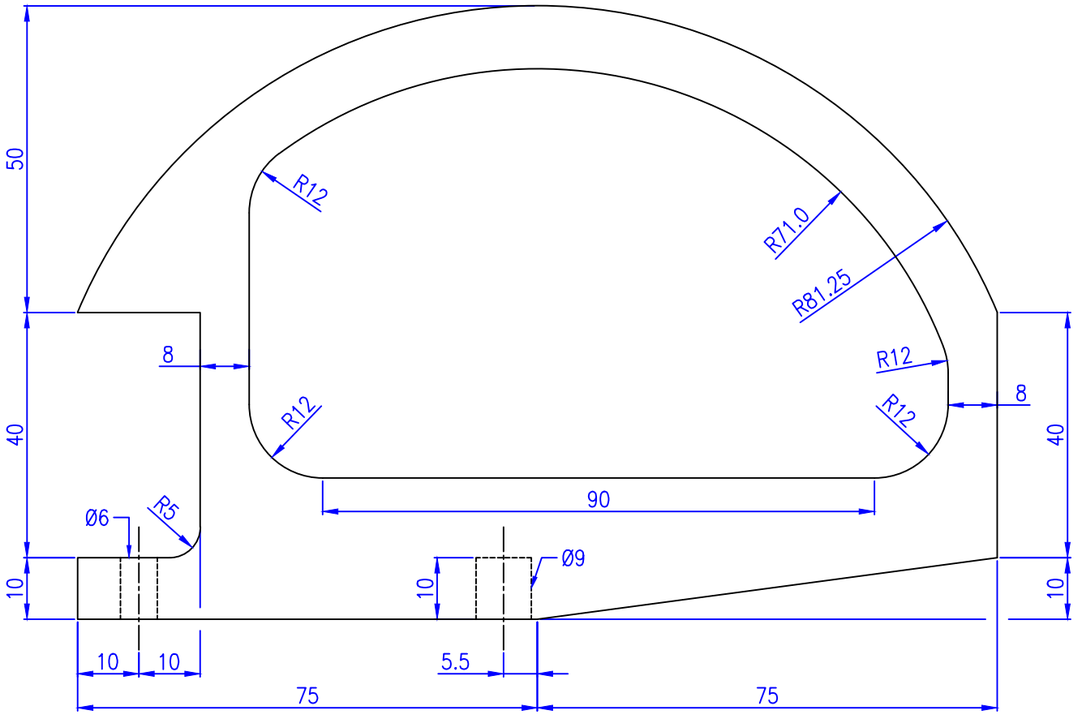

PART B
SCALE 1:1

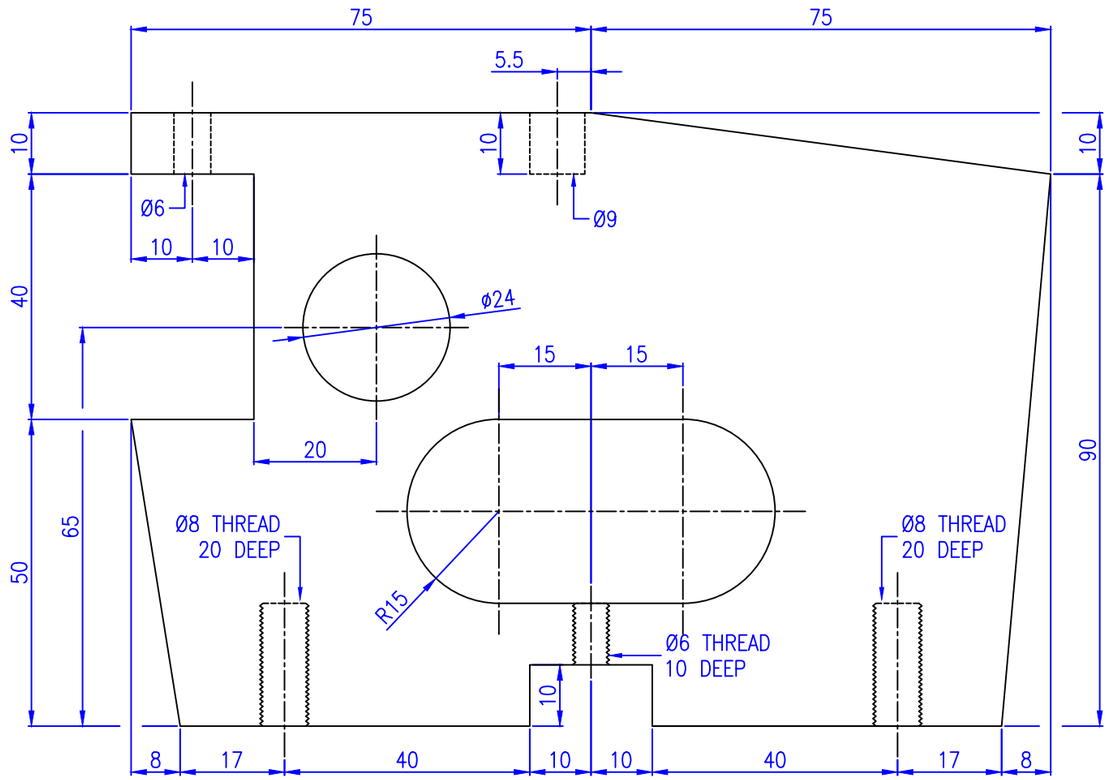

PART C – ELEVATION
SCALE 1:1

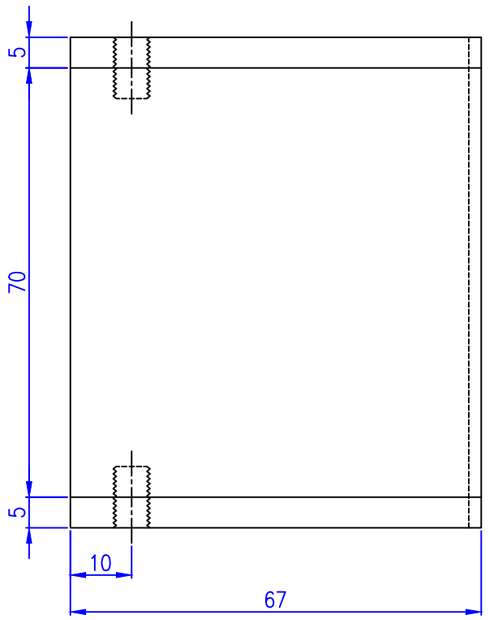

PART D
SCALE 1:1

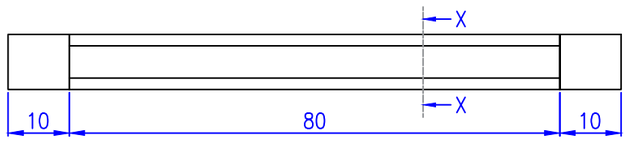

SECTION X–X
SCALE 1:1

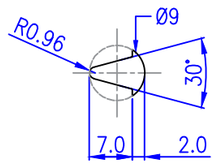

PART C – TOP VIEW
SCALE 1:1

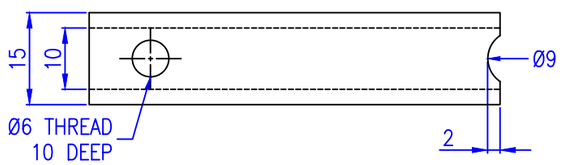

NOMENCLATURE			
PART	MATERIAL	DIMENSIONS	QUANTITY
A & B	MILD STEEL	PLATE 150x100 15 THK	2
C	MILD STEEL	PLATE 70x80 15 THK	1
D	SILVER STEEL	ROD Ø9 100 LONG	1

All Dimensions are in mm unless specified otherwise.

DATE: 10/10/2023	DOCUMENT: CHARPY IMPACT TESTER – MODIFICATIONS REPORT
SCALE/PAPER SIZE: 1:1 / A3	DRAWING: NEW PENDULUM HEAD – PARTS DETAILING
DRAWN BY (STUDENT NUMBER): CHUNDUNSING ABHAY NOOKANT NETRAPAL (2634879)	SHEET: 1 OF 1

ASSEMBLED IMPACT HEAD
SCALE 1:1

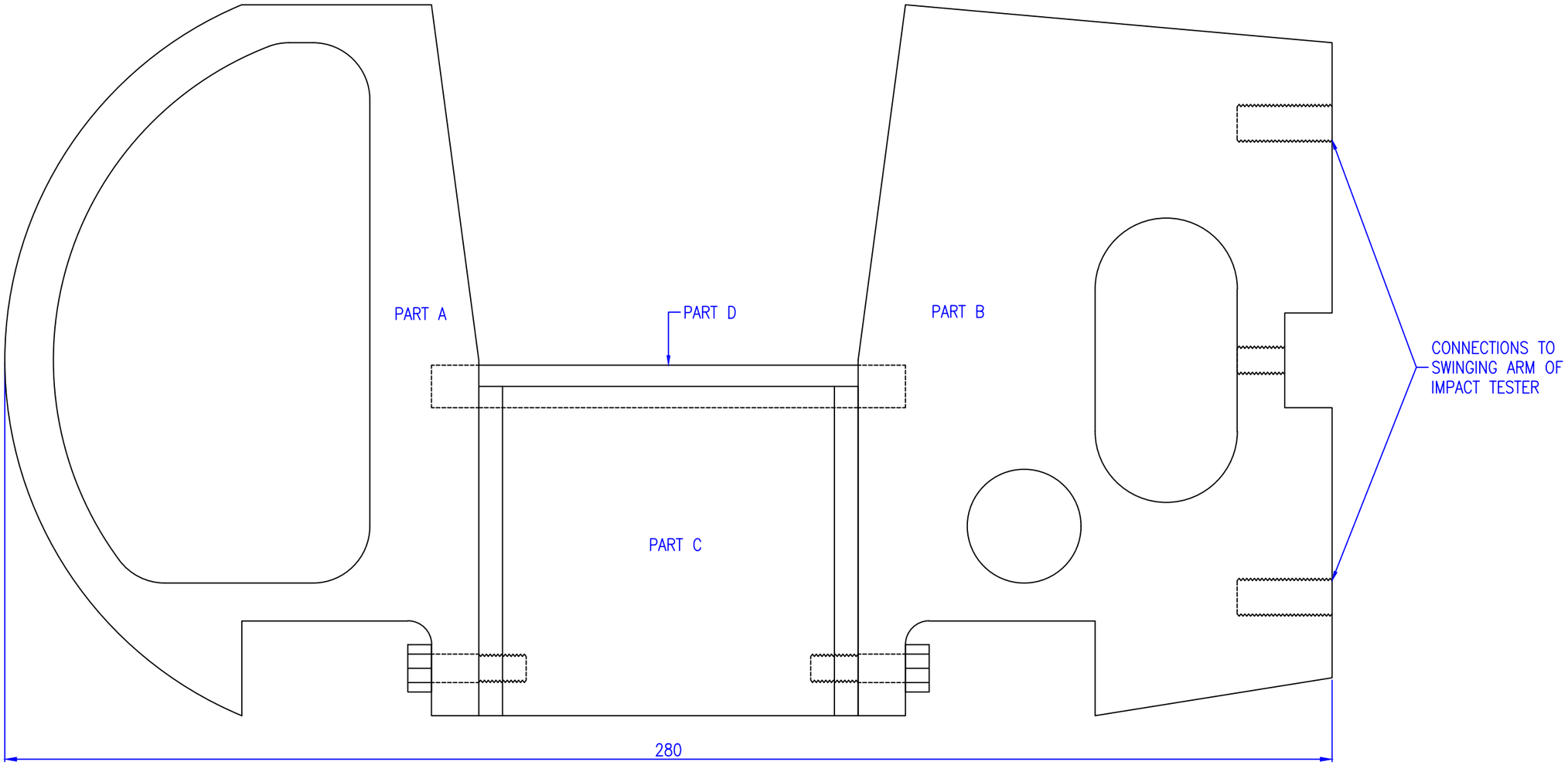

All Dimensions are in mm unless specified otherwise.

NOTE:
- PRIOR TO ASSEMBLY, PART D IS HARDENED.
- ENDS OF PART D ARE PRESS FITTED IN PARTS A & B AND GRUB SCREWS ARE USED ON THE SIDES TO AVOID ANY ROTATION OF PART.

DATE: 10/10/2023	DOCUMENT: CHARPY IMPACT TESTER – MODIFICATIONS REPORT
SCALE/PAPER SIZE: 1:1 / A3	DRAWING: NEW PENDULUM HEAD – ASSEMBLED DRAWING
DRAWN BY (STUDENT NUMBER): CHUNDUNSING ABHAY NOOKANT NETRAPAL (2634879)	SHEET: 1 OF 1

LEFT SIDE SUPPORT
FRONT VIEW
SCALE 1:1

LEFT SIDE SUPPORT
TOP VIEW
SCALE 1:1

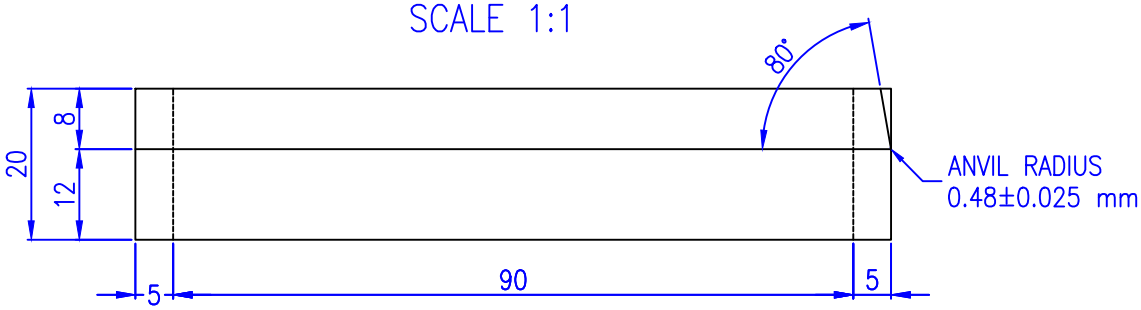

LEFT SIDE SUPPORT
FRONT VIEW
SCALE 1:1

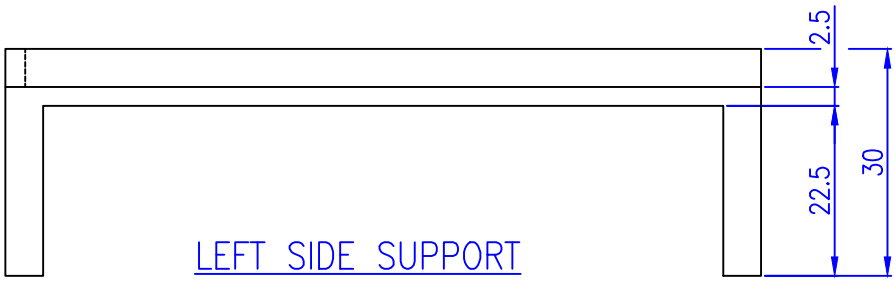

LEFT SIDE SUPPORT
TOP VIEW
SCALE 1:1

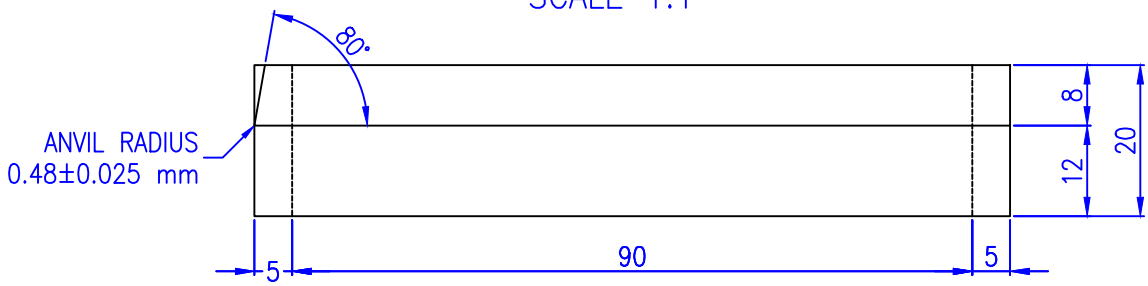

All Dimensions are in mm unless specified otherwise.

DATE: 10/10/2023	DOCUMENT: CHARPY IMPACT TESTER – MODIFICATIONS REPORT
SCALE/PAPER SIZE: 1:1 / A4	DRAWING: NEW ANVILS AND SUPPORTS – DETAILED DRAWING
DRAWN BY (STUDENT NUMBER): CHUNDUNSING ABHAY NOOKANT NETRAPAL (2634879)	SHEET: 1 OF 1

ANVIL & SUPPORTS CENTERING JIG
TOP VIEW
SCALE 4:1

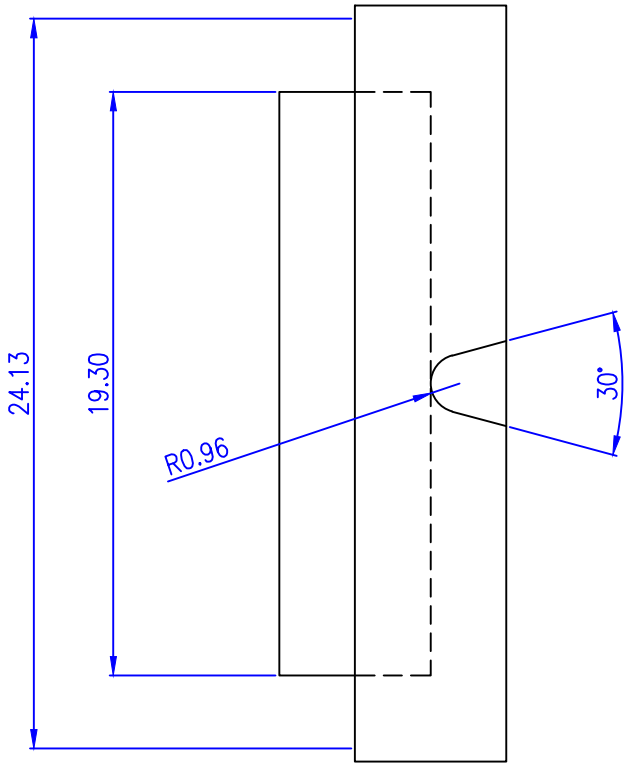

ANVIL & SUPPORTS CENTERING JIG
SIDE VIEW
SCALE 4:1

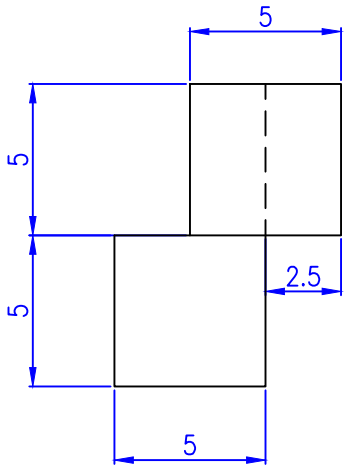

All Dimensions are in mm unless specified otherwise.

DATE:	DOCUMENT:
17/11/2023	CHARPY IMPACT TESTER – MODIFICATIONS REPORT
SCALE/PAPER SIZE:	DRAWING:
4:1 / A4	CENTERING JIG – DETAILED DRAWING
DRAWN BY (STUDENT NUMBER):	SHEET:
CHUNDUNSING ABHAY NOOKANT NETRAPAL (2634879)	1 OF 1

Annex 2 - Charpy Impact Tester - Calibration Report

Charpy Impact tester verification report

MIA Materials Lab

University of the Witwatersrand

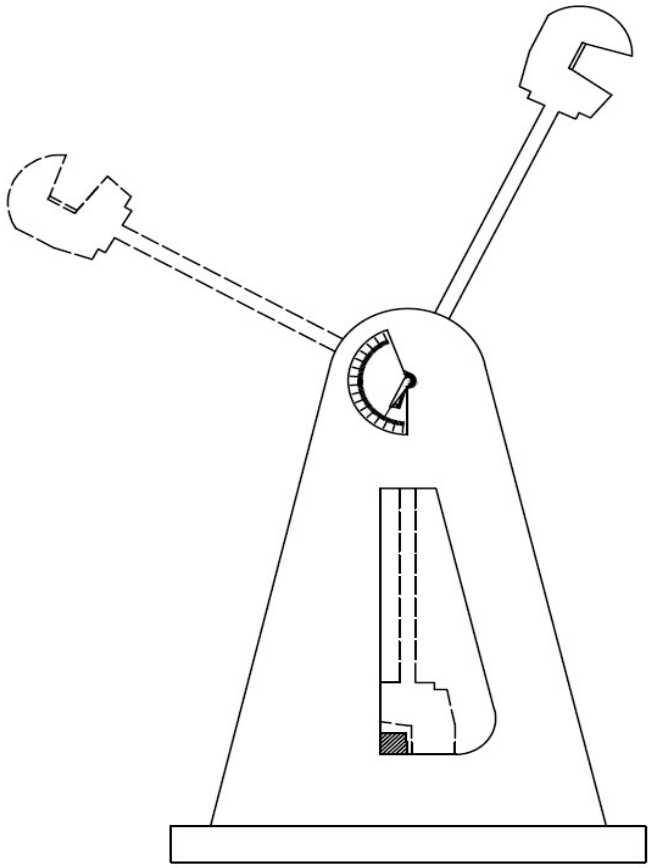

The aim of this report is to make suitable the Charpy Impact machine for acceptance testing of metallic materials. This is carried out by the calibration of the scale and the verification of compliance of specified dimensions.

Prepared By: Abhay Chundunsing

Date: October 2024

Contents

GENERAL

Details and Purpose of Verification

This document is a calibration and verification report that has for main objective of ensuring that the testing equipment of the School of Mechanical, Industrial and Aeronautical Engineering (MIA) at the University of the Witwatersrand is fit and proper to carry out charpy impact testing in accordance to international test standards. This document is attached to a Master's Dissertation report (Annex 2) whereby modifications were made to the pendulum, anvils and supports of the impact tester. These modifications are made with the intention of adapting the equipment to perform testing of Miniaturized Charpy V-Notch (MCVN) samples.

Methods and techniques that are employed in this report are based on 3 standards namely:
• ASTM E23 -18 [1].
• ASTM E2248 – 18 [2].
• SABS ISO 148-2:2011 [3].

Machine Identification

The equipment is found in the School of Mechanical, Industrial and Aeronautical Engineering, materials Laboratory and is of pendulum type from the German company FRANK-PTI. The description plate on the apparatus gives also some other information about the dates and model type as well as the supplier details. (see pictures below)

(a) 

(b) 

Figure 1 (a) the pendulum type Charpy Impact testing machine at the University of the Witwatersrand. (b) the nameplates found on the apparatus.

Test Machine Details

Modifications were brought to the impact tester for it to be able to accommodate and test Miniaturized, Charpy V-Notch, MCVN samples based on ASTM E2248. As specified by the test standard, testing of MCVN samples can be carried out using the typical test method and machine with modified anvils and striker. Minimum requirements are given in the standard for the measurement and recording of data from a standard equipment. This is done so as to obtain similar sensitivity and comparable measurements to standard CVN tests.

The crucial aspects required for MCVN testing as summarized in the test method are:
1. Suitable 3 point bend specimens.
2. Anvils and supports on which specimens are placed to receive the blow of the moving mass.
3. A striker released from a sufficient height to break the specimen placed in its path.
4. An indicating device capable of determining the absorbed energy of the broken specimen.

Below is a checklist for test machine suitability as per ASTM E2248:

Criteria	Check	Comments
Is the capacity sufficient to break the specimen in one blow without losing more than 80% of its initial potential energy	✓	Ratio of calculated absorbed energy to Range Capacity < 0.8
Can energy measurements be obtained with a resolution better than or equal to 0.1 J	✓	The readable division of 0.25°, when translated to calculated energy, is within range
Does specimen centreline coincide with centre of strike of pendulum	✓	Appropriate measurements and measures taken
Is the impact velocity of pendulum at centre of strike within acceptable range	✓	Calculated and within range

The principle in conducting MCVN tests is that the scalability of the stress fields are mantained. In addition to the samples, the striker radius, anvil radii, and the span of the anvils are also scaled by half proportionally to the normal CVN tests. The table below summarises the main dimensions that have been scaled down.

Part	Dimensions for CVN	Dimensions adjusted for MCVN	Comments
Striker	2 mm	0.96 mm	For more details of the changes and the exact geometry and dimensions, please refer to 'Annex 1 - Modifications report' of the Master's Dissertation.
Anvil Radius	1 mm ± 0.05	0.48 mm ± 0.025	
Span	40 mm ± 0.05	19.3 mm ± 0.025	

In the process of downsizing and modifying various components of the equipment, it became necessary to revise the testing specifications of the apparatus. As per the guidelines outlined in ASTM E23, it is stipulated that the verification of machines must be undertaken promptly after the replacement of parts that could potentially impact the measured absorbed energy, subsequent to repairs and adjustments, or whenever there arises doubt regarding the accuracy of the obtained results. The verification procedure for machines comprises two distinct facets: direct verifications involving a meticulous examination of the equipment to ensure strict adherence to the requisites delineated in Annexes 1 and 2 of the E23 testing standard, and indirect verifications which encompass the comprehensive testing of verification specimens.

Checklist for direct and indirect verifications of equipment

The test machines shall be a pendulum type of rigid construction. Below are the general requirements checklist that needs to be met and is found in ASTM E23:

Criteria	Check	Comments
Level of machine and axis of rotation of pendulum is within range and machine is properly secured.	✓	See Assumption 1&2
The analog scale display is graduated in degrees where readings can be estimated within range.	✓	See calculations below
Total frictional losses for analog scale are compensated and error in indicating device at any point within range.	✓	See direct verifications & calculations
Total frictional losses of machine and analog scale shall be within range of range capacity	✓	See direct verifications & calculations
The striker is within 2.5 mm from the test specimen when the pendulum is hanging freely and display reads within 0.2% of range capacity when pendulum is held against test specimen after indicating device has been set to read zero degrees in a free swing.	✓	Verified & Pointer positioned accordingly
Transverse play of pendulum at striker is < 0.75 mm under a transverse force of 4% of the effective weight of the pendulum applied at the centre of strike.	✓	See Assumption 3 & Verified
Impact velocity of pendulum at centre of strike is within range.	✓	See direct verifications
Height of centre of strike in latched position shall be within range.	✓	See calculations below
Pendulum release mechanism operates freely without initial impulse, retardation, or side vibration.	✓	See Assumption 4
Specimen Clearance is taken into consideration in anvil design for test specimen to exit machine with minimum interference.	✓	See Annex 1 of MSc, 'modifications report'
The cente of notch of test specimen is located within 0.25 mm of midpoint between the anvils.	✓	See Annex 1 of MSc, 'modifications report'
Supports are of the form and dimensions stated in ASTM E2248 standard and should be such that to minimize interference.	✓	See Annex 1 of MSc, 'modifications report'
Centre line of striker advances within 0.40 mm of the mid-point between the supporting edges of anvils.	✓	See Annex 1 of MSc, 'modifications report'
The striker is perpendicular to the longitudinal axis of the specimen within 5:1000 and parallel within 1:1000 to the face of a square specimen held against the anvils.	✓	See Assumption 5
The striker is conform to dimensions and tolerances stated in ASTM E2248 standard.	✓	See Annex 1 of MSc, 'modifications report'

Assumptions

Since the machine is relatively old and many factors are relatively difficult to obtain, it is required to make some assumptions.

1) Machine is securely bolted to concrete floor not less than 150 mm thick and bolts tightened as specified by the machine manufacturer.
2) Machine level checked in both directions using a level ruler and deemed to be within 3:1000.

3) Transverse force applied to measure transverse play of pendulum is approximated to be 4% of the effective weight of the pendulum.
4) Pendulum release mechanism does not induce any errors in the testing of samples.(assumption is based on a visual inspection of the mechanism)
5) The perpendicularity of the striker axis and the samples axis are checked using basic methods and are assumed to be within range. The squareness of the samples are checked and ensured during preparation

General Calculations

Errors in the indicating device at any point shall not exceed 0.2% of the range capacity or 0.4% of the reading.

maximum % error wrt range capacity	0.122

Note: The percentage error wrt the reading value is calculated in direct verifications section.

Total frictional losses during swing in the striking direction shall not exceed 0.75% of the range capacity. Additionally, pendulum losses shall not exceed 0.25% of scale capacity.

maximum % total losses wrt range capacity	0.362
% Scale losses wrt range capacity	0.122

The height of the centre of strike at the latched poition above its free hanging position shall be within 0.4% of the range capacity divided by the supporting force.
From direct verifications, the height of centre of strike in latched position as well as the height of rise of pendulum in free swing is known.

Height in latched position, m	1.499
% difference	0.361

Summary

The two sections that follows consists of going through the whole process of performing verifications on the charpy apparatus of the MIA laboratory at Wits. It is deemed necessary immediately after replacing parts that may affect the measured absorbed energy, after making repairs or adjustments, after it has been moved or whenever there is reason to doubt the accuracy of the results.

The verifications are carried out in order to adapt the impact tester to enable the testing of Miniaturized Charpy V-Notch specimens in conformity with ASTM E2248. A work method to ensure uniformity in determinations has been established from which all determinations will be made.

DIRECT VERIFICATION

The first part of verification of impact machine consists of performing direct verifications on specific items annually or prior to use. This part consists of inspecting the machine to ensure that the general requirements stated in the previous section are met. The steps in achieving this verification part are described below:

The specimen supports, anvils and striker are inspected and any of these parts that show signs of wear shall be replaced. The figures below represent the dimensions that the parts should conform to:

a)

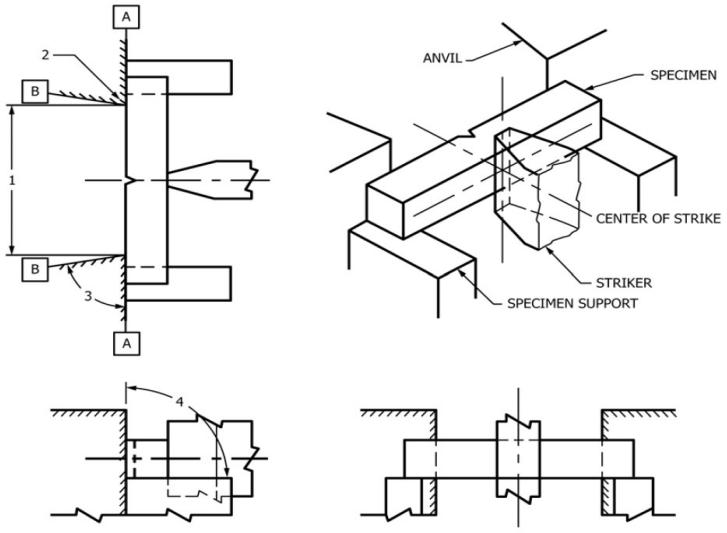

b)

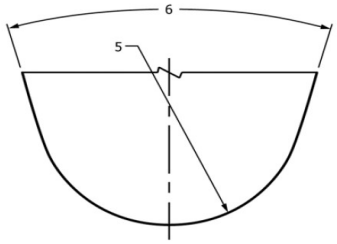

ID Num	Designation	Dimensions	Tolerance
1	Span between anvils	19.3 mm	± 0.025 mm
2	Anvil Radius	0.48 mm	± 0.025 mm
3	Anvil Angle	80°	± 2°
4	Anvil-support Angle	90°	± 0.15°
5	Striker Radius	0.96 mm	± 0.025 mm
6	Striker Angle	30°	± 2°
A and B	Surface finish Anvils	0.1 µm (Ra)	≤

Figure 2 (a) Charpy anvils and supports for Miniaturized Charpy impact tests (b) Scaled 2 mm Striker for use in Miniaturized Charpy impact testing. [1][2]

Measurements from Apparatus - Determination of Centre of strike, Supporting force and Height of drop

Before quantifying and determining aspects involved in charpy testing, it is required to measure three main quantities with a fair level of accuracy, namely the centre of strike, the supporting force and the height of drop.

The accuracy of these measurements is key as all other determinations shall depend on the values obtained.

According to E23 standard, to determine the centre of strike of the pendulum, a half thick specimen is used in the test position. With the specimen placed on the anvils and supports and the striker in contact with the specimen, a line is marked along the top edge of the specimen on the striker which will indicate the center of strike. However, since MCVN specimens (4.83 x 4.83 x 24.13 mm) will be tested and while special supports are designed according to ASTM E2248 to accomodate for these smaller specimens, the centre of strike is directly determined by placing a specimen of size 4.83 x 2.42 x 24.13 mm in the test position on the newly designed supports.

The distance from the pivoting axis to the marked centre of strike is accurately determined and recorded.

Note: the centre of strike shall be coincident or within 1 mm with the radial line from the axis of rotation of the pendulum to the centre of gravity (free hanging position).

Centre of Strike Distance (mm)	805

Note: In order to ensure that the position of the centre of strike is within range, new anvils and supports have been designed. More details on the newly designed supports with the exact geometry and dimensions, please refer to Annex 1 of the Master's Dissertation.

After the centre of strike has been determined, the supporting force is figured out. The supporting force will englobe all the different static forces (pendulum head weight, swinging arm weight, etc..). ASTM E23 standard provides a simple and straightforward technique in determining this supporting force.

The pendulum is supported horizontally within 15:1000 with it being supported with two supports, one at the bearings (centre of rotation) and the second at the centre of strike on the striker. An arrangement for supportting the pendulum at the centre of strike is then made so that the it is resting upon a weighing device. The weight is then determined within 0.4%.

Figure 3 pendulum arm set horizontally to measure the supporting force

Note:
While measuring the weight of the pendulum in the horizontal position, the weights of the supporting feature and leveling device shall be substracted from the final value.
The bench onto which the scale is placed upon should also be horizontal to ensure that the values determined are only the vertical components of forces.
To ensure a point contact, a round rod is placed perpendicularly to the striker at at the centre of strike.

Supporting force, N	30.1

Finally, the heights of fall and rise shall be determined based on the angles that can be read from the angular scale on the equipment.

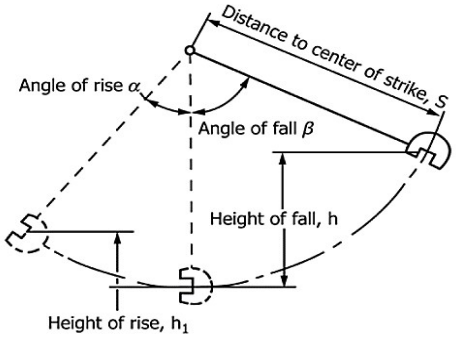

Figure 4 representing the dimensions for calculations of heights [1].

Determination of the angular values was done by adjusting the dial that moves the pointer in such a way that then the pendulum moves in either clockwise or anticlockwise direction, the pointer follows to indicate the angular displacement. (See Figure 5 below for labels)

To determine the height of drop, trigonometric functions are used. These trigonometric functions make use of the angular readings as well as the length of the pendulum, distance to the centre of strike, S. The following formulas are used for the calculations of the vertical height of the pendulum.

$$h = S\,(1-\cos\beta)$$
$$h1 = S\,(1-\cos\alpha)$$

Where:
h = Initial elevation of striker, m
S = Distance to Centre of Strike, m
β = Angle of fall
α = Angle of Rise
h1 = Height of rise, m

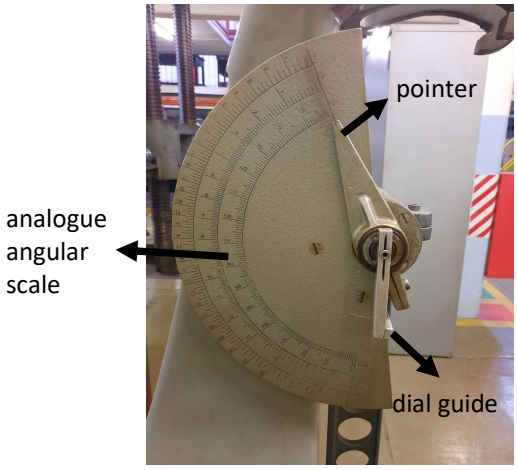

Figure 5 indicating the different components of the impact testing analogue scale.

Note: the values of h and h1 were calculated and directly integrated in the energy determinations.

Determination of equipment range capacity

The potential energy of the system is equal to the height from which the pendulum falls or rises (determined from the angular readings) times the supporting force determined using the weighing device.

The range capacity of the equipment, is calculated using the initial height of rise of the pendulum. The angle of rise in a free swing is used to determine the initial height of rise. This angle is determined by performing a free swing multiple times and adjusting the dial guide that moves the pointer by trial and error until the pointer reads 0°. For each trial of free swing, the pointer is always reset at the same initial point. Once the pointer reads 0° on the scale for a free swing, the pendulum is brought to rest and is secured in its free hanging position. (rest) The pointer is then moved so that it comes in contact with the dial guide. The angular reading is noted as the initial angle of rise, α.
The range capacity is then calculated by determining the energy at the angle of rise. The energy is obtained by the product of the perpenducular height of the pendulum rise at the centre of strike position to the centre of strike at the impact position and the supporting force.

Initial angle of rise, α, °	148.75
Range Capacity (energy), J	44.95

Determination of Total Frictional Losses

The equipment total losses can be divided into 2 major categories namely the frictional losses and the windage losses. The frictional losses occur as a result of components rubbing against each other in the swinging mechanism (bearings etc..) as well as on the scale (guide and pointer). To reduce the frictional losses prior to verifications and/or testing the equipment shall be cleaned and the pendulum shall be allowed to swing for 50-100 cycles. The windage loss on the other hand is a bit more complex as it occurs as the result of air resistance.

The friction and windage losses of the pendulum and frictional losses in the indicating device, if not corrected, will be included in the energy loss attributed to breaking the specimen and can result in erroneously high measurements of absorbed energy. The total losses is basically determined by the difference in height of fall and height of rise in a free swing. It is also important in that prior to that free swing, the scale pointer initialized.

Initialisation of scale pointer in this specific case is done by readjusting the pointer to the 151° reading on the analogue angular scale prior to any swing.

The suitability of analog scale display is first determined by calculating the smallest graduation that can be estimated or readable. This increment shall be within range of 0.25% of the range capacity.

Range Capacity (Degrees), °	148.75
Smallest estimatable increment (Degrees), °	0.250
% of Readable increment wrt Range Capacity	0.168

Energy loss determination corresponding to the total losses are as follows:

Recall that for this equipment the device dial and indicator can be adjusted such that the readings read zero degrees in a free swing. The angle of rise has been previously recorded in this manner and the range capacity of the pendulum was calculated.

To obtain the angle of fall, the dial and pointer is now adjusted at the free hanging position to read zero. The pendulum is lifted to the intital release position and secured. The pointer is adjusted to make sure that there is contact with the dial, the angular reading, β is noted.
The energy difference calculated based on the difference of these two heights determined from the angular readings shall give the total frictional losses.

Initial angle of rise, α, °	148.75
Angle of fall, β, °	149.5
Total Energy Losses, J	0.163

In addition to the determination of the total losses, the friction and windage loss by the pendulum and the frictional loss by scale guide and pointer can be further discerned. To achieve this, first thing that needs to be adjusted is the dial guide so that the reading reads 10° in a free swing of the pendulum. A similar approach to the range capacity determination, where by trial and error and each time resetting the pointer is adopted. Once the ajustments are complete such that the pointer is constantly reading 10° for every free swing, the pendulum is now repeatedly released from its initial position without initializing the pointer until no further movement in the pointer is noticed. The angular reading is noted. This reading will enable the determination of the frictional losses in the scale mechanism.
Using these determinations, the friction loss in the analog scale pointer mechanism as well as the friction and windage loss by pendulum alone can be determined.

Angular reading without pointer initialization, °	9.75
Friction Loss in scale mechanism, J	0.055
Friction and Windage Loss in pendulum, J	0.108
% Scale friction Losses wrt Range Capacity	0.122
% Pendulum Losses wrt Range Capacity	0.241

Determination of Impact Velocity

In order for tests to be considered valid, the impact velocity of the machine neglecting friction shall not be less than 3 nor more than 6 m/s.
Impact velocity can be determined using the following equation:

$$v = \sqrt{2gh}$$

Where:
v = Velocity, m/s
g = Acceleration due to gravity, 9.81 m/s²
h = Initial elevation of striker, m

Impact velocity, m/s	5.42

Determination % friction and windage loss

According to ASTM E23 standard, the percent friction and windage loss shall not exceed 0.4% of the range capacity being tested.

Calculations of the percent friction and windage loss is as follows:

- the pendulum is raised to latched position and pointer is reset to range capacity.
- the pendulum is then released without any specimens in place and allowed to make five complete cycles.
- prior to the sixth cycle, the the pointer is moved to around 20° on the scale and the sixth forward swing value is recorded.
- the value is converted to absorbed energy and divided by 10.
- the absorbed energy value obtained is divided by the range capacity being used and multiplied by 100 top get the percent friction and windage loss.

Angular reading on 6th forward swing, γ, °	7
Absorbed energy for 10 swings, N	1.69
Absorbed energy for 1 swing, N	0.169
Percent friction and windage loss	0.375

In order to consider the impact testing equipment up to standard in obtaining reliable and accurate results, ASTM E23 states that losses in the machine shall be within acceptable range. The table below summarizes the acceptable values stated and whether the ones determined are within range.

Loss	Acceptable range	Obtained Value
Percent friction and windage loss	< 0.4 %	0.375
Total frictional losses during swing in striking direction	< 0.75 %	0.241
Pendulum energy loss from friction in the analog scale pointer	< 0.25 %	0.122

Determination of the centre of percussion

To ensure that there is minimum force transmitted to the point of rotation, the position of the centre of percussion shall be within 1% of the distance from the axis of rotation to the centre of strike, S, in the specimen.
The position of the centre of percussion is determined using the following formula:

$$L = \frac{gp^2}{4\pi^2}$$

Where:
L = Distance from axis to centre of percussion, m
g = Acceleration due to gravity, 9.81 m/s²
π = 3.1416
p = Period of a complete swing (to and fro), s

The period of swing is determined as follows:
A time measuring device capable of measuring time up to an accuracy of 0.2s is used to record the time to complete 100 complete cycles after the pendulum is swung to an angle not greater than 15°. The period of the pendulum is then the time obtained divided by 100.

Recorded time for 100 swings, s	170
Distance from axis to centre of percussion, m	0.72
% difference between S and L	0.011

Calibration of indicating device

After changes to the pendulum head and supports were brought to the Impact testing equipment, a new conversion table had to be developped to enable conversion of angular readings to absorbed energy readings. The conversion table is developped for values over the entire scale capacity to ensure accuracy. However, for tests to be considered valid, testing for absorbed energy shall be limited to a maximum of 80% of the range capacity.
The process consists of determining by calculation the residual energies at percentage values of the range capacity. Frictional and windage losses are also determined proportionally by making use of the angular movement of the pendulum and scale pointer. Finally the calculated value of the absorbed energy is determined by substracting the sum of the residual energy and the proportional friction and windage loss from the potential energy at the latched position.

If the percent of the range capacity is known, the supposed reading of the angle of rise can be determined. Using this angular reading, the corresponding height is calculated and eventually the remaining energy calculated by the product of this height to the supporting force. The table below summarises the values.

Note: The range of the angular scale reading is 0° to 150°. The boundary values corresponds to 0% and 100% of the absorbed energy value respectively.

To determine the losses by friction and windage proportionally, angular displacement ratios are developped. The losses involved here are the frictional losses due to the scale pointer and the friction and windage losses of the pendulum arm.

Scale pointer friction loss calculations:
For this specific testing equipment, the scale pointer is engaged only during the rising portion of the arm. Therefore, determination of the losses associated to it shall be limited to this range only. The ratio equals to the difference of the angular scale reading from the initial angle of rise to the initial angle of rise.

Pendulum loss calculations:
The pendulum losses on the other hand is a bit different. The friction and windage loss due to the pendulum occurs for both the dropping and rising portion. When calculating the ratio, the angular reading must be substracted from (α°+β°) value.

INDIRECT VERIFICATION

Indirect verification consists of testing verification specimens with certified absorbed energy values to verify the accuracy of the Charpy Impact machine.

The verified range in this case consists of testing specimens at at least two to three energy levels namely, very low (<10 J), low (10-15 J) and high (>30 J).
In order to meet the verifications requirements, the average absorbed energy value determined at each energy level shall correspond to the certified absorbed energy values within 1.4 J or 5%, whichever is greater.

The Certified absorbed energy values in this case were determined by a local laboratory. Material blocks from which MCVN samples were fabricated at Wits for testing on the modified charpy impact tester were sent to that specific acredited lab for testing of normal charpy samples. Details about these three materials are as follows:

Material	Certified Absorbed Energy, J	Average scale reading, °	Calculated Absorbed Energy, J	Adjusted Absorbed energy value based on Certified Value, J	Absolute difference, J	% Energy Difference
Al 2024	6	6.75	1.62	6.1	0.10	1.67
Al 7075	11	10.75	2.70	10.5	0.50	4.55
Ti6Al4V	38	29.50	8.85	38.1	0.10	0.26

Note: The certification of the tested samples by the acredited lab is found in the Annex of this document.

The value of the calculated energy absorbed in the previous section is then adjusted such that it correlates with the values obtained from the verification process. This new value called the adjusted energy value gives a correct absorbed energy value.

FULL RANGE SCALE READINGS

Angular reading, °	Calculated Scale losses, J	Calculated Pendulum losses, J	Calculated Total losses, J	Calculated Vertical height, m	Calculated Residual energy, J	Calculated Absorbed Energy, J	Adjusted Absorbed Energy, J
0.00	0.055	0.108	0.163	1.493	44.945	0.00	0.00
0.25	0.055	0.108	0.163	1.491	44.890	0.05	0.20
0.50	0.054	0.108	0.162	1.490	44.835	0.11	0.40
0.75	0.054	0.108	0.162	1.488	44.779	0.17	0.60
1.00	0.054	0.108	0.162	1.486	44.723	0.22	0.80
1.25	0.054	0.108	0.162	1.484	44.666	0.28	1.01
1.50	0.054	0.108	0.162	1.482	44.609	0.34	1.21
1.75	0.054	0.107	0.161	1.480	44.552	0.39	1.42
2.00	0.054	0.107	0.161	1.478	44.494	0.45	1.64
2.25	0.054	0.107	0.161	1.476	44.436	0.51	1.85
2.50	0.054	0.107	0.161	1.474	44.377	0.57	2.07
2.75	0.054	0.107	0.161	1.472	44.318	0.62	2.29
3.00	0.054	0.107	0.161	1.470	44.259	0.68	2.51
3.25	0.053	0.107	0.160	1.468	44.199	0.74	2.73
3.50	0.053	0.107	0.160	1.466	44.139	0.80	2.96
3.75	0.053	0.107	0.160	1.464	44.079	0.86	3.19
4.00	0.053	0.107	0.160	1.462	44.018	0.92	3.42
4.25	0.053	0.107	0.160	1.460	43.957	0.99	3.65
4.50	0.053	0.106	0.159	1.458	43.895	1.05	3.89
4.75	0.053	0.106	0.159	1.456	43.833	1.11	4.13
5.00	0.053	0.106	0.159	1.454	43.771	1.17	4.37
5.25	0.053	0.106	0.159	1.452	43.708	1.23	4.61
5.50	0.053	0.106	0.159	1.450	43.645	1.30	4.85
5.75	0.053	0.106	0.159	1.448	43.582	1.36	5.10
6.00	0.052	0.106	0.158	1.446	43.518	1.42	5.35
6.25	0.052	0.106	0.158	1.444	43.454	1.49	5.60
6.50	0.052	0.106	0.158	1.442	43.389	1.55	5.86
6.75	0.052	0.106	0.158	1.439	43.324	1.62	6.11
7.00	0.052	0.106	0.158	1.437	43.259	1.68	6.37
7.25	0.052	0.105	0.157	1.435	43.193	1.75	6.63
7.50	0.052	0.105	0.157	1.433	43.127	1.81	6.89
7.75	0.052	0.105	0.157	1.431	43.061	1.88	7.16
8.00	0.052	0.105	0.157	1.428	42.994	1.95	7.43
8.25	0.052	0.105	0.157	1.426	42.927	2.01	7.69
8.50	0.052	0.105	0.157	1.424	42.860	2.08	7.97
8.75	0.051	0.105	0.156	1.422	42.792	2.15	8.24
9.00	0.051	0.105	0.156	1.419	42.724	2.21	8.52
9.25	0.051	0.105	0.156	1.417	42.656	2.28	8.80
9.50	0.051	0.105	0.156	1.415	42.587	2.35	9.08
9.75	0.051	0.105	0.156	1.413	42.517	2.42	9.36
10.00	0.051	0.104	0.155	1.410	42.448	2.49	9.64
10.25	0.051	0.104	0.155	1.408	42.378	2.56	9.93
10.50	0.051	0.104	0.155	1.406	42.308	2.63	10.22

10.75	0.051	0.104	0.155	1.403	42.237	2.70	10.51
11.00	0.051	0.104	0.155	1.401	42.166	2.77	10.81
11.25	0.051	0.104	0.155	1.399	42.095	2.84	11.10
11.50	0.050	0.104	0.154	1.396	42.024	2.91	11.40
11.75	0.050	0.104	0.154	1.394	41.952	2.99	11.70
12.00	0.050	0.104	0.154	1.391	41.879	3.06	12.00
12.25	0.050	0.104	0.154	1.389	41.807	3.13	12.31
12.50	0.050	0.104	0.154	1.387	41.734	3.20	12.61
12.75	0.050	0.103	0.153	1.384	41.660	3.28	12.92
13.00	0.050	0.103	0.153	1.382	41.587	3.35	13.23
13.25	0.050	0.103	0.153	1.379	41.513	3.42	13.55
13.50	0.050	0.103	0.153	1.377	41.439	3.50	13.86
13.75	0.050	0.103	0.153	1.374	41.364	3.57	14.18
14.00	0.050	0.103	0.153	1.372	41.289	3.65	14.50
14.25	0.049	0.103	0.152	1.369	41.214	3.72	14.82
14.50	0.049	0.103	0.152	1.367	41.138	3.80	15.14
14.75	0.049	0.103	0.152	1.364	41.062	3.87	15.47
15.00	0.049	0.103	0.152	1.362	40.986	3.95	15.80
15.25	0.049	0.103	0.152	1.359	40.910	4.02	16.13
15.50	0.049	0.102	0.151	1.357	40.833	4.10	16.46
15.75	0.049	0.102	0.151	1.354	40.756	4.18	16.79
16.00	0.049	0.102	0.151	1.351	40.678	4.26	17.13
16.25	0.049	0.102	0.151	1.349	40.600	4.33	17.47
16.50	0.049	0.102	0.151	1.346	40.522	4.41	17.81
16.75	0.048	0.102	0.151	1.344	40.444	4.49	18.15
17.00	0.048	0.102	0.150	1.341	40.365	4.57	18.49
17.25	0.048	0.102	0.150	1.338	40.286	4.65	18.84
17.50	0.048	0.102	0.150	1.336	40.207	4.73	19.19
17.75	0.048	0.102	0.150	1.333	40.127	4.81	19.54
18.00	0.048	0.102	0.150	1.330	40.047	4.89	19.89
18.25	0.048	0.101	0.149	1.328	39.967	4.97	20.25
18.50	0.048	0.101	0.149	1.325	39.886	5.05	20.60
18.75	0.048	0.101	0.149	1.322	39.806	5.13	20.96
19.00	0.048	0.101	0.149	1.320	39.724	5.21	21.32
19.25	0.048	0.101	0.149	1.317	39.643	5.29	21.68
19.50	0.047	0.101	0.149	1.314	39.561	5.37	22.05
19.75	0.047	0.101	0.148	1.312	39.479	5.45	22.41
20.00	0.047	0.101	0.148	1.309	39.397	5.53	22.78
20.25	0.047	0.101	0.148	1.306	39.314	5.62	23.15
20.50	0.047	0.101	0.148	1.303	39.231	5.70	23.52
20.75	0.047	0.101	0.148	1.301	39.148	5.78	23.90
21.00	0.047	0.101	0.147	1.298	39.065	5.87	24.27
21.25	0.047	0.100	0.147	1.295	38.981	5.95	24.65
21.50	0.047	0.100	0.147	1.292	38.897	6.03	25.03
21.75	0.047	0.100	0.147	1.289	38.813	6.12	25.41
22.00	0.047	0.100	0.147	1.287	38.728	6.20	25.79
22.25	0.046	0.100	0.147	1.284	38.643	6.29	26.18
22.50	0.046	0.100	0.146	1.281	38.558	6.37	26.57
22.75	0.046	0.100	0.146	1.278	38.473	6.46	26.96
23.00	0.046	0.100	0.146	1.275	38.387	6.54	27.35

23.25	0.046	0.100	0.146	1.272	38.301	6.63	27.74
23.50	0.046	0.100	0.146	1.270	38.215	6.71	28.13
23.75	0.046	0.100	0.145	1.267	38.129	6.80	28.53
24.00	0.046	0.099	0.145	1.264	38.042	6.89	28.93
24.25	0.046	0.099	0.145	1.261	37.955	6.97	29.33
24.50	0.046	0.099	0.145	1.258	37.868	7.06	29.73
24.75	0.046	0.099	0.145	1.255	37.780	7.15	30.13
25.00	0.045	0.099	0.145	1.252	37.692	7.23	30.54
25.25	0.045	0.099	0.144	1.249	37.604	7.32	30.94
25.50	0.045	0.099	0.144	1.246	37.516	7.41	31.35
25.75	0.045	0.099	0.144	1.243	37.427	7.50	31.76
26.00	0.045	0.099	0.144	1.240	37.339	7.59	32.18
26.25	0.045	0.099	0.144	1.238	37.250	7.68	32.59
26.50	0.045	0.099	0.143	1.235	37.160	7.77	33.00
26.75	0.045	0.098	0.143	1.232	37.071	7.86	33.42
27.00	0.045	0.098	0.143	1.229	36.981	7.94	33.84
27.25	0.045	0.098	0.143	1.226	36.891	8.03	34.26
27.50	0.045	0.098	0.143	1.223	36.801	8.12	34.68
27.75	0.044	0.098	0.143	1.220	36.710	8.22	35.11
28.00	0.044	0.098	0.142	1.217	36.619	8.31	35.53
28.25	0.044	0.098	0.142	1.214	36.528	8.40	35.96
28.50	0.044	0.098	0.142	1.211	36.437	8.49	36.39
28.75	0.044	0.098	0.142	1.208	36.346	8.58	36.82
29.00	0.044	0.098	0.142	1.204	36.254	8.67	37.25
29.25	0.044	0.098	0.141	1.201	36.162	8.76	37.69
29.50	0.044	0.097	0.141	1.198	36.070	8.85	38.12
29.75	0.044	0.097	0.141	1.195	35.978	8.95	38.56
30.00	0.044	0.097	0.141	1.192	35.885	9.04	39.00
30.25	0.044	0.097	0.141	1.189	35.792	9.13	39.44
30.50	0.043	0.097	0.141	1.186	35.699	9.22	39.88
30.75	0.043	0.097	0.140	1.183	35.606	9.32	40.32
31.00	0.043	0.097	0.140	1.180	35.513	9.41	40.77
31.25	0.043	0.097	0.140	1.177	35.419	9.50	41.21
31.50	0.043	0.097	0.140	1.174	35.325	9.60	41.66
31.75	0.043	0.097	0.140	1.170	35.231	9.69	42.11
32.00	0.043	0.097	0.139	1.167	35.137	9.79	42.56
32.25	0.043	0.096	0.139	1.164	35.042	9.88	43.01
32.50	0.043	0.096	0.139	1.161	34.947	9.97	43.47
32.75	0.043	0.096	0.139	1.158	34.852	10.07	43.92
33.00	0.043	0.096	0.139	1.155	34.757	10.16	44.38
33.25	0.042	0.096	0.138	1.152	34.662	10.26	44.84
33.50	0.042	0.096	0.138	1.148	34.566	10.35	45.30
33.75	0.042	0.096	0.138	1.145	34.471	10.45	45.76
34.00	0.042	0.096	0.138	1.142	34.375	10.55	46.22
34.25	0.042	0.096	0.138	1.139	34.279	10.64	46.69
34.50	0.042	0.096	0.138	1.136	34.182	10.74	47.15
34.75	0.042	0.096	0.137	1.132	34.086	10.83	47.62
35.00	0.042	0.095	0.137	1.129	33.989	10.93	48.09
35.25	0.042	0.095	0.137	1.126	33.892	11.03	48.56
35.50	0.042	0.095	0.137	1.123	33.795	11.12	49.03

35.75	0.042	0.095	0.137	1.120	33.698	11.22	49.50
36.00	0.041	0.095	0.136	1.116	33.601	11.32	49.97
36.25	0.041	0.095	0.136	1.113	33.503	11.42	50.45
36.50	0.041	0.095	0.136	1.110	33.405	11.51	50.92
36.75	0.041	0.095	0.136	1.107	33.307	11.61	51.40
37.00	0.041	0.095	0.136	1.103	33.209	11.71	51.88
37.25	0.041	0.095	0.136	1.100	33.111	11.81	52.36
37.50	0.041	0.095	0.135	1.097	33.013	11.91	52.84
37.75	0.041	0.094	0.135	1.093	32.914	12.00	53.32
38.00	0.041	0.094	0.135	1.090	32.815	12.10	53.81
38.25	0.041	0.094	0.135	1.087	32.716	12.20	54.29
38.50	0.041	0.094	0.135	1.084	32.617	12.30	54.78
38.75	0.040	0.094	0.134	1.080	32.518	12.40	55.27
39.00	0.040	0.094	0.134	1.077	32.418	12.50	55.76
39.25	0.040	0.094	0.134	1.074	32.319	12.60	56.25
39.50	0.040	0.094	0.134	1.070	32.219	12.70	56.74
39.75	0.040	0.094	0.134	1.067	32.119	12.80	57.23
40.00	0.040	0.094	0.134	1.064	32.019	12.90	57.72
40.25	0.040	0.094	0.133	1.060	31.919	13.00	58.22
40.50	0.040	0.093	0.133	1.057	31.819	13.10	58.71
40.75	0.040	0.093	0.133	1.054	31.718	13.20	59.21
41.00	0.040	0.093	0.133	1.050	31.618	13.30	59.71
41.25	0.039	0.093	0.133	1.047	31.517	13.40	60.21
41.50	0.039	0.093	0.132	1.044	31.416	13.50	60.71
41.75	0.039	0.093	0.132	1.040	31.315	13.60	61.21
42.00	0.039	0.093	0.132	1.037	31.214	13.70	61.71
42.25	0.039	0.093	0.132	1.034	31.112	13.80	62.21
42.50	0.039	0.093	0.132	1.030	31.011	13.90	62.72
42.75	0.039	0.093	0.132	1.027	30.909	14.00	63.22
43.00	0.039	0.093	0.131	1.024	30.808	14.11	63.73
43.25	0.039	0.092	0.131	1.020	30.706	14.21	64.24
43.50	0.039	0.092	0.131	1.017	30.604	14.31	64.75
43.75	0.039	0.092	0.131	1.013	30.502	14.41	65.26
44.00	0.038	0.092	0.131	1.010	30.400	14.51	65.77
44.25	0.038	0.092	0.130	1.007	30.297	14.62	66.28
44.50	0.038	0.092	0.130	1.003	30.195	14.72	66.79
44.75	0.038	0.092	0.130	1.000	30.092	14.82	67.30
45.00	0.038	0.092	0.130	0.996	29.990	14.92	67.82
45.25	0.038	0.092	0.130	0.993	29.887	15.03	68.33
45.50	0.038	0.092	0.130	0.990	29.784	15.13	68.85
45.75	0.038	0.092	0.129	0.986	29.681	15.23	69.37
46.00	0.038	0.091	0.129	0.983	29.578	15.33	69.88
46.25	0.038	0.091	0.129	0.979	29.475	15.44	70.40
46.50	0.038	0.091	0.129	0.976	29.372	15.54	70.92
46.75	0.037	0.091	0.129	0.972	29.268	15.64	71.44
47.00	0.037	0.091	0.128	0.969	29.165	15.75	71.97
47.25	0.037	0.091	0.128	0.965	29.061	15.85	72.49
47.50	0.037	0.091	0.128	0.962	28.958	15.95	73.01
47.75	0.037	0.091	0.128	0.959	28.854	16.06	73.53
48.00	0.037	0.091	0.128	0.955	28.750	16.16	74.06

48.25	0.037	0.091	0.128	0.952	28.646	16.26	74.58
48.50	0.037	0.091	0.127	0.948	28.542	16.37	75.11
48.75	0.037	0.090	0.127	0.945	28.438	16.47	75.64
49.00	0.037	0.090	0.127	0.941	28.334	16.58	76.17
49.25	0.037	0.090	0.127	0.938	28.230	16.68	76.69
49.50	0.036	0.090	0.127	0.934	28.125	16.78	77.22
49.75	0.036	0.090	0.126	0.931	28.021	16.89	77.75
50.00	0.036	0.090	0.126	0.927	27.917	16.99	78.28
50.25	0.036	0.090	0.126	0.924	27.812	17.10	78.82
50.50	0.036	0.090	0.126	0.921	27.707	17.20	79.35
50.75	0.036	0.090	0.126	0.917	27.603	17.31	79.88
51.00	0.036	0.090	0.126	0.914	27.498	17.41	80.41
51.25	0.036	0.090	0.125	0.910	27.393	17.51	80.95
51.50	0.036	0.089	0.125	0.907	27.288	17.62	81.48
51.75	0.036	0.089	0.125	0.903	27.183	17.72	82.02
52.00	0.036	0.089	0.125	0.900	27.078	17.83	82.55
52.25	0.035	0.089	0.125	0.896	26.973	17.93	83.09
52.50	0.035	0.089	0.124	0.893	26.868	18.04	83.63
52.75	0.035	0.089	0.124	0.889	26.763	18.14	84.16
53.00	0.035	0.089	0.124	0.886	26.658	18.25	84.70
53.25	0.035	0.089	0.124	0.882	26.553	18.35	85.24
53.50	0.035	0.089	0.124	0.879	26.448	18.46	85.78
53.75	0.035	0.089	0.124	0.875	26.342	18.56	86.32
54.00	0.035	0.089	0.123	0.872	26.237	18.67	86.86
54.25	0.035	0.088	0.123	0.868	26.132	18.77	87.40
54.50	0.035	0.088	0.123	0.865	26.026	18.88	87.94
54.75	0.035	0.088	0.123	0.861	25.921	18.98	88.48
55.00	0.034	0.088	0.123	0.858	25.815	19.09	89.03
55.25	0.034	0.088	0.122	0.854	25.710	19.20	89.57
55.50	0.034	0.088	0.122	0.851	25.604	19.30	90.11
55.75	0.034	0.088	0.122	0.847	25.499	19.41	90.65
56.00	0.034	0.088	0.122	0.844	25.393	19.51	91.20
56.25	0.034	0.088	0.122	0.840	25.287	19.62	91.74
56.50	0.034	0.088	0.122	0.837	25.182	19.72	92.29
56.75	0.034	0.088	0.121	0.833	25.076	19.83	92.83
57.00	0.034	0.087	0.121	0.830	24.970	19.93	93.38
57.25	0.034	0.087	0.121	0.826	24.865	20.04	93.92
57.50	0.034	0.087	0.121	0.823	24.759	20.14	94.47
57.75	0.033	0.087	0.121	0.819	24.653	20.25	95.02
58.00	0.033	0.087	0.120	0.816	24.548	20.36	95.56
58.25	0.033	0.087	0.120	0.812	24.442	20.46	96.11
58.50	0.033	0.087	0.120	0.809	24.336	20.57	96.66
58.75	0.033	0.087	0.120	0.805	24.231	20.67	97.21
59.00	0.033	0.087	0.120	0.801	24.125	20.78	97.75
59.25	0.033	0.087	0.120	0.798	24.019	20.88	98.30
59.50	0.033	0.087	0.119	0.794	23.913	20.99	98.85
59.75	0.033	0.086	0.119	0.791	23.808	21.09	99.40
60.00	0.033	0.086	0.119	0.787	23.702	21.20	99.95
60.25	0.033	0.086	0.119	0.784	23.596	21.31	100.50
60.50	0.032	0.086	0.119	0.780	23.491	21.41	101.05

60.75	0.032	0.086	0.118	0.777	23.385	21.52	101.60
61.00	0.032	0.086	0.118	0.773	23.279	21.62	102.15
61.25	0.032	0.086	0.118	0.770	23.174	21.73	102.70
61.50	0.032	0.086	0.118	0.766	23.068	21.83	103.25
61.75	0.032	0.086	0.118	0.763	22.962	21.94	103.80
62.00	0.032	0.086	0.118	0.759	22.857	22.04	104.35
62.25	0.032	0.086	0.117	0.756	22.751	22.15	104.90
62.50	0.032	0.085	0.117	0.752	22.646	22.25	105.45
62.75	0.032	0.085	0.117	0.749	22.540	22.36	106.00
63.00	0.032	0.085	0.117	0.745	22.435	22.46	106.55
63.25	0.031	0.085	0.117	0.742	22.329	22.57	107.10
63.50	0.031	0.085	0.116	0.738	22.224	22.68	107.65
63.75	0.031	0.085	0.116	0.735	22.119	22.78	108.20
64.00	0.031	0.085	0.116	0.731	22.013	22.89	108.75
64.25	0.031	0.085	0.116	0.728	21.908	22.99	109.30
64.50	0.031	0.085	0.116	0.724	21.803	23.10	109.85
64.75	0.031	0.085	0.116	0.721	21.698	23.20	110.40
65.00	0.031	0.085	0.115	0.717	21.593	23.31	110.95
65.25	0.031	0.084	0.115	0.714	21.488	23.41	111.50
65.50	0.031	0.084	0.115	0.710	21.383	23.52	112.06
65.75	0.030	0.084	0.115	0.707	21.278	23.62	112.61
66.00	0.030	0.084	0.115	0.703	21.173	23.72	113.16
66.25	0.030	0.084	0.114	0.700	21.068	23.83	113.71
66.50	0.030	0.084	0.114	0.696	20.963	23.93	114.26
66.75	0.030	0.084	0.114	0.693	20.858	24.04	114.81
67.00	0.030	0.084	0.114	0.689	20.754	24.14	115.36
67.25	0.030	0.084	0.114	0.686	20.649	24.25	115.91
67.50	0.030	0.084	0.113	0.683	20.544	24.35	116.46
67.75	0.030	0.084	0.113	0.679	20.440	24.46	117.01
68.00	0.030	0.083	0.113	0.676	20.336	24.56	117.56
68.25	0.030	0.083	0.113	0.672	20.231	24.66	118.11
68.50	0.029	0.083	0.113	0.669	20.127	24.77	118.66
68.75	0.029	0.083	0.113	0.665	20.023	24.87	119.20
69.00	0.029	0.083	0.112	0.662	19.919	24.98	119.75
69.25	0.029	0.083	0.112	0.658	19.815	25.08	120.30
69.50	0.029	0.083	0.112	0.655	19.711	25.18	120.85
69.75	0.029	0.083	0.112	0.651	19.607	25.29	121.40
70.00	0.029	0.083	0.112	0.648	19.503	25.39	121.95

REFERENCES

[1] ASTM International, *E23 -18, Standard Test Methods for Notched Bar Impact Testing of metallic Materials,* West Conshohocken, Pennsylvania, United States: American Society for Testing and Materials, 2018.

[2] ASTM International, *E2248 - 18, Standard Test Method for Impact Testing of Miniaturized Charpy V-notch Specimens,* West Conshohocken, Pennsylvania, United States: American Society for Testing and Materials, 2018.

[3] ISO, *ISO 148-2, Metallic materials - Charpy Pendulum impact test - Part 2: Verification of testing machines,* Geneva: The International Organization for Standardization, 2008.

ANNEXES

IMP LABS
CK 1996/060917/23
MATERIALS TESTING LABORATORY
Tel: 011 421 9026
www.implabs.co.za | E-mail:admin@implabs.co.za
25 Moore Avenue, Benoni Ext 7
ilac-MRA
sanas Testing Laboratory T0862

Certificate No:	**23-2900-1**		
Customer:	SCROOBY'S LABORATORY SERVICES		
Attention:	Alan Scrooby	**Order No:**	PO005303
Address:	21 O'Reilly Merry Street	**Date Received:**	14-Nov-2023
	Rynfield,1501	**Date Tested:**	21-Nov-2023
	Benoni	**Date Reported:**	21-Nov-2023
		Heat No:	N/A
Telephone:	011 425 1074	**Ref No:**	N/A
Email:	scrooby@scroobyslab.co.za		
Description:	Al 7075 sample	**, As Received.**	

TEST REPORT ISSUED IN ACCORDANCE WITH EN10204 3.1

IMPACT TEST					
MATERIAL SPECIFICATION:	NO SPECIFICATION PROVIDED			**TEST METHOD:**	ASTM E23
Test temp. °C:	20	**Charpy V-Notch:**	KV(8)	**Notch Location:**	PARENT METAL
IMPACT RESISTANCE:		**Energy Absorbed (Joules):**		**LATERAL EXPANSION (mm):**	**SHEAR (%):**
Specimen 1:		12			
Specimen 2:		10			
Specimen 3:		11			
Specimen Average (J):		11			
Specification Average (J):		N/A		**Impact Size (mm):**	10 x 10
Additional information:					
Tested by: E. LE ROUX		**Witnessed by: N/A**		**Technical Signatory:**	Juane benjamin Mohr Digitally signed by Juane benjamin Mohr Date: 2023.11.21 11:26:36 +02'00'
RESULT:	**NO SPECIFICATION PROVIDED**				

IMP LABS
CK 1996/060917/23
MATERIALS TESTING LABORATORY
Tel: 011 421 9026
www.implabs.co.za | E-mail:admin@implabs.co.za
25 Moore Avenue, Benoni Ext 7
ilac-MRA
sanas Testing Laboratory T0862

Certificate No:	**23-2900-3**		
Customer:	SCROOBY'S LABORATORY SERVICES		
Attention:	Alan Scrooby	**Order No:**	PO005303
Address:	21 O'Reilly Merry Street	**Date Received:**	14-Nov-2023
	Rynfield,1501	**Date Tested:**	21-Nov-2023
	Benoni	**Date Reported:**	21-Nov-2023
		Heat No:	N/A
Telephone:	011 425 1074	**Ref No:**	N/A
Email:	scrooby@scroobyslab.co.za		
Description:	Al 2024 sample	**, As Received.**	

TEST REPORT ISSUED IN ACCORDANCE WITH EN10204 3.1

IMPACT TEST					
MATERIAL SPECIFICATION:		NO SPECIFICATION PROVIDED		**TEST METHOD:**	ASTM E23
Test temp. °C:	20	**Charpy V-Notch:**	KV(8)	**Notch Location:**	PARENT METAL
IMPACT RESISTANCE:		**Energy Absorbed (Joules):**		**LATERAL EXPANSION (mm):**	**SHEAR (%):**
Specimen 1:		7			
Specimen 2:		6			
Specimen 3:		6			
Specimen Average (J):		6			
Specification Average (J):		N/A		**Impact Size (mm):**	10 x 10
Additional information:					
Tested by: E. LE ROUX		**Witnessed by: N/A**		**Technical Signatory:**	Juane benjamin Mohr Digitally signed by Juane benjamin Mohr Date: 2023.11.21 11:27:13 +02'00'
RESULT:		**NO SPECIFICATION PROVIDED**			

IMPLABS
CK 1996/060917/23

Tel: 011 421 9026
www.implabs.co.za | E-mail:admin@implabs.co.za
25 Moore Avenue, Benoni Ext 7

CERTIFICATE No:	23-2900

Testing was carried out according to IMPLABS procedures.

SCOPE OF TEST METHODS

MATERIALS TESTED	TEST TYPE	METHOD ID	ACCREDITATION STATUS	UNCERTAINTY OF MEASUREMENT (IF APPLICABLE)
METALLIC MATERIALS	Tensile Testing: At room temperature Tensile testing up to 600 kN Determination of tensile strength, yield strength (upper and lower), yield point elongation,0,2% proof stress, elongation and area reduction	ASTM E8/E8M, ISO6892-1	ACCREDITED	12.76 Mpa
	Impact Testing: Determination of absorbed energy up to 300J	ASTM E23, ISO 148-1	ACCREDITED	5.75J
	Hardness Testing: Determination of Brinell Hardness	ASTM E10, ISO6506-1	ACCREDITED	3.18 HBW
	Bend Testing: Determination of fusion strength between weld metal and base metal	ASME IX, AWS D1.1/D1.1M	ACCREDITED	Not Applicable
	Hardness Testing: Vickers HV0.3; HV5; HV10	ASTM E92/E384, ISO6507-1	ACCREDITED	5.37 HV
	Hardness Testing: Rockwell C- Scale and B-Scale	ASTM E18	ACCREDITED	0.69 HRC
Ferrous & Non-Ferrous Metals	Laboratory spectrometric chemical analysis for determination of C, Mn, P, S, Cu, Ni, Cr, Mo, Nb, V, Ti, Al, As, B, Bi, Ca, Ce, Co, Si, Sn, , Zr, Sb, Pb, Fe, Ta, La, and W by OES	ASTM E415	ACCREDITED	Please Request for uncertainty of measurement if required

Disclaimers:

1. The Test Results relate ONLY to items tested
2. Whilst making every effort to ensure the accuracy of our results, they are without guarantee or warranty.
3. Results marked “Not SANAS Accredited” in this report are not included in the SANAS Schedule of Accreditation for this laboratory.
4. Results marked “Subcontracted Test” in this report are not included in the SANAS Schedule of Accreditation for this laboratory
5. "Opinions and Interpretations" expressed herein are outside the scope of SANAS accreditation.
6. While every endeavour has been made to ensure that the results quoted above are accurate neither IMPLABS nor staff members shall be liable for any error or ommission or for any damage or loss that may arise from the issue of this certificate.
7. This Certificate may not be reproduced except in full, without the written consent of the of IMPLABS.

PLEASE NOTE: SAMPLES WILL BE DISCARDED AFTER 30 DAYS. Testing temperature 23°C±5°C.

DECISION RULE

A result that is a definite pass / fail, will be documented as pass / fail by IMPLABS on the Test Report. Should a result fall within the Guard Band, IMPLABS will state "Result within Guard Band". By taking the Uncertainty of Measurement into considiraton, it is up to the Customer to make the decision on whether a result passes or fails.

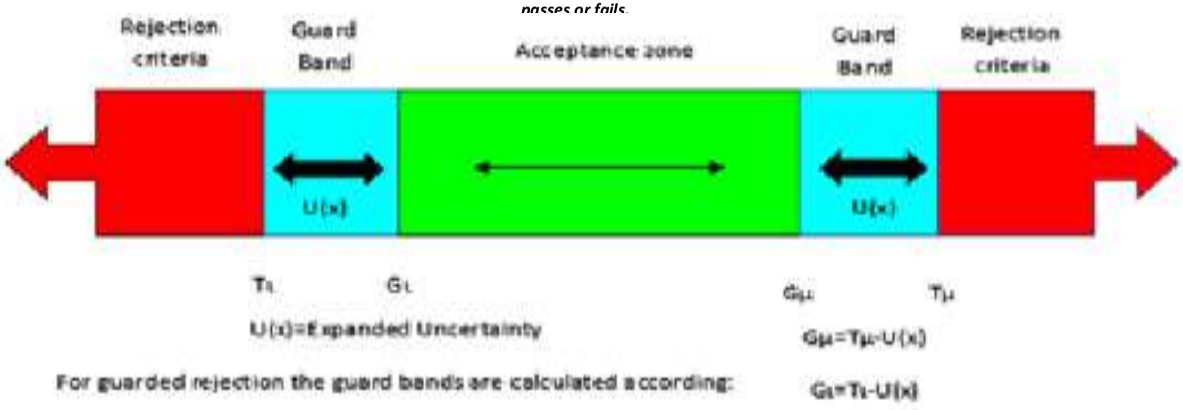

IMP LABS
CK 1996/060917/23

MATERIALS TESTING LABORATORY
Tel: 011 421 9026
www.implabs.co.za | E-mail:admin@implabs.co.za
25 Moore Avenue, Benoni Ext 7

ilac-MRA
sanas Testing Laboratory T0862

Certificate No:	**24-0757**		
Customer:	SCROOBY'S LABORATORY SERVICES		
Attention:	Alan Scrooby	**Order No:**	TBA
Address:	21 O'Reilly Merry Street	**Date Received:**	3-Apr-2024
	Rynfield,1501	**Date Tested:**	3-May-2024
	Benoni	**Date Reported:**	3-May-2024
		Heat No:	N/A
Telephone:	011 425 1074	**Ref No:**	SEE BELOW
Email:	scrooby@scroobyslab.co.za		
Description:	60 x 60mm square block **, As Received.**		

TEST REPORT ISSUED IN ACCORDANCE WITH EN10204 3.1

IMPACT TEST

MATERIAL SPECIFICATION:		NO SPECIFICATION PROVIDED		**TEST METHOD:**	ASTM E23
Test temp. °C:	20	**Charpy V-Notch:**	KV(8)	**Notch Location:**	PARENT METAL

IMPACT RESISTANCE:	**Energy Absorbed (Joules): M6**	**Energy Absorbed (Joules): M3**	**SHEAR (%):**
Specimen 1:	41	36	
Specimen 2:	36	35	
Specimen 3:	38	35	
Specimen Average (J):	38	35	
Specification Average (J):	N/A	**Impact Size (mm):**	10 x 10

Additional information*:*

Juane benjamin Mohr
Digitally signed by Juane benjamin Mohr

Tested by: A. Van Aswegen	**Witnessed by: N/A**	**Technical Signatory:**

RESULT: **N/A**

DOCUMENT ID: QSP 7,8-TC03 **01/07/2020** **REVISION STATUS: 00**

IMP LABS
CK 1996/060917/23

Tel: 011 421 9026
www.implabs.co.za | E-mail:admin@implabs.co.za
25 Moore Avenue, Benoni Ext 7

CERTIFICATE No:	24-0757

Testing was carried out according to IMPLABS procedures.

SCOPE OF TEST METHODS

MATERIALS TESTED	TEST TYPE	METHOD ID	ACCREDITATION STATUS	UNCERTAINTY OF MEASUREMENT (IF APPLICABLE)
METALLIC MATERIALS	Tensile Testing: At room temperature Tensile testing up to 600 kN Determination of tensile strength, yield strength (upper and lower), yield point elongation,0,2% proof stress, elongation and area reduction	ASTM E8/E8M, ISO6892-1	ACCREDITED	12.76 Mpa
	Impact Testing: Determination of absorbed energy up to 300J	ASTM E23, ISO 148-1	ACCREDITED	5.75J
	Hardness Testing: Determination of Brinell Hardness	ASTM E10, ISO6506-1	ACCREDITED	3.18 HBW
	Bend Testing: Determination of fusion strength between weld metal and base metal	ASME IX, AWS D1.1/D1.1M	ACCREDITED	Not Applicable
	Hardness Testing: Vickers HV0.3; HV5; HV10	ASTM E92/E384, ISO6507-1	ACCREDITED	5.37 HV
	Hardness Testing: Rockwell C- Scale and B-Scale	ASTM E18	ACCREDITED	0.69 HRC
Ferrous & Non-Ferrous Metals	Laboratory spectrometric chemical analysis for determination of C, Mn, P, S, Cu, Ni, Cr, Mo, Nb, V, Ti, Al, As, B, Bi, Ca, Ce, Co, Si, Sn, , Zr, Sb, Pb, Fe, Ta, La, and W by OES	ASTM E415	ACCREDITED	Please Request for uncertainty of measurement if required

Disclaimers:

1. The Test Results relate ONLY to items tested

2. Whilst making every effort to ensure the accuracy of our results, they are without guarantee or warranty.

3. Results marked “Not SANAS Accredited” in this report are not included in the SANAS Schedule of Accreditation for this laboratory.

4. Results marked “Subcontracted Test” in this report are not included in the SANAS Schedule of Accreditation for this laboratory

5. "Opinions and Interpretations" expressed herein are outside the scope of SANAS accreditation.

6. While every endeavour has been made to ensure that the results quoted above are accurate neither IMPLABS nor staff members shall be liable for any error or ommission or for any damage or loss that may arise from the issue of this certificate.

7. This Certificate may not be reproduced except in full, without the written consent of the of IMPLABS.

PLEASE NOTE: SAMPLES WILL BE DISCARDED AFTER 30 DAYS. Testing temperature 23°C±5°C.

DECISION RULE

A result that is a definite pass / fail, will be documented as pass / fail by IMPLABS on the Test Report. Should a result fall within the Guard Band, IMPLABS will state "Result within Guard Band". By taking the Uncertainty of Measurement into considiraton, it is up to the Customer to make the decision on whether a result passes or fails.

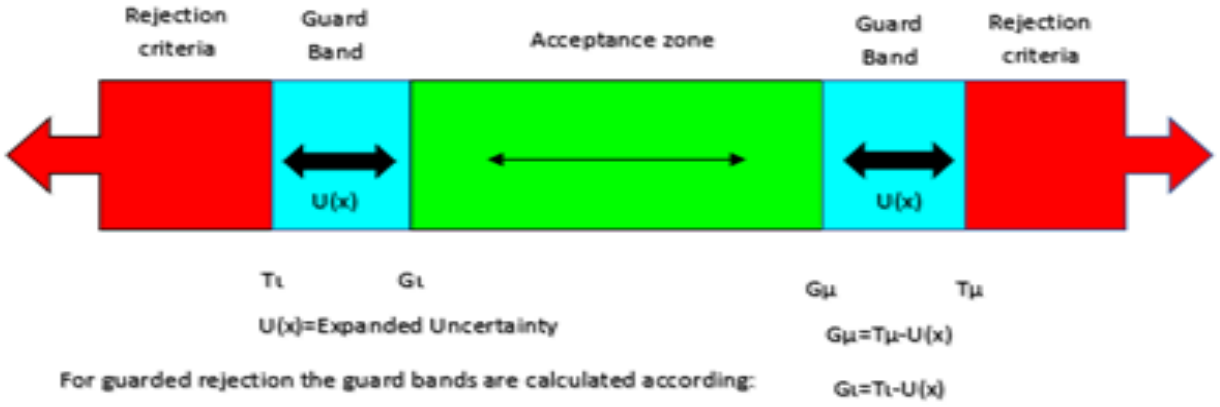

Annex 3 – Sample Holding Jig Design for LSP

LSP JIG 1& 2 VIEW
SCALE 1:1

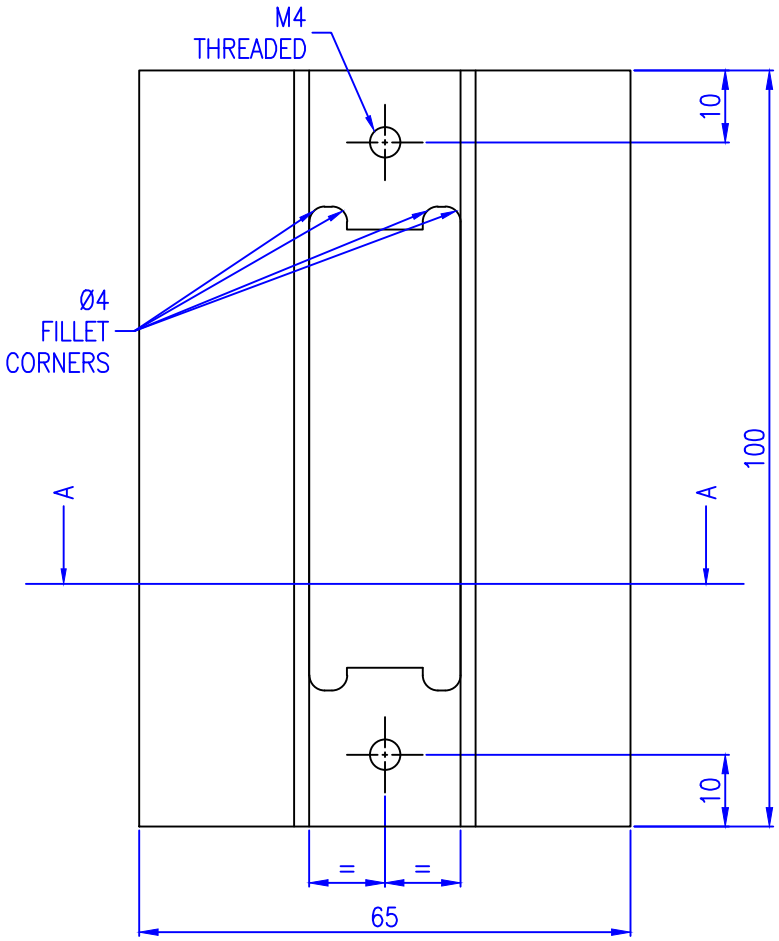

LSP JIG 1 SECTION A–A
SCALE 1:1

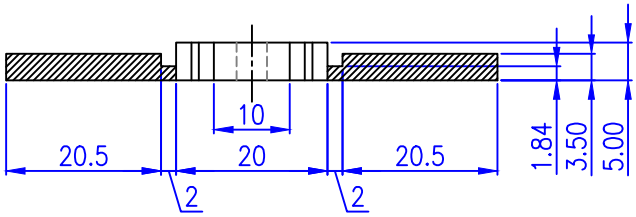

LSP JIG 2 SECTION A–A
SCALE 1:1

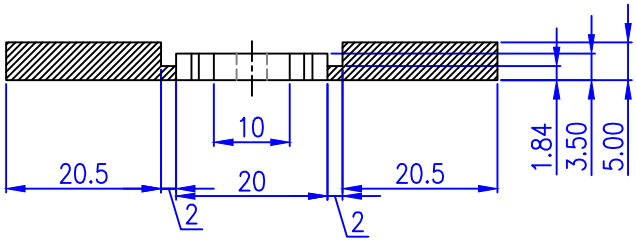

NOMENCLATURE			
PART	MATERIAL	DIMENSIONS	QUANTITY
JIG 1&2	MILD STEEL	PLATE 100x65 5 THK	2

All Dimensions are in mm unless specified otherwise.

DATE: 27/08/2024	DOCUMENT: MSc REPORT – ANNEX 3
SCALE/PAPER SIZE: 1:1 / A4	DRAWING: LSP SAMPLE MOUNTING JIG
DRAWN BY (STUDENT NUMBER): CHUNDUNSING ABHAY NOOKANT NETRAPAL (2634879)	SHEET: 1 OF 1

Annex 4 – Abstracts and Awards

Characterisation of Laser Powder Bed Fusion, As-Built, and Laser Shock Peened Ti6Al4V by Miniaturised Charpy Impact Toughness

Abhay Chundunsing[1], Claudia Polese[1,2], Tristan Strydom[1]

[1]School of Mechanical, Industrial and Aeronautical Engineering, University of the Witwatersrand, 2000 Johannesburg, South Africa
[2]DSI-NRF Centre of Excellence in Strong Materials, hosted by the University of the Witwatersrand, 2000 Johannesburg, South Africa
2634879@students.wits.ac.za; Claudia.Polese@wits.ac.za; Tristan.Strydom@wits.ac.za

Abstract

Laser Powder Bed Fusion (L-PBF) Additive Manufacturing (AM) has been well documented to produce inconsistent material properties during production, affecting part reliability. Traditionally, post-processing heat treatment has effectively been adopted to mitigate these issues. However, the significant increase in production time, resources required and associated costs undermine the advantages and efficient nature of L-PBF AM. An alternative to traditional thermal treatments is Laser Shock Peening (LSP), a mechanical processing technology. LSP can target surface and near-surface aspects, e.g. to close pores and introduce beneficial compressive residual stresses. It can also bring subtle alterations to the intrinsic microstructure of the L-PBF parts by reducing elongated epitaxial grains towards a more equiaxed form, decreasing part anisotropy. Accordingly, with the influence on part properties established, effective control measures need to be set up. Adequate documentation can only be achieved by testing at various levels of complexity. For preliminary testing, an efficient and cost-effective laboratory approach is key to eliminating products with compromised properties. To this end, the Miniaturised Charpy V-Notch (MCVN) impact test was used to assess L-PBF-produced Ti6Al4V samples in this research. The sensitivity of this unconventional testing method was assessed by two preliminary tests each having samples with three varied levels of porosities. Samples were produced on the HYRAX 3D printer using optimum manufacturing parameters but varying hatch distances. A previous study, using an identical manufacturing setup, found certain hatch spacing parameters induced certain porosity levels - the results of which were used to inform hatch spacing parameter selection in the current study. A progressive refinement of the test method first included varied sample porosities of ~ 0% to 10% and then porosities of ~ 0% to 1%. Preliminary results enabled refinement of the main experiment, which consisted of six samples with porosity levels ranging from ~ 0% to 5%. LSP post-processing was also investigated in an attempt to achieve the best potential of the parts produced. Three of the six levels were selected for LSP post-processing. Further tests such as X-Ray Diffraction (XRD), Scanning Electron Microscopy (SEM), Optical Microscopy (OM) and Computed Tomography (CT) scans were carried out. The analysis of Residual Stresses (RS), fractured surfaces, changes in the grain structure and alterations to pore shape and size before and after LSP were observed. Preliminary results have shown that increasing porosity decreases the impact toughness. MCVN tests have been deemed sensitive enough to discern between porosities of ~ 1%. The work suggests that using MCVN tests can provide an effective assessment method early in L-PBF production. The beneficial effects of LSP were also showcased and appraised by MCVN and the complementary assessments as a viable alternative for the overall improvement of the manufacturing technique.

Synertronic Designs

alc
african laser centre

LRI
Laser Research Institute

15th ALC Workshop
November 2024, Stellenbosch

Award

We are honoured to present you with this prize for your achievements and hard work. Photonics remains an exciting field and it is good to see the next generation joining us on the way forward.

With kind regards,

Timo Stehmann (Director, Synertronic Designs (Pty) Ltd)

This is to certify that

Mr Abhay Chundunsing

was awarded a merit prize for

an exceptional presentation at the

15th AFRICAN LASER CENTRE WORKSHOP 2024 STELLENBOSCH

Chairman .....

20 November 2024

Stellenbosch UNIVERSITY IYUNIVESITHI UNIVERSITEIT

SPI Stellenbosch Photonics Institute

Title: Corrosion Behaviour of Conventional Aeronautical Aluminium Alloy 7075 Processed by Laser Shock Peening without Coating

Aluminium alloys are still used in approximately 50-90% of modern airframe structures due to their good mechanical behaviour, ease of design and manufacture. High strength, i.e. peak-aged aluminium alloys are typically selected for conventional primary structures because of their favourable weight/strength ratio and good corrosion resistance. However, these aluminium alloys remain the subject of numerous studies due to their susceptibility to localised corrosion attack in more aggressive environments. Especially in a chloride environment, peak-aged aluminium alloys tend to show increased susceptibility to pitting corrosion and stress corrosion cracking. Therefore, additional surface protection is usually provided by various types of coatings or, in cases in which both mechanical and microstructural enhancements are required, with different surface engineering processing techniques. In this regard, Laser Shock Peening (LSP) is an innovative surface treatment that has attracted interest because of its ability to increase the performance of aluminium aeronautical components and has already been widely approved as a potential substitute for the standard mechanical Shot Peening (SP) technology, for both manufacturing and maintenance. In comparison to SP, the LSP process enables several beneficial effects, such as higher fatigue strength with a delay in fatigue crack initiation and retarded fatigue crack growth due to greater depths of higher compressive residual stresses and enhanced surface finish. Yet, despite several research focused on LSP influence on residual stress fields and fatigue, detailed investigations devoted to a deeper analysis of surface integrity and localised corrosion and stress-corrosion cracking susceptibility is rather limited, especially on heat-treated, peak-aged aluminium alloys. In this work, the corrosion behaviour of a conventional AA7075-T651 after LSP without protective coating was investigated. The laser processing parameters varied were power intensity (1-5 GW/cm2), spot size (diameter 0.8-1.5 mm) and coverage (2.5-40 spots/mm2). For LSPeened samples, Scanning Electron Microscope images showed rough surfaces with areas of re-melting and solidification and some micro-cracks. Energy Dispersive X-ray microanalysis revealed an increase in oxygen content, indicating the formation of an oxide film. Higher surface roughness values were recorded due to intense surface ablation. Electrochemical corrosion tests (open-circuit potential and potentiodynamic polarisation scans) were carried out in 3.5 wt% NaCl solution, with LSPeened specimens tested and compared with the unpeened (baseline) samples under similar conditions. The results showed higher corrosion rates for most LSPeened samples. Relationships between the observed results and LSP processing parameters were identified for microstructure, Knoop and Vickers microhardness and residual stress, helping in reaching a better understanding of the potentials and limits of the without coating LSP process for the aeronautical industry.

A097

Title:

Investigation of Corrosion Behaviour of Aeronautical Aluminium Alloy 7075 Processed by Laser Shock Peening without Coating

Authors & Affiliations:

Shonhai, N.[1,2], Chundunsing, A.N.N.[3,4], Polese, C.[2,3], Cornish, L.A.[1,2] and Ramasawmy, H.[4]

1 School of Chemical and Metallurgical Engineering, University of the Witwatersrand, 1 Jan Smuts Avenue, Johannesburg, 2000, South Africa

2 DSI-NRF Centre of Excellence in Strong Materials, hosted by the University of the Witwatersrand

3 School of Mechanical, Industrial and Aeronautical Engineering, University of the Witwatersrand, 1 Jan Smuts Avenue, Johannesburg, 2000, South Africa

4 Mechanical and Production Engineering Department, University of Mauritius, Reduit, 80837, Mauritius

Abstract:

Laser shock peening (LSP) is a surface treatment aimed at inducing favourable compressive residual stresses in metallic structures, thus improving their fatigue resistance. Therefore, the introduction of LSP technology during production and/or maintenance has the potential to significantly increase the performance of aeronautical components. Due to their good mechanical behaviour, ease of design and manufacturing, aluminium alloys are still representing up to 50-90% of modern airframe structures, even if some are susceptible to localised corrosion.

In this work, the corrosion behaviour of a conventional AA7075-T651 after LSP without protective coating was investigated, varying power intensity (1-5 GW/cm^2), spot size (diameter 0.8-1.5 mm), and coverage (2.5-40 spots/mm^2). For LSPeened samples SEM micrographs showed rough surfaces with areas of re-melting and solidification and some micro-cracks, EDX revealed an increase in oxygen content, indicating the formation of an oxide film and higher roughness values were measured due to intense surface ablation. Potentiodynamic polarisation tests in 3.5 wt% NaCl solution showed higher corrosion rates for most LSPeened samples. Interrelationships between the observed results and LSP processing parameters were drawn, in conjunction with microstructural, Knoop and Vickers microhardness and residual stress data. Further work will include stress corrosion cracking.

Keyword:

Laser Shock Peening without Coating; Corrosion; Aluminium Alloy 7075

A098

Title:

Reaction Characteristics of Laser-induced Graphene-based Hydrogen Sensors Using UV Laser

Authors & Affiliations:

Jinsu Kim, Sungmoo Hong, Bo Sung Shin

Abstract:

Graphene has an sp2 bond structure with three bonds connected to one vertex of each carbon